©Copyright 2013
Megan Karalus

An Investigation of Lean Blowout of Gaseous Fuel Alternatives to Natural Gas

Megan Karalus

A dissertation submitted in partial fulfillment of
the requirements for the degree of

Doctor of Philosophy

University of Washington

2013

Committee:

John Kramlich, Chair

Philip Malte, Chair

Igor Novosselov

Teodora Shuman

Program Authorized to Offer Degree:
Mechanical Engineering

University of Washington

Abstract

An Investigation of Lean Blowout of Gaseous Fuel Alternatives to Natural Gas

Megan Karalus

Co-Chairs of the Supervisory Committee:
Professor John Kramlich
Mechanical Engineering

Professor Philip Malte
Mechanical Engineering

This work examines lean premixed flame stability for multi-component fuel mixtures to support fuel flexibility for industrial combustors. A single Jet Stirred Reactor (JSR), a generic recirculation stabilized combustor, along with gaseous fuels of hydrogen, methane, and hydrogen/methane blends are chosen for the study. Experimental data on blowout are collected and a series of models are used to understand the mechanism of extinction in this recirculation-stabilized flame environment. By studying this more generic combustor, the aim is to develop generalizable results and methodologies for understanding and predicting lean blowout of multicomponent fuels.

Experimental data approaching blowout are taken for fuels of pure hydrogen, pure methane, and hydrogen/methane blends in 10% by volume increments. The data relate inlet equivalence ratios to experimentally measured temperatures for each fuel approaching blowout and reveal the final blowout condition for each fuel. These blowout data are obtained by holding the air flow rate constant and decreasing the fuel flow rate until the flame is extinguished. Doing so holds the flow field and turbulence parameters approximately constant as blowout is approached. The reactor is stabilized to lower equivalence ratios and temperatures as the percentage of hydrogen

in the fuel increases.

In order to gain insight on the mechanism controlling blowout, two dimensional, axisymmetric computational fluid dynamic (CFD) simulations are carried out for the lean premixed combustion of both hydrogen and methane as the fuel. Hydrogen requires only 9 species to fully describe its chemistry. Therefore, the detailed mechanism of Li *et al.* is chosen for the hydrogen simulations. Methane combustion is described by the full GRI-3.0 chemical mechanism with 35 species. To facilitate reasonable computational times a skeletal mechanism of 22 species is developed from GRI-3.0 using the Directed Relation Graph method developed by Lu and Law. The CFD simulations for both hydrogen and methane combustion are run similarly to the experiments. The fuel flow rate is reduced until the CFD model no longer produces a burning solution. Contour plots from the CFD model illustrate the evolution of the flow-field, temperature profiles, and flame structure within the JSR as blowout is approached for both fuels. The modeling suggests that lean blowout in the JSR does not occur in a spatially homogeneous condition, but rather under a zonal structure. Analysis of the models from the perspective of a combusting fluid particle traveling through the jet, into the recirculation zone, and then entraining back into the jet suggests that the blowout condition is dependent on the development of the pool of radicals. The flame remains stable as long as the radical pool develops significantly enough to achieve ignition before the hypothetical combusting fluid particle is re-entrained. As the fuel flow decreases, the induction period increases and the ignition event is pushed further around the recirculation zone. Eventually, the induction period becomes so long that the ignition is incomplete at the point where the recirculating gas is entrained. This threshold leads to overall flame extinction.

Two Chemical Reactor Network (CRN) models are developed using the flow field and reaction fields from the detailed CFD models in an attempt to capture the bulk

of the physical processes responsible for flame stability. The single Plug Flow Reactor (PFR) model follows the concept of the hypothetical combusting fluid particle and assumes that only convective transport is responsible for stability. This model matches hydrogen blowout well, reproducing the ignition event and the development of the pool of radicals before re-entrainment. While the single PFR model with the UCSD chemical mechanism does predict the blowout temperature across the full range of methane/hydrogen fuel blends well, it fails to adequately predict blowout equivalence ratio for fuels with high methane concentrations.

A two PFR model is subsequently developed in which the core jet region (of constant mass flow) exchanges mass with the recirculation region through turbulent diffusive transport. Entrainment of flow by jet action is confined entirely to the recirculation region, represented by the exhaust of the recirculation PFR being convectively re-entrained at its entrance. The two PFR model performs about as well as the single PFR model in predicting blowout for hydrogen in the JSR and shows significant improvement over the single PFR model in both following the experimental data approaching blowout, and predicting the blowout condition for methane. In fact the two PFR model shows good agreement with both equivalence ratio and temperature at blowout across the full range of H_2/CH_4 blends.

Regardless of the chemical mechanism applied, or whether we consider transport by convection only as in the single PFR model, or transport by both convection and diffusion as in the two PFR model, the story regarding the onset of blowout remains the same and is consistent with that given by CFD as well: the key to the stable operation of the reactor is the ignition event in the recirculation zone, resulting in the development of the radical pool. For pure hydrogen combustion as the fuel flow rate is reduced and the reactor moves towards blowout the destruction of the fuel slows and spreads, and the development of the radical pool moves further around

the recirculation zone. The radical pool must develop (i.e. ignition must occur) before re-entrainment or the reactor will extinguish. For methane we similarly see the destruction of methane spread, and the net production of CO, and subsequently the net production of OH move further around the recirculation zone until the re-entrainment of radicals can no longer sustain the combustion. For methane, transport of the CO and radicals through turbulent diffusion appears to be a controlling process in this ignition event. The ignition event for hydrogen, on the other hand, is affected very little by the inclusion of diffusive transport of radicals. This is most likely due to the fact that the breakdown of hydrogen directly produces an H radical that feeds the chain propagating reaction, however the direct breakdown of methane has no such feedback. It is only in the destruction of methane intermediates that the H radical needed to feed the chain propagating reaction is produced.

ACKNOWLEDGMENTS

My warmest thanks to both of my Co-advisors, Professors John Kramlich and Philip Malte. I am deeply grateful for their patience, guidance, encouragement, and friendship. Thank you too to Dr. Igor Novosselov for sharing the science and art of computational fluid dynamic modeling. And thank you to Professor Teodora Shuman for being my mentor.

I wish to thank my fellow graduate students for their intellectual and moral support as well as their friendship. In particular thank you to Boyd Fackler, Shazib Vijlee, Heather Dillon, Kristen Thyng, and Patrick McGah.

Financial support for this project was provided by the California Energy Commission through the University of California-Irvine. I wish to acknowledge Marla Mueller, the technical lead, and Vincent McDonell, who is Project Manger at UC Irvine. I would also like to thank the Seattle Chapter ARCS Foundation and the Department of Mechanical Engineering for additional financial support during my graduate studies.

Finally, I would like to thank my husband, Chris, for his love and support, for being my never failing friend, and for being my on-call systems administrator and mathematical and computational adviser. And thank you to my parents, and my sister and brother for their love and support throughout my time at the University of Washington.

DEDICATION

To all of the educators in my life.

For inspiring curiosity and instilling perseverance.

TABLE OF CONTENTS

LIST OF FIGURES

LIST OF TABLES

Chapter 1
INTRODUCTION

1.1 Overview and Motivation

Premixed flame stabilization in high intensity combustion is an important topic of study for the high efficiency and low emission operation of gas turbine combustors and industrial furnaces. Current lean premixed (LPM) combustion technology primarily focuses on burning natural gas. In the future, however, industrial combustion devices will be run on a variety of fuels and fuel blends. These alternative fuel blends will have a wide range of heating values, flame speeds, and compositions ranging from syngases with high H_2 content to landfill and digester gases, mainly composed of CH_4, CO_2, and N_2. The largest barrier to the fuel-flexibility of most combustors is the large differences between natural gas and the proposed replacement fuels in terms of heating values, flame speeds, and chemical kinetic properties. Regardless of which fuel is used, an end-user must meet the current emissions regulations which often means running very near the lean blowout of a system. Blowout, however, continues to be a phenomenon that is difficult to predict across reactor types and fuel compositions. Determining phenomenological correlations or developing simplified models to describe the lean blowout behavior of combustors under various fuel compositions is important to furthering the implementation of fuel-flexible technologies.

This study focuses on blowout in LPM combustion devices with an emphasis on the effects of varying fuel composition. All data and modeling are conducted on an atmospheric pressure, single-jet stirred reactor (JSR). It is a good candidate for studying the lean blowout of premixed fuels as applicable to industrial burners for two basic reasons: (1) stirred reactors have been used since the 1950's by researchers such

as Longwell and Weiss to understand stabilization in high intensity combustion [1, 2], and (2) much like a gas turbine combustor, JSRs have two distinct flow features - a jet (i.e. shear layer) and a recirculation zone. As with both the aerodynamically swirled and bluff body combustors common in industrial burners, the flame is stabilized by the recirculation zone.

This work is motivated in part by preliminary data taken by Fackler [3]. Although Fackler focused on emissions from the LPM combustion of alternative fuels, he also obtained blowout data on several alternative fuels of interest to industry on the JSR used in this study. These various alternative fuels can be broken down into five categories, which are listed in Table 1.1 with sample fuel compositions for each. Figure 1.1 shows the agreement between Fackler's data and the work of Longwell and Weiss [1, 2]. It is clear from this graphic that fuel type or composition is an important factor in experimental correlations of blowout. There appear to be three categories of behavior: hydrocarbons (CH_4,C_2H_6, Iso-octane), hydrogen and H_2/CO blends, and methane with diluents.

To further motivate the work, let us examine a fuel in each of the categories listed above. The simplest way to model blowout is to assume the reactor volume is homogeneously mixed and can therefore be approximated as a 0-Dimensional reactor, also known as a Perfectly Stirred Reactor (PSR). Modeled blowout is then found by fixing the mass flow rate and inlet equivalence ratio at the values measured experimentally at blowout and reducing the volume until combustion is extinguished. This is done with several different chemical kinetic mechanisms where applicable (all of which are reviewed below). In addition, heat loss is applied, the rate chosen to match that found in the experiments, 20% of the energy input [3]. As can be seen from Figure 1.2, only for the H_2/CO mixture does the experimental data of measured temperature and actual reactor volume fall near the modeled blowout volume and temperature. For the other three fuels the modeled blowout volume and temperature is significantly different from that measured experimentally. Barat [4] suggests this discrepancy is

Table 1.1: Summary of gas compositions plotted in Figure 1.1 adapted from Fackler [3].

Category	Source	H_2	CO	CH_4	CO_2	N_2	C_2	C_3
1	High H_2	100						
2	Process and Refinery			50			50	
3	Gasified Coal/Petcoke (O2 Blown)	45	45		10			
4	Landfill and Digester Gas			50	35	15		
5	LNG/Shale/Associated Gas			75			25	

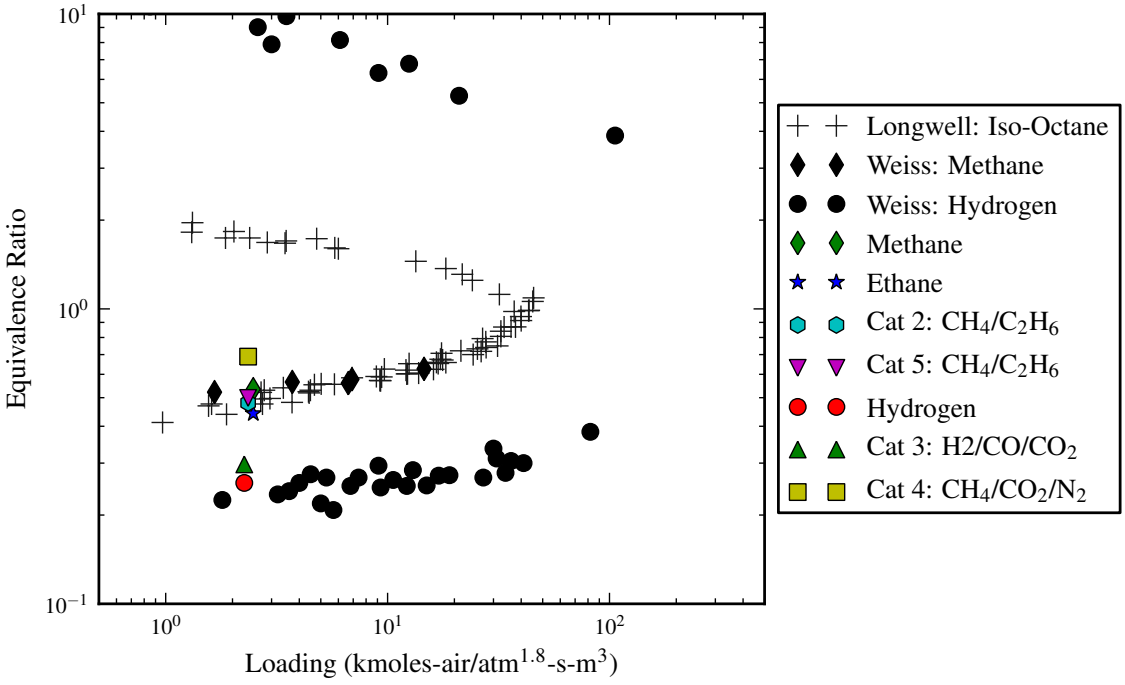

Figure 1.1: Blowout data from Fackler [3] plotted on blowout data from Longwell and Weiss [1, 2]. All data not labeled as Longwell or Weiss is attributed to Fackler.

due to the fact that as global extinction is approached the actual reactive volume is reduced due to mixing limitations. For this JSR, despite the fact that the 'mixing' for each fuel is approximately constant because of the constant air flow rate across experiments, the 'reactive volume' is not. This simple example illustrates that the problem of predicting blowout in a single reactor for a wide variety of fuels is non-trivial.

Finally, Fackler [3] notes that when blowout is approached in the JSR with hydrogen rich fuels a distinct "popping" is heard. He theorizes that the popping is due to extinction/reignition events but he does not attempt to characterize these time localized acoustic events. These acoustic events in time are not heard when approaching blowout with methane rich fuels in our JSR. Very little has been reported in the literature regarding such behavior near blowout although Nair and Lieuwen [5] as well as Muruganandam and Sietzman [6] report a similar phenomena for bluff body and swirl stabilized combustors burning methane. Instabilities such as these are very undesirable in industrial combustors, they therefore need to be characterized and their origins explored.

1.2 Literature Review

The literature review is divided into three sections. The first section focuses solely on blowout, specifically experimental correlations of blowout data. The second section provides definitions and literature coverage of Chemical Reactor Network (CRN) modeling to provide background for this dissertation. The third reviews the comprehensive and multicomponent kinetic mechanisms currently available.

1.2.1 Experimental Correlations for Blowout

Most work done to date in predicting blowout has relied on experimental correlations of blowout data. In the literature, three basic characterizations of the physical phenomena responsible for blowout have been discussed and as noted by Glassman [7] all three can be reduced to a similar correlation relating blowout to a Damkohler number

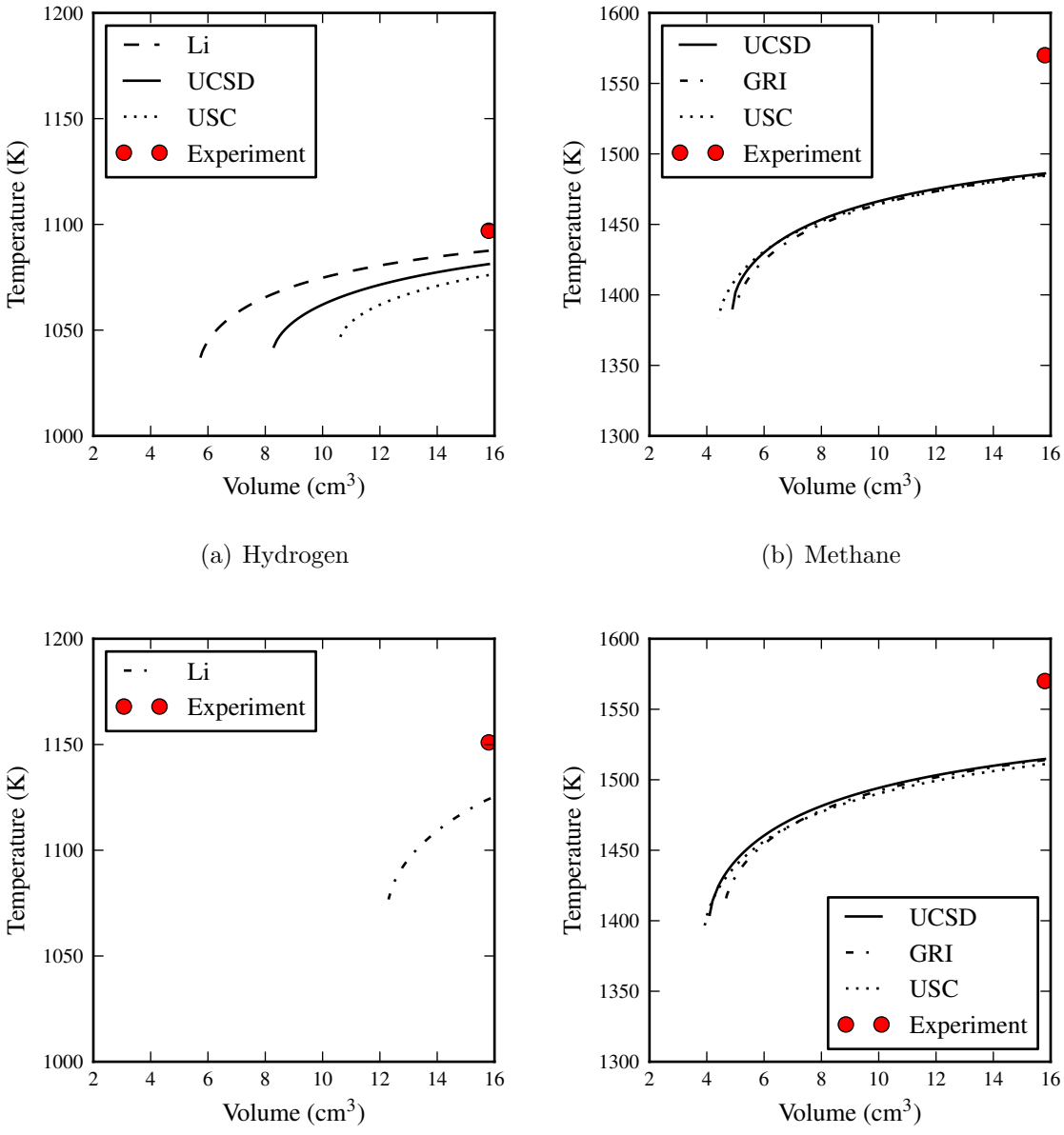

(a) Hydrogen

(b) Methane

(c) Category 3: $H_2/CO/CO_2$

(d) Category 4: $CH_4/CO_2/N_2$

Figure 1.2: Comparing a PSR model to experimental blowout data from Fackler [3].

(i.e. a ratio of fluid dynamic or residence time to a chemical time). Longwell *et al.* [8] suggested that stabilization is accomplished through the entrainment and ignition of fresh reactants into the recirculation zone with blowout being determined by the balance between the rate of burning and the rate of entrainment. Zukoski and Marble [9, 10] proposed that at the blowout condition the free-stream combustible mixture has a contact time with the wake behind the stabilizer equal to the ignition time associated with the mixture. Finally, Yamaguchi *et al.* proposed a flamelet description based on local extinction due to flame stretch [11]. The discussion that follows illustrates the fact that these experimental correlations tend to be reactor specific (e.g. bluff body vs. swirl), geometry specific (e.g. axisymmetric vs. 2D bluff body), and fuel type specific.

A large body of literature exists on experimentally measuring and correlating blowout limits for bluff body and swirl stabilized combustors [12, 13]. Most recently, Shanbhogue *et al.* have compiled 536 data points from the literature on bluff body blowout data for hydrocarbon fuels (propane, gasoline, diesel oil, and LPG). They showed that the blowout data can be reduced to a basic Damkohler correlation as a function of a Reynolds number, although the specific correlation was still somewhat dependent on reactor geometry (axisymmetric vs. 2D bluff bodies) [12]. Zhang [14, 15] and Noble [16] have explored correlating blowout limits for non-hydrocarbon fuels. They collected blowout data on a swirl stabilized combustor for various syngas compositions (H_2/CO/CH_4). Application of a simple Damkohler number correlation to the data showed blowout occurred at a nearly constant value of Damkohler number for low to medium H_2 mixtures (up to about 50%). High H_2 mixtures showed a blowout Damkohler number trend that was monotonically decreasing with increasing H_2 content. Noble suggested that the change in blowout Damkohler number for high H_2 mixtures may be due to preferential diffusion effects. Calculating the mixture properties (i.e. chemical time scale) using an adjusted equivalence ratio resulted in the determination of a constant blowout Damkohler number across the fuel range [16].

Akbari [17] applied the same technique to correlate blowout for CH_4/H_2 blends in an atmospheric high swirl combustor.

In 1955 Longwell and Weiss published a seminal work correlating blowout equivalence ratio and reactor loading parameter in what was later dubbed the "Longwell reactor" [1]. Iso-octane was the fuel of choice for the 1955 paper, but in 1958 Weiss *et al.* extended the work to a variety of other fuels including methane and hydrogen [2]. All three fuels are plotted in Figure 1.1, illustrating the fact that H_2 behaves very differently than its hydrocarbon counterparts.

1.2.2 Chemical Reactor Network Modeling

Begining in the 1950's, engineers began using chemical reactor models to understand the combustion process. Bragg [18] introduced the concept of modeling a combustor by a Perfectly Stirred Reactor (PSR) to represent the flame zone, followed by a Plug Flow Reactor (PFR) to capture the burn-out section. The PSR and PFR are the two fundamental reactor types used in Chemical Reactor Network Models (CRNs) and are defined below.

1. Perfectly Stirred Reactor (PSR) in which perfect mixing is achieved (the ratio of mixing to chemical times is zero [19]). It operates under steady state conditions and is considered a 0-D model.

2. Plug Flow Reactor (PFR) in which a non-mixing plug of gases flows steadily through the reactor. It operates under steady state, steady flow conditions and is considered a 1-D model.

These two reactor types are described in detail by Turns [20]. A third reactor type is a Partially Stirred Reactor (PaSR), which is also referred to as a Well-Stirred Reactor by Swithenbank [21]. Fundamentally the PaSR addresses the interaction between chemical reactions and turbulence. While the only fluid dynamic influence in a PSR

is the reactor residence time, a PaSR is controlled by both the reactor residence time and the turbulent mixing time. The PaSR can also be thought of as 'bounded' by a PSR and PFR model. Under very fast mixing, the contents of a PaSR will be homogeneous and the PaSR's behavior will limit to that of a PSR. Under very slow mixing or no mixing at all, the pockets of gas in the PaSR will remain segregated and evolve in time as though each flows through a PFR.

There are two implementations of a PaSR, the first being Swithenbank's Well-Stirred Reactor (WSR) which was originally developed by Vulis [22]. In this development the WSR can be thought of as a PSR with an effective reaction rate, k_{eff}, such that $k_{eff} = 1/(\tau_D + \tau'_K)$ where τ_D is the mixing time due to turbulence and τ'_K is the kinetic time defined as the inverse of the temperature dependent kinetic rate. This has been used by both Swithenbank [21] and Sturgess [23, 19] in modeling diffusion flames. The second implementation uses a probability density function to describe the composition and temperature in the PaSR. Therefore a joint PDF transport equation must be solved and a molecular mixing closure model such as Curl's or IEM chosen [24].

Using the reactors described above, many reactor networks have been developed to describe two basic categories of combustor behavior: blowout and pollutant emissions. A summary of these findings is given in Table 1.2. The initial work on predicting blowout focused on non-premixed combustion of hydrocarbons in gas turbine can combustors. The work of Swithenbank [21] in this area advanced the idea of zonal-combustion such that the two-reactor model proposed by Bragg [18] was extended to 7 or more. With advances in CFD, Sturgess [23] then proposed a hybrid modeling approach in which CFD aided in defining the zones for the reactor network. He too worked on non-premixed combustion and gas turbine can combustors. Barat [4] showed for a variety of premixed fuels that the Toroidal Jet-Stirred Reactor (TJSR) - developed by Nenninger [25] - did not perform as a perfectly stirred reactor near blowout. In fact, experimentally TJSR's extinguish at higher temperatures and longer

residence times (or larger volumes) than those predicted by a PSR model. As a result, Barat suggested that as global extinction is approached the actual reactive volume is reduced due to mixing limitations. Strakey *et al.* [26] on the other hand used a single PSR to predict the equivalence ratio at blowout for CH_4/H_2 mixtures in a Low Swirl Stabilized Combustor. The residence time was chosen to reproduce the lean extinction data for pure methane. The hydrogen concentration was then varied over the range of experimental values (0% to 80%) and a new extinction equivalence ratio found. They saw reasonable agreement between the measured and predicted extinction equivalence ratios. Although, it should be noted that this is in contrast to the findings of Zhang and Noble [14, 15, 16], and Akbari [17].

As the focus of CRN work moved from the prediction of blowout to the prediction of emissions, several advances in the development of CRNs and their application were made. For instance, Longwell [27] also recognized the non-PSR like behavior of the TJSR and proposed a single PaSR model to predict exhaust gas compositions for the TJSR. To predict emissions for a Turbulent Jet Diffusion Flame (TJDF), Broadwell and Lutz [28] suggested a two reactor model, claiming that the reaction happens primarily in the shear region of the jet. This is also referred to as the coherent flame model. Fuel moves from the core to the flame sheet (shear region), and products move from the flame sheet into the core by diffusion. It is proposed that this process can be fully approximated by replacing the flame sheet at every axial location by a perfectly stirred reactor and the core by a plug flow reactor with the diffusion process accounted for by equivalent convective flows. The residence time of the flame sheet is then a model input, and this value scales with the Reynold's number of the jet. Finally, Novosselov [29] advanced the idea that a CRN can require a large number of elements with his 15 element network predicting NOx formation for a gas turbine can combustor and Monaghan [30] took this idea even further with a 1114 element network of PSRs to predict CO and NOx formation in the Sandia D jet flame.

Table 1.2: Summary of Chemical Reactor Network Modeling for gaseous combustion. Reactor Type Acronymns: Toroidal Jet Stirred Reactor (TJSR), Gas Turbine Can (GTC), Low Swirl Combustor (LSC), Turbulent Jet Diffusion Flame (TJDF).

Author	Year	Number of Elements	Element Types(s)	Premixed?	Reactor Type	Fuel Type	Reactor Mass Exchange
Blowout							
Swithenbank [21]	1970	7	WSR, PFR	No	GTC	Propane	Convection
Barat [4]	1992	1	PSR	Yes	TJSR	H_2/CO, CH_4, C_2H_4	
Sturgess [23]	1996	8	PSR, PFR	No	GTC	JP5/JP8/JP-A	Convection
Strakey *et al.* [26]	2007	1	PSR	Yes	LSC	CH_4/H_2	
Emissions							
Longwell [27]	1989	1	PaSR	Yes	TJSR	H_2/CO, C_2H_4	
Broadwell [28]	1998	2	PSR, PFR	No	TJDF	H_2/CO, CH_4	Convection & Diffusion
Bass [31]	2003	1	PaSR	Yes	TJSR	C_2H_4	
Novosselov [29]	2006	15	PSR, PFR	Yes	GTC	CH_4	Convection
Monaghan [30]	2012	1114	PSR	No	TJDF	CH_4	Convection & Diffusion

1.2.3 Chemical Kinetic Mechanisms

A large number of reaction mechanisms have been published in the literature. Many of these are for a single component fuel (e.g. H_2), and claim to describe only a single combustion phenomena (e.g. ignition delay) over a limited parameter space. Few are comprehensive, describing a large parameter space and combustion phenomena, and few are multicomponent. Table 1.3 summarizes the mechanisms that are both comprehensive and multicomponent. As Li points out in [32], it is important to keep in mind when evaluating mechanisms that the "comprehensive" label does not imply "completeness" or "uniqueness" and thus two mechanism with different elementary reactions and rate parameters can produce the same result. In addition we see improvements in both experimental observations and kinetic information in the literature over time. Thus there is no one "right" mechanism and revisions of these mechanisms are likely to be necessary in perpetuity.

Table 1.3: Detailed mechanisms for multicomponent fuels.

Name	Fuels	Species (w/o NOx)	Reactions (w/o NOx)	Release Date
GRI-3.0[33]	$H_2/CO/CH_4/C_2H_6$	36	219	2000
UCSD [34]	H_2/CO/C1-C3	46	235	2005
USC [35]	H_2/CO/C1-C4	111	784	2007
Li *et al.* [32]	$H_2/CO/CH_2O/CH_3OH$	18	84	2007

GRI is the baseline mechanism for hydrocarbon combustion developed by researchers under the funding by the Gas Research Institute. It was designed to predict NOx formation for natural gas flames under industrial combustion conditions. The approach used to develop GRI [33] is summarized below from Frenklach [36]:

1. Assemble a reaction database of a complete set of elementary reactions.

2. Assign values to their rate constants from the literature or judicious estimation. Treat temperature and pressure dependences. Evaluate error limits and the thermodynamics used for the equilibrium rate constants.

3. Identify experimental data that depend on some or all of the rate and transport parameters in the model.

4. Model the experimental data with the given reaction kinetics. Also apply sensitivity analysis to determine how the model rate constants affect the final result.

5. Choose experimental targets that are sensitive to a representative cross-section of the rate parameters. Select the parameters making the largest impact on a given target.

Targets for optimization of fuel oxidation include: shock-tube ignition delay measurements; shock-tube species profile measurements for CH_3, CO, and OH; concentrations of CO_2 in a flow reactor; laminar flame speeds for fuels CH_4, $CO-H_2$, and C_2H_6. GRI was optimized for a temperature range of 1000 to 2500 K, pressures of 10 Torr to 10 atm, and equivalence ratios of 0.1 to 5 for premixed systems [33]. Cautious use of GRI outside this range is reasonable and it has been used extensively in the literature to model a wide range of combustion phenomena over large parameter spaces. In addition GRI is optimized for methane and natural gas as a fuel and thus includes additional hydrocarbons found in natural gas (e.g. ethane and propane), however on the release page for GRI-Mech 3.0 it states: "GRI-Mech should not be used to model the combustion of pure fuels such as methanol, propane, ethylene, and acetylene even though those compounds are on the GRI-Mech species list" [33].

The UCSD [37] mechanism was developed as a "small" comprehensive mechanism. For instance to describe the same same chemistry in GRI (H_2/CO/C1), UCSD has only 30 species and 134 steps compared to 36 species and 219 steps in GRI. The

mechanism is built upon a base of well-validated and tested submechanisms for hydrogen, carbon monoxide, methane, methanol, ethane, ethylene, acetylene, propane, propene, allene, and propyne combustion. The mechanism is designed for pressures under 100 atm, temperatures above 1000 K, and equivalence ratios under 3. It is validated with shock-tube ignition delay measurements, laminar flame speeds, diffusion flame structure measurements and flow-reactor data [31].

In contrast, the USC [35] mechanism is much larger. It was developed and optimized similarly to GRI [38] and is based in part on the kinetic parameters from GRI-3.0 and GRI-1.2 in addition to an updated H_2/CO mechanism [39], an acetylene and ethylene submechanism [40], a more general C3 submechanism [41] and finally a 1,3-butadiene oxidation submechanism [42]. It has been validated against ignition delay measurements, shock tube species profiles, laminar flame speeds, flow reactor, and burner stabilized flame data. The parameter space of validity is not specified in the mechanism documentation.

The mechanism by Li *et al.* describes H_2 combustion with 9 species and 19 reactions, H_2/CO combustion with 11 species and 31 reactions, and mixtures including formaldehyde and methanol with 18 species and 84 reactions in total. It too is developed similarly to GRI and is validated against data from shock tubes, flow reactors, and laminar premixed flames. No general parameter space of validity is given for the mechanism, although the parameter space over which it is validated is given. For the H_2 only mechanism it is equivalence ratios from 0.25 to 5.0, temperatures from 298-3000 K and pressures from 0.3 to 87 atm [43]. For CO it is given as equivalence ratios from 0.4 to 6.1, temperatures from 300 to 3000 K and pressures from 0.15 to 9.6 atm. Similar ranges are given for CH_2O and CH_3OH.

Very little direct comparison of mechanisms has been done in the literature. Kochar *et al.* in [44] compared USC and UCSD mechanisms in predicting laminar flame speed measurements for propane/air mixtures with varying carbon dioxide and nitrogen dilution and found the two mechanisms to be in close agreement. In

addition, GRI-3.0 and UCSD are compared for laminar flame speeds of methane and ethane-air mixtures. Again, GRI-3.0 and UCSD are found to be in close agreement. Bergthorson and Dimotakis [45] compare GRI-3.0, UCSD, and USC mechanism in modeling premixed methane, ethane, and ethylene stagnation flames. They find that GRI-3.0 does well for methane and ethane flames but not ethylene flames (although it was not optimized for ethylene), that USC yields reasonable agreement for stoichiometric and rich flames but consistently underpredicts the flame speed for lean conditions for all fuels, and finally that UCSD yields the best overall agreement with the experimental data for all three fuels. Finally Strakey *et al.* [26] suggest that GRI-3.0 significantly underpredicts the laminar flame speed for pure hydrogen, and therefore will not adequately capture lean extinction for pure hydrogen combustion. For hydrogen, Ò Connaire [46] showed that GRI overpredicts the ignition delay time for pure hydrogen, and the work of Weydahl [47] suggested that Li is one of five candidate mechanisms better adapted to hydrogen than GRI.

1.3 Research Objectives

The literature review above illustrates that the majority of the effort on understanding blowout to date has focused solely on hydrocarbon fuels from traditional, fossil fuel sources. In addition, progress in developing predictive correlations for blowout has far surpassed progress in predictive modeling tools. Therefore, the purpose of this work is to develop simple modeling tools for predicting lean blowout of both hydrocarbon fuels and alternative multicomponent fuels. Doing so requires further understanding of the mechanism of lean blowout and experimental validation. By studying a simplified and more generic recirculation stabilized combustor (e.g. the JSR), the aim is to develop generalizable results and methodologies.

The objectives of this research study include:

- Experimentally determine blowout for CH_4/H_2 blends in the JSR.

- Characterize the time-localized acoustic events which are precursors to hydrogen blowout.
- Develop a CH_4 skeletal chemical kinetic mechanism for CFD applications.
- Use CFD and CRN modeling of the JSR to characterize the blowout behavior of H_2 and CH_4 as fuels.
- Establish and validate a methodology for developing a CRN from CFD to predict blowout for both H_2, CH_4 and H_2/CH_4 blends.

Chapter 2
SKELETAL MECHANISM

Computational Fluid Dynamics (CFD) simulations of lean-premixed (LPM) combustion must combine complex kinetics with descriptions of the fluid dynamics and heat and mass transfer in the modeled reactor. Because of the significant computational costs associated with large mechanisms, inclusion of detailed chemistry requires reduction. A review by Tomlin, *et al.* [48] identifies three main mechanism reduction strategies: (1) mechanism reduction without time-scale analysis, (2) reduction considering time-scales, and (3) fitted kinetic models. While the terms *skeletal*, *reduced*, and *global* have been used interchangeably to describe various simplified mechanisms in the literature, the following definitions will be employed when discussing mechanism reduction here.

1. *skeletal* mechanism: from an established full mechanism without time-scale analysis and without alteration of the elementary Arrhenius reaction rates in which redundant reactions have been removed.

2. *reduced* mechanism: from a skeletal or full mechanism with time-scale analysis, employing the Quasi Steady State Approximation (QSSA) and Partial Equilibrium (PE) Assumption.

3. *global* mechanism: derived using intuition and the 'fitting' of parameters for one or more reactions to experimental data or detailed kinetic simulations.

2.1 Review of Reduction Strategies

The following provides a brief description of the methods employed for each level of mechanism simplification, advantages, disadvantages, and literature references.

2.1.1 Skeletal

If one begins with a comprehensive chemical mechanism, the first level of simplification is to a skeletal mechanism. This is accomplished by first determining the parameters of interest, (typically heat release, or *important* species concentration profiles) and second, identifying and eliminating *redundant* species and elementary reactions. There are three basic methods for identifying the *redundant* species: detailed reduction, sensitivity analysis and directed relation graph (DRG).

The detailed reduction method, developed by Wang and Frenklach [49] identifies reactions which do not contribute to the accumulation/depletion of the *important* species by comparing individual reaction rates with a reference reaction, typically the rate limiting step or fastest reaction. They further proposed that the computations used to obtain the data required for this analysis did not need to be performed with a fully coupled fluid-dynamic/chemical-kinetic model, but simplified 0-D and 1-D models would suffice. The method is based on the assumption that if a skeletal reaction mechanism can accurately describe the time evolution characteristics of both thermal and chain reaction processes of a more complex mechanism, then it will describe the chemical processes to the same degree of accuracy in reactive flow simulations.

Nicol [50] applied the detailed reduction method of Wang and Frenklach, but pointed out that the generalization of this method to processes of varying chemical time scales (e.g. the inclusion of NOx formation) had not been demonstrated. Nicol modified the method, including results from both a 0-D Chemical Reactor Network Model (CRN) and a Laminar One-Dimensional Model (L1DM) to eliminate redundant species. As reactions were subsequently combined, the Arrhenius rate coefficients of

the final reactions were modified slightly to improve agreement between the skeletal and full mechanism, resulting in more of a quasi-global rather than true skeletal mechanism.

In keeping with the idea of the detailed reduction but applying an alternative mathematical technique, the redundant species can also be determined by investigating the Jacobian of the kinetic system of ODEs. The Jacobian and normalized Jacobian will show information about the concentration of species in relation to the rate of production of *important* species. The detailed method of Wang and Frenklach requires several simulations of different reduced order models each time a species is eliminated, while the alternative mathematical approach requires a single simulation of the original model with the Jacobian calculated at several reaction times. While the alternative method may be more computationally efficient it cannot be used to investigate the effects on other important features such as ignition time [48].

Sensitivity analysis is the formal and mathematically rigorous approach to simplifying mechanisms. It is used to investigate the output of models as a function of parameters. For example, the *local sensitivity coefficients* are defined as the partial derivatives of each species concentration with respect to the chemical rate constants (the parameters of interest). A rate is then perturbed at time t_1 and the resulting change in species concentrations studied at time t_2 [48]. The normalized sensitivity coefficients indicate the relative importance of each reaction to species concentration [51]. The CHEMKIN-II post-processing program KINALC includes SENKIN which provides sensitivity analysis functionality. ChemkinPro provides the ability to evaluate first-order sensitivity coefficients of the gas temperature, and species fractions.

The method of DRG, developed by Lu and Law [52] maps each species in a detailed mechanism to a node in directed graph. An edge is then drawn between two species if the two species are strongly coupled through reactions. The edges are weighted and this weight can be compared to a specified error tolerance to determine if the edge should be removed. By removing edges based on a specified error tolerance, groups

of coupled species will be removed from the graph and subsequently the elementary reactions associated with them. Unlike in detailed reduction, the Arrhenius rates of the elementary reactions are never altered and unlike in sensitivity analysis the method does not require iteration. Further details are discussed in Sections 2.3 and 2.3.1.

2.1.2 Reduced

Further reduction requires two assumptions - quasi-steady state for species, and partial equilibrium for reactions - which generally allow some species to be related by algebraic equations. There are three basic reduction methods applying these assumptions: Quasi-Steady State Approximation (QSSA), Computational Singular Perturbation (CSP), and the slow manifold approach (intrinsic low-dimensional manifold, ILDM). All three of these methods rely on the idea that there are certain modes in the model equations which work on a faster time-scale than others, and therefore may be decoupled. Separating the time-scales reduces both the size and stiffness of the reaction mechanism.

The QSSA method is a well established technique, relying on both chemical intuition and mathematical analysis for the identification of quasi-steady state species and reactions in partial equilibrium. Peters has produced a number of reduced mechanisms for different fuels based on this method [53, 54]. Reduced mechanisms based on the QSSA method are derived from homogeneous systems but applied to spatially distributed systems where error propagation can be important. Yannacopoulos, *et al.* give a qualitative description of these possible errors [55]. They find that the error introduced depends significantly on the spatial gradients, with larger gradients introducing larger errors. They also comment that the error will blow up for some nonlinearities and some advection velocities. Law, *et al.* points out that these errors, the result of the deterioration or failure of the QSS assumption in certain regions of the computaitonal domain (e.g. the low temperature flame zone), can lead to

convergence problems in CFD simulations [51].

While the QSSA method was introduced in the mid-twentieth century, the CSP and ILDM methods have only been in use for the last 20 to 30 years. Unlike QSSA, the latter methods establish partial-equilibrium and quasi-steady state relationships without using any chemical intuition or expertise, but rather provide complex numerical methods to automate the process. The CSP method produces a reduced mechanism of a similar form to that found with the QSSA method. Lu and Law point out several flaws in how QSS species are identified empirically in the QSSA method and claim that by using CSP to rigorously identify QSS species, some of the numerical difficulties discussed above can be abated [56]. It should be noted however that the reduced mechanism developed with this method also has the fewest number of species identified as QSS and therefore should have a wider range of applicability by nature.

The goal of ILDM is slightly different than CSP. Rather than trying to reduce the stiffness of the system of equations by introducing algebraic relations, ILDM reduces the "state space" of the system to facilitate the creation of a species concentration look-up table [57]. This couples nicely with the standard ISAT (In situ adaptive tabulation) algorithm for the generation of these lookup tables in CFD simulations. A presumed probability density function (PDF) approach using the tabulated chemistry is typically combined with RANS modeling of the turbulence. Lu and Law point out that ILDM still relies on the QSS assumption and therefore the reduced mechanisms still suffer from the same numerical difficulties described above [51]. Recently, extended versions of ILDM have attempted to remedy this problem. The Flame Prolongation of ILDM (FPI) [58] and the Flame-Generated Manifold (FGM) [59] method both tabulate chemistry effects for unstrained premixed laminar flamelets. While ILDM mechanism reduction can be an automated process, a new lookup table must be generated for each fuel mixture under investigation.

Table 2.1: Sample of Reduced Mechanisms for CH_4/Air combustion found in the literature

Name	**Species**	**Reactions**	**Year**	**Full Mech**	**Reduction Method**
15-step [56]	19 (21)	15 (17)	2008	GRI 3.0	CSP
10-step [60]	10 (15)	7 (10)	2007	GRI 3.0	CSP
12-step ARM [61]	16 (19)	12 (15)	2000	GRI 3.0	QSSA
4-step [53]	6	4	1986	see paper	QSSA

2.1.3 Global

Fitted kinetic models have a long history, being used before detailed kinetic models were developed. Even the comprehensive GRI 3.0 mechanism in common use today has been optimized by fitting the parameters of some reaction steps to bulk experimental data [48]. The fitting strategies used to reduce detailed mechanisms fall into two basic categories: Quasi-Global Kinetic Models which tend to include a subset of the original mechanism as a base such as the H_2/CO, while fitting one or more fuel oxidation steps; and Fitted Global Kinetic Models which fit a set of data to a small global reaction scheme.

Quasi-Global Kinetic Models

Edelman and Fortune [62] were probably the first to combine global and elementary kinetics. The oxidation of the hydrocarbon to CO and H_2 was represented by a global reaction while the oxidation of CO and H_2 was the described by the elementary steps. Tomlin [48] points out that in reality, the hydrocarbon, CO and H_2 oxidation will compete for the radicals. The oxidation of CO and H_2 is over predicted without this coupling.

Gokulakrishnan, *et al.* [63] applies this method to develop a quasi-global mechanism to predict the ignition delay time and laminar flame speed measurements of

CH_4, H_2, CH_4/H_2, CH_4/CO, and CO/H_2 mixtures. The oxidation of methane to CH_2O and H_2 is represented as a global rate and then a detailed $CH_2O/H_2/O_2$ mechanism is used to include the intermediate combustion radicals. The claim is that these radical concentrations are necessary to predict ignition and extinction phenomena simultaneously in order to properly account for flame-holding and stability. The resulting quasi-global mechanism consists of 15 species and 40 reactions which includes prediction of NO emissions. This mechanism is employed in a 2D simulation of a backward-facing step combustor, burning CH_4/Air at atmospheric pressure at equivalence ratios ranging from 0.5 to 1.5.

Fitted Global Kinetic Models

The fitted global kinetic models rely on first identifying the overall global scheme to be used. Hydrocarbon oxidation takes place in several steps. Tomlin identifies them as the following:

1. Hydrocarbons decompose to olefins (endothermic)
2. Oxidation of H_2 (exothermic)
3. Oxidation of Olefins to CO (endothermic)
4. Oxidation of CO to CO_2 (exothermic)

The scheme of Hautman, *et al.* [64] includes all of these stages:

$$C_nH_{2n+2} \rightarrow \tfrac{n}{2}C_2H_4 + H_2 \tag{2.1}$$

$$C_2H_4 + O_2 \rightarrow 2CO + 2H_2 \tag{2.2}$$

$$CO + \tfrac{1}{2}O_2 \rightarrow CO_2 \tag{2.3}$$

$$H_2 + \tfrac{1}{2}O_2 \rightarrow H_2O \tag{2.4}$$

Kiehne, *et al.* [65], developed a global mechanism for high temperature propane flames based on the above scheme. They concluded that the reverse reactions were needed to account for CO and H_2 as stable products and to aid in achieving numerical stability, therefore the Hautman scheme was extended to eight steps.

Jones and Lindstedt [66] developed their global scheme for hydrocarbon combustion by looking at a two-reaction zone flame model. In the primary zone, the fuel is converted to CO and H_2 and in the secondary zone these are oxidized to H_2O and CO_2.

$$C_nH_{2n+2} + \tfrac{n}{2}O_2 \rightarrow nCO + (n+1)H_2 \tag{2.5}$$

$$C_nH_{2n+2} + nH_2O \rightarrow nCO + (2n+1)H_2 \tag{2.6}$$

$$H_2 + \tfrac{1}{2}O_2 \rightleftharpoons H_2O \tag{2.7}$$

$$CO + H_2O \rightleftharpoons CO_2 + H_2 \tag{2.8}$$

The rate of each of these reaction steps is given in Arrhenius form with various powers of species concentrations, present or not present in the reaction. Early global reaction rates using the above schemes were derived directly from experimental results. The work of Nicol [67] and Novossolov [68] aimed to simplify known detailed mechanisms for use in CFD applications, fitting the global reaction rates to data from Chemical Reactor Network Modeling (CRM) employing the detailed mechanism. This resulted in 5-step and 8-step reaction schemes, respectively, with the 8-step accounting for all four NO_x formation pathways. Pressure dependence is accounted for in the exponents of the species concentrations.

While all of the global kinetic schemes discussed so far were developed from simple intuition, Jiang, *et al.* [69], used QSSA and partial equilibrium assumptions to first develop a reduced mechanism. Then, rather than leaving the rates of the reduced mechanism as algebraic relations of the elementary steps, they created new global Arrhenius rates for each reaction, both forward and backward, in the following reduced

scheme.

$$CH_4 + OH \rightleftharpoons CO + 2H_2 + H \tag{2.9}$$

$$H_2 + M \rightleftharpoons 2H + M \tag{2.10}$$

$$H + OH \rightleftharpoons H_2O \tag{2.11}$$

$$CO + OH \rightleftharpoons CO_2 + H \tag{2.12}$$

The alternative fitted kinetic model for use in a CFD code is known as the 'response modelling technique.' This combustion chemistry approach was developed at NASA Glenn Research Center by Molnar and Marek [70]. It begins by considering that reaction rates are controlled by either kinetics or mixing. The mixing time is determined in the turbulence modelling, while the kinetic time is developed as an expression of the ignition delay time as a function of equivalence ratio, temperature, and pressure. Lamnaouer, *et al.* [71], also employ this method, and describe the reasoning for using the ignition delays times. To summarize their logic: the goal is to model gas turbine combustors - this combustion can be represented by adiabatic, constant pressure, well-stirred reactors; these reactors correspond to the post-shock conditions of shock heating a fuel/oxidizer mixture at constant enthalpy and constant pressure conditions; and finally, modelling the kinetic times based on an isothermal process instead does not affect the results appreciably. Although CO and NO_x were included in the method development, the ability of the model to accurately predict these emissions is still unclear. Several methods for trimming chemical mechanisms have been suggested, and these are reviewed by Griffiths [72], Tomlin *et al.* [48], Law *et al.* [51], and most recently by Lu and Law [73].

2.2 Choosing a Reduction Strategy

Previous restrictions on the number of species (~ 6) in a simulation favoured global mechanisms, in which rate parameters for several global reactions are fit using results

from detailed kinetic simulations. As computational resources increased, implementation of reduced mechanisms became feasible. In their development, intuition and mathematical analysis are used to identify species in quasi-steady state, and reactions in partial equilibrium in order to relate some species by algebraic equations. Lu states however that simulations of turbulent combustion can currently incorporate 20-30 species [73], making it possible to reduce only to the skeletal mechanism for which unimportant species and elementary reactions are removed from a detailed mechanism. There are numerous methods, reviewed in the articles above, for identifying the unimportant species and reactions. Lu points out that the method of Directed Relation Graph (DRG) has 3 advantages over its competitors [52]:

1. It features the fastest reduction algorithm for large mechanisms.

2. It can identify all candidate skeletal mechanisms sorted by accuracy in a single run.

3. It provides the ability to specify an upper error bound on the resulting mechanism.

It is therefore the chosen method for this study.

The goal of the present study is to predict ppm emissions of CO and NOx, in addition to describing heat release and other major species concentrations in CFD modeling of LPM combustion with a mechanism of 30 species or less. Focus is on the industrial atmospheric combustor and high pressure gas turbine for $CH_4/H_2/CO_2$ fuel mixtures. Homogeneous systems provide expedient sampling for the development of skeletal mechanisms and it is appropriate to apply skeletal mechanisms developed from 0-D modeling to problems with transport provided some pre-validation is performed. In addition Perfectly Stirred Reactors (PSRs) capture the high temperature flame chemistry and kinetic extinction relevant to LPM combustion. While including

auto-ignition modeling would increase the comprehensiveness of the resulting skeletal mechanism, it is not important in predicting emissions from steady, LPM combustion and therefore is not included. Thus the parameter space is chosen to include pressures from 1 to 30 atm, equivalence ratios from 0.4 to 1.0, and mean PSR residence times from slightly greater than blowout to 3ms. The preheat temperature is from 300 to 500 K for atmospheric combustion and is set for higher pressures as the outlet temperature of the compression process. (This assumes compression from 1 atm and 300 K to the pressure of interest with an 85% efficiency.)

The following describes the method of Directed Relation Graph (DRG) for finding a skeletal mechanism and it's extension Directed Relation Graph Sensitivity Analysis (DRGASA). The application of DRG to develop a skeletal oxidation mechanism for methane is described. This is followed by a discussion of the application of DRGASA to develop a skeletal NOx mechanism to append to the methane mechanism. Finally the skeletal oxidation and NOx mechanisms are validated against full GRI in both PSR and laminar flame speed calculations.

2.3 DRG Background

The detailed mechanism GRI-3.0 [33] has 35 (36 with Ar) species and 219 reactions describing fuel oxidation and an additional 17 species and 106 reactions describing NOx production. It was designed and optimized to describe natural gas combustion and it is still in standard use today. The mechanism reduction used here is guided by a database of solutions of 0-D, adiabatic, homogeneous reactors (PSRs) in the parameter space of interest.

Eliminating unimportant species and reactions from the detailed mechanism requires an understanding of the pairwise relationship among the species. Graphs, the abstract representation of objects (nodes) and their connections (edges), are well suited to this type of analysis. More specifically, directed graphs with weighted edges provide the level of detail necessary to rigorously remove unimportant species. The

method of Directed Relation Graph (DRG) developed by Lu and Law [74, 52, 75, 73], maps species couplings to a directed graph, weights these couplings, and removes weak couplings based on a user specified error tolerance. Species strongly coupled to the major ones, such as fuel or oxidizer, are then discovered through a graph search. The method of DRG by itself does not guarantee the smallest possible skeletal mechanism for the desired error tolerance since it retains species if their removal has a non-negligible effect on *any* of the other species in the mechanism. It is still possible then to further reduce the mechanism by removing species that have only a minor effect on the major species of interest or other global parameters. This is accomplished through DRG-aided sensitivity analysis (DRGASA), which is similar to traditional sensitivity analysis except that it evaluates the error induced by the elimination of species instead of the perturbation of species concentration. Details of both the DRG method and its extension, DRGASA, are discussed in the following.

2.3.1 Skeletal Reduction with DRG

A simple, but abstract mechanism can be used to illustrate the concept of skeletal reduction with DRG. Assume a reaction mechanism of the form below with fuel and product species A, B, C, D, E, F and reaction progress rates of q_1 to q_5.

$$
\begin{aligned}
(R1) \qquad & A \longleftrightarrow B, && q_1 \\
(R2) \qquad & B \longleftrightarrow D, && q_2 \\
(R3) \qquad & B + D \longleftrightarrow C, && q_3 \\
(R4) \qquad & E \longleftrightarrow C, && q_4 \\
(R5) \qquad & E \longleftrightarrow F, && q_5
\end{aligned}
$$

An unweighted, directed graph (digraph) showing the coupling of all species can be drawn and is shown in Figure 2.1, with the nodes corresponding to the species and the

edges, connections through reactions. The graph illustrates the problem of removing species from a mechanism; because of the strong coupling of the species through the many reactions, removal of one species may significantly affect the concentration prediction of another species even if they never appear together in any elementary reaction (i.e. removing species D may significantly affect the prediction of A although they are not directly connected). A weighted edge is needed to quantify the error induced by the removal of a species, so that a new digraph can be drawn in which the edge between A and B (for example), is kept if and only if the removal of species B would directly induce significant error to the production/destruction of species A.

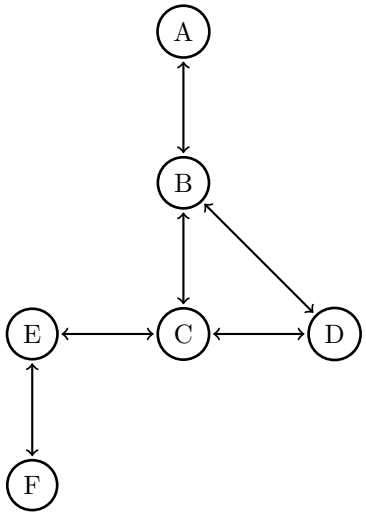

Figure 2.1: Digraph Example.

The production rate of A, R_A, in a mechanism with N reversible reactions can be expressed as

$$R_A = \sum_{i=1,N} \nu_{A,i} q_i \tag{2.13}$$

$$q_i = k_{fi} \prod_{j=1}^{K} [X_j]^{v'_{ji}} - k_{ri} \prod_{j=1}^{K} [X_j]^{v''_{ji}} \tag{2.14}$$

$$k_{fi} = A_i T^{\beta_i} exp\left(\frac{-E_i}{RT}\right) F_i \tag{2.15}$$

$$k_{ri} = \frac{k_{fi}}{K_{ci}} \tag{2.16}$$

where the subscripts i and j refer to the ith elementary reaction and jth species, ν_{Ai} is the stoichiometric coefficient of A in reaction i, q_i is the rate of progress of reaction i, k is the reaction rate, and the subscripts f and r refer to forward and reverse rates respectively. Furthermore ν' and ν'' refer to the stoichiometric coefficients of the reactants and products respectively, C is the molar concentration of a species, A, β, and E are the Arrhenius reaction rate parameters and F the correction factor for special effects. Finally T is the temperature and K_c the equilibrium constant.

The production of species j by reaction i is given by ω_{ji},

$$\omega_{ji} = v_{ji} q_i \tag{2.17}$$

where v_{ji} is the stoichiometric coefficient of j in reaction i, and q_i is the rate of progress of reaction i. To quantify the direct influence of one species on another, a normalized contribution of species B to species A is defined as r_{AB}. Influence on both net production and net destruction is accounted for by using the absolute value of the contributing terms. Lu and Law [74] explore two alternate definitions for this normalized contribution but find that the definition given by Equation 2.18 performs correctly for mechanisms involving both Quasi-Steady State (QSS) species and Partial Equilibrium (PE) reactions.

$$r_{AB} = \frac{\sum_{i=1,N} |\omega_{Ai}\delta_{Bi}|}{\sum_{i=1,N} |\omega_{Ai}|} \tag{2.18}$$

$$\delta_{Bi} = \begin{cases} 1 & \text{if the } i\text{th elementary reaction involves species B} \\ 0 & \text{otherwise} \end{cases} \tag{2.19}$$

With r_{AB} defined to measure the extent of the coupling of A to B as the relative error induced to species A by the elimination of B, Figure 2.1 can be redrawn such that an edge is kept if and only if $r_{AB} > \varepsilon$, where ε is a user specified threshold relative error. A possible resulting digraph is shown in Figure 2.2.

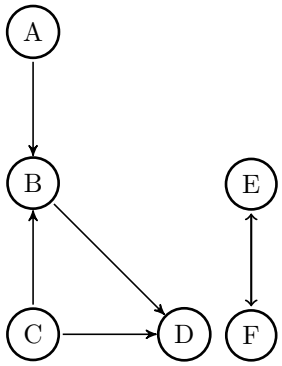

Figure 2.2: Digraph example after edge removal.

With the graph formed, species for the starting set are selected. This is typically a single species such as the fuel through which the oxidizer and all products of interest are coupled. Note that because third body species are not accounted for in the definition of the relative error, any inert species of interest should also be included in the starting set to ensure they remain in the skeletal mechanism. For each starting species, A, a depth first search (DFS) is applied to the digraph to identify the dependent set of A. The union of the dependent sets of species for each starting species is then the skeletal mechanism. The elementary reactions kept are all those from the detailed mechanism which include only the species from the now defined skeletal mechanism.

With some relative error ε the group $E - F$ is decoupled from the group $A - B - C - D$. While the intra-group coupling of E and F may be strong, the inter-group coupling of $E - F$ and $A - B - C - D$ is relatively weak. This sort of behaviour accounts for sudden jumps in the number of species retained as ε is varied.

2.3.2 Further Skeletal Reduction with DRGASA

Because of the highly non-linear coupling of the species in a reaction mechanism, the error caused by the removal of a set of species is not necessarily the sum of the errors caused by the removal of each species individually. DRGASA is an iterative procedure that attempts to obtain a final skeletal mechanism with the required overall accuracy. To apply DRGASA, the following procedure is used:

1. A DRG analysis is applied to obtain the critical value of ε for each species, and any species with a smaller than user-specified level is eliminated as described above.

2. The sensitivities E_i, defined as the worst-case relative error induced to the parameters of interest (e.g. NO concentration) due to the elimination of each species i, are then computed for each species with ε greater than the user-specified tolerance and still under consideration for removal.

3. The species are sorted by their E_i values in ascending order, and starting with the species with the smallest E_i, are eliminated one at a time.

4. A new reduced mechanism is created with just one of these species eliminated, the models re-run, and the sensitivities re-calculated.

The relative error is defined by Equation 2.20, where x_0 is the species concentration with the reduced mechanism and x is the species concentration with the detailed mechanism. The sensitivity E_i is the maximum δ in the parameter space.

$$\delta = \frac{|x - x_0|}{x} \tag{2.20}$$

The skeletal mechanism obtained by a DRGASA analysis is considered to be a minimal size, such that further elimination of any species would result in larger than acceptable error.

2.4 Mechanism Reduction Procedure

Detailed chemical kinetic simulations are completed using CHEMKIN-PRO with a 0-D, adiabatic, homogeneous reactor (PSR) to create a database of solutions in the parameter space of interest. The variables of this space are residence time, preheat temperature, equivalence ratio, and pressure. Each is varied independently and the final matrix is found in Appendix A. A PSR is run under each set of conditions, for a total of 108 data points, and the results of species concentrations and rates of production are saved in a text-file for post-processing. These detailed chemical kinetic simulations are completed using CHEMKIN-PRO. GRI-3.0 is chosen as the detailed mechanism but fuel oxidation and NOx formation are treated separately resulting in the generation of two databases: one using full GRI-3.0 and the other using GRI-3.0 without the NOx chemistry.

Post-processing of the CHEMKIN output files and implementation of the reduction algorithm is accomplished using SAGE [76], a Python based, open-source mathematics software. SAGE has a robust graph-theory package and the Python language is adept at string manipulation, allowing for the integration of post-processing and reduction. The reduction algorithm is outlined below:

1. A single result file from a PSR calculation is taken and post-processed: a list of species (nodes) is extracted and a list of r_{AB} is calculated (weighted edges). This is then repeated for all result files in the parameter space, and a master list of weighted edges for each graph from each results file is compiled.

2. A threshold value is chosen.

3. A graph (results file) is chosen and each of its weighted edges (r_{AB}) is compared to the chosen threshold value. If the weighted edge is less than the threshold, it is removed. A new digraph is then constructed using the list of species and

the new list of weighted edges greater than the chosen threshold. A DFS is performed starting with the species of interest (either the fuel, CH_4), or NO here) which returns a list of species to be saved (the dependent set of CH_4 or NO).

4. Step 3 is repeated for each graph, corresponding to each results file, to compile a master list of species to be saved.

5. Steps 3 and 4 are then repeated for each new threshold value chosen such that a new master list of species to be saved is compiled.

The results of the application of this algorithm are described in what follows.

2.4.1 Methane Oxidation

Figure 2.3 shows the dependence of the number of species in the skeletal mechanism on the value of the threshold ε. The figure shows large jumps in the number of species retained. This occurs most prominently at $\varepsilon = 0.025$ in which 10 species are removed (mostly C2 species). Smaller jumps occur at $\varepsilon = 0.225$ and 0.335 at which 3 and 4 species are removed. These jumps, as mentioned above, are due to the elimination of strongly coupled groups of species. Since these groups should be kept together, the threshold should be chosen either right before or right after one of these jumps. Choosing a threshold slightly larger than the first jump, $\varepsilon = 0.03$ removes the largest strongly coupled group while retaining species crucial for the the description of prompt NOx formation. The resulting skeletal mechanism retains 22 species: H_2, H, O, OH, H_2O, HO_2, H_2O_2, O_2, CO, HCO, CO_2, CH_4, CH_3, C, CH, CH_2OH, CH_3OH, $CH_2(S)$, CH_2, CH_3O, CH_2O, N_2. In addition, the skeletal mechanism retains 122 reactions by eliminating all elementary reactions in GRI-3.0 with any reactant or product not contained in this set of species. It should also be noted that all species and reactions of the H_2/CO submechanism are retained.

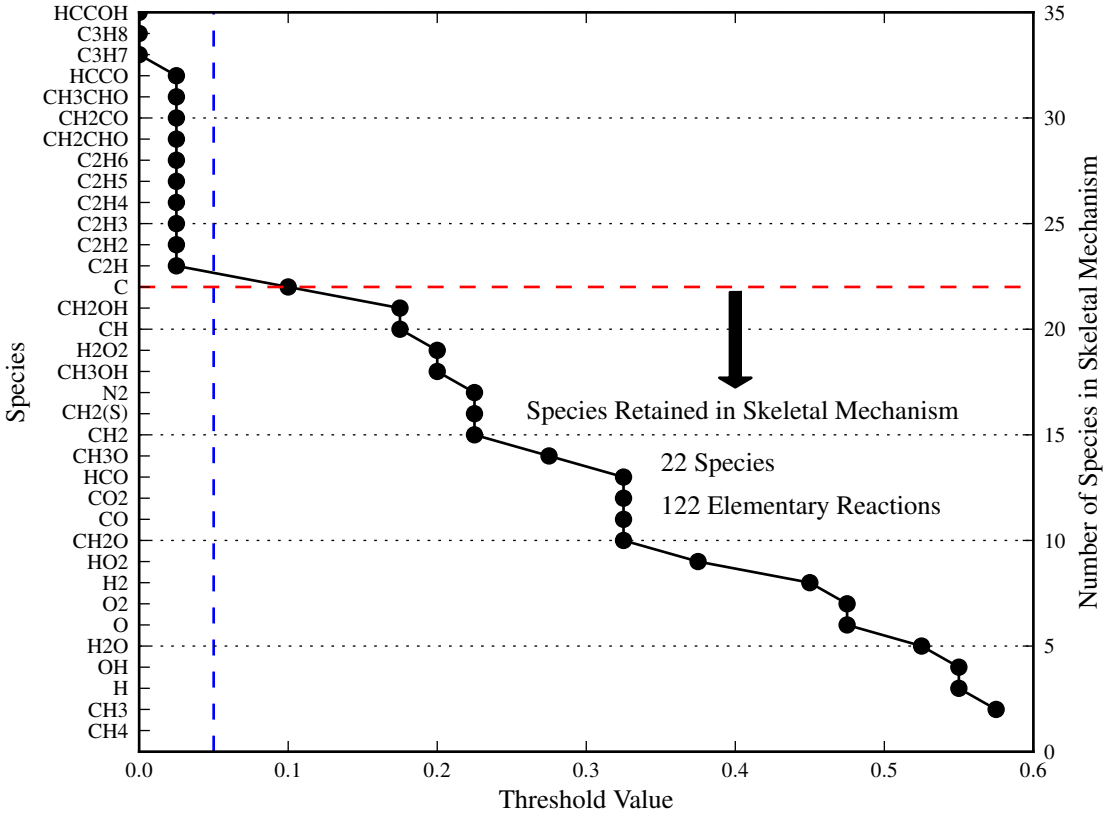

Figure 2.3: Dependence of the number of species in a skeletal mechanism on the threshold value ε for DRG. The blue line indicates a chosen threshold value and the red line shows species retained by the given skeletal mechanism.

Lu and Law [56] applied the method of DRG to generate a skeletal mechanism with a database of both PSR and auto-ignition behaviour. Their parameter space included pressures of 1-30atm, equivalence ratios of 0.5-1.5, and initial temperatures of 1000-1600K for autoignition and 300 K for PSR. They chose a threshold of 0.13, resulting in a mechanism with 30 species and 184 reactions. In addition to the species included in the skeletal mechanism derived in this work, their mechanism included C_2H_2, C_2H_3, C_2H_4, C_2H_5, C_2H_6, CH_2CHO, CH_2CO, and HCCO.

2.4.2 NOx

With the skeletal oxidation mechanism defined, the reduction of NOx chemistry can now be evaluated. Because of the very small NOx concentrations near blowout the same parameter space is used except that the blowout residence times are replaced with residence times 15% larger than blowout (these residence times will be referred to as being "near blowout" in the following text). This is then run with full GRI including NOx chemistry. A plot similar to Figure 2.3 is created using NO as the starting species rather than CH_4, but only nitrogen containing species are plotted for clarity since the oxidation mechanism will not be altered. We see from Figure 2.4 that at a threshold of 0.2, nine additional species including NO are retained. The resulting mechanism is considered the baseline for NOx reduction for a total of 32 species.

In an effort to reduce the mechanism further however, DRGASA is applied with NO chosen as the species of interest. Figure 2.5 shows the relative error of NO concentration as compared to full GRI across the full parameter space for the baseline case (32 species) and then the baseline case with each of the listed species removed one at a time. Although all baseline case N containing species were tested in this way, those listed in the figure were the only ones which induced small enough errors to be considered for removal. Also, as the concentration of NO decreased, the error significantly increased therefore two lower limits were considered, 5 and 10 ppm. If the NO concentration was below the chosen limit the error was not included in determining the maximum relative error. In addition, the maximum errors are shown for residence times near blowout and 3ms separately.

The results of Figure 2.5 indicate that NO_2 and HNO are possible candidates for removal. Removal of NO_2 has a more significant effect on results near blowout than at 3ms, while the removal of HNO seems to have an equal effect on results at both blowout and 3ms. In addition there is very little change in the maximum relative

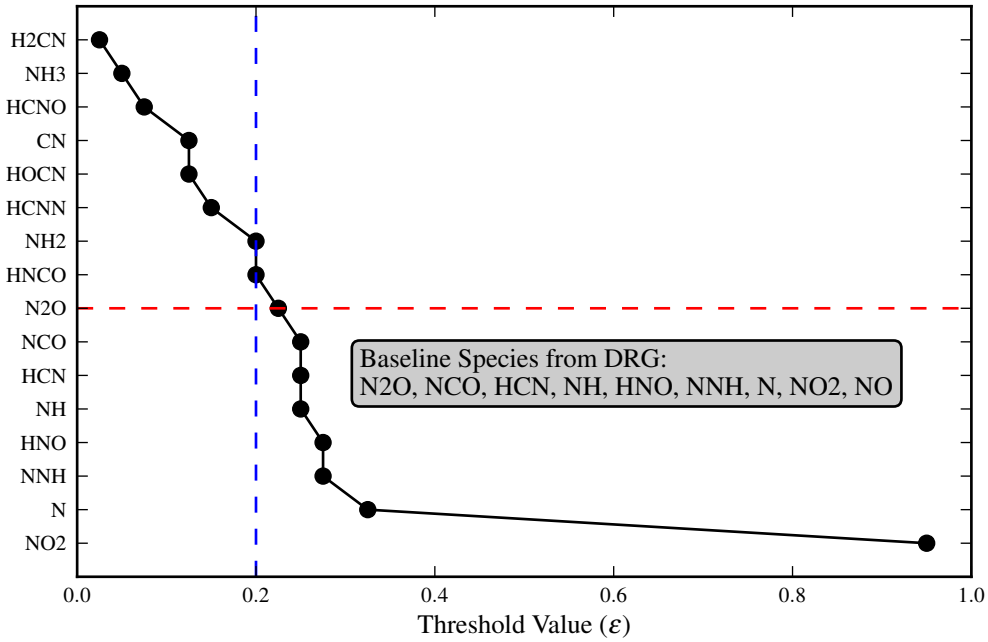

Figure 2.4: DRG applied to GRI with full NOx chemistry. Threshold values are plotted for N containing species only for clarity. The blue line indicates a chosen threshold value and the red line shows the NOx species retained by the given skeletal mechanism.

errors of the baseline case and that with NO_2 removed, therefore NO_2 is the only species chosen for removal. The fact that NO_2 was a candidate for removal at all may come as a surprise considering the results of Figure 2.5 which show removal of NO_2 to be possible only under the largest threshold value when DRG alone is applied. NO_2 can often be assumed to be a quasi-steady state species as most reactions involving NO_2 are simply shuffling NO to NO_2 and vice versa. This is an excellent illustration of the fact that the application of DRG alone does not necessarily result in the smallest skeletal mechanism possible. It also indicates that, contrary to the suggestion in [77] to only choose a range of thresholds (i.e. 0.2 to 0.4) over which to apply DRGASA, further reduction is still possible by looking at species with minimum removal thresholds as large as 0.95. Finally it should be noted that NO_2 is a candidate

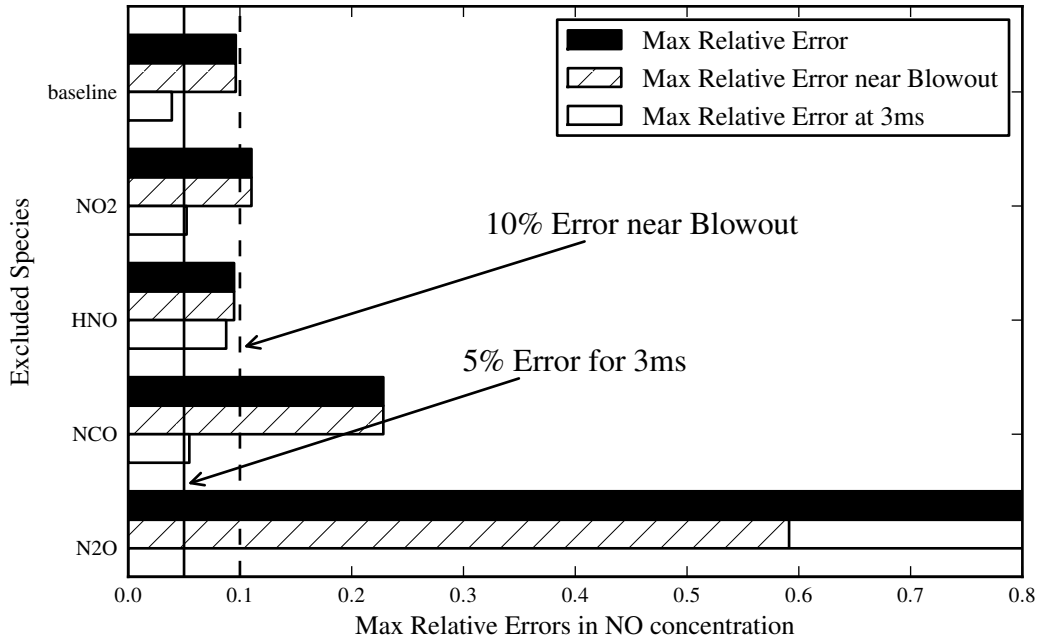

(a) NO > 5ppm

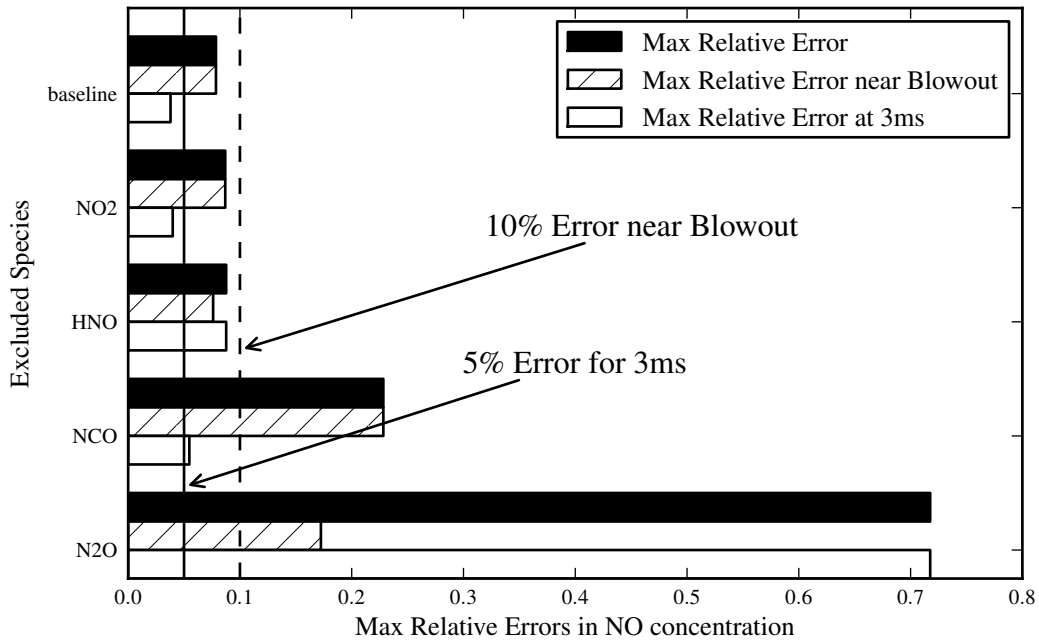

(b) NO > 10ppm

Figure 2.5: Relative error of NO concentration (compared to full GRI) when each of the listed species is removed individually from the baseline skeletal mechanism, which was developed using only DRG.

for removal because we are unconcerned with the distinction between NO and NO_2 in predicting NOx emissions and assume NO is an acceptable surrogate for both NOx species.

The final skeletal oxidation mechanism with skeletal NO chemistry has 30 species, the N containing species being N_2O, NCO, HCN, NH, HNO, NNH, N, NO, N_2. This ensures that a truncated version of each NO formation pathway is still present: NCO and HCN for the prompt route, NH and NNH for for the NNH route, N_2O for the nitrous oxide route, and N for Zeldovich.

2.5 Validation

To verify the applicability of the skeletal mechanism with NO chemistry, prediction of the blowout residence time, and NO concentrations in a PSR are compared against that predicted with full GRI-3.0. This is done for the full parameter space over which DRG was originally applied (although only to near blowout residence times for NO concentrations and only for concentrations greater than 5ppm). In addition, Laminar Flame Speeds calculated using the two mechanisms are compared to ensure the skeletal mechanism can be extended to models which include species transport. Agreement between the full and skeletal mechanisms is quantified using the relative error given by Equation 2.20 above. The color scheme used to indicate the chosen pressure is the same among the following figures in this chapter with the dashed blue line indicating an inlet temperature of 500K and the solid blue line an inlet temperature of 300K.

Figure 2.6 shows the ability of the skeletal oxidation mechanism to capture extinction. The two sets of calculations for atmospheric pressure lie on top of each other at less than 5% error, and the calculations at higher pressures all tend to agree as well trending to larger errors as equivalence ratio decreases. This is hypothesized to be due to the increased importance of the C2 pathways at extending stability at lower equivalence ratios and higher pressures. As a result the skeletal mechanism tends to

under predict the blowout residence time. Figures 2.7 and 2.8 show the increasing relative error in the prediction of NO concentrations as pressure increases, however errors are still reasonable, being consistently below 10%. It should be noted that the skeletal mechanism tends to over predict NO concentrations as compared to GRI. Finally Figure 2.9 shows the applicability of the skeletal mechanism to multidimensional models. The skeletal mechanism tends to overpredict the laminar flame speed and errors increase with lower equivalence ratios and higher pressures.

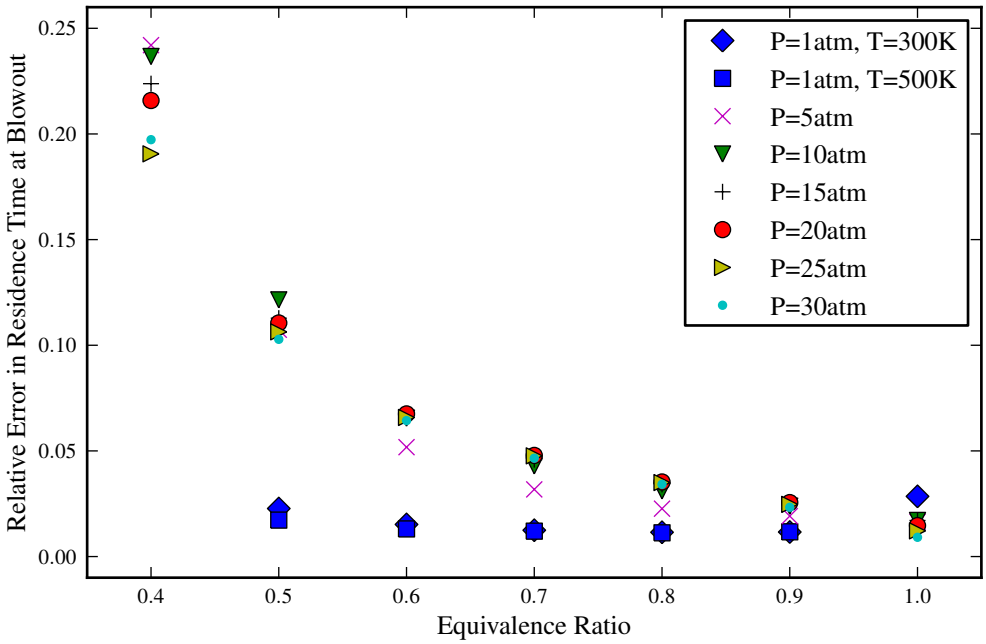

Figure 2.6: Relative error in the prediction of residence time near blowout, detailed vs. skeletal mechanism.

2.6 Conclusions from the Development of a Skeletal Mechanism

A skeletal mechanism for the description of methane oxidation and the prediction of NO_x emissions from lean premixed (LPM) methane combustion is developed through the application of the methods of Directed Relation Graph (DRG) and DRG-aided

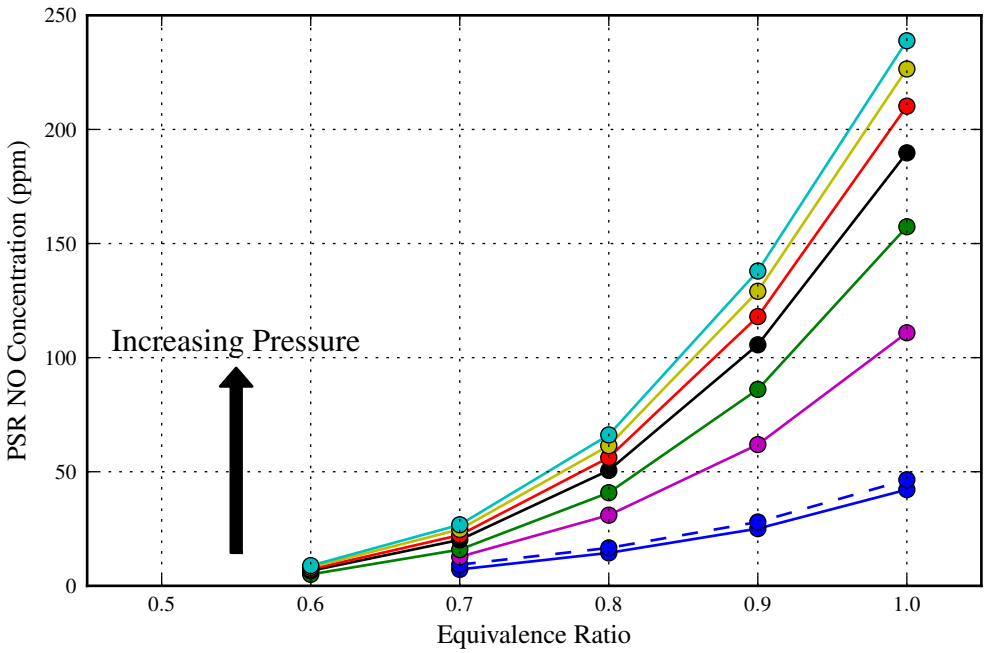

(a) NO concentration near blowout, detailed mechanism

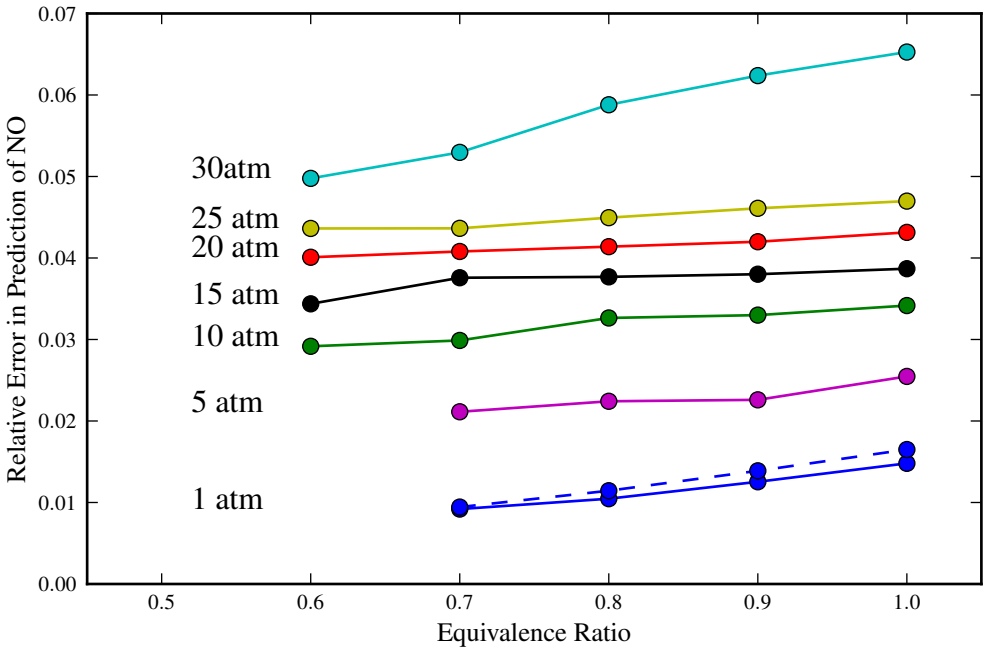

(b) Relative error in prediction of NO near blowout by skeletal mechanism

Figure 2.7: Validation of NO prediction by the skeletal mechanism in a PSR near blowout, for all pressures in the parameter space, through plots of both magnitude and relative error.

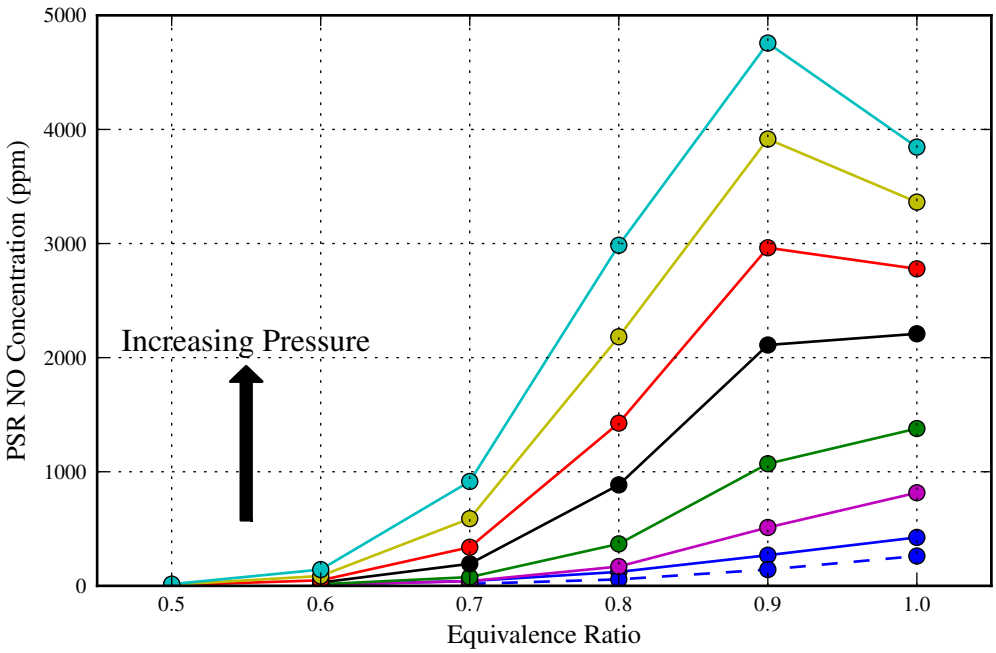

(a) NO concentration at 3ms, detailed mechanism

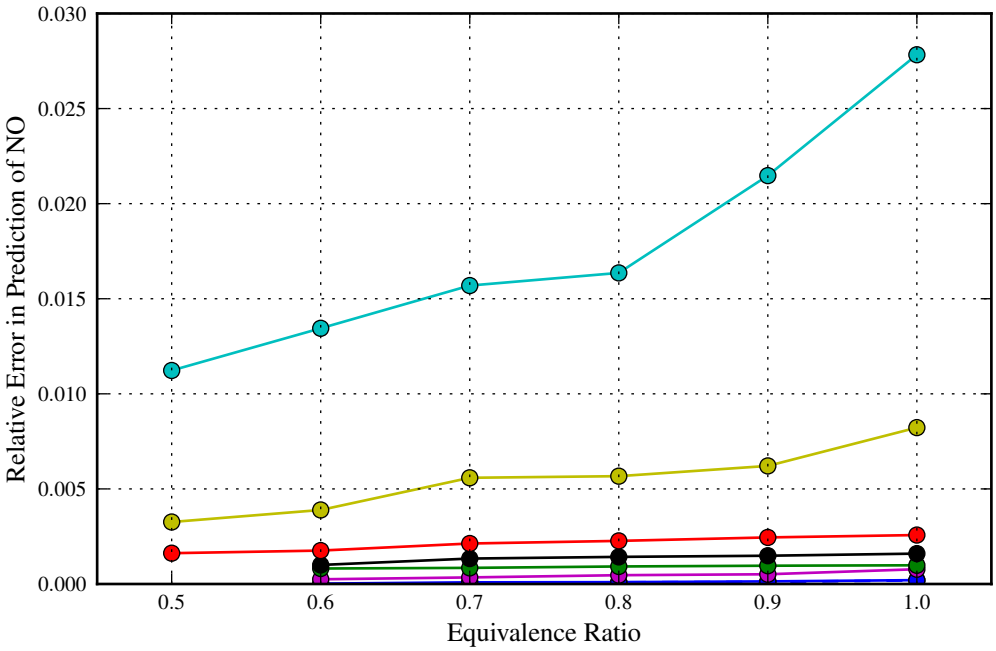

(b) Relative error in prediction of NO at 3ms by skeletal mechanism

Figure 2.8: Validation of NO prediction by the skeletal mechanism in a PSR at a residence time of 3ms, for all pressures in the parameter space, through plots of both magnitude and relative error.

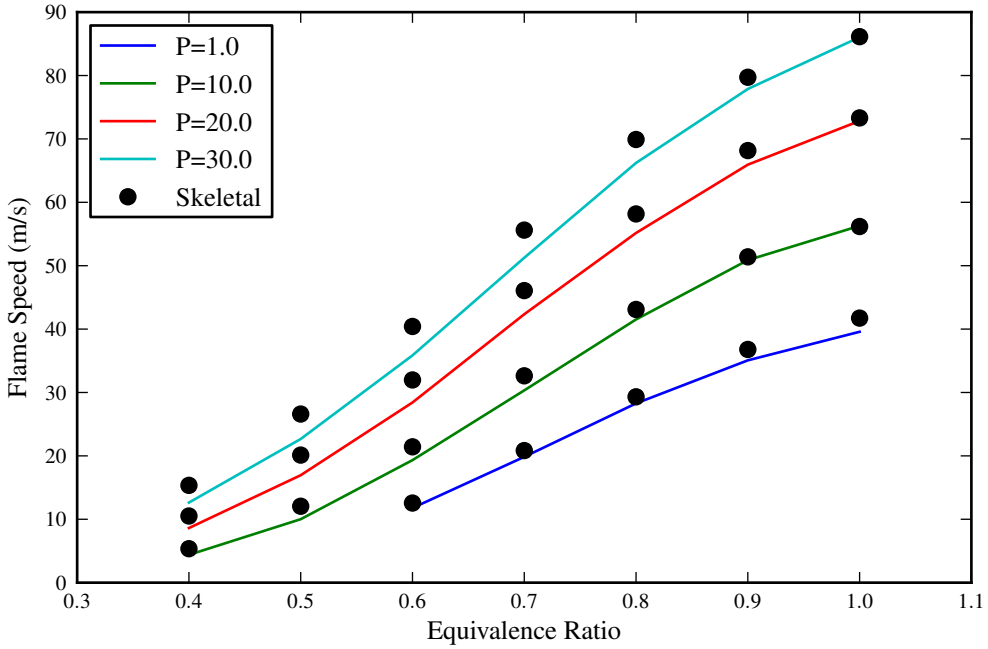

(a) Prediction of Laminar Flame Speed, Skeletal (points) vs. Detailed (lines)

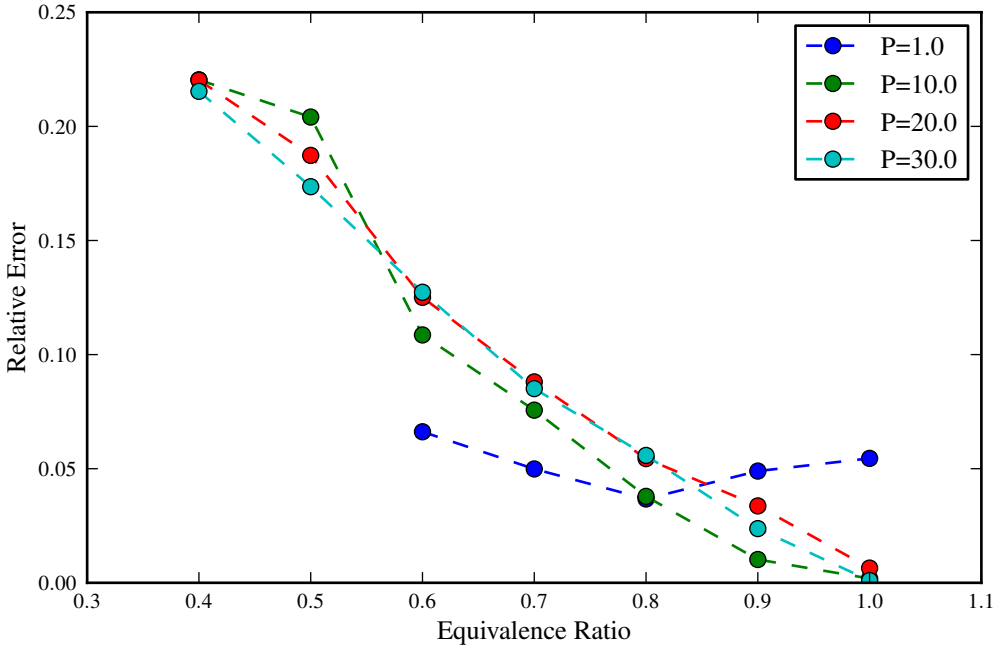

(b) Relative Error in the Prediction of Laminar Flame Speed

Figure 2.9: Validation of laminar flame speed calculations with the skeletal mechanism through plots of both magnitude and relative error.

sensitivity analysis (DRGASA). The mechanism consists of 22 species for methane oxidation and an additional 8 describing NO_x formation and may be found here [78]. The H_2/CO submechanism is retained and all four NO_x formation pathways are described by the final 30 species skeletal mechanism. The mechanism performs well against detailed GRI 3.0. NO_x emissions are predicted within 7% near blowout and 3% at 3ms, laminar flame speeds and residence times at blowout are both predicted within 20% over the range of equivalence ratios and pressures. Examples of the application of the skeletal mechanism in CFD modeling of methane combustion for the prediction of NO_x emissions can be found in the work of Fackler **??**.

Chapter 3
EXPERIMENTAL WORK

The experimental work focuses exclusively on pure H_2 and CH_4 as fuels, as well as CH_4/H_2 blends. The majority of the work characterizes blowout although some data are taken at the nominal stable operating condition of 1800 K in the recirculation zone to be used for later model validation. The chapter describes the experimental setup, the measurement tools used and presents the data obtained. Finally an analysis of the blowout data and audio recordings is provided.

3.1 Experimental Setup

All of the data presented here are obtained from the high intensity, backmixed, single-jet, stirred reactor as shown in Figure 3.1. It consists of a stainless steel premixer, an Inconel nozzle block, and an alumina reactor. The fuels used for the experiments are purchased with the following purities: methane (99.9%), and hydrogen (99.999%). Dry, filtered facility air is provided at nominally 100 psig. The air is preheated to 573 K, its flow rate is held constant at 1.084E-3 kg/s and the line pressure is set to 30 psig. The air flow rate is controlled with a Fischer and Porter rotameter and the fuel flow rates with a Brooks Instrument mass flow controller. Both the fuel and air enter through the premixer, and attain a nominal mixture temperature of approximately 550 K, entering the reactor cavity through a choked 2 mm nozzle with a sonic jet velocity of approximately 450 m/s. The total volume of the reactor cavity is 15.8 cc. Temperature and species are measured at 2/3 reactor height with the nominal sampling location being 2.7 mm inside the reactor wall, thus avoiding both thermal and fluid boundary layers as well as jet effects. The combustion gas

temperature is measured with an R type thermocouple that is coated with alumina to prevent catalytic effects. For the blowout experiments, the measured temperature is between 21 and 43 K below the reported temperature, which has been corrected for radiation loss from the thermocouple bead to the walls and convective transfer from the hot combustion gases (see Appendix B for further details on this calculation). Calculations indicate that the pressure inside the JSR is approximately 1.5 atm. Finally, the reactor is non-adiabatic and a heat loss analysis has bee completed in Appendix B revealing a nominal heat loss of 20% of reactor input.

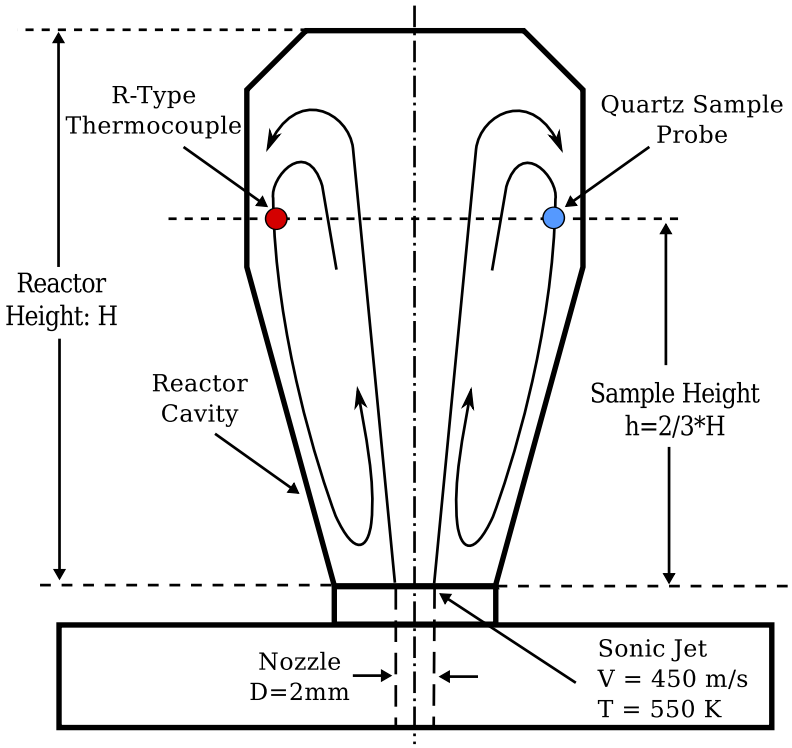

Figure 3.1: A schematic of the JSR illustrating sampling locations and other details of the experimental setup.

Gas samples are withdrawn from the JSR using a water-cooled quartz probe of the design by Kramlich and Malte [79]. A detailed description of the probe is provided by Steele [80] and oxidation of CO in the probe has been noted by both [80] and

[3]. The dried sample from the probe is sent to a three gas analyzer: the CO_2 and CO analyzers operate on the NDIR principle, and the O_2 analyzer is paramagnetic. Additional analysis with a Gas Chromatograph can be performed.

There are many ways to conduct a blowout test. For example, one may hold the fuel rate constant while increasing the air flow rate or increase both fuel and air flow rates at constant equivalence ratio. We choose to approach blowout by holding the air flow rate constant while decreasing the fuel flow rate because we wish to keep the flow field and turbulence parameters approximately constant as we approach blowout. This means that as blowout is approached the Damkohler number changes principally via a change in the chemical time, and the mixing time stays essentially constant. The one change in the flow field is the increase in the density as the temperature decreases approaching blowout. In addition, because the JSR is not adiabatic, the effects of thermal hysteresis must be eliminated from the observed blowout temperature. This is accomplished by holding each fuel flow rate increment constant for 15 minutes to allow the reactor body and combustion process to come to a thermal steady state. Decreasing the fuel flow rate too rapidly will lead to a situation in which the hotter reactor body will temporarily support what would otherwise be an unstable combustion condition. Estimates of the time constant of the thermal response of the reactor body to changes in surface temperature suggest that the 15 minute wait time is appropriate (see Appendix B).

For blowout experiments with hydrogen rich fuels, time-localized acoustic events are recorded. The General Radio Company's Precision Sound-Level Meter and Analyzer (model 1933) is used with an electret-condenser microphone with a flat frequency response from 5 Hz to 100 kHz. The microphone is located approximately 2 m from the combustor. The microphone output is captured with Audacity, an open source program for recording and editing sounds, at an audio sampling frequency of 96 kHz. As the fuel flow rate is decreased, an audio recording begins as soon as the acoustic events are detected and continues until final global extinction occurs. It should be

noted that these acoustic events do not occur with methane combustion.

3.1.1 Gas Chromatograph

The Gas Chromatograph (GC) is a PerkinElmer Clarius 480. The columns were purchased from Sigma Aldrich and the sampling valve and heated valve enclosure from Valco Intruments. Unburned hydrocarbons (methane, ethane, and propane) can be measured using the flame ionization detector (FID) and unburned hydrogen with the thermal conductivity detector (TCD). Specifications for the packed columns used with each detector are given in Table 3.1 and the standard method parameters used are given in Table 3.2.

Table 3.1: Column Specifications

Type	HAYESEP D	CARBOXEN 1000
Detector Type	FID	TCD
Mesh Size	80/100	60/80
Length	10 feet - stainless steel	15 feet - stainless steel
Nominal O.D.	0.125 inches	0.125 inches
Max Temp	290 C	225 C

A 10-port valve is used to obtain a gas sample of known volume as shown in Figure 3.2. If analysis with the TCD is desired, the gas sample is loaded into the sample loop with the 10-port valve in the"FID" position (Figure 3.2(b)). Rotating the valve into the "TCD" position (Figure 3.2(a)) causes the sample to be carried into the Carboxen column with the Argon carrier gas. Likewise, if analysis with the FID is desired, the gas sample is loaded into the sample loop with the 10-port valve in the"TCD" position (Figure 3.2(a)). Rotating the valve into the "FID" position (Figure 3.2(b)) causes the sample to be carried into the HAYESEP-D column. The

Table 3.2: GC Method Parameters

	FID	TCD
Carrier Gas	100 vol % Helium	100 vol % Argon
Carrier Gas Flow Rate	30 mL/min	30 mL/min
Carrier Setpoint	21.5	30.0
Carrier Gas Pressure	Bottle (50 psig), GC (30 psig)	Bottle (50 psig), GC (30 psig)
Volume of Sample	Sample loop size (0.1 mL)	Sample loop size (1 mL)
Detector Temp	150 C	110 C
Range	1	1
Attenuation	0 to -6	0 to -6
Oven Temp	120 C	40 C
Sample Loop Temp	120 C	40 C
Polarity	–	Negative

TotalChrom software provided by PerkinElmer, performs the integration of the peak area of each eluted species.

The device is calibrated for methane (99.9%), ethane (99%), propane (99%) and hydrogen (99.999%) using the 8.4 L sample tank. A Welch Vacuum pump is used to evacuate the tank to 14 inches of Hg. The pump is turned off and the valve is shut. A gas sample ranging in volume from 0.5 to 50 cc is taken from a cylinder using a syringe. The gas sample is injected into the sample tank and the valve opened to re-pressurize the tank. This produces 8.4 L of a known concentration of the desired gas component. This calibration sample can then be pumped out of the sample tank using a metal bellows pump, through the sample valve and the response of the detector determined. Each data point for the calibration is repeated three times, and the tank i evacuated and re-pressurized twice between injections. Hydrogen is calibrated on the TCD and the hydrocarbons on the FID. Concentrations range from ∼120 ppm

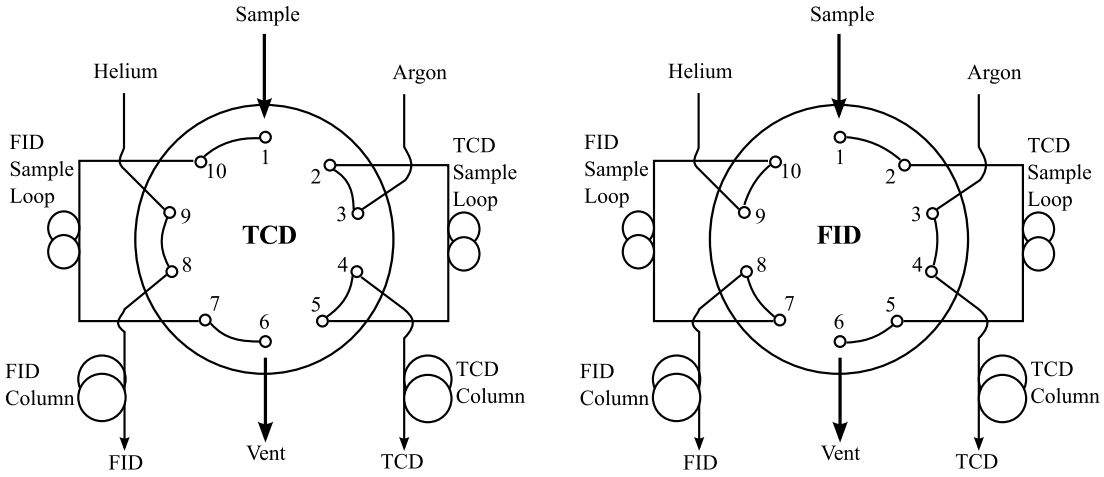

(a) Valve Position for Injecting Sample TCD (b) Valve Position for Injecting Sample FID

Figure 3.2: Layout of the gas chromatograph with 10-port valve.

to ∼6000 ppm for H_2, and ∼60 to ∼6000 ppm for the hydrocarbons. The calibration curves are very linear over the ranges tested.

3.2 Experimental Results

Blowout data are taken for fuel blends of methane with hydrogen across the full range of hydrogen content. Increments of 10% hydrogen are used in the blends when allowed by the range on the mass flow controllers (a 90% methane, 10% hydrogen blend was not able to be completed). Each blowout test is conducted as described above. For each data point in the fuel blend matrix, the blowout experiment is repeated at least three times. Statistics for a small number of observations [81] are applied to obtain 95% confidence intervals on the average equivalence ratios and temperatures at blowout. All raw experimental data are contained in Appendix D.

For pure hydrogen and methane, plots of average temperature vs. equivalence ratio for three to four experimental runs are given in Figure 3.3. Ninety-five percent

confidence intervals on temperature are given when multiple data points are obtained at the same equivalence ratio.

Figure 3.4 shows the equivalence ratio and temperature trends as blowout is approached. With increasing hydrogen content in the fuel the combustion is more stable, being sustained to lower equivalence ratios and temperatures. The blowout equivalence ratio is typically known to within 0.01 or better and the blowout temperature to within 25 K or better.

A sample of an audio recording from a hydrogen blowout experiment is shown in Figure 3.5. Time localized, acoustic events are apparent in the waveform and present as audible 'pops' approaching blowout. Their amplitude and frequency appear to increase as blowout is approached and then around 17.5 s in the recording the acoustic events cease, indicating blowout has occurred. Note that the blending threshold for acoustic events is observed to be 30/70 CH_4/H_2. For blends with less H_2 content acoustic events are not observed.

To support model validation, GC measurements of methane concentration at the nominal stable operating condition of 1800 K (as defined by Fackler [3]) are reported for four radial locations in Figure 3.6. Methane concentration peaks in the jet and falls off quickly as we move into the shear region and out into the recirculation zone. No appreciable concentrations of methane could be measured beyond 3 mm from the centerline. The methane profile is complementary to the temperature profile taken by Fackler [3] at the same condition which will also be used for validation. In addition, GC measurements of hydrogen concentration at the nominal sampling location are reported in Figure 3.7 as a function of equivalence ratio as blowout is approached. The hydrogen concentration rises rapidly as incipient blowout approaches. It should be noted that the majority of the measurements reported in Figures 3.6 and 3.7 are made in regions of high free-radical activity. There is concern that oxidation chemistry in the probe may distort the composition of the gas sample [80] and cause under-reporting of reactive species such as CH_4, H_2 and CO. Therefore the measurement of these

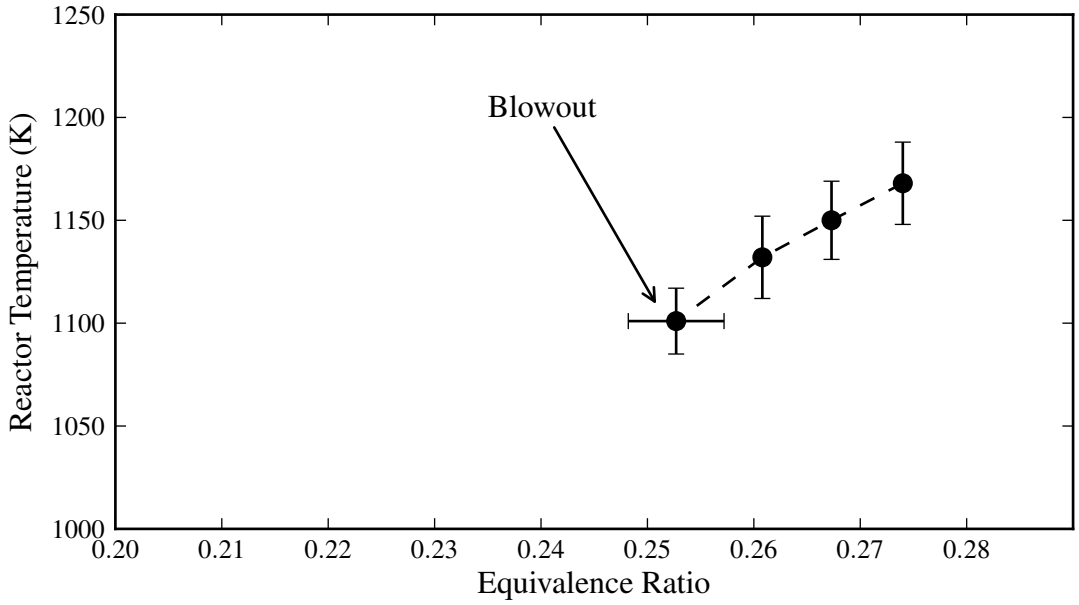

(a) Hydrogen

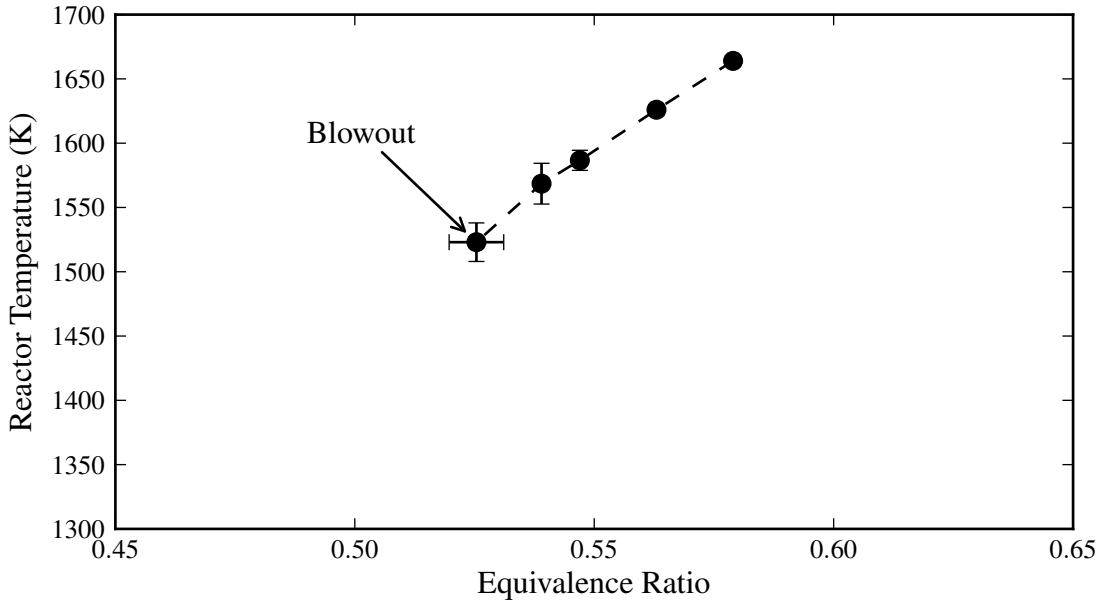

(b) Methane

Figure 3.3: Reactor temperature (adjusted for heat transfer effects) plotted as a function of equivalence ratio as blowout is approached. Blowout is the point of lowest equivalence ratio and temperature.

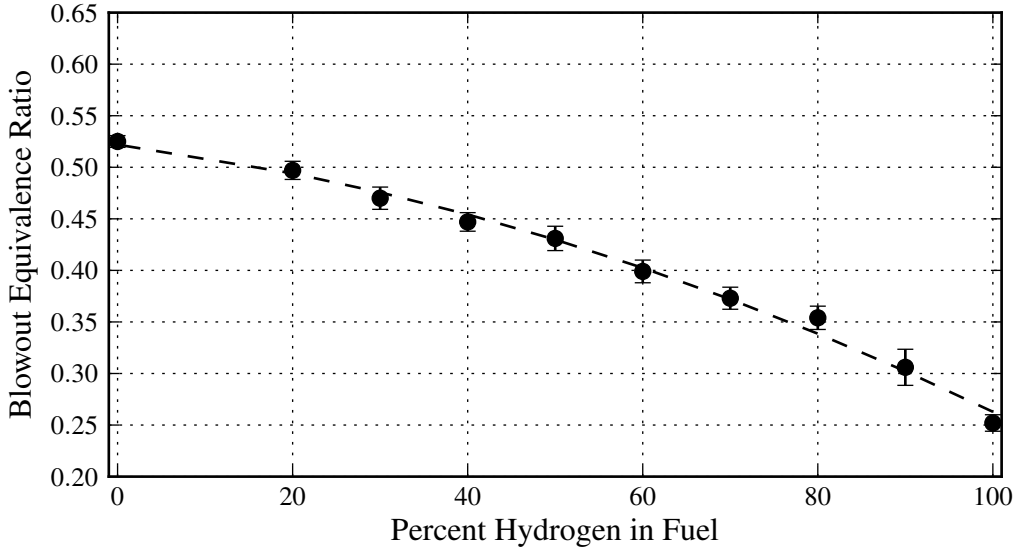

(a) Equivalence Ratio

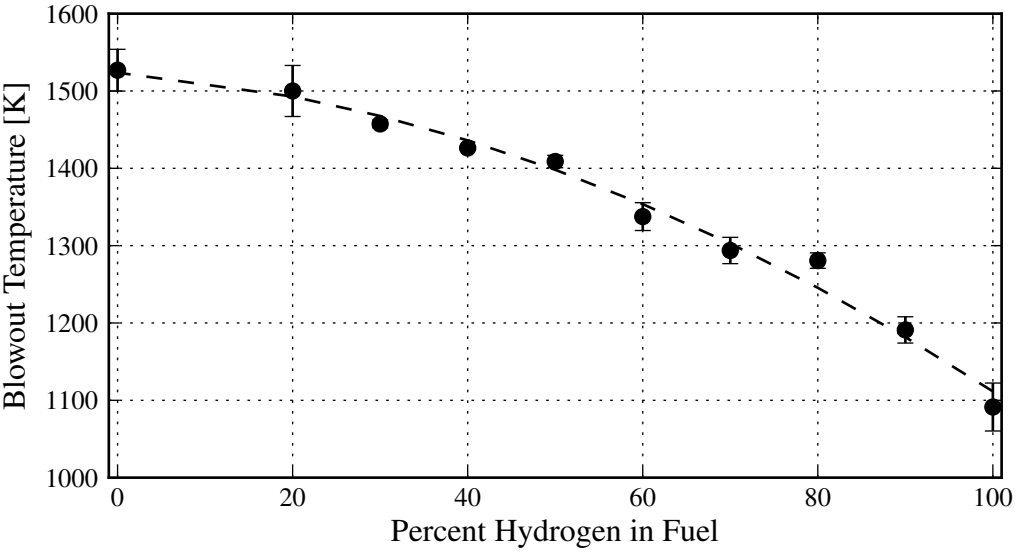

(b) Temperature

Figure 3.4: Experimentally determined blowout (a) temperature (adjusted for heat transfer effects) and (b) equivalence ratio for CH_4 mixed with increasing amounts of H_2.

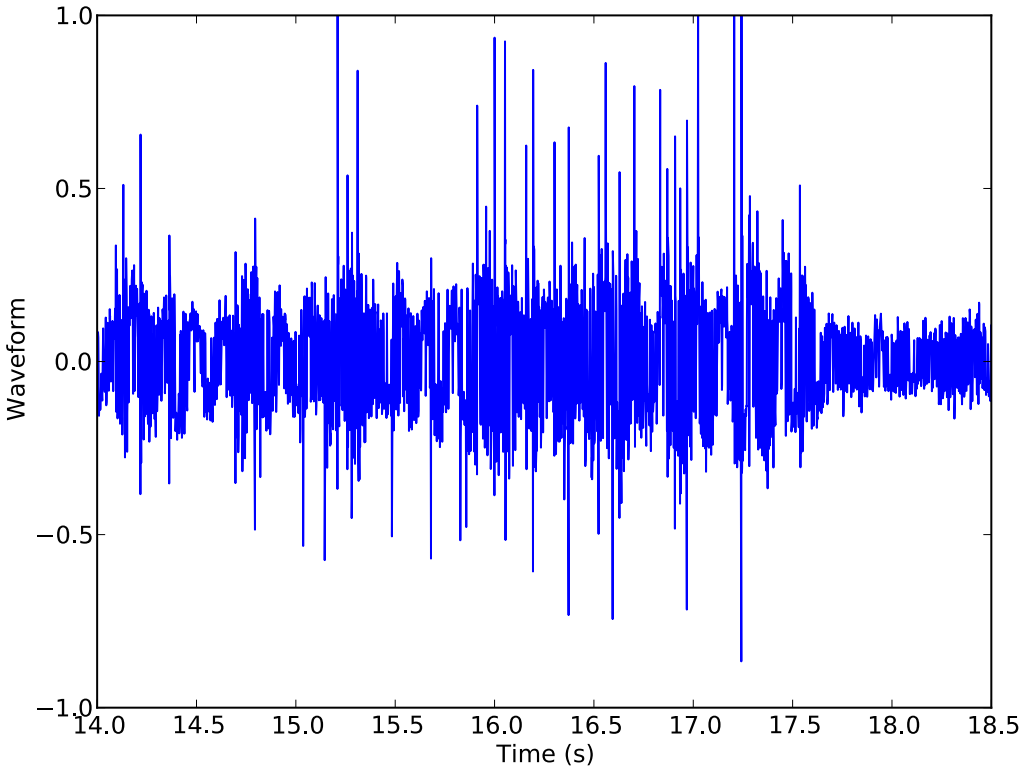

Figure 3.5: Audio recording from a hydrogen blowout experiment.

species only shows trends, although we do expect the methane data taken in the jet region to be the most accurate. This will be explored further when these data are compared to the subsequent modeling, it is also likely the reason that measurements of methane at the nominal sampling location as blowout is approached could not be made.

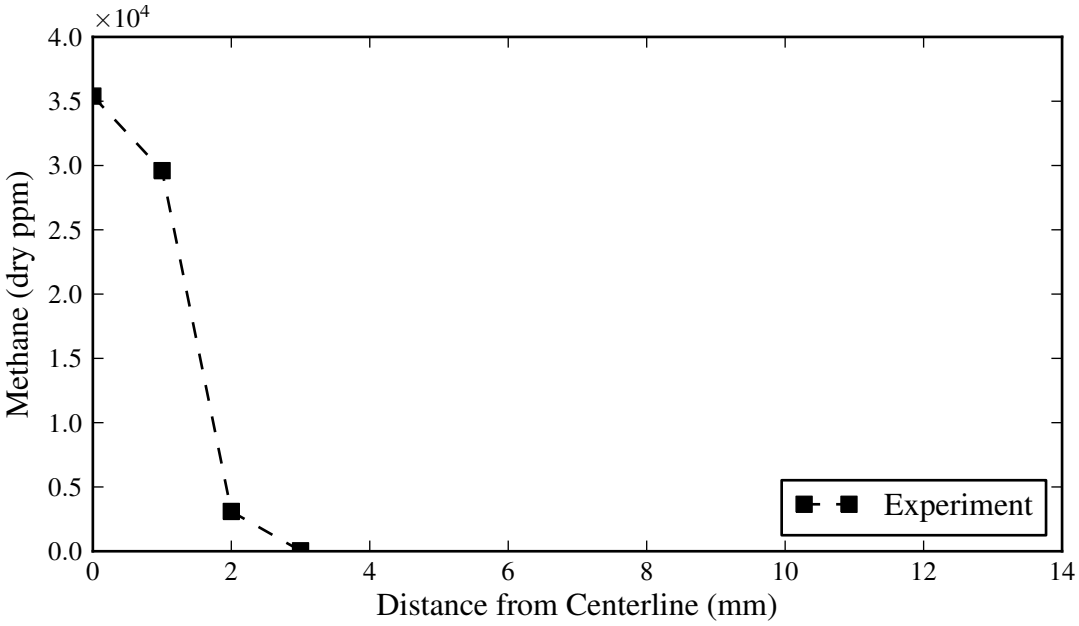

Figure 3.6: Measured methane concentration at the nominal stable operating condition [ppm, dry]. See Appendix D for raw data.

3.3 Analysis of Experimental Results

Standard analysis of experimental blowout data involves determining a Damkohler number for the blowout condition as identified in Chapter 1. A Damkohler Number (Da) is defined as the ratio of a relevant fluid time scale to a relevant chemical time scale. A chemical time can be determined in two ways: using a laminar flame speed or using the residence time of a PSR at blowout. Equation 3.1 gives a chemical time based on a laminar flame speed, using the thermal diffusivity (α) of the fuel/air

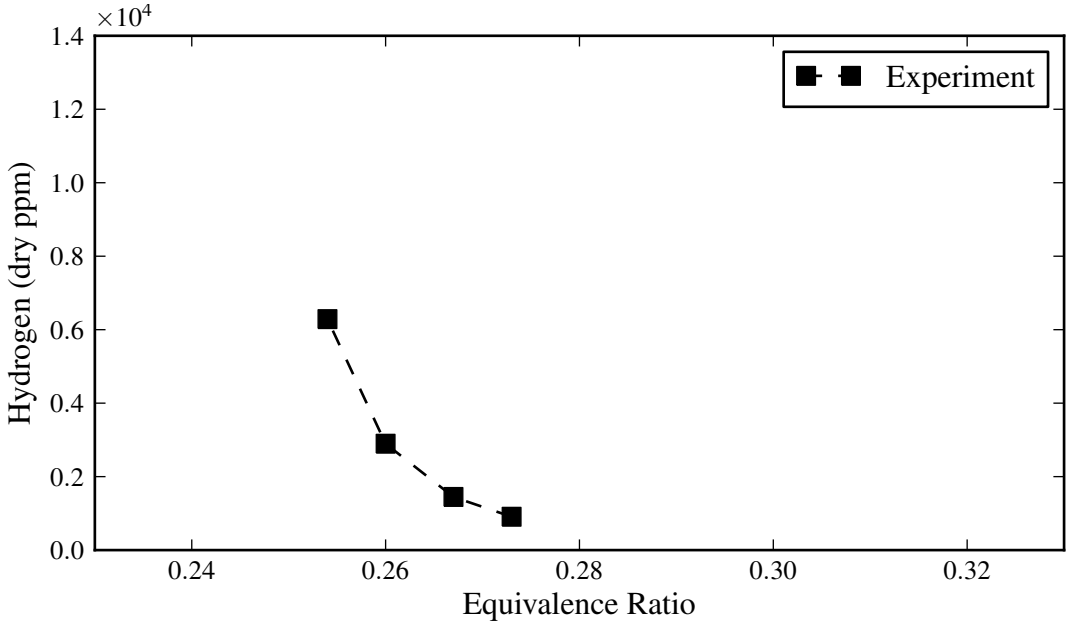

Figure 3.7: Experimentally measured hydrogen concentration at the nominal reactor sampling location plotted as a function of equivalence ratio as blowout is approached. See Appendix D for raw data.

mixture at the reactor inlet temperature, and the laminar flame speed (S_L) of the fuel/air mixture at the experimentally measured blowout condition. Second, the residence time of a model perfectly stirred reactor at blowout can be found. The inlet conditions of the PSR are set to the measured equivalence ratio and inlet temperature at experimental blowout, the nominal 20% heat loss is applied, and the residence time of the PSR is reduced until it reaches incipient blowout. Both methods of determining a relevant chemical time are applied to the H_2/CH_4 blowout data taken in the JSR using the UCSD chemical kinetic mechanism. Chemkin is the used for the calculations. The results are given in Figures 3.8(a) and 3.8(b) and both figures show a similar trend in the chemical time at blowout as a function of the percent of hydrogen in the fuel. A total of 35 data points are plotted in Figure 3.8, each representing a single blowout experiment.

$$\tau_{chem} = \frac{\alpha}{S_L^2} \tag{3.1}$$

Both methods of determining a chemical time as shown in Figures 3.8(a) and 3.8(b) reveal a similar trend. The chemical time at blowout is fairly constant over the range of fuel blends, increasing only slightly for high hydrogen blends. While the trends are consistent, the absolute values of the two times are different, with the PSB time being about twice that determined by the laminar flame speed. It should be noted that the chemical time determined by the laminar flame speed at blowout corresponds to the characteristic time of for one cycle of the recirculation zone by a fluid particle. The nominal number of cycles made by a fluid particle in the JSR is estimated to be about 4 based on the percentage of entrained flow (75%).

Finally a fluid dynamic time is needed. For the JSR the average residence time at blowout in the entire reactor is used and shown in Figure 3.8(c) as a function of hydrogen content of the fuel. In Figure 3.8(d) we see the Damkohler number at blowout as a function of hydrogen content of the fuel using both τ_{chem} (upper, dashed line) and τ_{PSB} (lower, solid line). Using τ_{chem}, the Damkohler number at blowout is essentially constant across the fuel blends. Using τ_{PSB} we see a slight upward trend as hydrogen content is increased. If we compare our trend for the Damkohler number at blowout to Zhang's [15] we see a marked difference. Taking blowout data on a gas turbine simulator at 1.7 atm with swirl and a center body for stabilization, he saw a decrease in Damkohler number of several orders of magnitude as hydrogen content increased. The change in the chemical time was the largest contributor to the Damkohler number change; τ_{PSB} for Zhang varied by 5 orders of magnitude from pure methane to pure hydrogen, while the fluid dynamic time changed only by a single order of magnitude.

The main culprit for the disparity between Zhang's results and ours is most likely Zhang's definition of blowout in the gas turbine simulator for high hydrogen blends. Zhang saw that at high hydrogen contents the blowout event in his combustor was not

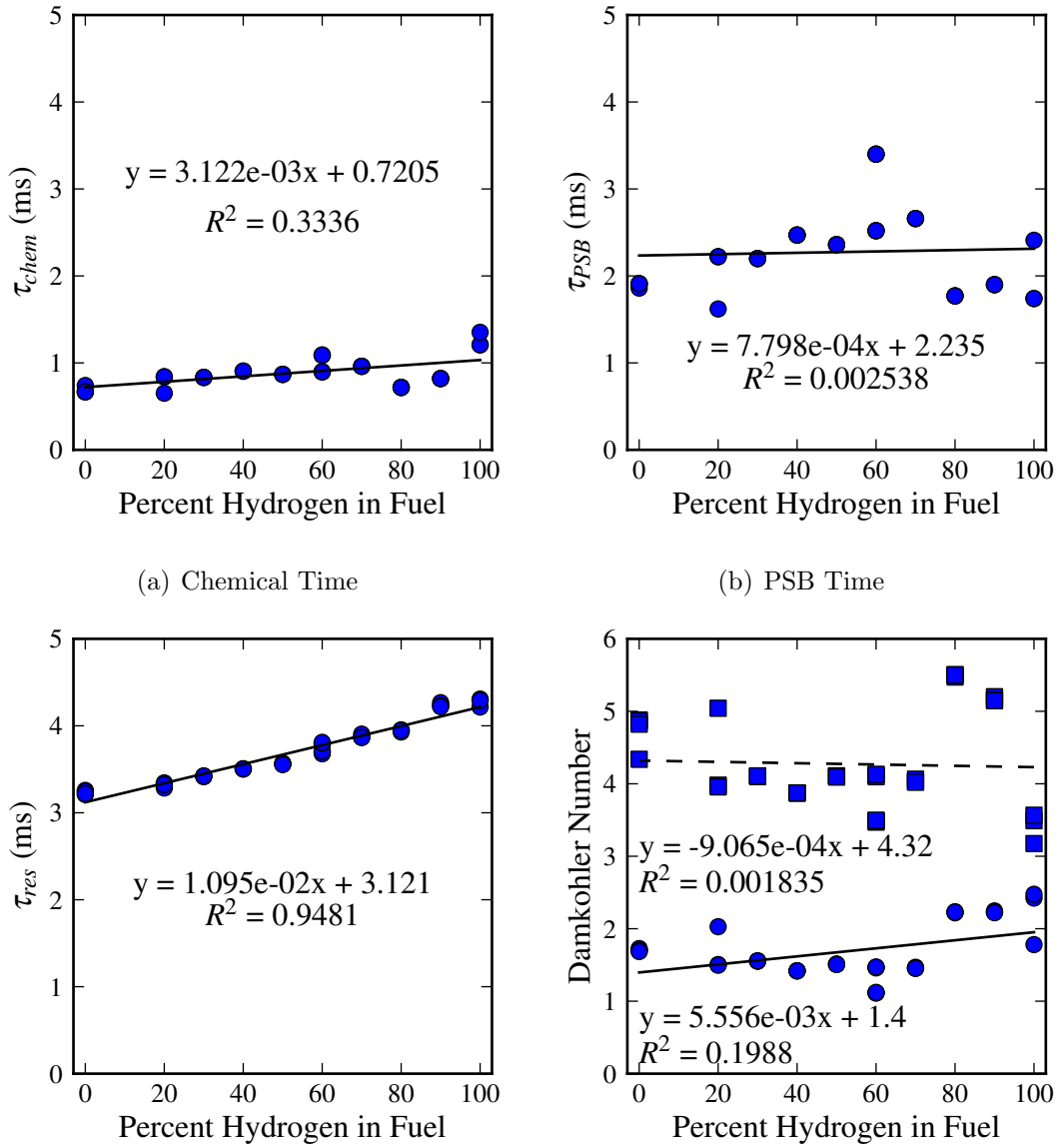

(a) Chemical Time

(b) PSB Time

(c) Residence Time

(d) Damkohler Number

Figure 3.8: Time scale analysis of experimentally measured blowout for H_2/CH_4 fuel blends: (a) chemical time scale using Equation 3.1, (b) chemical time using a perfectly stirred reactor with 20% heat loss at blowout, (c) average residence time in the JSR at blowout, (d) Damkoher number at blowout found using the chemical time from (a) and (b), shown with the squares and circles (dashed and solid lines) respectively.

distinct (unlike with methane), and therefore chose to define blowout to be the point at which the flame visually left the optically accessible combustor. This resulted in much lower equivalence ratios of stabilization for the high hydrogen blends in Zhang's gas turbine simulator when compared to the JSR. Zhang saw blowout equivalence ratios for pure hydrogen below 0.20. An order of magnitude analysis on a PSB with hydrogen as the fuel shows fairly constant blowout residence times from $\phi = 0.25$ to $\phi = 0.2$, but a two order of magnitude increase in the blowout residence time from $\phi = 0.2$ to $\phi = 0.18$ (using GRI-3.0 as Zhang did). Akbari [17] showed a similar trend in the chemical time at blowout for his high swirl atmospheric combustor running H_2/CH_4 blends. The blowout event was not distinct for high hydrogen blends, and the combustor was stabilized to much lower equivalence ratios for pure hydrogen (as low as 0.15). The non-linear response of blowout residence time to inlet equivalence ratio with high hydrogen contents may account for the much larger range of τ_{PSB} seen by Zhang and Akbari. This alone may be enough to explain why Zhang saw such a dramatic decrease in Damkohler number at blowout for high hydrogen content fuels while we saw a fairly constant Damkohler number.

A consequence of Figure 3.8(b) is that a single PSR with 20% heat loss and a constant residence time might predict the equivalence ratio at blowout for the range of fuels tested. Three constant PSB residence times were used: (1) average τ_{PSB} for pure methane (1.823 ms) [26] (2) average τ_{PSB} for pure hydrogen (1.908 ms) (3) average τ_{PSB} for the whole data set (2.235 ms). The residence time is fixed, the air flow rate is set, and then for each H_2/CH_4 fuel blend the fuel flow rate is decreased until blowout occurs and the predicted equivalence ratio at blowout recorded. A nominal 20% heat loss rate is applied based on the inlet equivalence ratio. Plots of predicted versus measured blowout equivalence ratio and temperature are given in Figure 3.9.

Figure 3.9(a) shows the single PSR with a constant residence time predicts the equivalence ratio at blowout within 95% confidence intervals for all fuel blends. There

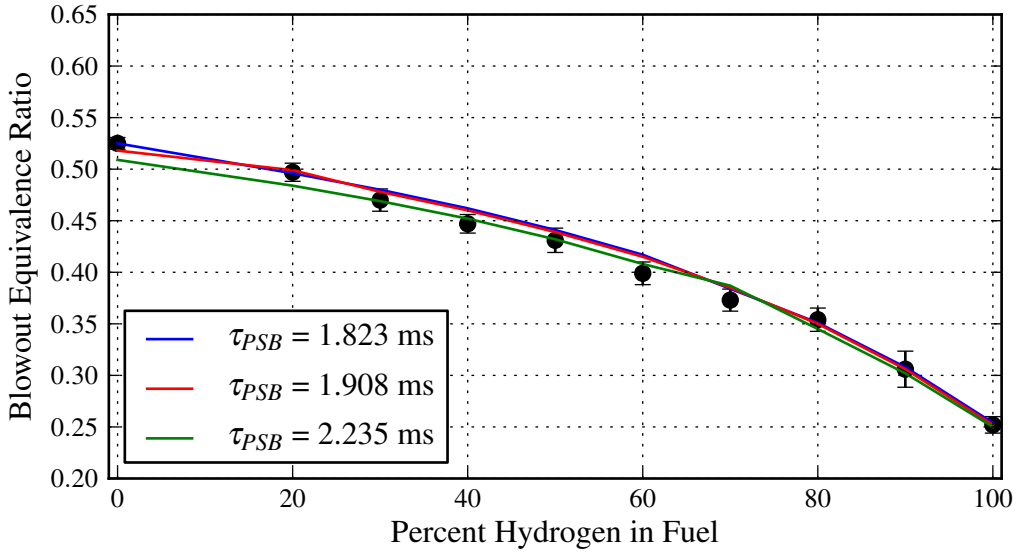

(a) Equivalence Ratio

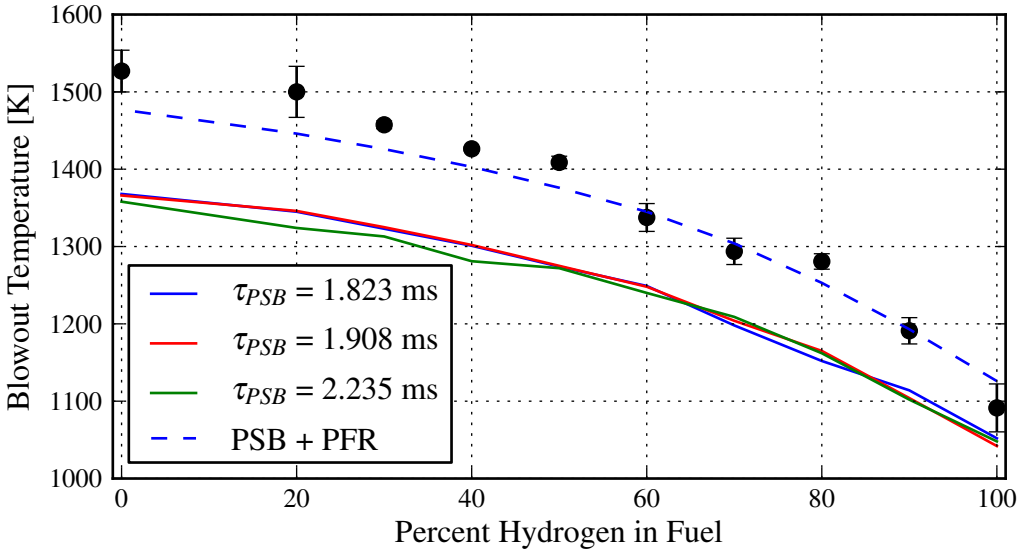

(b) Temperature

Figure 3.9: PSB predictions of blowout compared against experimentally determined blowout (a) temperature and (b) equivalence ratio for CH_4 mixed with increasing amounts of H_2.

is little difference in the predictive capability for the three different residence times chosen. Figure 3.9(b) shows a significant under-prediction of the temperature especially for blends with high CH_4 content. Much of the late heat release will occur from the oxidation of CO for these blends and therefore a PSR+PFR configuration is added in an attempt to better predict the temperature at blowout. A PSR with τ_{PSB}=1.823 ms is chosen and a PFR added in series. For each fuel blend the PSR volume at the blowout condition is recorded and the PFR volume set to make up the difference in the reactor volume. This brings the temperature up significantly, although we are still under-predicting for high CH_4 concentrations by up to 50 K.

Finally, while this approach has an excellent predictive quality to it, the physical implications of the success of this approach for the JSR are unclear. If we compare the work of Zhang [15], Strakey [26] and ours, the ability of a single PSR at a constant residence time to predict the equivalence ratio at blowout for a wide range of fuel blends depends on the definition of blowout and the combustor under study. We wish to gain more physical insight on what's controlling blowout as the fuel blend changes. This motivates the subsequent modeling work in Chapters 4 and 5.

3.3.1 Acoustic Events

Every turbulent combustion process produces some amount of noise, referred to as direct combustion noise. When a volume of gas expands at constant pressure due to heat addition from the combustion process a propagating sound wave is produced. The shape and frequency range (100-2000 Hz) of the sound power curve is largely independent of combustor size, engine power and flame temperature, although the magnitude of the radiated sound power is proportional to the engine power [82]. Direct combustion noise is coloquially referred to as "combustion roar". The general sound power curve from a combustor can be altered by combustion instabilities, which result from the interaction of oscillating heat release rates and pressures inside the combustor. The Rayleigh Criterion [83] is the basis for analysis of combustion in-

stabilities and is defined as the product of the heat release rate perturbation and the pressure fluctuation integrated over one period of oscillation. A positive result indicates that the fluctuating heat release is more in-phase than out-of-phase with the pressure oscillation and so the oscillation is maintained. The resulting changes in the spectrum of the combustion noise are described by Lefebvre to fall into two categories: growl which is in the low frequency range of 50 to 180 Hz, and howl which is typically from 200 to 500 Hz [82]. Further information on the coupling and driving mechanisms of these combustion instabilities can be found in [84].

The acoustic events heard in the JSR seem to be time-localized, and therefore do not affect the overall frequency spectrum of the combustion noise as a 'growl' or a 'howl' would. We therefore focus on time-localized acoustic events in the combustion process as seen by Nair and Lieuwen [5]. Here they explore acoustic detection of blowout in premixed flames for three different lean premixed combustors running on methane: a piloted burner, a bluff-body stabilized burner, and swirl stabilized burner. They saw time-localized acoustic events for both the bluff-body and swirl stabilized burners which increased in frequency as blowout was approached. In addition to the audio recordings they also presented high speed camera images for the bluff-body burner and OH* chemiluminescence time series data for the swirl burner. The high speed images show that near blowout one of the flame branches almost disappears from view before re-emerging, suggesting extinction followed by reignition of unburnt premix in the shear layer. It also appears that the flame is lifted prior to blowout. OH* chemiluminescence from the swirl-stabilized combustor confirms that the acoustic events are preceded by large dips in the optical signal which coincide with temporary loss of flame. Unfortunately no further information is given to diagnose the flame loss and reignition mechanism.

Exploration of the extinction/reignition mechanism (corresponding to acoustic events) for a swirl-stabilized dump combustor is given by Muruganandam and Sietzman [6]. During stable combustion they found that the flame is attached to the center

body formed by the inner hub of the final swirler. Occasionally a part of the flame detaches due to turbulent fluctuations, and as the equivalence ratio is reduced the duration, frequency and extent of the detachment increases. When the extent of the flame detachment allows enough cold unburned pockets of gas to move around the inner recirculation zone, thus reducing the entrainment of heat and radicals necessary for stabilization, the flame detaches completely from the center body. This appears as an extinction event, however instead of the flame being lost completely it splits into two parts, one near the inlet and one near the exit of the combustor. With the heat release relocated, the flow field now changes as the recirculation zones and swirl respond. The flame now appears as a 'tornado', stabilized by the hot walls of the combustor. Occasionally a reignition event will occur when this 'tornado' sends a flame packet towards the inlet which if strong enough will reattach to the center body resulting in a return to the original flame configuration.

In our JSR, we hypothesize that a similar extinction/reignition behavior results in the acoustic events we detect. The flow field in the JSR is much simpler than that in a swirl stabilized or bluff body combustor and may allow for some simple time scale analysis. We hypothesize that the time between events corresponds to a fluid-dynamic or chemical time or some combination of these that exist near blowout for H_2 and not for CH_4. The following are proposed as possible time scales of interest:

- Mean reactor residence time near blowout
- Mean time to reach stagnation point
- Mean time for a turbulent flame to propagate across the reactor
- Time to ignition

The first two times are simple fluid dynamics times that can be easily determined. We take mean reactor residence time to be $\rho * V/ \cdot m$, where the density ρ is found

using the ideal gas equation at atmospheric pressure and the measured temperature and the volume V is taken to be that of the reactor, 15.8 cc. The mean residence times for H_2 and CH_4 at blowout are 4.2 and 3.2 ms respectively. The mean time to reach the stagnation point can be determined from path lines in a Fluent model and is determined to be approximately 0.3 ms for both fuels. The final two times are chemical times and are more difficult to determine. A first attempt at comparing ignition times is given in Appendix F but work is still needed to determine a relevant turbulent flame speed for the two fuels.

Cross-correlation is used to identify the acoustic events more easily and assist in determining the time between acoustic events. In signal processing it is used to measure the similarity of two wave-forms, and the time shift which produces the greatest similarity. It is commonly used for searching a long-duration signal for a shorter known feature. It is defined in Equation 3.2 in which we consider a noisy signal, $f(n)$, expressed as a vector with index n of length N, which contains some known signal to identified, $s(n)$. If the length of $s(n)$ is less than $f(n)$ then $s(n)$ is padded with zeros. A new signal of length N is produced by taking the dot product of $f(n)$ and $s(n)$ while $f(n)$ is fixed and $s(n)$ is shifted to both the left and the right (in time) through k. Large values in this new signal then indicate the time around which $s(n)$ is centered when $f(n)$ most nearly contains it.

$$\sum_{n=0}^{N} f(n) \cdot s(n-k) \qquad\qquad k = 0, \pm 1, \pm 2 \ldots \tag{3.2}$$

To apply cross-correlation to our case, a sample acoustic event is extracted from the raw data and taken to be $s(n)$ as shown in Figure 3.10. A half-second interval is chosen from the recording for illustration and both the waveform and the absolute value of the cross-correlation are plotted in Figure 3.3.1. A threshold of 1.0 is then chosen in order to identify events. In the interval shown there are 10 events. This can also be confirmed with the original audio recording. By playing the half-second sample at a reduced rate, such as 8 kHz instead of the 96 kHz at which it was

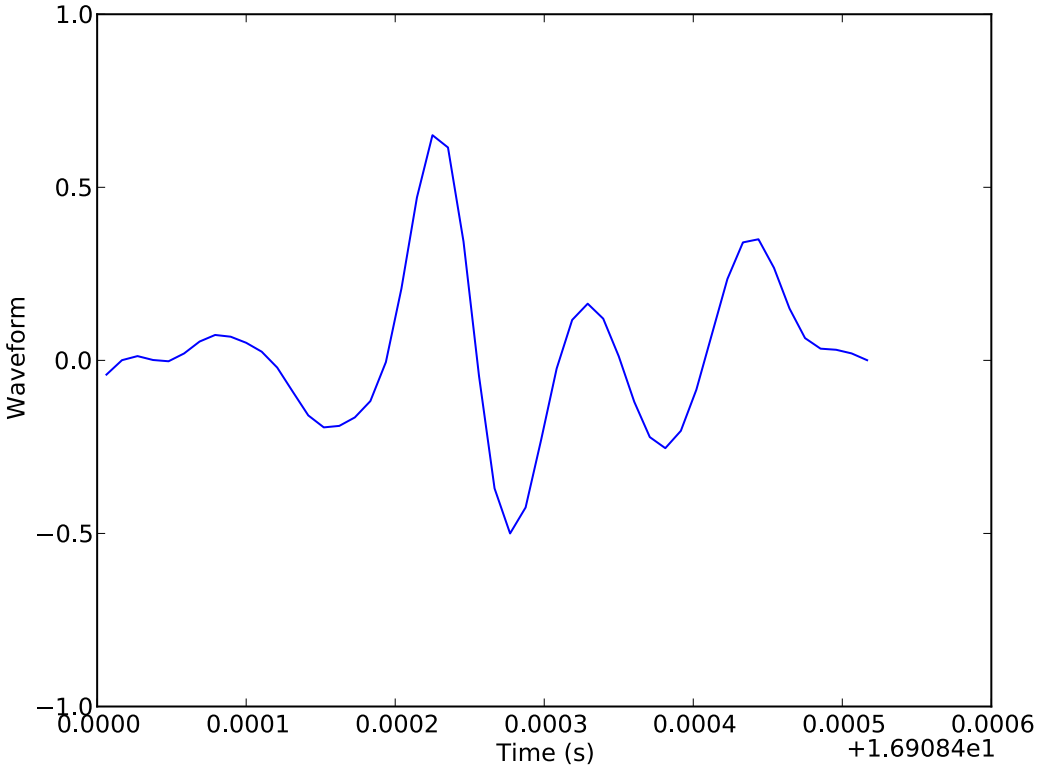

Figure 3.10: Sample $s(n)$ used in cross-correlation to identify acoustic events near blowout.

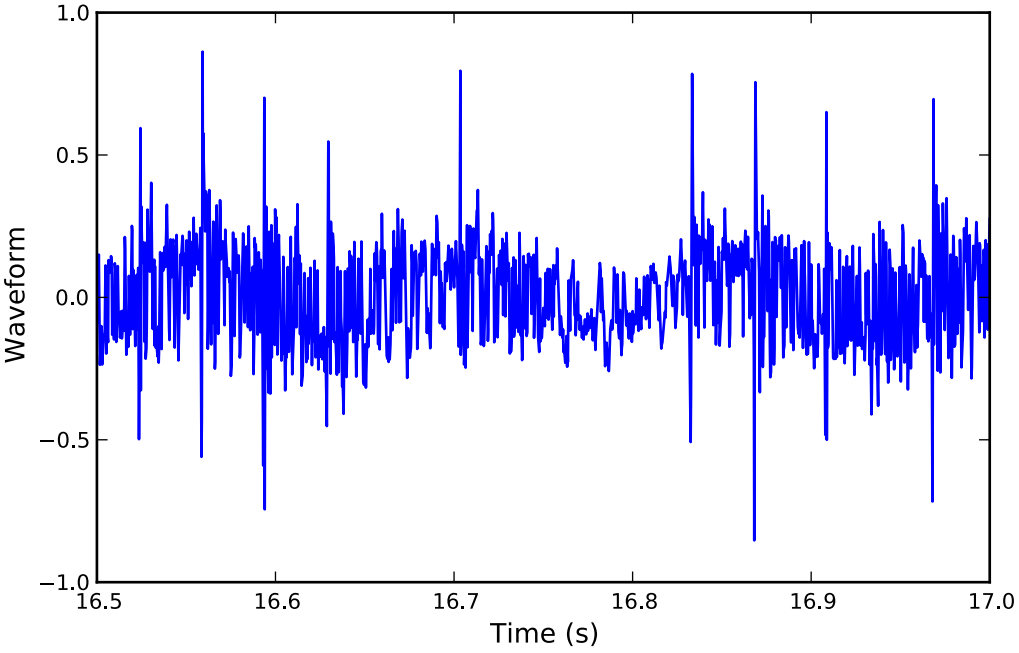

(a) Waveform

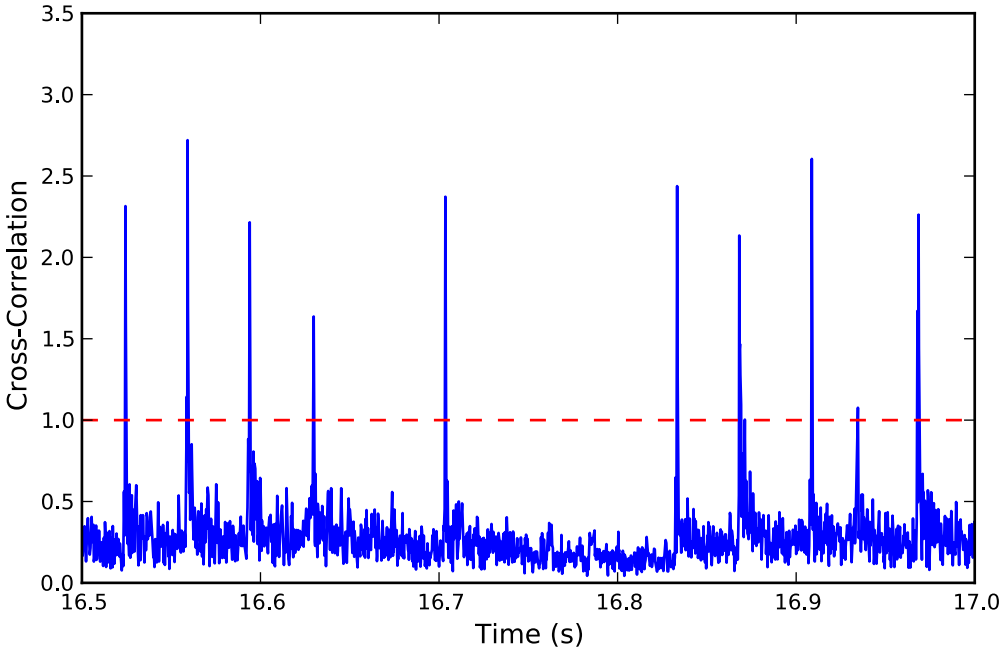

(b) Cross-Correlation

recorded, the sample play time is lengthened to 6 seconds and the acoustic events can be identified by ear and counted. The 10 events every half-second gives a mean time between events of 50 ms. If Figure 3.3.1 is looked at again, one might argue that events are "missing". Initially there are four regularly spaced events and then a gap before the fifth. Likewise there appears to be two missing events before the 6th peak. Then the events proceed regularly for the rest of the interval, with one more missing at the end. Therefore the time scale of interest might be 35 ms, with missing events, rather than 50 ms.

Recordings for pure hydrogen were repeated and there is some variance in the number of events in a half-second interval (6-14). The frequency also depends somewhat on proximity to blowout. Recordings for hydrogen blended with methane through a 70/30 blend show that the mean time between acoustic events immediately before blowout does not change appreciably as the amount of methane is increased. And a 60/40 blend produces no acoustic events. Further work is needed to identify the corresponding physical time scales to the now identified frequency of the acoustic events.

3.4 Conclusions from the Experimental Work

Blowout data is taken on the JSR for the full range of CH_4/H_2 fuel blends in 10% increments by volume. The data is collected by holding the air flow rate constant and reducing the fuel flow rate until the flame extinguishes. By using this approach the flow field and turbulence parameters are held approximately constant as blowout is approached. Results show that the JSR is stabilized to lower equivalence ratios and temperatures as the amount of hydrogen in the fuel increases. The trends in equivalence ratio and temperature at blowout as a function of the percentage of hydrogen in the fuel are nonlinear. A time scale analysis of the blowout data shows that the JSR extinguishes at an approximately constant chemical time. A consequence of this analysis is that a predictive model can be applied to the data. The blowout equiva-

lence ratio and temperature for each fuel blend is well predicted by a PSR with 20% heat loss and this observed constant chemical time (set as the residence time of the PSR) in series with an adiabatic PFR. While this model is predictive it does not give detailed insight on the controlling processes in the JSR as blowout is approached for the range of fuel blends. This goal motivates the subsequent modeling work described in Chapters 4 and 5.

When the blowout condition for each fuel blend was being collected, time-localized acoustic events are observed and recorded for fuel blends with 70% or more of hydrogen. These events occur approximately every 35-50 ms immediately before extinction, and their frequency is not substantially affected by the percentage of hydrogen in the fuel blend, except for the fact that they completely cease for blends of 60% hydrogen and less.

Finally, a profile of methane concentration across the reactor at the nominal 1800 K condition is collected with the GC to assist in CFD model validation. This complements the temperature profiles taken by Fackler [3] at the same condition. And the concentration of hydrogen is measured at the nominal sampling location as blowout is approached, again to be used for model validation.

Chapter 4

COMPUTATIONAL FLUID DYNAMICS MODEL

4.1 CFD Model Development

Two dimensional axisymmetric CFD simulations of the combustion of a pure fuel (hydrogen or methane) premixed with air are carried out with the ANSYS Fluent 13.0 software package [85]. A diagram of the computational domain is shown in Figure 4.1 with the solid in grey and the fluid in white. The entire domain is comprised of approximately 36,000 cells.

4.1.1 Fluid Dynamics and Heat Transfer

Calculations in the fluid portion are conducted with the steady-state Reynolds-Averaged Navier Stokes (RANS) equations and the 5 equation Reynolds Stress Model (RSM) as the turbulent closure model. The RSM options chosen include: linear pressure-strain model, enhanced wall treatment, and viscous heating. The nozzle is choked and the density in the reactor is modeled using the ideal gas equation. The solid is included to address the non-adiabatic nature of the JSR. Conduction, convection, and radiation are all included. The Discrete Ordinates (D-O) model accounts for the radiation from H_2O and CO_2 inside the JSR. Radiation on the outer surfaces of the reactor body, nozzle block, and exposed section of the premixer are modeled as a simple gray body with an emissivity specific to the material and a view factor of unity. An analytical calculation is used to estimate the natural convection heat transfer coefficients on each of the exposed surfaces.

The goal of the CFD work is to explore the flame extinction process (i.e. blowout). This is approached in the model by reducing the inlet equivalence ratio until blowout

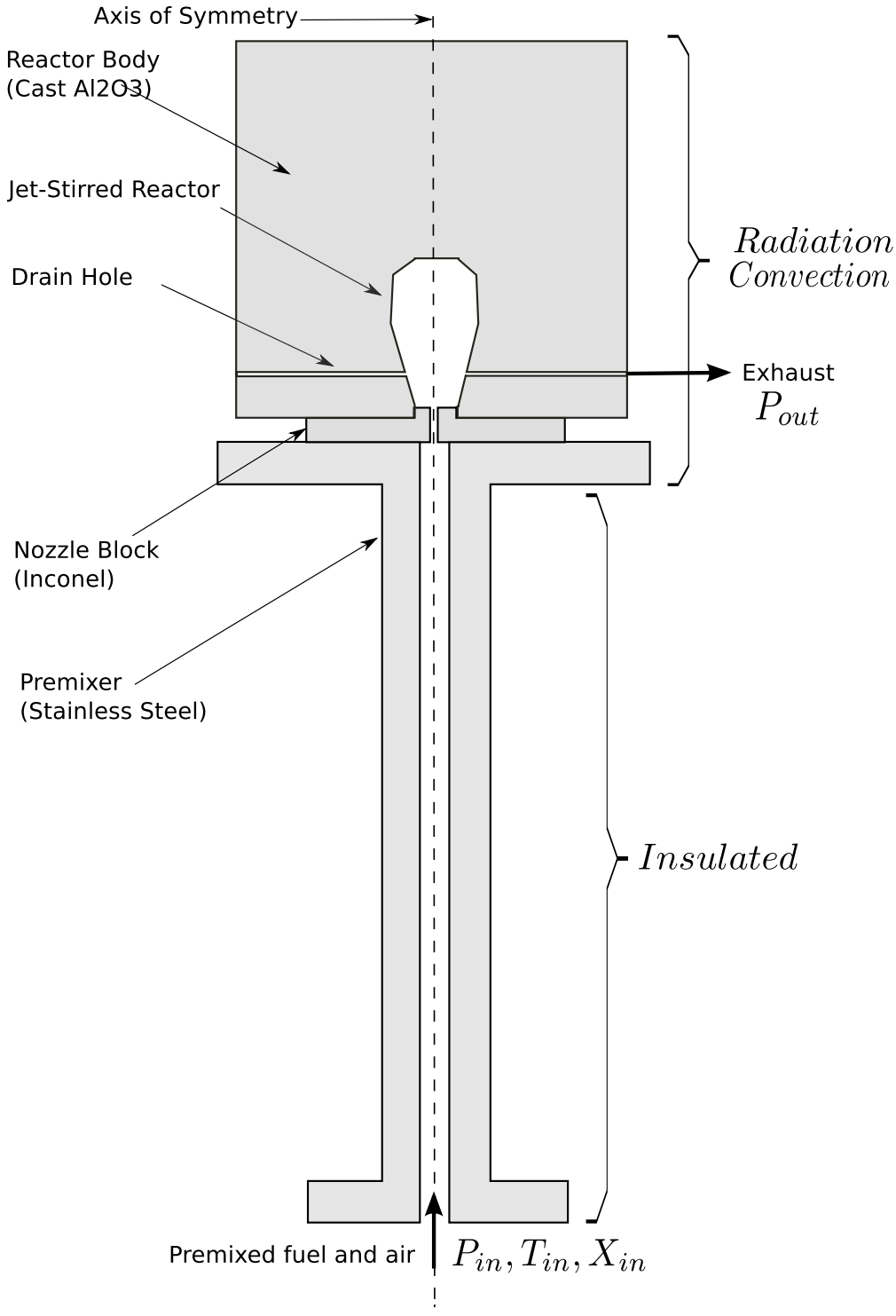

Figure 4.1: Illustration of the CFD computational domain and boundary conditions.

in the CFD model is achieved. Several strategies outlined in a paper by Nanduri *et al.* [86] are used to mitigate numerical influences on this event. The RSM is chosen as the turbulent closure model over k-ε because of the highly recirculating nature of the flow in the JSR, and because it is a less dissipative turbulence model. In addition, higher-order discretization schemes are used because they reduce numerical diffusion. According to Nanduri *et al.* [86], artificial sources of dissipation and diffusion can lead to premature blowout in the CFD model. Table 4.1 outlines the discretization schemes chosen.

Table 4.1: Computational conditions.

Model Parameter	Spatial Discretization
P-V Coupling	SIMPLE
Pressure	PRESTO!
Momentum	QUICK
Species	MUSCL
Energy	MUSCL
D-O	2^{nd} Order

Although the fluid dynamics of the reactor are well represented by a 2D axisymmetric simulation, the geometry is only quasi-two dimensional. The four distinct outlets are each 2 mm in diameter, offset 90 degrees from one another. In order to simplify the model, these four outlets are represented by a single slot. We could not, however, use the same area for the slot as that given by the four outlets in the original reactor. This is due to numerical issues associated with the resulting sub-millimeter width of the slot. Increasing the area of the outlet slot to avoid these numerical issues resulted in underestimating the actual pressure drop between the reactor and the environment and thus the pressure and jet dynamics in the JSR. To remove the numerical issues and correctly predict the jet dynamics in the 2D model, the pressure

at the outlet, P_{out}, was adjusted such that the over-pressure in the JSR matched that predicted by the 3D model which was run with the original outlets at the nominal operating condition [87]. The absolute pressure in the reactor cavity in the 3D model is approximately 1.5 atm [3]. In addition, an adiabatic boundary condition is set for the walls of the drain hole (now a slot) to prevent excessive back-heating of the ceramic reactor caused by the significant increase in surface area.

4.1.2 Turbulent Combustion

The turbulent combustion within the reactor is computed using the Eddy-Dissipation-Concept (EDC) model developed by Magnussen [88, 89, 90, 91, 92]. The EDC model is derived from principles of the energy cascade of turbulent energy, describing the transfer of energy from larger to smaller turbulent structures, and the final dissipation of energy in the smallest structure referred to as the fine structures. An expression for the volume fraction of the fine structures can then be derived

$$(\gamma^*)^3 = (C_\gamma)^3 \left(\frac{\nu\varepsilon}{k^2}\right)^{3/4} \tag{4.1}$$

where k is the turbulent kinetic energy, ν is the kinematic viscosity, ε is the dissipation of turbulent kinetic energy, C_γ is a constant and γ^* is the fractional length of the fine structures. In addition, the residence time in the fine structures is closely related to the Kolmogorov turbulent time scale and is given by

$$\tau^* = C_\tau \left(\frac{\nu}{\varepsilon}\right)^{1/2} \tag{4.2}$$

Here C_τ is a second constant. The values of these constants are linked to the constants found in most turbulence models, and information on their determination can be found in [91].

The chemical reactions in the fine structures are assumed to occur in a perfectly stirred reactor over a residence time, τ^*, with the reactor feed conditions being the species concentrations of the surrounding fluid in the computational cell. The mean

reaction rate of a computational cell is then modeled as a mass transfer between the fine structure regions and the surrounding fluid. The expression for the mean reaction rate is:

$$\tilde{R}_i = \frac{\tilde{\rho}(\gamma^*)^2}{\tau^*}(Y_i^* - Y_i^o) \tag{4.3}$$

where Y_i^* denotes the mass fraction of species i in the fine structures and Y_i^o denotes the mass fraction of the species in the surrounding fluid. The averaged cell composition is obtained by:

$$\tilde{Y_i} = (\gamma^*)^3 Y_i^* + (1 - (\gamma^*)^3) Y_i^o \tag{4.4}$$

such that Equation 4.3 can be rewritten with cell averaged values ($\tilde{}$) as:

$$\tilde{R}_i = \frac{\tilde{\rho}(\gamma^*)^2}{\tau^*[1 - (\gamma^*)^3]}(Y_i^* - \tilde{Y}_i) \tag{4.5}$$

Equation 4.5 corresponds to the implementation of the EDC-model in Fluent [85]. It should be noted however, that for combustion under low Damkohler number conditions due either to high intensity turbulence or slow reaction chemistry, it may be important to account for reactions in the surrounding fluid [89, 93]. Because the extension of the reactions into the surrounding fluid is not addressed in the implementation of the EDC model in Fluent, nor developed further in Magnussen's work, the high Damkohler number condition is a key assumption of the current implementation of the model.

In addition, the EDC model generates some problematic behavior near the wall. Figure 4.2 illustrates the behavior of the EDC model in this region. The reaction rate of hydrogen, the coefficient of $\tilde{R}_i$ in Equation 4.5 $[(\gamma^*)^2/(\tau^*(1-(\gamma^*)^3))]$, and the length fractions of the EDC model $[\gamma^*]$ are all plotted as a function of y^+ from a point at the top of the centerline of the reactor where the reacting jet impinges on the wall. Even though the distance plotted in this figure is only 0.2 mm, the destruction rate of hydrogen increases by a factor of 6. The reaction of hydrogen closely follows the coefficient of $\tilde{R}_i$, which is strongly dependent on γ^*. In fact $(\gamma^*)^2/\tau^*$ goes as ε/k.

Thus, the EDC model breaks down in the boundary layer because k goes to zero at the wall. As shown in Figure 4.2(c), if γ^* is calculated strictly from the turbulence quantities it quickly exceeds 1 and grows very large as k becomes small (i.e. the portion of the cell that is a reacting fine structure becomes larger than the cell). Because this is not physical, Fluent limits the EDC length fraction to 0.755 such that $(\gamma^*)^2/(1-(\gamma^*)^3) \leq 1$ holds everywhere. As the flow transitions from the fully turbulent log-law region, to the buffer layer, and subsequently to the viscous sublayer for decreasing y^+: the EDC model, which was developed assuming a fully turbulent flow, breaks down. It is believed that when the turbulence weakens as the wall is approached, the reactions shift to a slower, laminar rate.

Thus, two limitations of the EDC model have been identified: (1) EDC overpredicts the reaction rate near the wall (2) EDC may underpredict reaction rates under low Damkohler number conditions.

A first order correction to the problem (1) is to artificially eliminate all reactions in the boundary layer. This is accomplished with a User Defined Function (UDF). The transition from the fully turbulent region to the buffer region of the boundary layer is assumed to occur at $\mathrm{Re}_y = y\sqrt{k}/\nu = 200$ where y is the distance from the wall, k is the turbulent kinetic energy and ν is the viscosity. This is in keeping with the criteria used by other wall treatments for the turbulence and heat transfer models [85]. For $\mathrm{Re}_y < 200$ a reaction source term that is equal in magnitude to that of the EDC model but is of opposite effect is added to the conservation equations for each species and the conservation of energy equation. An example of such a UDF is given in Appendix C.

A first order correction to problem (2) is to artificially increase the volume of the fine scales, essentially forcing the model to account for reactions taking place in a larger portion of the cell. Fluent limits the quantity $(\gamma^*)^2/(1-(\gamma^*)^3)$ to unity, therefore $(\gamma^*) = 0.755$ can produces the largest reaction rate possible considering a constant EDC residence time, and this can be thought of as the EDC limit. We

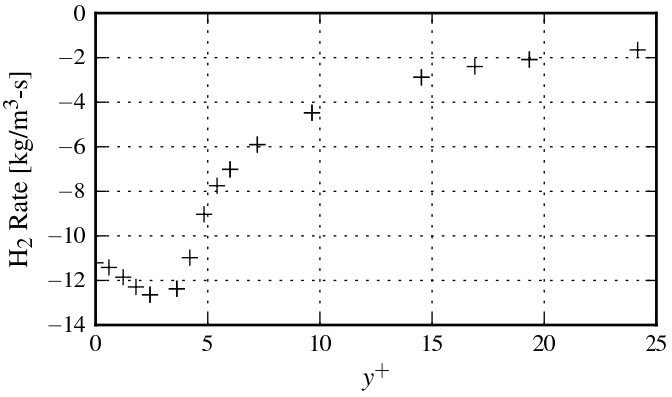

(a) Hydrogen Reaction Rate

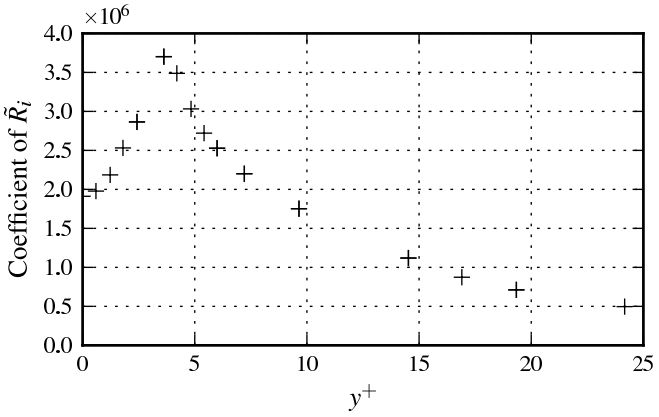

(b) Coefficient of R_i

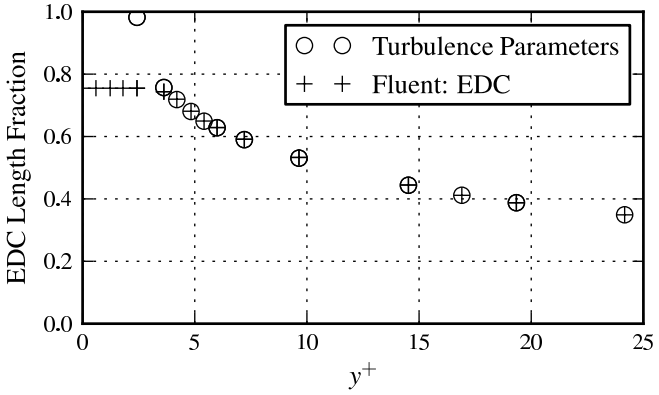

(c) EDC Length Fraction

Figure 4.2: Illustration of EDC model behavior near a wall and the connections among H_2 reaction rate [kg/m^3-s], coefficient of $\tilde{R}_i$ in Equation 4.3$[(\gamma^*)^2/(\tau^*(1-(\gamma^*)^3))]$, and EDC length fraction (γ^*), plotted as a function of $y^+ = u_\tau y/\nu$.

therefore explore the effect of raising γ^* to the EDC limit everywhere in the reactor volume. This is accomplished by raising C_γ.

4.2 CFD Validation

Before the CFD model is used to explore blowout, it is validated against temperature profiles taken by Fackler [3] for pure CH_4 and pure H_2, and a complementary methane profile obtained with the GC at a nominal stable operating condition of 1800K in the recirculation zone. All temperatures were corrected for heat transfer effects by Fackler. CFD runs with all three versions of the EDC model are compared to the experimental data at the nominal operating condition: (1) EDC, (2) EDC without reactions in the boundary layer, and (3) EDC Limit without reactions in the boundary layer.

The hydrogen results in Figure 4.3 show that EDC and EDC without reactions in the boundary layer both provide similar results. The temperature is underpredicted

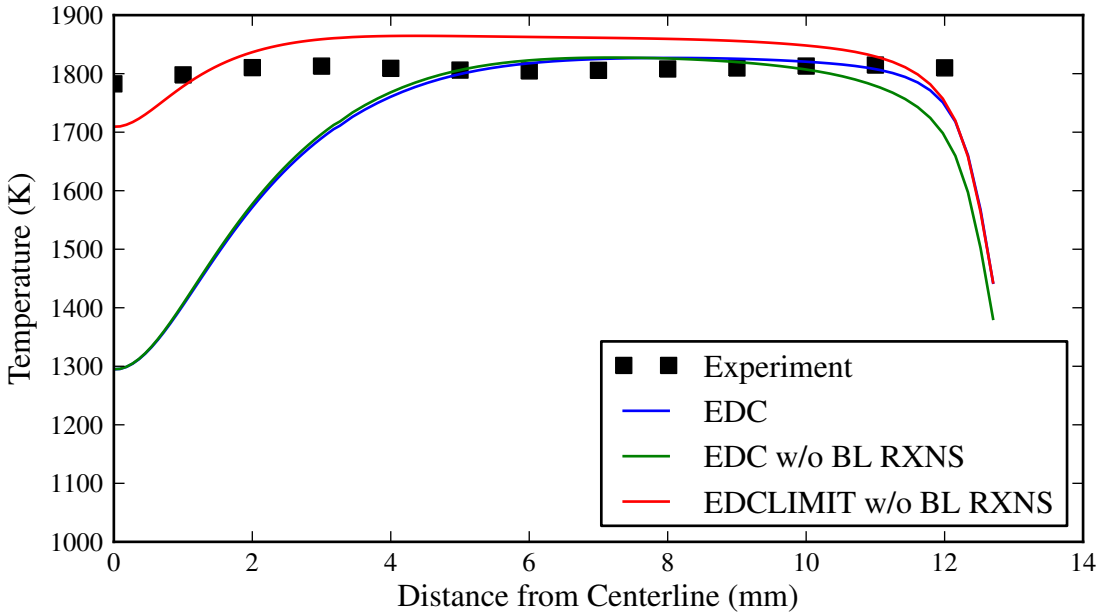

Figure 4.3: Profile of temperature taken from reactor centerline to wall, measured and predicted by CFD for H_2 combustion.

on centerline, but matches experimental data well in the recirculation zone. This can most likely be attributed to the fact that EDC was developed under a high Damkohler number assumption, but the jet region experiences slow chemistry and fast mixing. The model with EDC at its limit raises both the overall heat release and the temperature on the centerline for hydrogen combustion.

The methane results in Figure 4.4 show less of a difference in the ability of the three versions of the EDC model to predict the experimentally measured temperature profile. The overall heat release is raised with EDC at its limit, mostly likely due to better CO oxidation in the recirculation zone, however the temperature trend along the probe line is the same. We do see a significant difference in the ability of the models to match the methane profile taken by the GC. The experimental data points taken at 0 mm and 1 mm are considered to be the most accurate. The low temperature ($\sim$1200 K) and small concentrations of radicals should prevent oxidation of methane in the probe before it reaches the GC. Points taken at 2 mm and 3 mm are more likely to be subject to oxidation in the probe. Given this, the EDC models with and without reactions in the boundary layer match the methane profiles quite well. The underprediction of methane across the reactor by the model with EDC at its limit is most likely due to the increased reaction rates.

We can show that the measured methane concentration on centerline corresponds to dilution only with no reactions having occurred. The amount of mass entrained by the jet at the axial location of the probe can be determined from the measured methane concentration ($X_{\mathrm{CH_4}}$ converted to a wet basis) using Equations 4.6 and 4.7, where MW_{mix} is the molecular weight of the gas mixture, $MW_{\mathrm{CH_4}}$ is the molecular weight of methane, m_{inlet} is the total fuel/air flow rate into the reactor, $m_{\mathrm{CH_4}}$ is the fuel flow rate into the reactor, and m_{total} is the total amount of mass flow in the jet at a prescribed axial location. The amount of mass entrained in the jet can also be determined from the CFD model by integrating the downward mass flow across the reactor at the axial location of the probe measurements. The percentage of mass flow

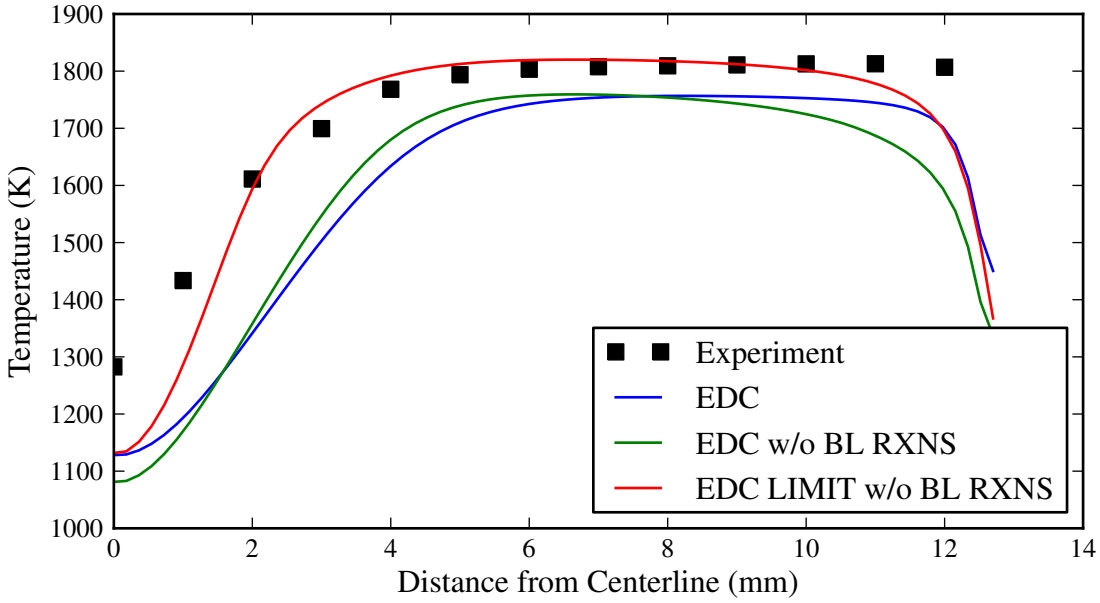

(a) Temperature

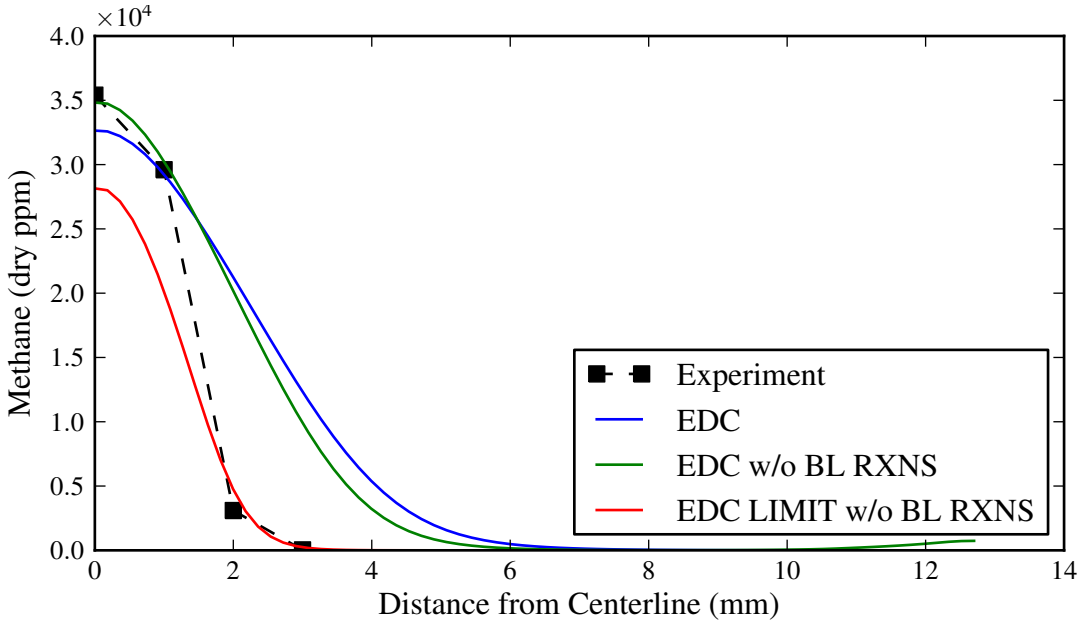

(b) Methane (dry ppm)

Figure 4.4: Profiles of (a) temperature and (b) methane (dry ppm) taken from reactor centerline to wall, measured and predicted by CFD for CH_4 combustion.

entrained assuming the measured concentration of CH_4 is due to entrainment only (no reactions have occurred) is 52%. This compares well with the entrained mass flow calculated by the velocity profiles from CFD at the same axial location (56%). Note that the version of the EDC model chosen does not affect the determination of the entrained mass flow calculated from CFD.

$$m_{total} = \frac{m_{\mathrm{CH_4}} * (MW_{mix}/MW_{\mathrm{CH_4}})}{X_{\mathrm{CH_4},wet}} \tag{4.6}$$

$$\text{Entrained } \% = \frac{m_{total} - m_{inlet}}{m_{total}} * 100 \tag{4.7}$$

4.3 CFD Modeling Results: Hydrogen

The effect of the eliminating reactions in the boundary layer with a UDF and raising the volume fraction of the fine scales to their limit, here referred to as the EDC limit, is shown in Figure 4.5. Removing reactions in the boundary layer significantly affects visualization, however it does not significantly affect the prediction of the blowout condition. Eliminating reactions in the boundary layer allows a burning numerical solution to be obtained at a slightly lower equivalence ratio. Stabilization to the slightly lower equivalence ratio without reactions in the boundary layer is attributed to the fact that unburned fuel and radicals are re-entrained into the jet rather than consumed near the wall, resulting in increased global stability. The large destruction rate of H_2 near the base of the flame as shown in Figure 4.5(b) is a direct result of this re-entrainment. Raising the volume fraction of the fine scales at which reaction occurs also significantly improves stability of the flame because a larger volume of each cell is allowed to react and therefore more fuel can be consumed at lower equivalence ratios.

The comparison of all three models to the experimental data is given in Figure 4.6. We see that all models match the blowout temperature reasonably well. The first two models (EDC and EDC w/o BL RXNs) match the blowout equivalence ratio well and follow a similar temperature vs. equivalence ratio profile approaching

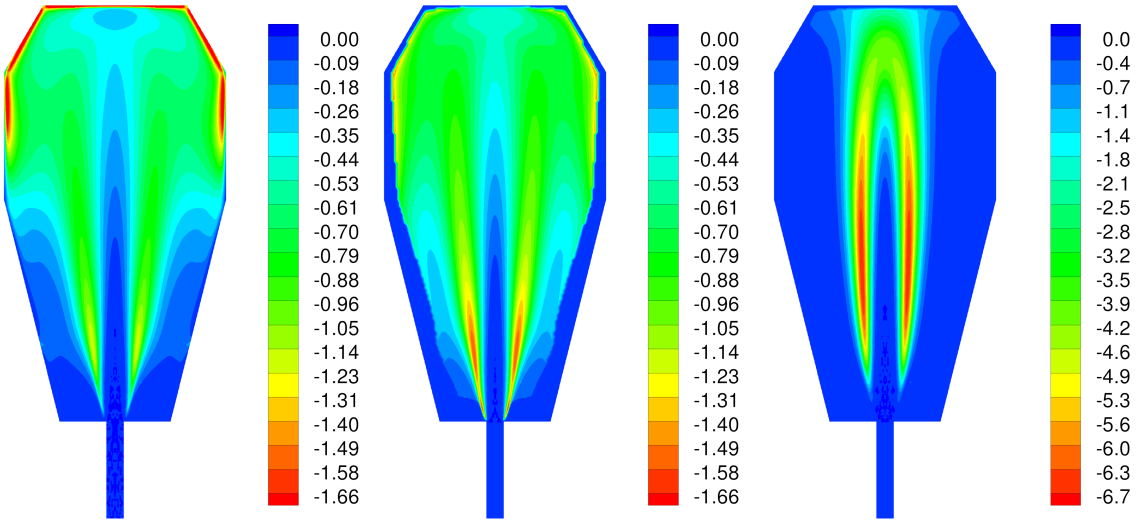

(a) EDC (b) EDC w/o BL RXNs (c) EDC Limit w/o BL RXNs

Figure 4.5: Comparison of the reaction rate of H_2 at an equivalence ratio of 0.27 for three versions of the EDC model: (a) the original EDC model, (b) the EDC model with the UDF eliminating reactions in the boundary layer, and (c) the EDC model at the EDC limit with the UDF eliminating reactions in the boundary layer. Note that the reaction rate range for (a) and (b) have been set equal.

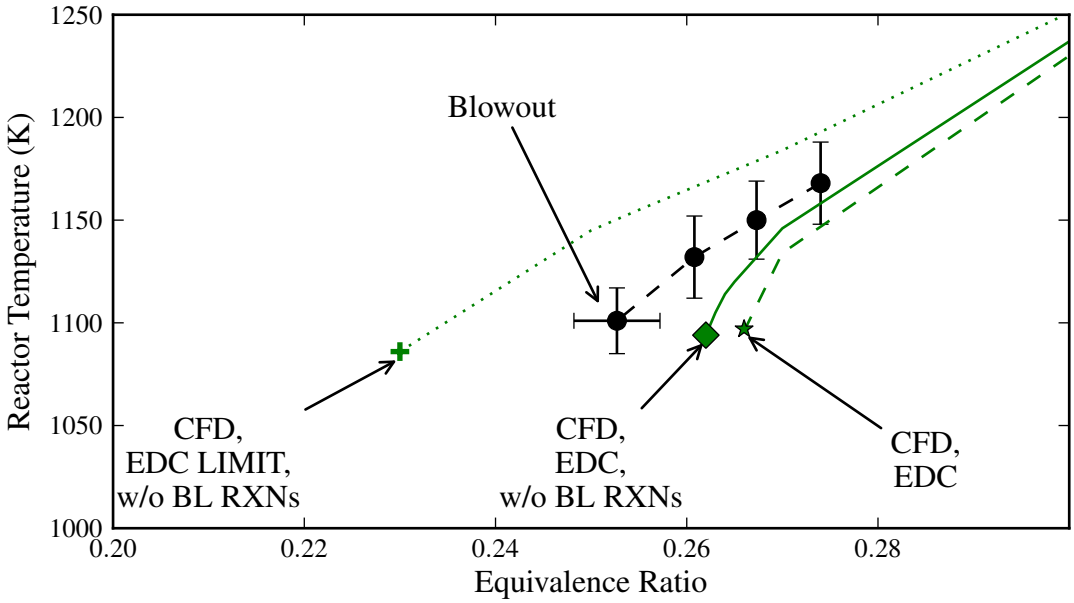

Figure 4.6: CFD blowout for hydrogen combustion compared against the experimental data.

blowout. The third model (EDC Limit) significantly underpredicts the equivalence ratio at blowout and produces a temperature vs. equivalence ratio profile above that measured experimentally.

For validation purposes we compare the measured hydrogen concentration at the nominal sampling location approaching blowout to that predicted by each EDC model variation in Figure 4.7. It is assumed, that due to the presence of radicals in the recirculation zone, there will be oxidation of H_2 in the probe. We therefore expect the measured H_2 concentration to be less than that predicted by the CFD. Both the EDC model and the EDC model without reactions in the boundary layer show this to be the case. The EDC model at its limit however, significantly underpredicts the H_2 concentration. Because of this and the analysis above, the EDC model at its limit will not be pursued further for methane combustion as blowout is explored.

Figures 4.8, 4.9, and 4.10 are taken from the EDC model with reactions eliminated

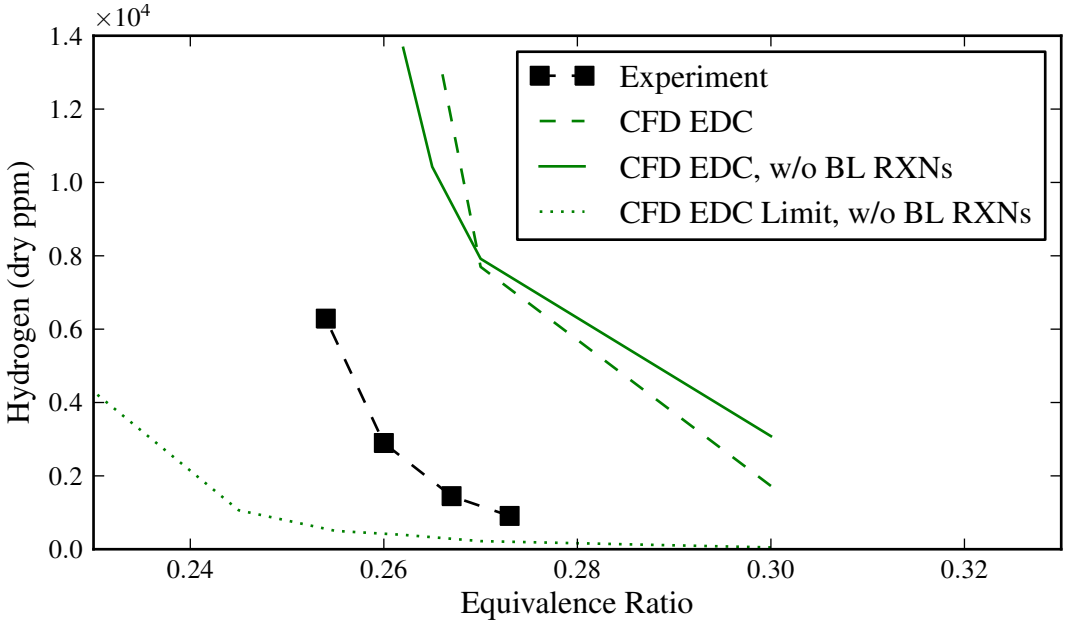

Figure 4.7: Comparison of the measured and CFD predicted hydrogen concentration at the nominal sampling location as blowout is approached.

in the boundary layer (although the trends shown are very similar regardless of the modifications made to the EDC model). These figures illustrate the evolution of the flame structure and temperature profiles of the hydrogen flame as the equivalence ratio is reduced. All reveal the non-homogeneity of the reactor. As blowout is approached, the destruction of the hydrogen encompasses more of the physical volume of the reactor (requiring more time to complete), and the radical pool decreases in quantity and is convected further around the recirculation zone. In our analysis, we approach the problem from the perspective of a combusting fluid particle traveling through the jet, into the recirculation zone and then entraining back into the jet. Figures 4.8 and 4.9 suggest that the blowout condition is dependent on the development of the radical pool. The flame remains stable as long as the radical pool develops significantly enough to achieve ignition before the hypothetical combusting fluid particle is re-entrained. If it fails to ignite before being re-entrained, the combustion in the entire

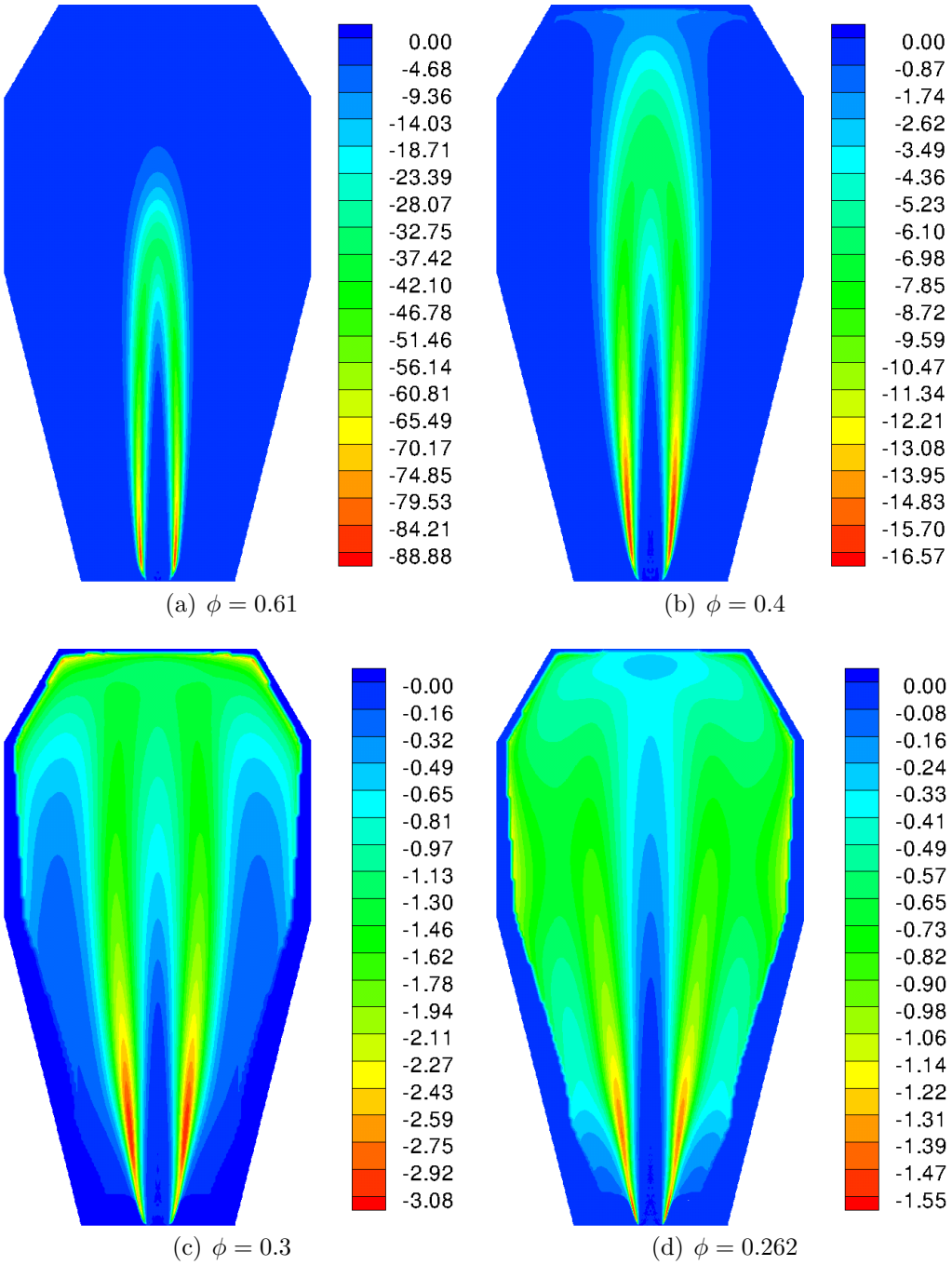

(a) $\phi = 0.61$ (b) $\phi = 0.4$

(c) $\phi = 0.3$ (d) $\phi = 0.262$

Figure 4.8: Reaction rate of H_2 [kg/m^3-s] as the equivalence ratio, ϕ, is decreased and the reactor moves towards blowout.

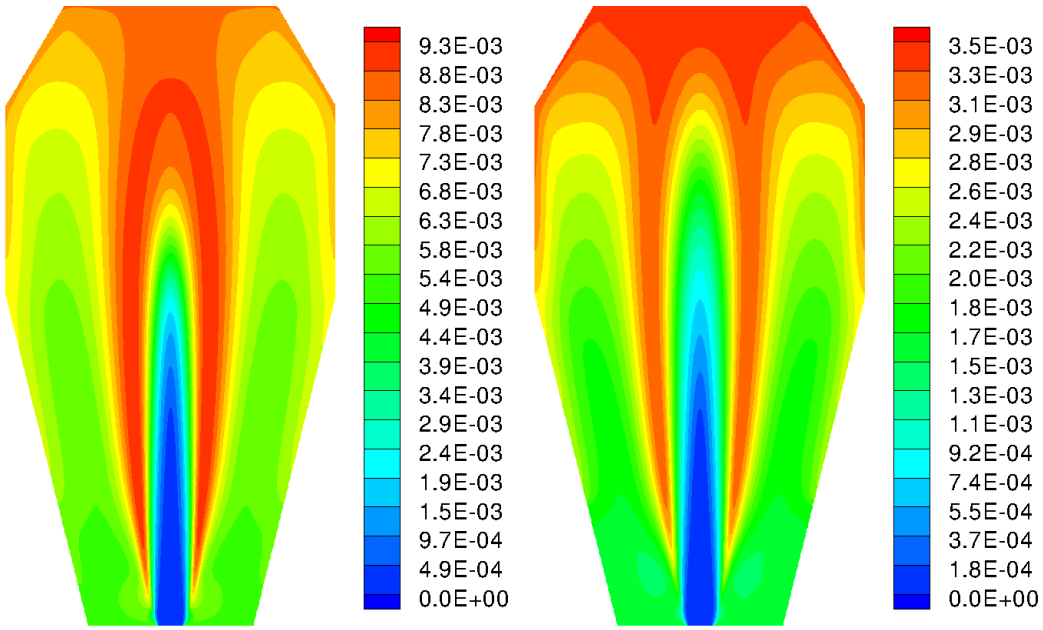

(a) $\phi = 0.61$ (b) $\phi = 0.4$

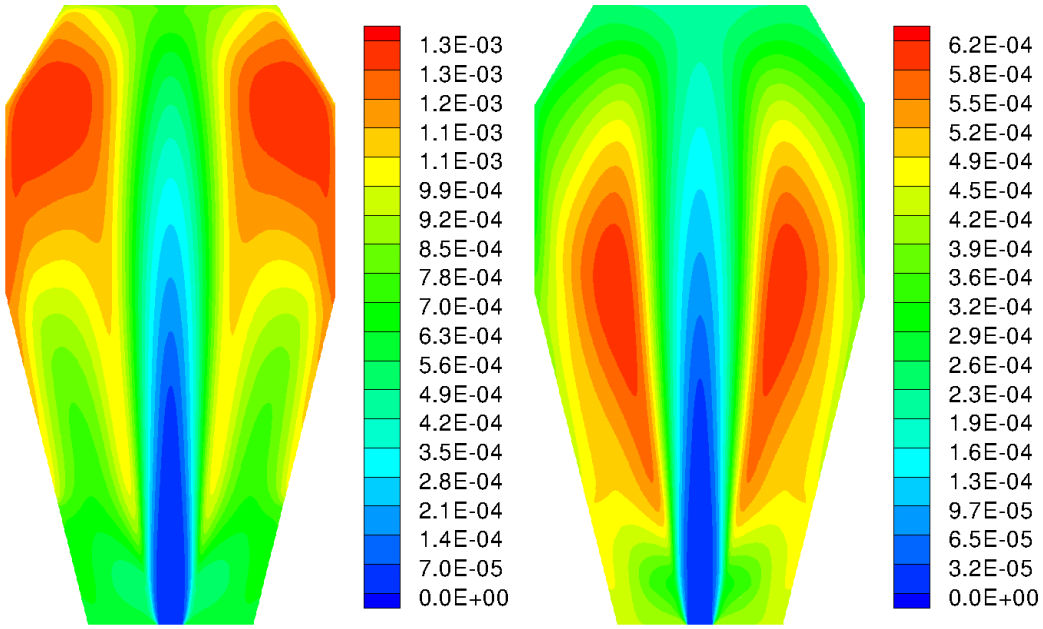

(c) $\phi = 0.3$ (d) $\phi = 0.262$

Figure 4.9: Mole fraction of OH as the equivalence ratio, ϕ, is decreased and the reactor moves towards blowout.

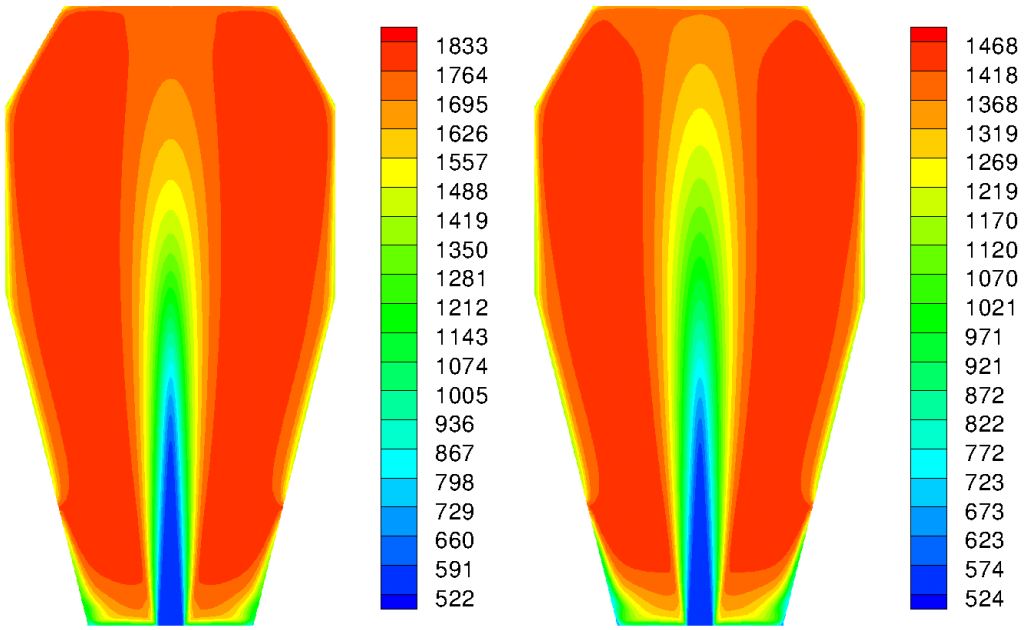

(a) $\phi = 0.61$ (b) $\phi = 0.4$

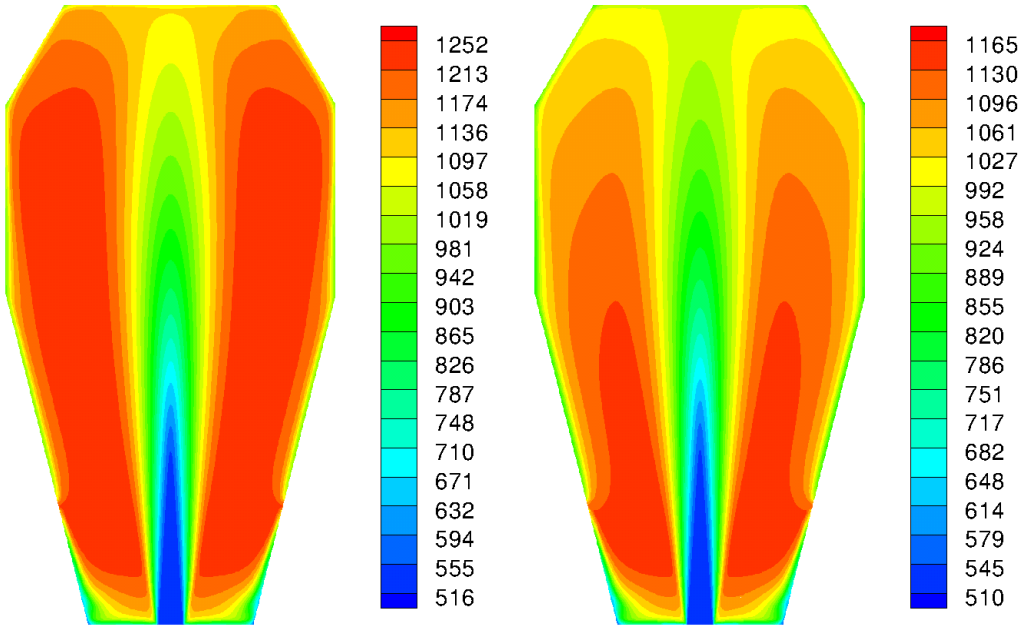

(c) $\phi = 0.3$ (d) $\phi = 0.262$

Figure 4.10: Temperature as the equivalence ratio, ϕ, is decreased and the reactor moves towards blowout.

reactor is extinguished. This is discussed further in Chapter 5.

4.3.1 Turbulent Regime Analysis

The detailed CFD results provide an opportunity for an in-depth turbulent regime analysis of the reactor as it moves towards blowout. The turbulent regime diagram adapted from Peters [81] is used (Figure 4.11), along with standard turbulence scalings. The turbulent quantities of interest include: u_0', the velocity fluctuation at the integral scale defined as $u_0' = \sqrt{2k/3}$, and l_0, the integral length scale, defined as $l_0 = 0.37(u_0'/\varepsilon)$. The chemical quantities of interest include: l_L, the laminar flame thickness, taken as $l_L = \alpha/S_L$ where α is thermal diffusivity, and S_L, the laminar flame speed. Since the turbulent regime analysis is done with local turbulence quantities, we determine local chemical quantities as well. A chemical time can be expressed in two ways: (1) as αS_L^2 and as (2) $\rho\tilde{Y}_{H2}/\tilde{R}_{H_2}$. By setting these two equations equal to each other a local laminar flame speed can be found by Equation 4.8 as a function of the local reaction rate of H_2 and the local H_2 mass fraction. Finally, l_K refers

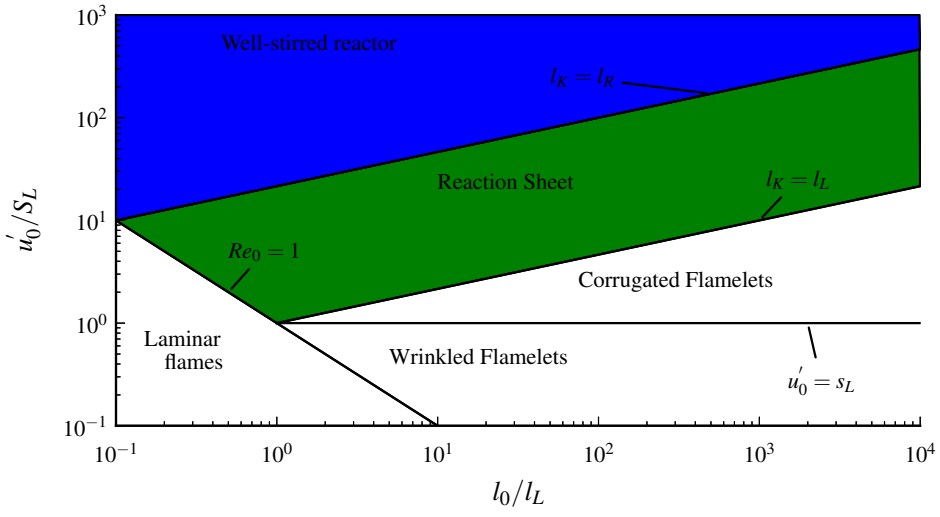

Figure 4.11: Turbulent regime diagram adapted from Peters [94].

to the Kolmogorov length scale, l_R the thickness of the reaction sheet, and Re_0, the turbulent Reynolds number.

$$S_L^2 = \frac{\alpha \tilde{R}_{H_2}}{\rho \tilde{Y}_{H_2}} \tag{4.8}$$

Figure 4.12 shows the reactor volume colored by the local turbulent flame regime, where green indicates the reaction sheet, and blue the well-stirred reactor regime (also indicated on the Peter's diagram). An outline of the flame zone is shown for reference and is defined as the iso-line equal to 10% of the maximum H_2 destruction rate. The percentage of the flame zone volume in the reaction sheet regime is 76%, 66%, 50%, and 40% for the equivalence ratios of 0.4, 0.3, 0.27, and 0.262 respectively. We see that as blowout is approached more of the flame zone volume operates under well-stirred conditions however a large portion of the reactor is still in the reaction sheet regime. This analysis provides some justification for the continued applicability of EDC in the modeling of the JSR even near blowout.

4.4 CFD Modeling Results: Methane

Now for methane, the effect of the eliminating reactions in the boundary layer and raising the volume fraction of the fine scales to their limit, here referred to as the EDC limit, is shown in Figure 4.13. For methane combustion the effect of eliminating reactions in the boundary layer appears to be more pronounced than for hydrogen but it still has only a small effect on the prediction of the blowout condition. Eliminating reactions in the boundary layer allows a burning numerical solution to be obtained at a slightly lower equivalence ratio. Stabilization to the lower equivalence ratio is attributed to the fact that CO, a chain branching species, and radicals are re-entrained into the jet rather than consumed near the wall, resulting in increased global stability. The large destruction rate of CH_4 near the base of the flame as shown in Figure 4.13(b) is a direct result of this re-entrainment. As with hydrogen, raising the volume fraction of the fine scales results in a more compact flame. Because of its poor

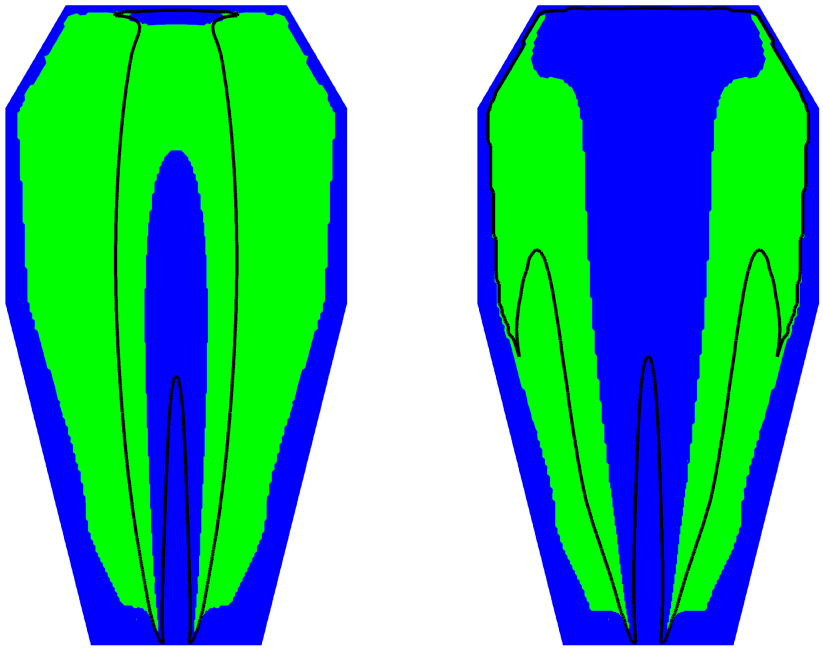

(a) $\phi = 0.4$ (b) $\phi = 0.3$

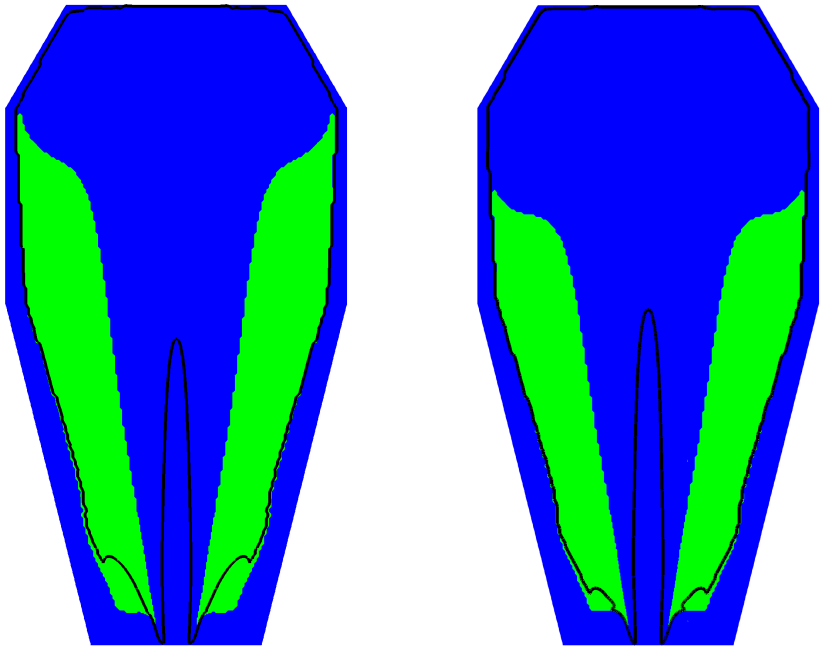

(c) $\phi = 0.27$ (d) $\phi = 0.262$

Figure 4.12: Identifying the local turbulent regime as, ϕ, is decreased and the reactor moves towards blowout. Green indicates reaction sheet and blue the well-stirred reactor regime as shown in 4.11 above. An outline of the flame area is given for each ϕ, and is taken as an iso-line equal to 10% of the maximum destruction rate of H_2.

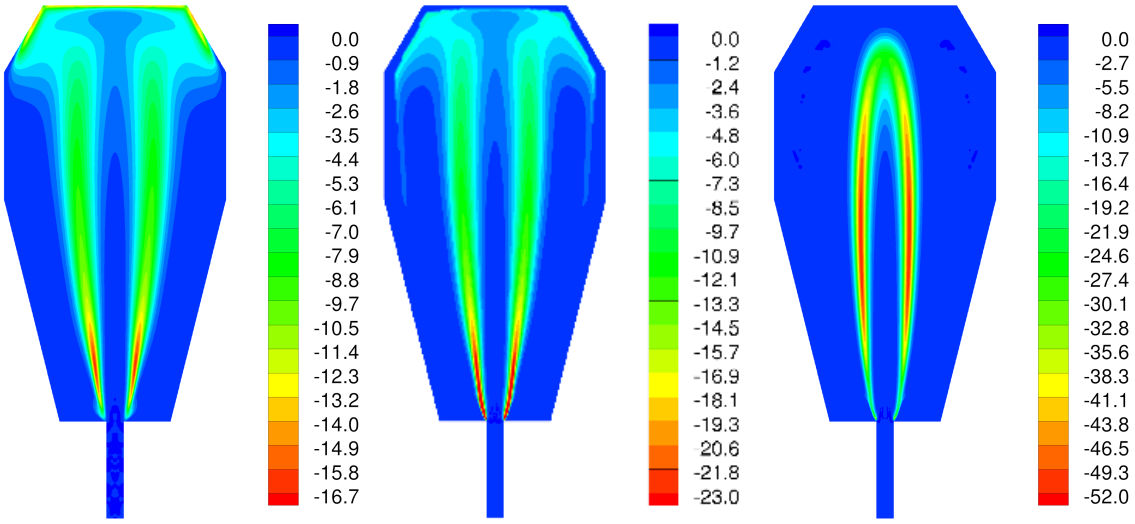

(a) EDC (b) EDC w/o BL RXNS (c) EDC Limit w/o BL RXNS

Figure 4.13: Comparison of the reaction rate of CH_4 at an equivalence ratio of 0.59 for three versions of the EDC model: (a) the original EDC model, (b) the EDC model without reactions in the boundary layer, and (c) the EDC model at the EDC limit with wihtout reactions in the boundary layer. Note that the reaction rate range for (a) and (b) have been set equal for this illustration.

performance in predicting hydrogen blowout, EDC limit is not pursued further for methane combustion. A comparison of CFD predicted blowout, using the remaining two models, to the experimental data is given in Figure 4.14. The two models follow each other closely, although EDC without reactions in the boundary layer is stable to a lower equivalence ratio and matches the measured blowout temperature well.

The following contour plots are taken from the EDC model with reactions eliminated in the boundary layer. The trends for decreasing equivalence ratio shown in the following figures are very similar regardless of the modifications made to the EDC model. Figures 4.15, 4.16, 4.17, and 4.18 illustrate the evolution of the flame structure and temperature profiles of the methane flame as the equivalence ratio is reduced.

While hydrogen combustion can be thought of as a single step process in which H_2 is combined with O_2 to produce H_2O, methane combustion is more of a two step process in which the fuel is first broken down to carbon monoxide and then the carbon

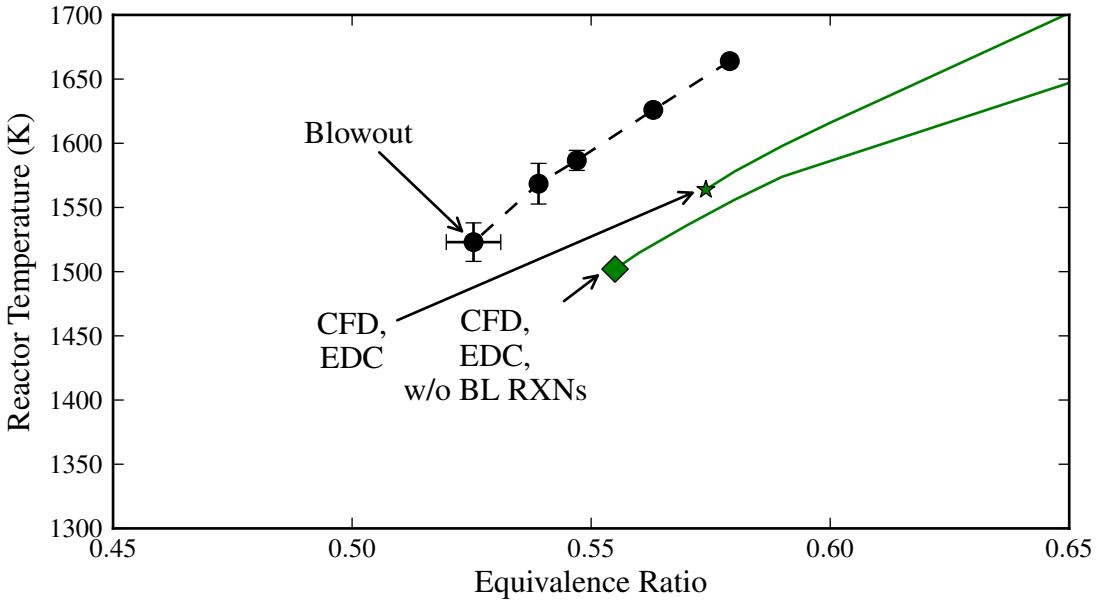

Figure 4.14: CFD blowout for methane combustion as compared to the experimental data.

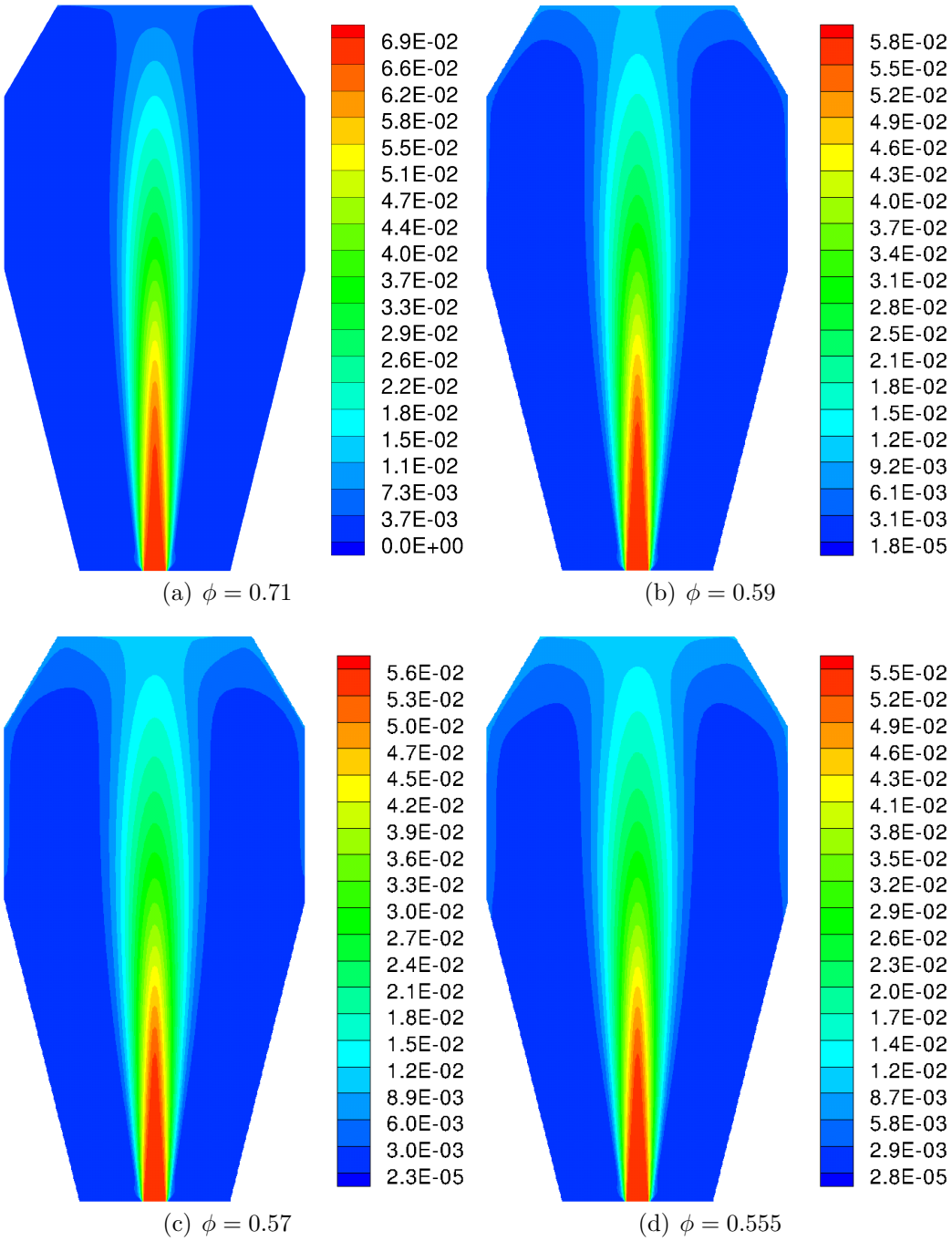

(a) $\phi = 0.71$ (b) $\phi = 0.59$

(c) $\phi = 0.57$ (d) $\phi = 0.555$

Figure 4.15: Mole Fraction of CH_4 as the equivalence ratio, ϕ, is decreased and the reactor moves towards blowout.

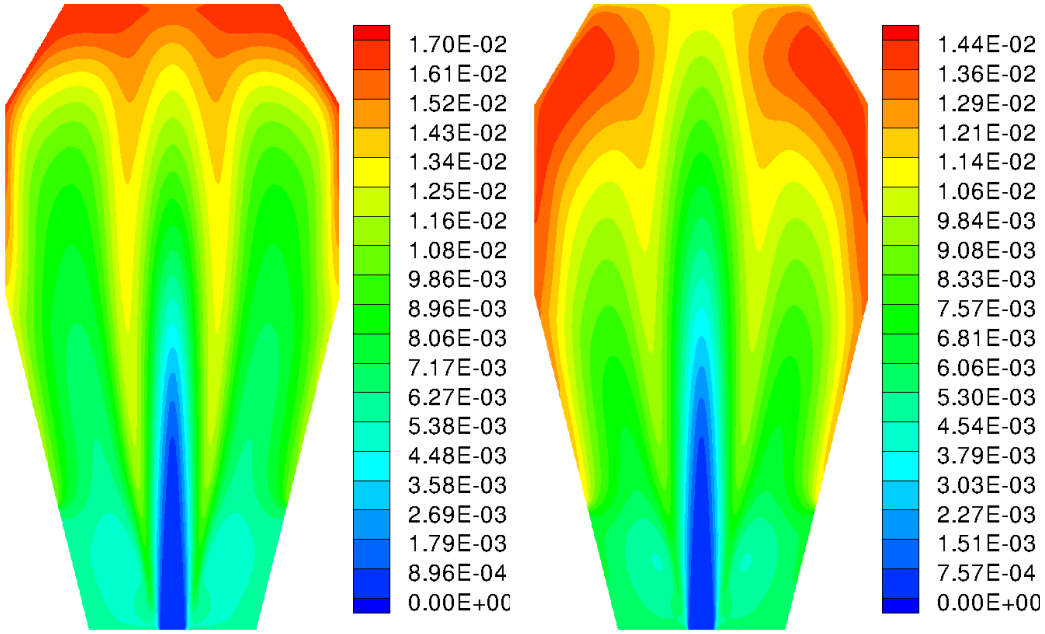

(a) $\phi = 0.71$ (b) $\phi = 0.59$

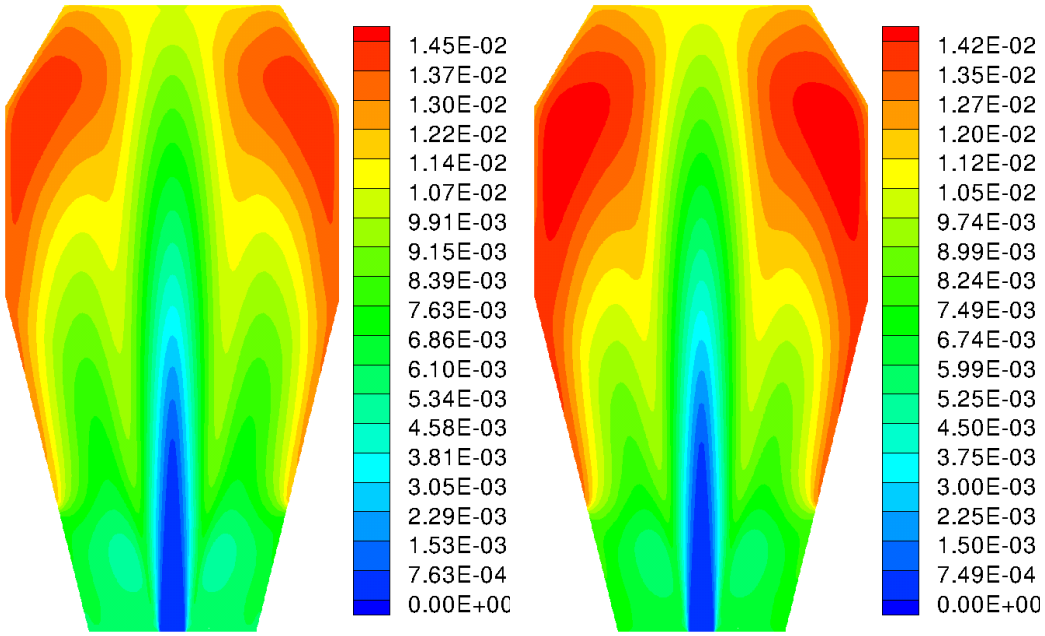

(c) $\phi = 0.57$ (d) $\phi = 0.555$

Figure 4.16: Mole Fraction of CO as the equivalence ratio, ϕ, is decreased and the reactor moves towards blowout.

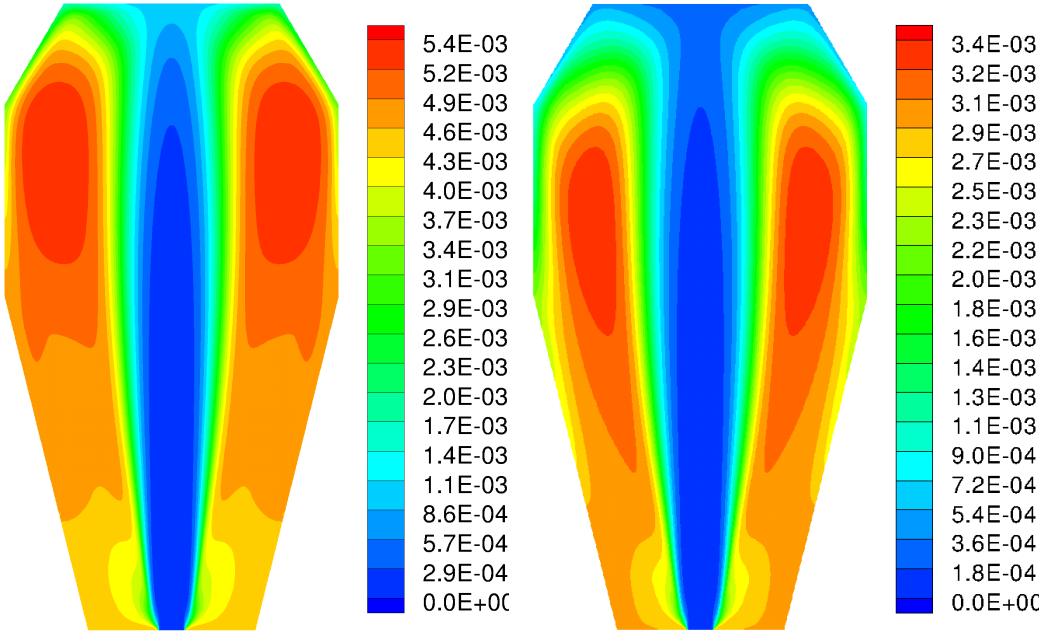

(a) $\phi = 0.71$ (b) $\phi = 0.59$

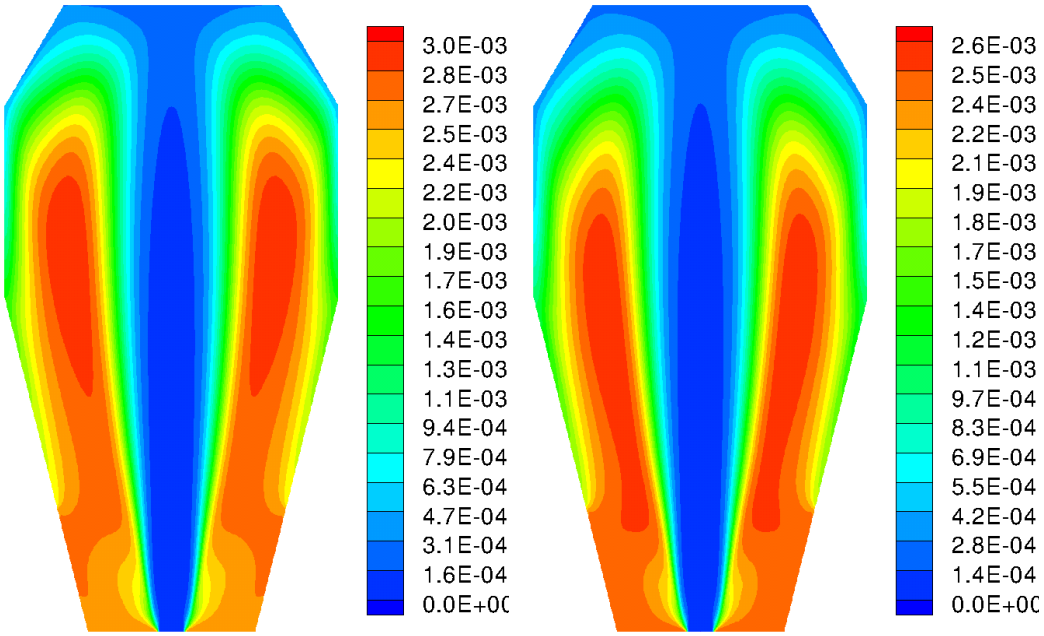

(c) $\phi = 0.57$ (d) $\phi = 0.555$

Figure 4.17: Mole Fraction of OH as the equivalence ratio, ϕ, is decreased and the reactor moves towards blowout.

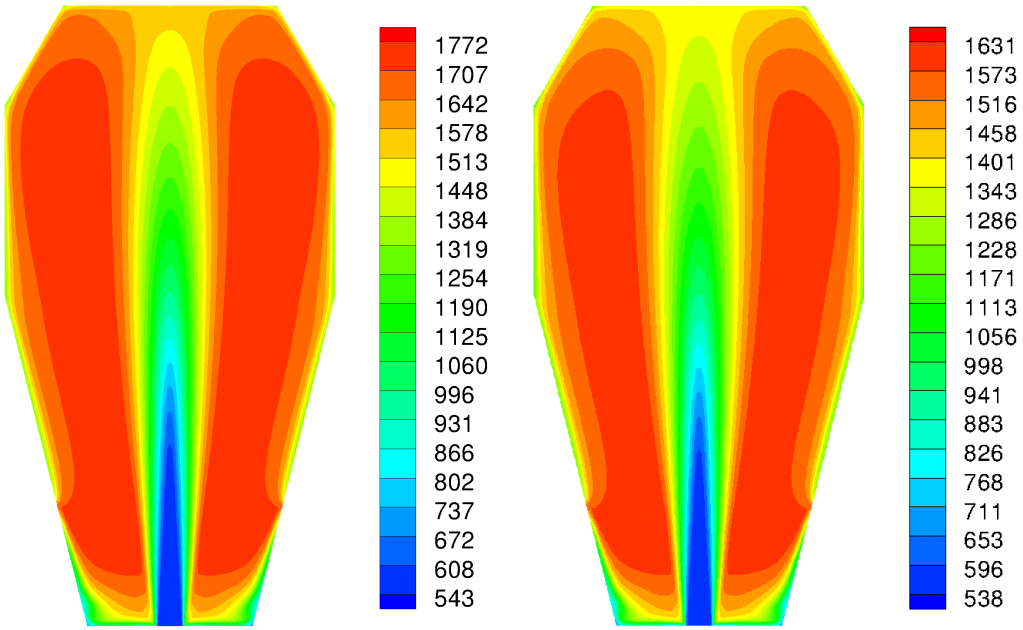

(a) $\phi = 0.71$ (b) $\phi = 0.59$

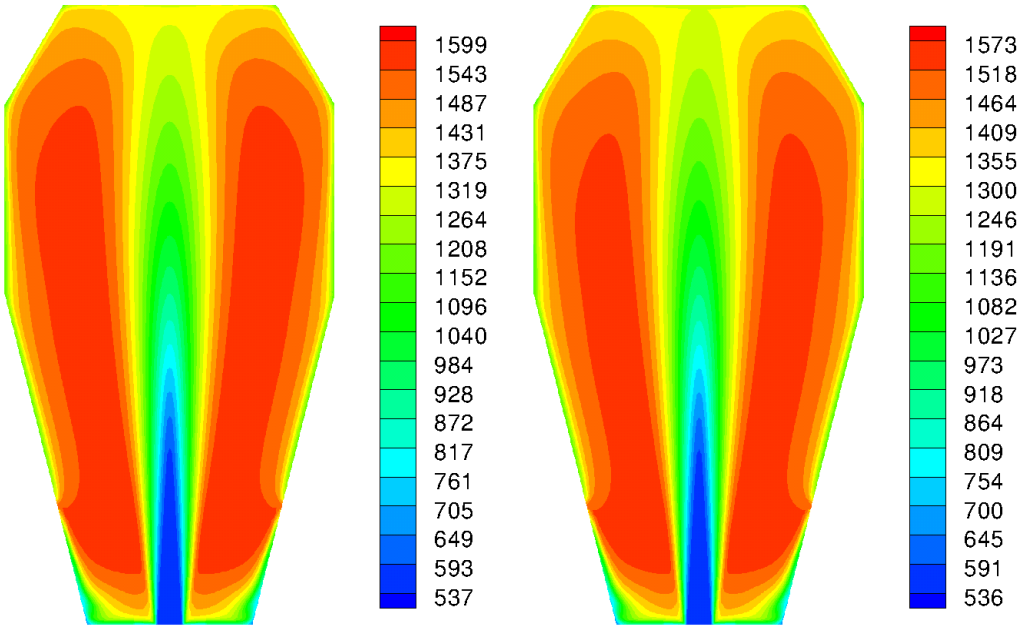

(c) $\phi = 0.57$ (d) $\phi = 0.555$

Figure 4.18: Temperature as the equivalence ratio, ϕ, is decreased and the reactor moves towards blowout.

monoxide is oxidized to carbon dioxide. This is in part why Law [95] identifies the following as the two reactions most important in a combustion process:

$$H + O_2 \rightarrow O + OH \tag{4.9}$$

$$CO + OH \rightarrow CO_2 + H. \tag{4.10}$$

For hydrogen combustion only the first of these reactions, which is chain branching, sustains the combustion. For methane the source of the atomic hydrogen for chain branching is more complicated. Some of the H will come from the oxidation of intermediates in the breakdown of methane such as HCO, CH_3, and H_2. What builds the radical pool in the recirculation zone however is the second chain propagating reaction involving CO. The oxidation of CO is also responsible for the late heat release in methane combustion. Thus the methane CFD must be analyzed differently than the hydrogen CFD.

As blowout is approached, the total amount of methane destruction remains relatively constant. Watching the minimum value of methane given in the legends of Figure 4.15 we see that the minimum amount of methane in the reactor increases only 10 ppm as the equivalence ratio is decreased from 0.59 to 0.555 (a decrease of 0.3% methane input). Figure 4.15 also shows that almost all of the methane is consumed before reaching the recirculation zone for all equivalence ratios approaching blowout. In addition, less CO is oxidized as blowout is approached, and both the pool of CO (Figure 4.16) and the radical pool (Figure 4.17) is pushed further around the recirculation zone. Although it is clear that CO plays a large role in the stabilization of the methane flame, the mechanism of flame stability is not as clear as that for the hydrogen flame. Finally, Figures 4.15 and 4.16 shows that each 'step' of methane combustion appears to occur in a different 'zone', therefore methane is often referred to as experiencing 'two-zone' combustion.

4.5 Joint Analysis

To illustrate the chemical reactions with respect to the fluid dynamics in the JSR we plot the reaction rate of hydrogen, methane, and carbon monoxide on uniform velocity vectors at blowout in Figures 4.19, 4.20(a), 4.20(b). Note that for visualization purposes the methane destruction rate in Figure 4.20(a) is scaled to half the maximum destruction rate. In addition two sets of lines are plotted for reference. The lines beginning at the jet inlet and traveling up and around the reactor to the exhaust ports indicate where radial velocity is zero and thus the boundary where radial transport of species and heat is by diffusion only. We refer to these lines as the core boundary. The second set of lines beginning at the jet inlet and ending at the eye of recirculation

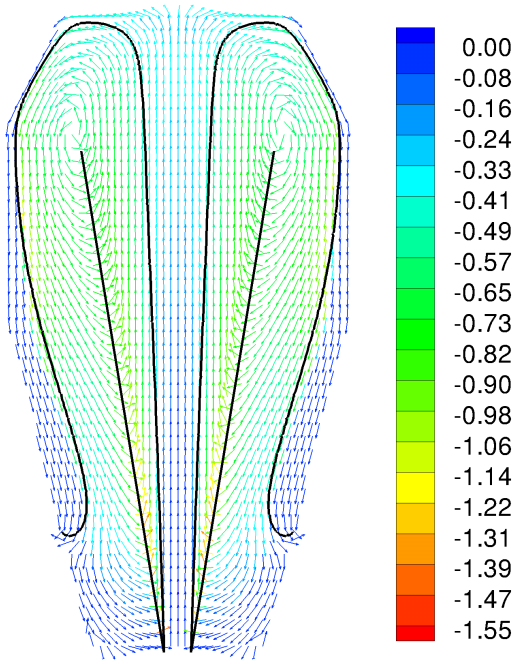

Figure 4.19: For hydrogen combustion at blowout, $\phi = 0.262$, using EDC without boundary layer reactions, reaction rate [kg/m^3-s] for hydrogen is plotted on velocity vectors. The lines traveling from the jet inlet to the exhaust ports indicate lines of zero net mass transport and the lines from the jet inlet to the eye of recirculation indicate an axial velocity equal to zero.

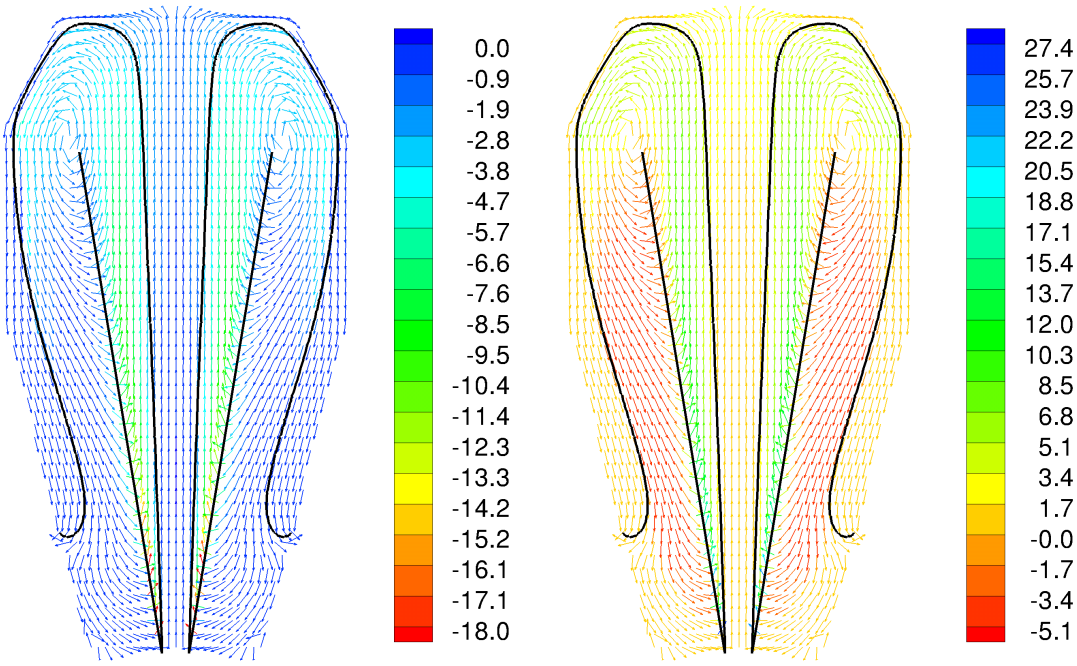

(a) Methane (b) CO

Figure 4.20: For methane combustion at blowout, $\phi = 0.555$, using EDC without boundary layer reactions, reaction rates [kg/m^3-s] for two species are plotted on velocity vectors: (a) Methane (scaled to half of the maximum destruction rate) (b) CO. The lines traveling from the jet inlet to the exhaust ports indicate lines of zero net mass transport and the lines from the jet inlet to the eye of recirculation indicate an axial velocity equal to zero.

indicate where axial velocity is zero and thus the boundary where the recirculating flow joins the jet. We refer to these lines as "shear lines." The shear lines correspond to a jet angle of 10^0 which is consistent with the standard expansion angle for a submerged jet of 9.7^0. It is clear from Figure 4.19 that the maximum rates of fuel destruction tend to lie between the shear lines and the inside core boundary lines (region of positive axial velocity). For methane combustion, Figure 4.20 shows that again the maximum rates of fuel destruction lie between our reference lines nearest the reactor centerline, however most of the CO destruction occurs around the eye of recirculation as we travel back down the reactor (region of negative axial velocity).

4.6 Conclusions from the CFD Modeling

In order to gain insight on the mechanism controlling blowout, two dimensional, axisymmetric computational fluid dynamic (CFD) simulations are carried out for the lean premixed combustion of both hydrogen and methane as the fuel. The models are validated at the 1800 K condition with temperature profiles from Fackler **??** and a complementary methane concentration profile collected in this work.

The Eddy Dissipation Concept (EDC) model is chosen to account for turbulent-chemistry interaction. The EDC model is identified as overpredicting reaction rates in the boundary layer and having limitations in the low Damkohler number regime, for example situations of slow chemistry (CO oxidation) or fast mixing (the jet region of of the JSR). Two modifications are explored as a result: (1) reaction rates are artificially eliminated in the boundary layer, and (2) the reactive volume of each cell is increased to its limit in the EDC model. Eliminating reactions in the boundary layer has little effect on the prediction of the temperature profiles at the 1800 K condition for either hydrogen or methane when compared with original EDC. The temperature profiles show poor agreement on centerline for both hydrogen and methane. This is likely due to the low Damkohler number limitation of the EDC model. Both EDC and EDC without reactions in the boundary layer produce similar methane profiles, although

the modified EDC does better predict methane on centerline. Finally we show that EDC without reactions in the boundary layer has little effect in predicting the blowout condition for hydrogen and provides a slight improvement in predicting the blowout condition for methane. Finally, while the temperature profiles produced with EDC at its limit agree the best for both hydrogen and methane, the methane profile is in poorest agreement with the experimental data when compared with the other two versions of EDC. The CFD blowout study for hydrogen conducted with EDC at its limit shows the poorest agreement with the experimental data for hydrogen. As a result it is not explored further for methane. With this analysis it is determined that EDC without reactions in the boundary layer provides the best option for exploring the blowout behavior of hydrogen and methane as fuels in the JSR.

Contour plots from the CFD modeling illustrates the evolution of the flow-field, temperature profiles, and flame structure within the JSR as blowout is approached for both fuels. All reveal the non-homogeneity of the reactor as blowout is approached. For hydrogen, the destruction of the fuel encompasses more of the physical volume of the reactor and the radical pool decreases in quantity and is convected further around the recirculation zone. For methane, the destruction of the fuel spreads but not as significantly as for hydrogen. This is because methane has a key intermediate chain propagating reaction involving CO. Volume is required for the oxidation of CO and the chain branching production of the radical pool. As with hydrogen, both of these events move further around the recirculation zone. Analysis of the models from the perspective of a combusting fluid particle traveling through the jet, into the recirculation zone and then entraining back into the jet suggests that the blowout condition is dependent on the development of the radical pool. The flame remains stable as long as the radical pool develops significantly enough to achieve ignition before the hypothetical combusting fluid particle is re-entrained. If it fails to ignite before being re-entrained, the combustion in the entire reactor is extinguished. Plotting boundary lines of core region, across which no convective transport takes

place shows the possible importance of diffusive transport of fuel and radicals as well as the convective entrainment of the hypothetical fluid particle. The implications of this are explored further in the development of reduced-order chemical reactor network models in Chapter 5.

Chapter 5

CHEMICAL REACTOR NETWORK MODEL

The goal of this section is to use the flow field and reaction fields from CFD to generate a Chemical Reactor Network (CRN) model that captures the bulk of the physical processes responsible for combustion stabilization. A single PFR model and a two PFR model are developed. Each is applied to pure H_2 and CH_4 and then to CH_4/H_2 blends. The effect of varying the chemical mechanism is explored here and the effect of varying the heat loss is given in Appendix E.

5.1 Single PFR Model

5.1.1 Model Development

The hydrogen CFD model is used to develop a chemical reactor network consisting of a single plug flow reactor (PFR) with recirculation as shown in Figure 5.1. The PFR volume is equal to the JSR volume of 15.8 cc. The flow fraction of recirculation is determined from the CFD by integrating the downward mass flow at several axial locations along the height of the reactor. With the mass flow in and out of the reactor known, the mass flow recirculating can be determined using mass conservation. This calculation indicates that approximately 75% of the recirculating flow is re-entrained into the jet while 25% is exhausted. This is in keeping with the results obtained from the 3D simulation of this JSR in [87]. A heat transfer analysis is completed (see Appendix B) and a nominal heat loss of 20% of the energy input to the reactor is chosen. In the CRN a constant heat flux is set along the length of the PFR such that the total heat loss is 20% of the energy input for any given inlet condition. Fuel enters at 300 K and air at 573 K.

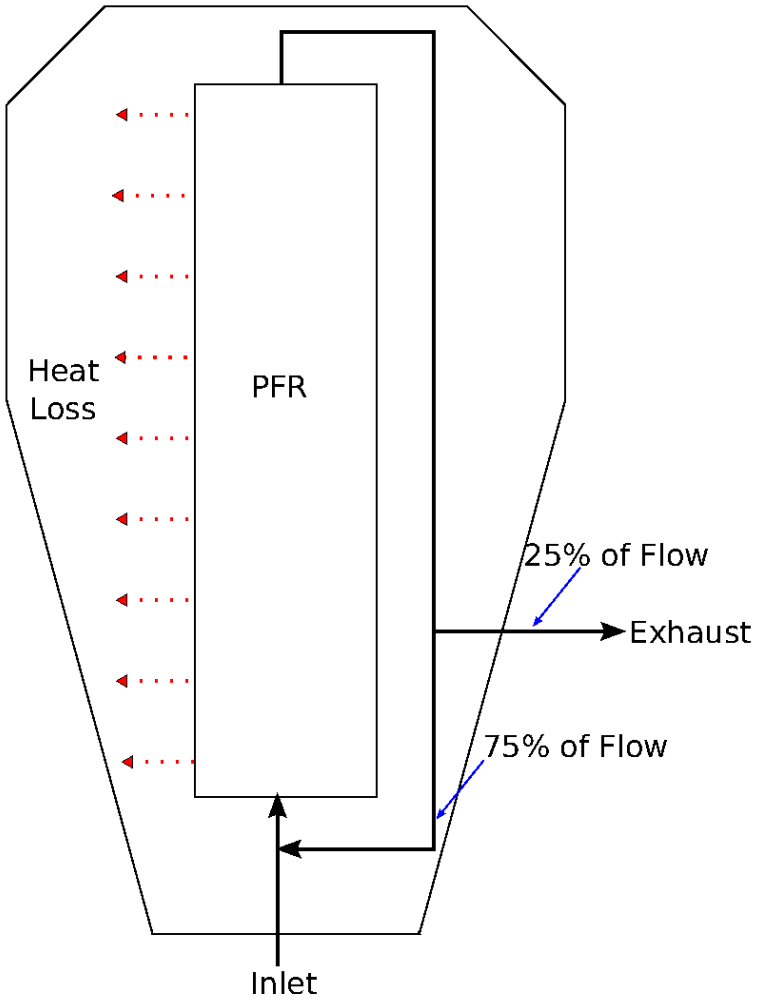

Figure 5.1: Chemical Reactor Network constructed from the calculated flow field within the CFD Model.

CHEMKIN-PRO is chosen as the solver for the single PFR model, which is used to predict the blowout equivalence ratio and temperature. Because a PFR has no inherent flame stabilization mechanism, the recirculation stream must be initialized with a burning solution. This is taken to be a solution from an adiabatic perfectly stirred reactor at a stable equivalence ratio. To illustrate the dependence of the solution on the chemical mechanism, results using three mechanisms are compared: Li [32, 43], GRI 3.0 [33], and UCSD [34].

5.1.2 Modeling Results: Hydrogen

Figure 5.2 presents the blowout predictions of the single PFR model as compared to the experimental results. Both the inlet equivalence ratio and temperature at the nominal sampling location, which is taken as the maximum temperature of the PFR, are reported. The single PFR model with the Li and UCSD mechanisms performs well

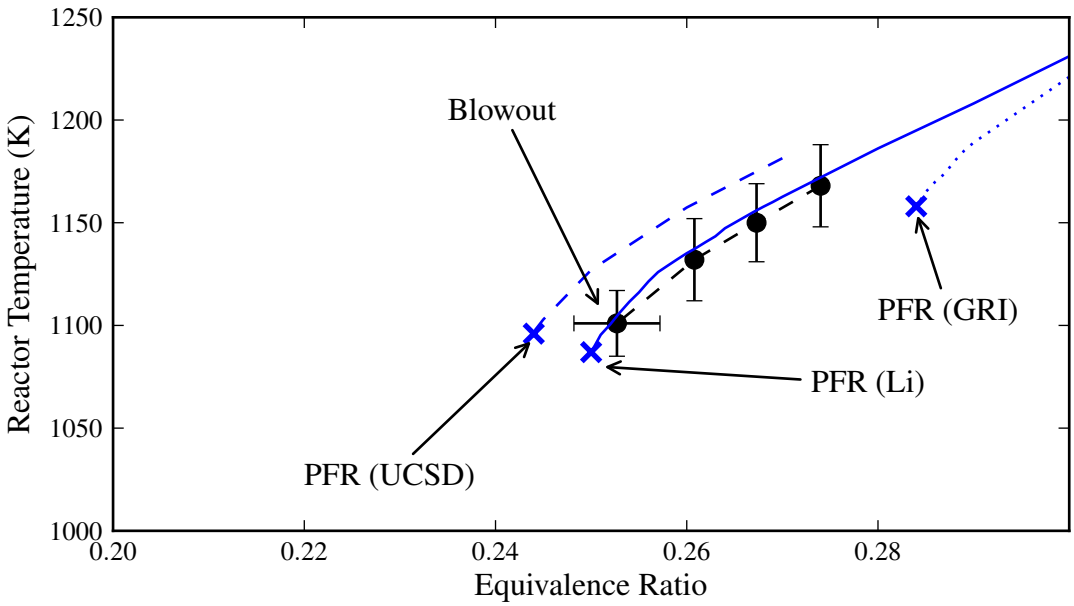

Figure 5.2: Single PFR modeling results for hydrogen. Experimental results are given for comparison.

in predicting the blowout condition, being within 3% of the experimental equivalence ratio. The GRI mechanism provides poor agreement, with a blowout equivalence ratio within 11% of the experimental value and a 61 K temperature difference. We begin by comparing Li and GRI mechanisms in what follows.

Figures 5.3, 5.4, and 5.5 show respectively the temperature profile, fuel consumption, and the development of the radical pool, represented by the concentration of OH. Although blowout for Li and GRI occurs at different equivalence ratios, the behavior of the single PFR near blowout is similar. The plot of the OH radical concentration using either mechanism resembles that of an ignition event in which chain branching leads to a sudden production of radicals and subsequently fuel consumption. The movement of the radical pool towards the exit of the PFR tells the same story as the movement of the radical pool into the recirculation zone in the CFD model. As the fuel flow rate is reduced, the induction time increases until ignition can no longer be achieved before the gas is re-entrained into the jet. In addition, the plot of H_2 concentration in the single PFR model reinforces the plot of H_2 destruction in the CFD model, both of which illustrate the delay and spreading of the chemistry as blowout is approached preventing complete combustion before re-entrainment.

It should be noted that although there appear to be two peaks (or valleys) in radical concentration, including a minor one near the inlet and a major one further downstream, there is only one ignition event. The first valley in OH concentration occurring at approximately 10 μs is due to equilibration of the radical pool entrained from the exit of the PFR after mixing with the cold reactants. The destruction of OH and O is countered by production of H through radical-radical reactions such that the radical pool re-establishes partial-equilibrium. The downstream major peak is associated with ignition.

Comparing the behavior of the single PFR with both the Li and GRI mechanisms elucidates the importance of the development of the radical pool in predicting H_2 combustion blowout. Li points out that the H_2/O_2 system is very sensitive to both

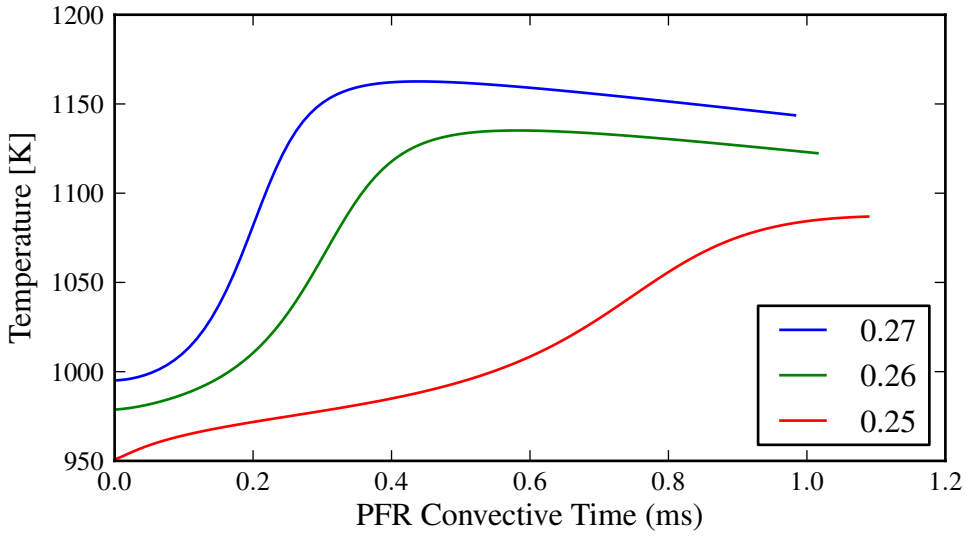

(a) Li

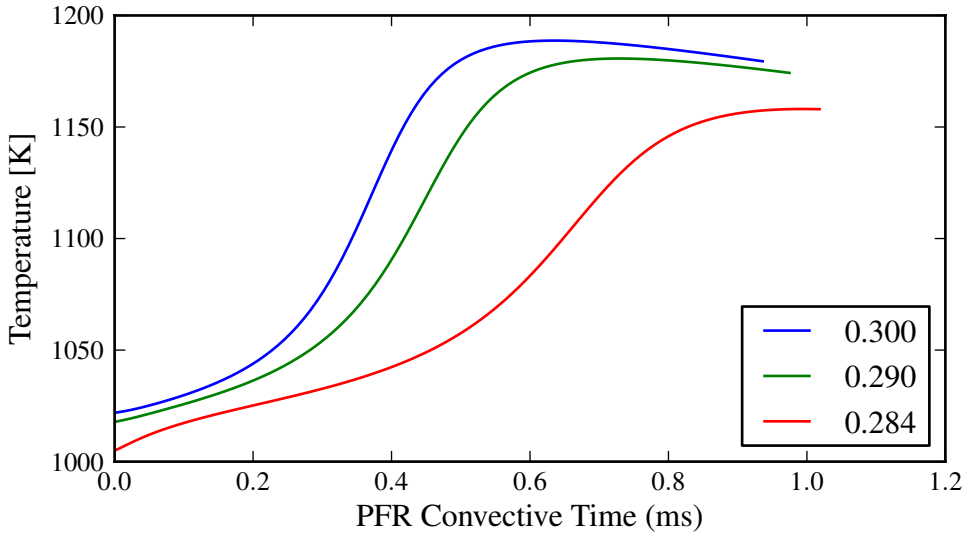

(b) GRI

Figure 5.3: Temperature, plotted from the inlet to the outlet of the PFR as a function of time time along the PFR for both the Li and GRI mechanisms. Results are given from three different equivalence ratios as blowout is approached.

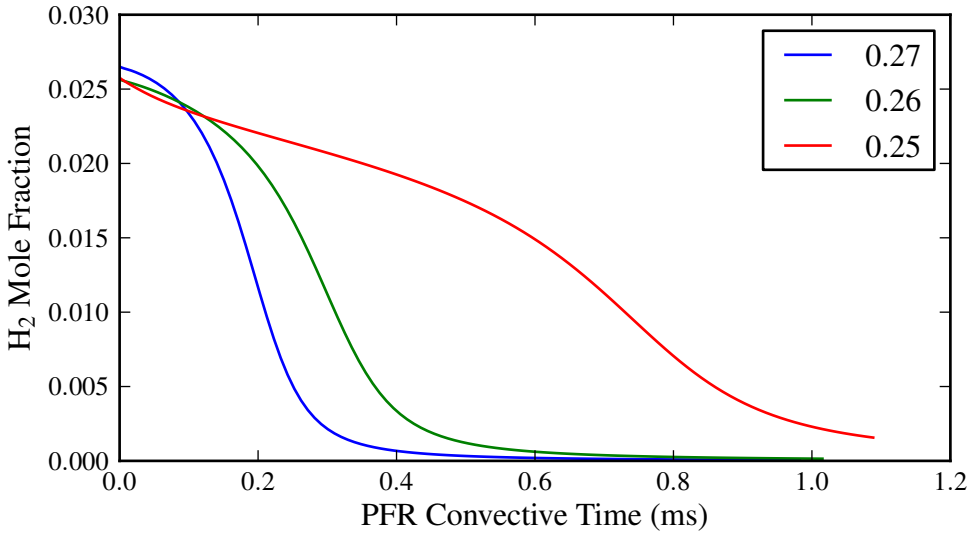

(a) Li

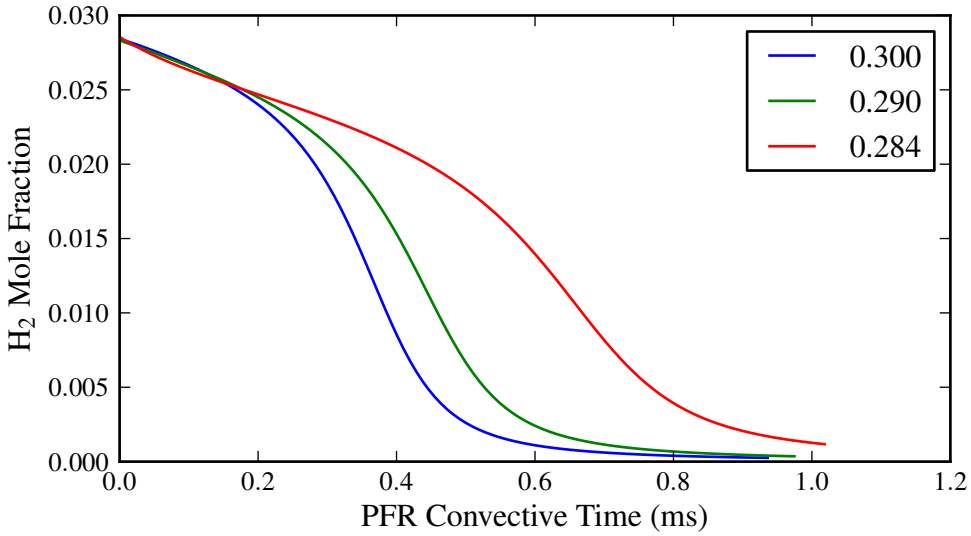

(b) GRI

Figure 5.4: Mole fraction of the fuel, H_2, plotted from the inlet to the outlet of the PFR as a function of time time along the PFR with both the Li and GRI mechanisms. Results are given from three different equivalence ratios as blowout is approached.

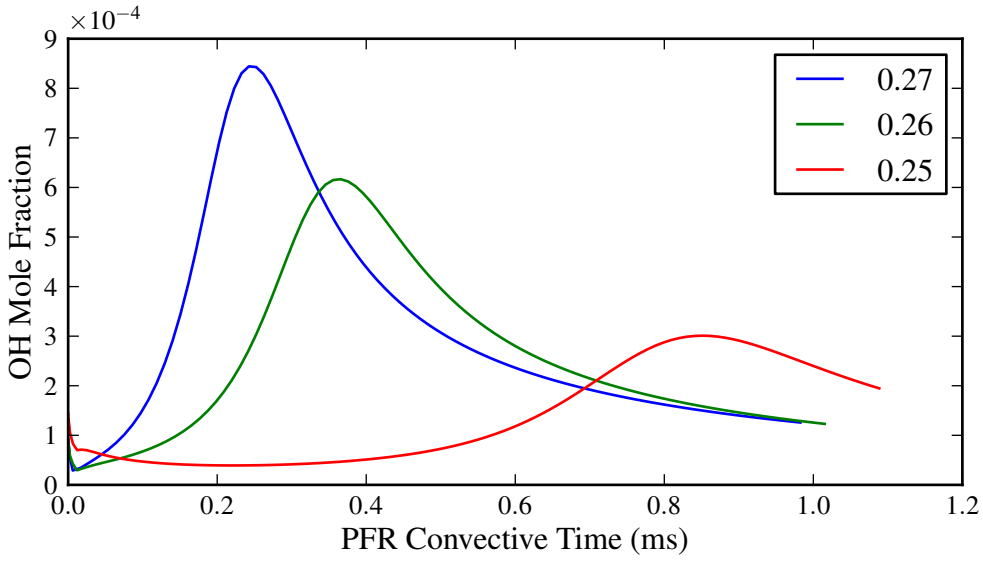

(a) Li

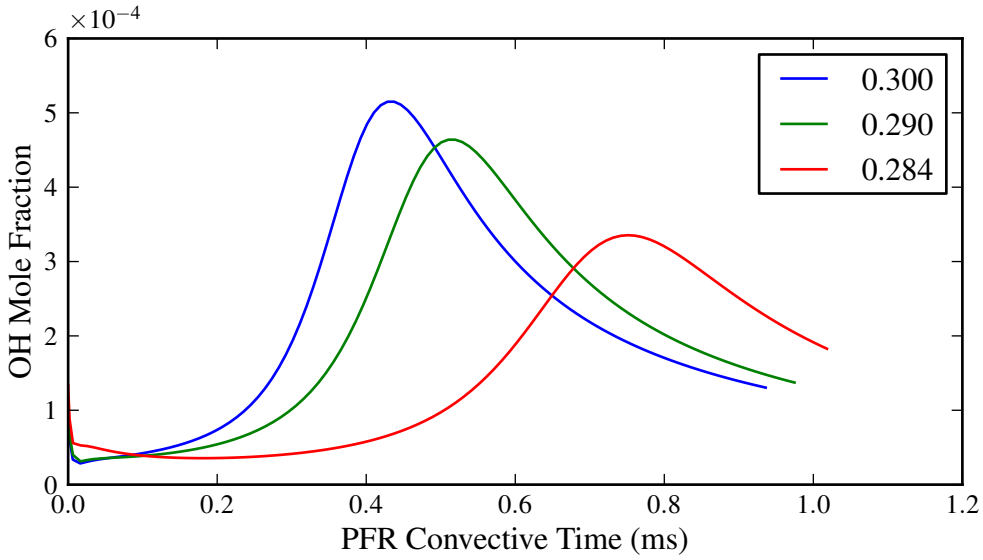

(b) GRI

Figure 5.5: Mole fraction of OH radical, plotted from the inlet to the outlet of the PFR as a function of time along the PFR with both the Li and GRI mechanisms. Results are given from three difference equivalence ratios as blowout is approached.

the key chain-branching reaction involving H (Reaction 5.1) and the key competing reaction (Reaction 5.2) [43]. This is where the two mechanisms differ most. Li's mechanism has a slightly faster rate for Reaction 5.1 and a significantly slower rate for Reaction 5.2. This means that for the same equivalence ratio the Li mechanism will produce a larger radical pool and produce it more quickly, thus enhancing stability. This is consistent with the work of Ò Connaire [46] which shows that GRI overpredicts the ignition delay time for pure hydrogen, and the work of Weydahl [47] which suggests that Li is one of five candidate mechanisms better adapted to hydrogen than GRI.

$$H + O_2 \longrightarrow OH + O \tag{5.1}$$

$$H + O_2 + M \longrightarrow HO_2 + M \tag{5.2}$$

The effect of these two reactions is demonstrated by running the single PFR model with a modified version of GRI. We take the GRI mechanism and substitute Li's rates for the two reactions above. The results are presented in Table 5.1 and show the significant effect these two reactions have on the prediction of the blowout condition.

While these two rates have a first order effect on the prediction as illustrated, they alone do not close the gap between GRI and Li. The Li mechanism has 16 reactions in total whose rate constants differ in varying degrees from GRI. Three of

Table 5.1: Detailing the effect of the two reactions given by Reactions 5.1 and 5.2 on the prediction of the blowout equivalence ratio and temperature by substituting Li's rates for GRI's rates.

Reaction Rate Replaced	ϕ	Temp (K)
Baseline GRI	0.284	1158
Reaction 5.2	0.261	1113
Reaction 5.1 & 5.2	0.258	1107

four chain branching reactions, three of four dissociation/recombination reactions, all of the HO_2 reactions and five of the eight H_2O_2 reactions differ between the two mechanisms (note that the number of reactions is in reference to the Li mechanism). Most of these differences are relatively small, but their sum can have enough of an effect on the development of the radical pool to close the difference between GRI and Li.

Finally we can explain why UCSD and Li behave similarly for H_2 by comparing Reactions 5.1 and 5.2 as well. While the UCSD rates for both of these reactions vary slightly from Li, their ratio, often referred to as the branching ratio, follows that of Li exactly.

5.1.3 Modeling Results: Methane

Figure 5.6 presents the blowout predictions of the single PFR model as compared to the experimental results. The single PFR model with the GRI mechanism predicts the blowout equivalence ratio within 4% of the experimental value, however it underpredicts the blowout temperature by almost 100 K. The UCSD mechanism predicts the temperature more closely but overpredicts the blowout equivalence ratio by 19%. Finally because the skeletal GRI mechanism was used in the CFD model it is compared here as well. It follows full GRI-3.0 fairly closely but does predict blowout at a slightly lower equivalence ratio. It is thought that the significant difference in predicted blowout equivalence ratios between UCSD and GRI-3.0 might be explained by GRI's tendency to predict shorter auto-ignition times than those measured experimentally at atmospheric conditions [96]. This implies that GRI-3.0 allows methane to ignite earlier in the PFR than UCSD at the same inlet equivalence ratio and will therefore show that the single PFR model stabilizes to a lower equivalence ratio for methane. Regardless of the mechanism chosen, however, the single PFR model does not follow the experimental data as blowout is approached.

Figures 5.7, 5.8, 5.9, 5.10 show temperature and concentrations of CH_4, CO, and

OH as blowout is approached in the single PFR model using both the GRI and UCSD mechanisms. The CRN shows that even near blowout the fuel (methane) disappears entirely before the end of the PFR. This is in contrast to the results from hydrogen blowout. In the remaining residence time in the PFR, CO first peaks and then the OH peaks later. As blowout is approached CO increases in concentration and OH decreases in concentration while both move further along the PFR, or around the recirculation zone. This behavior is also seen in the CFD models of methane blowout above (Figures 4.16 and 4.17).

5.1.4 H_2/CH_4 Blends

Note that we wish to be able to use a single mechanism to describe the blowout behavior of the H_2/CH_4 blends. The Li mechanism showed the best agreement with pure hydrogen, however Li does not have hydrocarbon chemistry and cannot be used

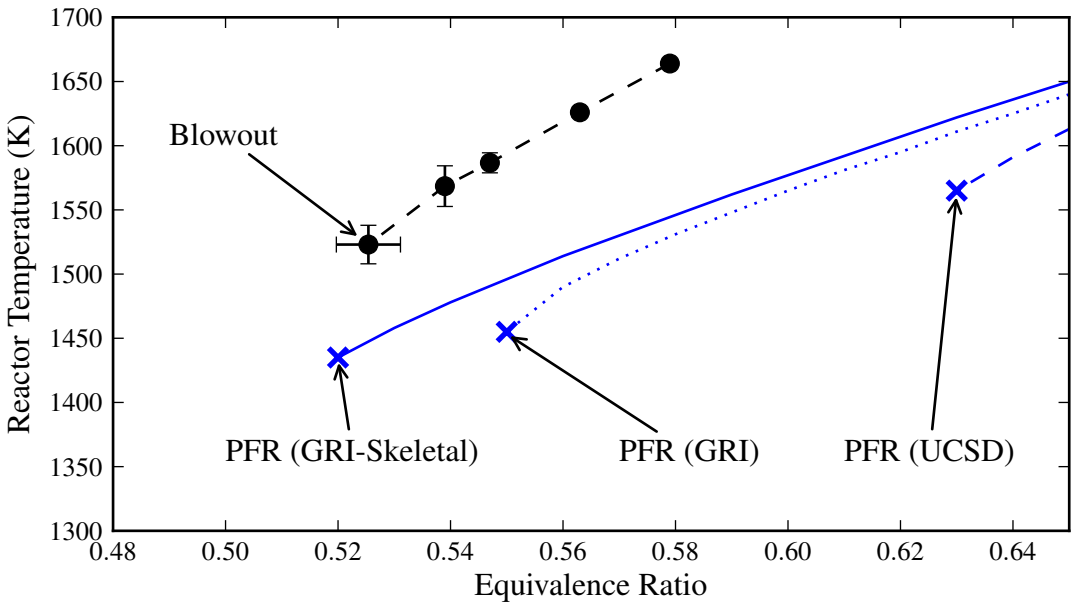

Figure 5.6: Single PFR modeling results for methane. Experimental results are given for comparison.

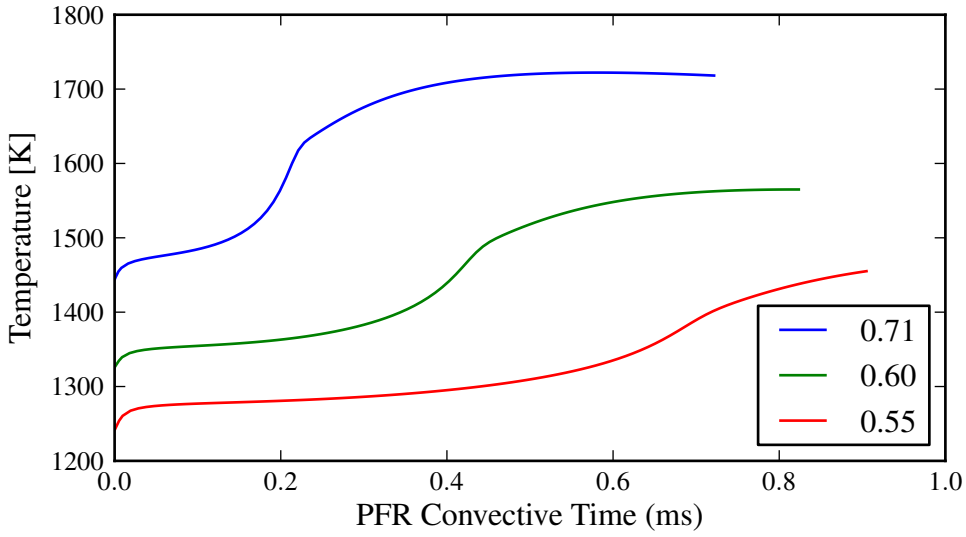

(a) GRI

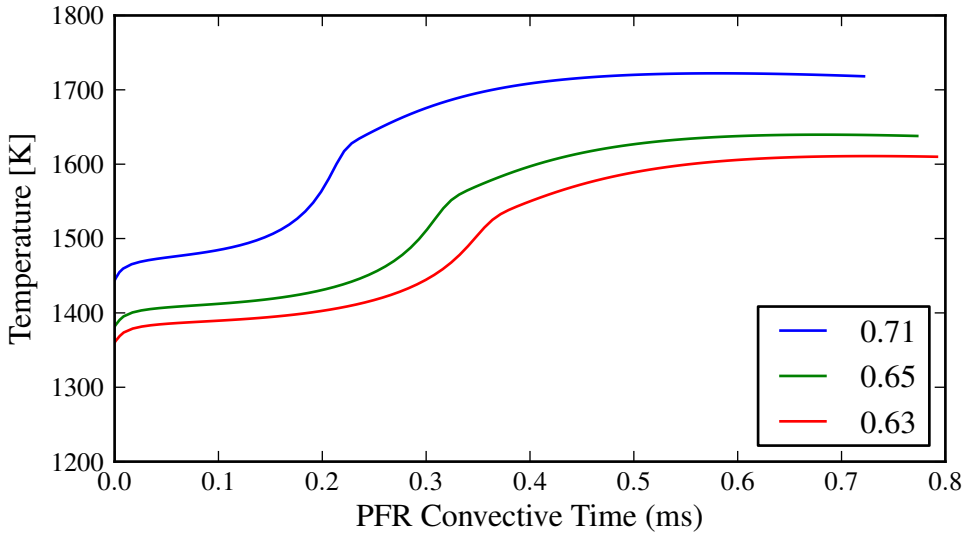

(b) UCSD

Figure 5.7: Plots of temperature for the single PFR model with methane as the fuel using GRI and UCSD as the mechanisms. Results are given for three different equivalence ratios as blowout is approached.

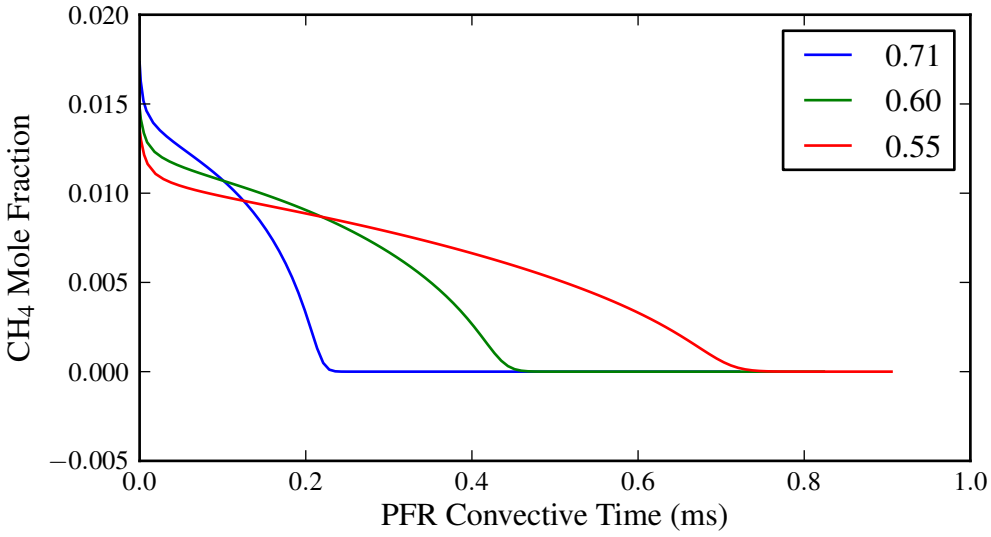

(a) GRI

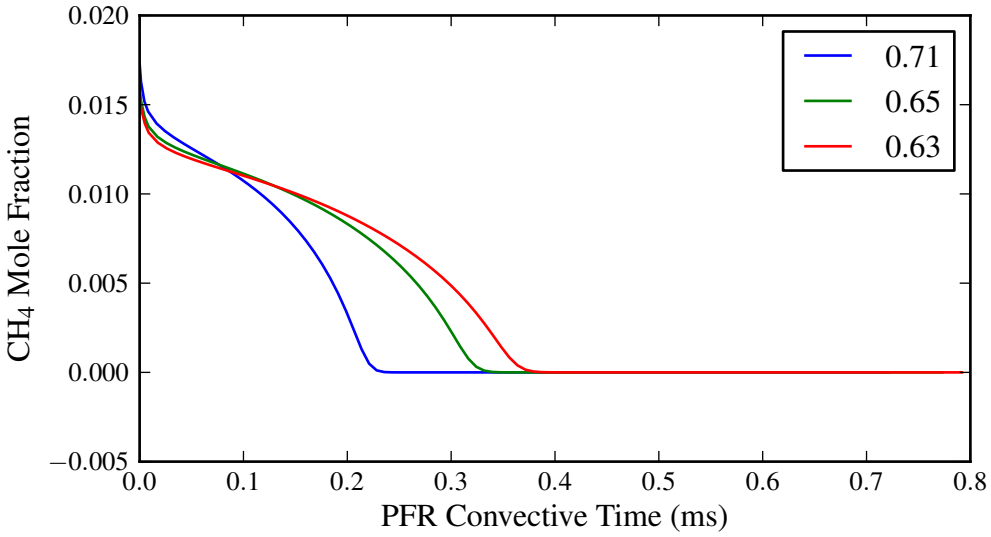

(b) UCSD

Figure 5.8: Plots of CH_4 mole fraction for the single PFR model with methane as the fuel and GRI and UCSD as the mechanisms. Results are given for three different equivalence ratios as blowout is approached.

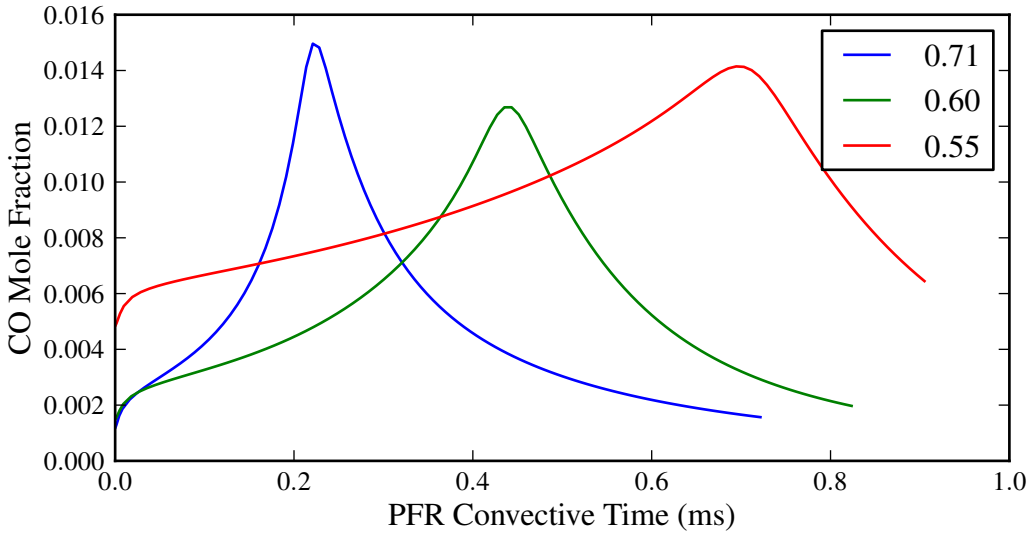

(a) GRI

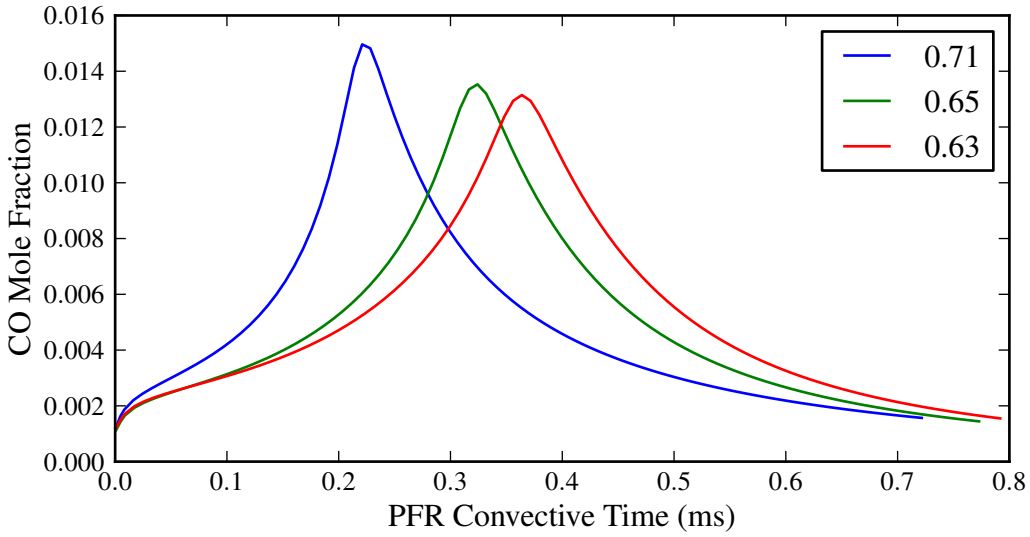

(b) UCSD

Figure 5.9: Plots of CO mole fraction for the single PFR model with methane as the fuel and GRI and UCSD as the mechanisms. Results are given for three different equivalence ratios as blowout is approached.

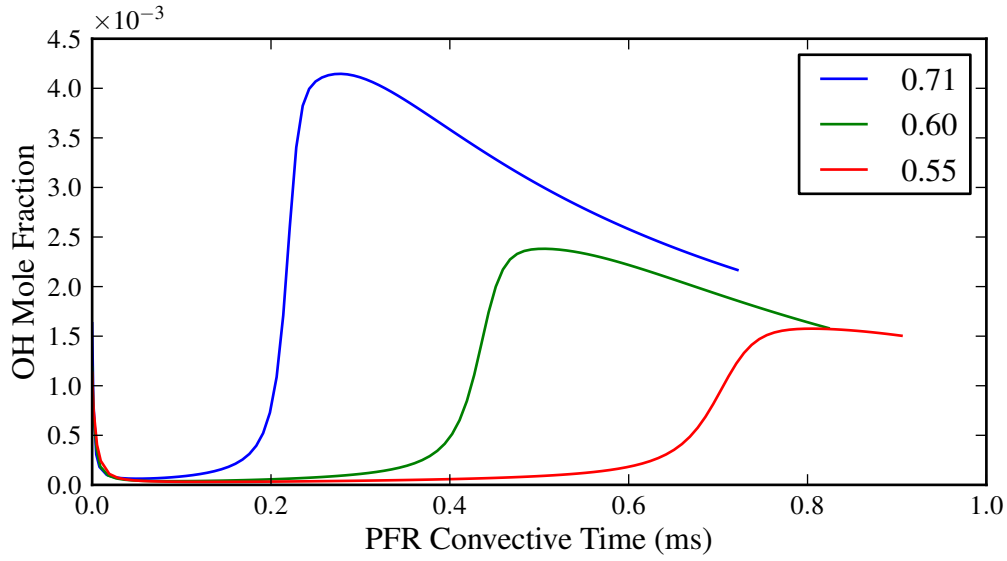

(a) GRI

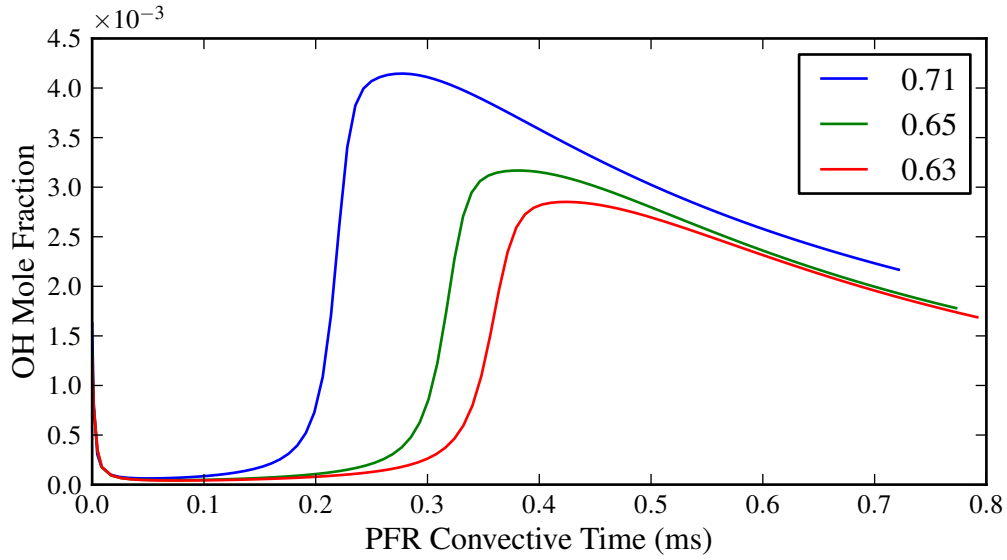

(b) UCSD

Figure 5.10: Plots of OH mole fraction for the single PFR model with methane as the fuel and GRI and UCSD as the mechanisms. Results are given for three different equivalence ratios as blowout is approached.

for H_2/CH_4 blends. GRI showed good agreement for pure methane in equivalence ratio at blowout but not temperature, and GRI is known in the literature and shown in this work to poorly predict hydrogen [46, 47]. Therefore UCSD is chosen as the mechanism for studying CH_4/H_2 blends. A plot of the single PFR model predictions of blowout temperature and equivalence ratio are shown in Figure 5.11. The single PFR model predicts blowout temperature well. The small deviations are assumed to be due to the step size of 0.01 in equivalence ratio used in determining blowout. The two PFR model provides good agreement on blowout equivalence ratio for pure hydrogen, however it begins to diverge from the experimental results around blends of 70% hydrogen, and for pure methane significantly overpredicts the blowout equivalence ratio.

Despite the ability of the single PFR model to match some of the species trends shown by the CFD as blowout is approached for methane, it does not follow the JSR data and misses the measured blowout condition. It does not appear that this is due to the choice of chemical mechanism or as Appendix **??** shows, any small error in the specification of the heat loss. This implies that the single PFR model is missing a key physical process that is important to the stabilization of methane combustion in the JSR but has little affect on the stabilization of hydrogen combustion. This is explored in the development of the two PFR model.

5.2 Two PFR Model

5.2.1 Model Development

The single PFR model allows transport by convection only. The two PFR model developed here attempts to account for turbulent diffusive transport as well. The concept is inspired by both the CFD modeling of the JSR as it approaches blowout for both hydrogen and methane, as well as previous CRN work on turbulent jet flames by Broadwell [28] and Monaghan [30]. Both Broadwell and Monaghan's work was

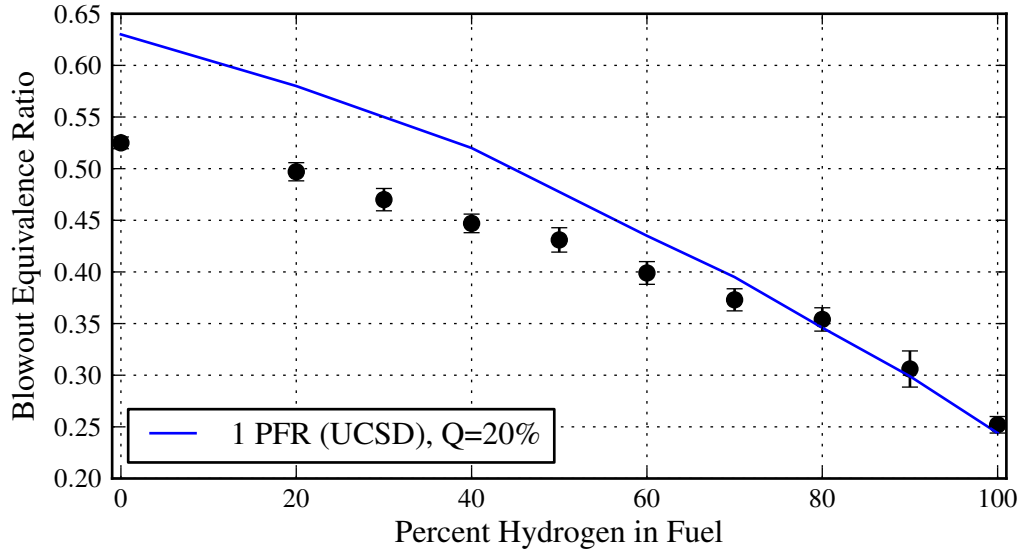

(a) Equivalence Ratio

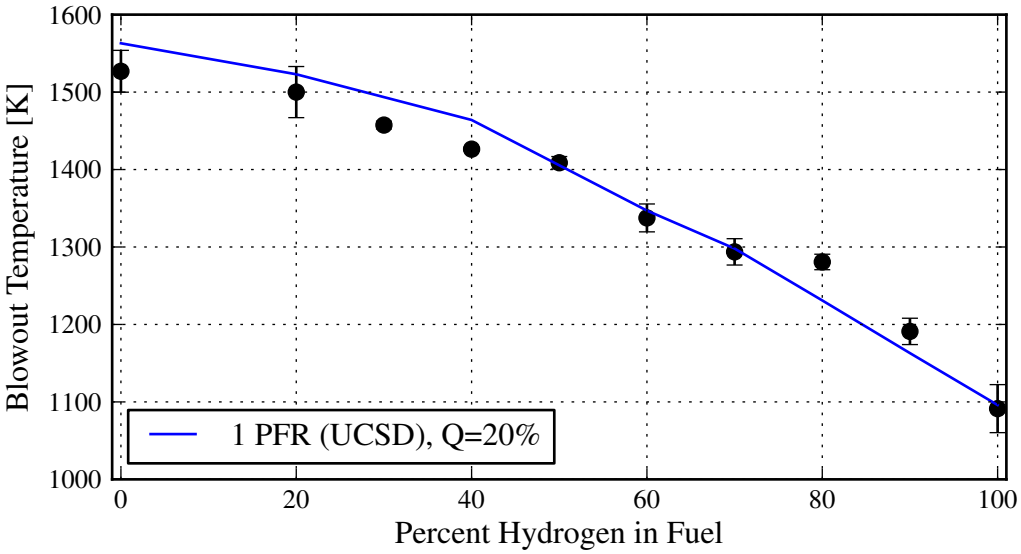

(b) Temperature

Figure 5.11: Single PFR model predictions of blowout compared against experimentally determined blowout (a) temperature and (b) equivalence ratio for CH_4 mixed with increasing amounts of H_2.

focused on the prediction of NOx and CO emissions. Broadwell studied methane, CO-H_2 and pure hydrogen diffusion flames while Monaghan focused exclusively on methane diffusion flames.

Broadwell's coherent flame model consists of two PSR's, one for the core of the jet and one for the flame sheet. The flame sheet receivs fuel from the core PSR via diffusion and entrained air from the surroundings to ensure a stoichiometric condition in the flame sheet. The flame sheet then returned combustion products to the core via diffusion. Monaghan's model of the Sandia flame discretizes the CFD domain into a network of PSRs which exchanged mass both by convection and diffusion. The temperature of each PSR is specified by the CFD model.

We attempt to combine these CRN modeling concepts and apply them to the premixed, recirculating jet flame in the JSR. The JSR is divided into two regions as shown in Figure 5.12(a): a core region defined by the expanding jet for which mass flow remains constant (the boundary is indicated by the dashed-dot line), and a recirculation region. Sample pathlines from the CFD are shown for each region in blue. The flow in the core begins at the JSR nozzle, traveling up and around the reactor until reaching the drain hole. Flow in the recirculation region begins at the base of the jet and travels up through an expanding shear region before turning around the eye of the recirculation and traveling down the reactor to be entrained at the base of the jet. The division between the flow directions in the recirculation region is established by a line of zero axial velocity, indicating the entrainment boundary of the jet. The total flow through the core region remains at the inlet mass flow rate of fuel and air, and the total flow through the recirculation zone is three times the inlet mass flow. This gives 75% of the total flow in the reactor through the recirculation region and 25% through the core retaining the known entrainment rate. Heat loss is applied uniformly along the edges of the reactor. The core and recirculation zone exchange mass by diffusion along the core boundary. Since diffusion should result in no net transport of mass, equal and opposite mass flows are used in the exchange

between these two zones.

Figure 5.12(b) illustrates the two PFR model concept. Because of the side-stream addition necessary in order to account for diffusion we choose to approximate the PFR's by a series of PSRs (much like both Broadwell and Monaghan). The grid of 92 PSRs used in the following work is shown in Figure 5.13. A grid study is performed to verify that the solution is independent of the size of the grid. The volume of each PSR is found using the Divergence Theorem to determine the volume of revolution of each grid cell. Summing the volumes of the PSRs returns the total physical volume of the reactor, with 28% of the reactor volume in the core region and 72% in the recirculation region. The Divergence Theorem is given by Equation 5.3 where F is a vector field, V is a volume and S is a surface. A volume of revolution can be determined by using the vector field $\mathbf{F} = 1/3(x, y, z)$. Each edge of the grid cell (which is a PSR) is identified, a normal vector for each edge segment determined, and the right hand side of Equation 5.3 evaluated. Note that for our volume of revolution $dS = \pi dl$ where l is the path length of the edge of the cell being rotated about the axis of symmetry. The total volume of revolution is determined by performing this calculation for each edge of the grid cell (i.e. PSR) and summing the results. A class is written in Python to assist in storing and operating on the pertinent data for each cell.

$$\iiint_V (\nabla \cdot \mathbf{F}) dV = \iint_S (\mathbf{F} \cdot \mathbf{n}) dS \tag{5.3}$$

The equivalent diffusive mass flow exchange between the core and recirculation regions must be determined and validated for the JSR. Broadwell determines the diffusive flow between the core and the flame sheet to be that which is necessary to produce a stoichiometric mixture in the flame sheet reactor after it has convectively entrained air from the surroundings. This methodology does not apply to a premixed flame. Monaghan proposes that the diffusive mass flow is $\dot{m_{diff}} = \rho A D_T / L$. The question then becomes what the appropriate length scale is. Monaghan argues it is

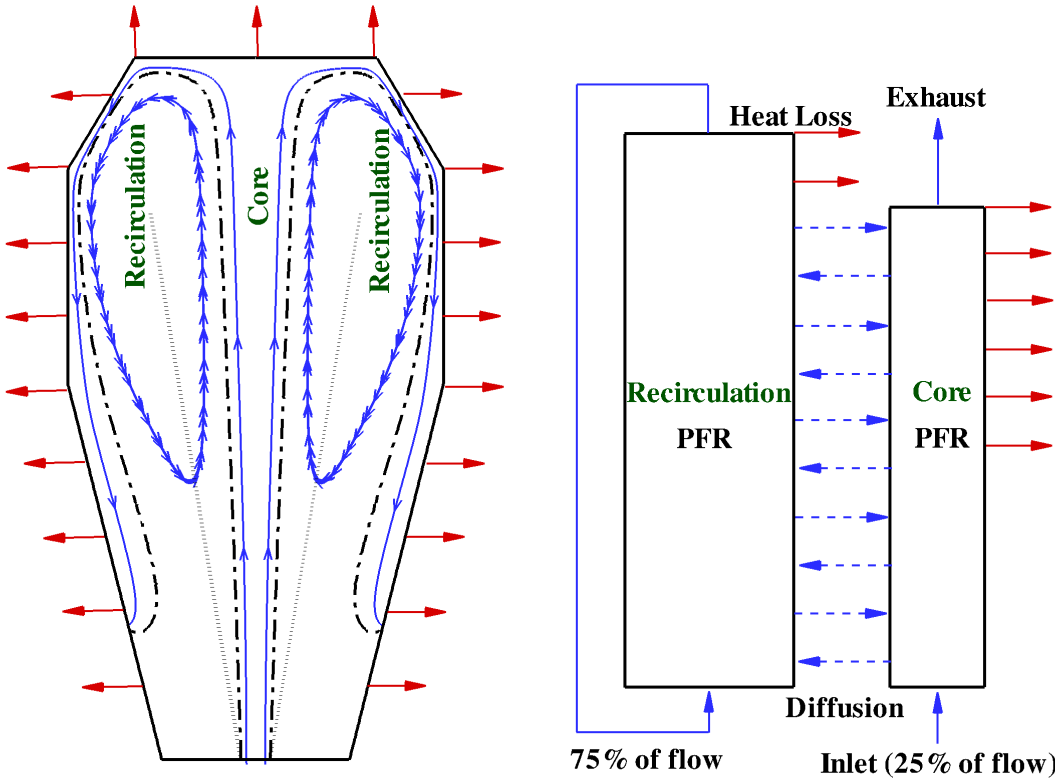

(a) Zones for Two PFR Model

(b) Two PFR Model Diagram

Figure 5.12: The geometry, advective and diffusive flows are described here: (a) shows the division of the core and recirculation zones with the dash-dot line indicating the boundary, blue lines indicating the advective flow and red lines indicating the surfaces of heat loss, and (b) shows the CRN diagram with two PFRs exchanging mass via diffusion.

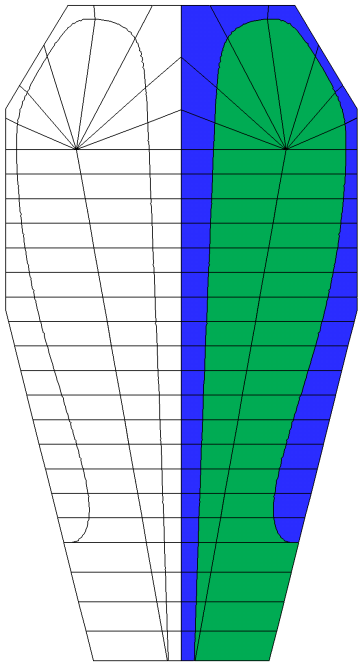

Figure 5.13: Grid of PSRs which make up each PFR in the Two PFR Model. The core PFR is shown in blue and the recirculation PFR in green. The reflection of the cells across the line of symmetry (centerline) is shown for reference.

the length scale of the CFD cells along the boundary of the PSRs. We argue that logical consistency requires it to be the distance between the centerlines of the PSRs on either side of the boundary of diffusive exchange.

Figure 5.14 shows the key components in determining the equivalent diffusive mass flow rates for the JSR. Two PSRs are shown in the figure, one in the core and one in the recirculation zone. The PSR interface (s) is the boundary over which the diffusion is taking place. Equation 5.4 shows a standard boundary condition equation along (s) where u_s is the"mass transfer coefficient", or equivalent diffusive velocity, and Y is the mass fraction of a particular species of interest in each PSR. Equation 5.5 gives a first order representation of the derivative of Y with respect to r. Since Y_1 and Y_2 are averaged concentrations of Y in each PSR than the appropriate length scale for approximating the derivative should be the distance between the centerlines of the PSRs. Substituting Equation 5.5 in 5.4 gives Equation 5.6 which shows that the diffusive velocity is equal to the coefficient of turbulent diffusion divided by the length scale L which has now been defined as the distance between the centerlines of the PSRs. The total diffusive mass exchange for each PSR along the interface (s) is determined by Equation 5.7 where ρ, D_T and L are functions of the path length along the core boundary.

$$\rho A_s D_T \frac{dY}{dr}\Big)_s = \rho A_s u_s (Y_1 - Y_2) \tag{5.4}$$

$$\frac{dY}{dr}\Big)_s = \frac{Y_1 - Y_2}{L} \tag{5.5}$$

$$u_s = \frac{D_T}{L} \tag{5.6}$$

$$\dot{m}_{diff,cell} = \int_s \rho (D_T/L) dA_s \tag{5.7}$$

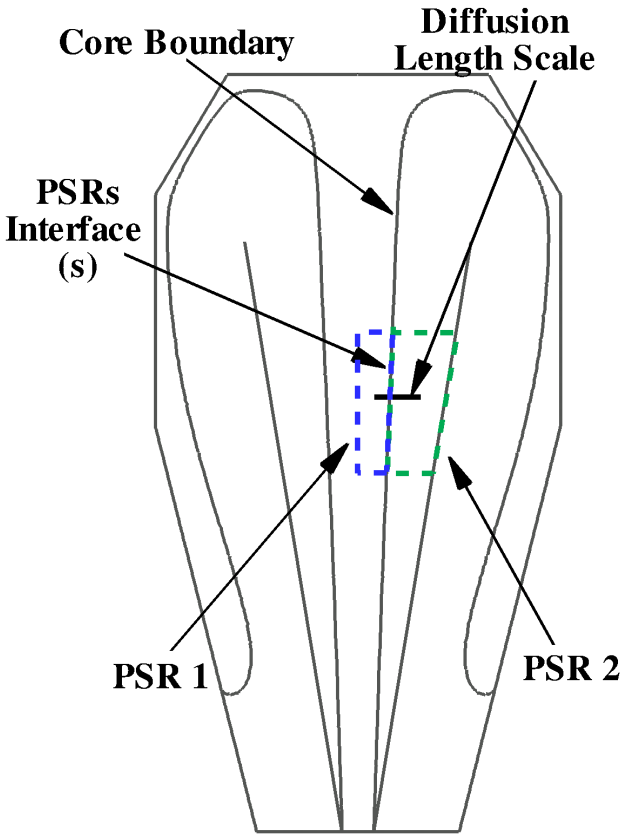

Figure 5.14: Diagram of key components for determining the diffusive mass flow between two PSR (cells) in the core and recirculation zones.

An analytical solution for the average mole fraction of methane in the core can be obtained. This calculation assumes that the mole fraction of methane in the core changes only by dilution due to diffusion and that the surroundings (i.e. the recirculation zone) do not contain methane. The decay of the inlet mass fraction of methane, as a function of the path length (l) along the core boundary (cb) is given by Equation 5.8 where Y_o is the initial mass fraction of methane at the inlet and m_{in} is the total fuel/air mass flow at the jet inlet. A comparison of the analytical solution, which gives an average methane concentration in the core, against CFD results giving local concentrations along two bounding pathlines - the first along the center of the jet and the second along the boundary of the core region - and the experimentally measured mole fraction of methane is given in Figure 5.15. Values of ρ and D_T are taken from the boundary of the core region in the CFD model of methane combustion at the nominal stable operating condition. The analytical solution falls between the two bounding pathlines up to the probe location. This is consistent with the methane concentration fall off being due to dilution only through where the experimental data point is taken. The CFD solution predicts lower concentrations after about 0.035 m due to methane reaction.

$$Y_{\mathrm{CH_4}}(l) = Y_o \exp\left[-\frac{1}{\dot{m}_{in}} \int_l \rho(D_T/L)\, \mathrm{dA}_{cb}\right] \tag{5.8}$$

Using a single definition of the diffusive mass flow for both methane and hydrogen at varying equivalence ratios is desired. The cumulative diffusive mass flow normalized by the inlet mass flow rate is given as a function of the path length along the core boundary in Figure 5.15(b). The density and turbulent diffusivity are taken along the boundary of the core region for four CFD cases: hydrogen and methane at the nominal stable operating condition equivalence ratios and hydrogen and methane at their blowout conditions. From the jet inlet to the top of the reactor (around a path length of 0.05 m) the resulting diffusive mass flow rates match very closely. Hydrogen at blowout deviates from the other three cases especially once the core region has hit

the top of the reactor and begun moving towards the exhaust port. This is due mostly to the much lower temperature in the recirculation zone near blowout, resulting in a denser gas. Note that the cumulative diffusive mass transport normalized by the inlet mass flow rate is consistent with an average fluid particle completing about four cycles in the recirculation zone. Figure 5.15 gives us some confidence that a single specification of the diffusive mass flow rate between the core and recirculation regions can be used.

This type of CRN model is difficult to handle through the graphical user interface in CHEMKIN-PRO, therefore all of the work done here on the two PFR model is through the command-line interface with CHEMKIN-PRO. Scripts to generate the input files for CHEMKIN-PRO with the appropriate volumes, heat loss, mass flow rates, and flow connections between the PSRs are developed in Python. In addition, model execution scripts and data processing scripts written in Python assist in automating the modeling process.

5.2.2 Modeling Results: Hydrogen

We perform a grid study with pure hydrogen as the fuel. Figures 5.16 and 5.17 compare the development of OH in the core and recirculation regions respectively as a function of convective residence time in each PFR. Three grid sizes are compared and the development of OH is presented for both the stable operating condition (1800 K) and blowout as predicted by the two PFR model. Finally Table 5.2 shows the predicted blowout equivalence ratio, maximum temperature in the recirculation PFR, the temperature at the approximate location of the probe, and the total computation time for each grid.

Table 5.2 gives computational times and blowout results for three different grid sizes. The models were run on a workstation with an Intel Xeon X5550 dual quad core processor and 24 GB of RAM, although CHEMKIN-PRO currently only takes advantage of a single core for networks of PSRs. Table 5.2 reveals that all three grids

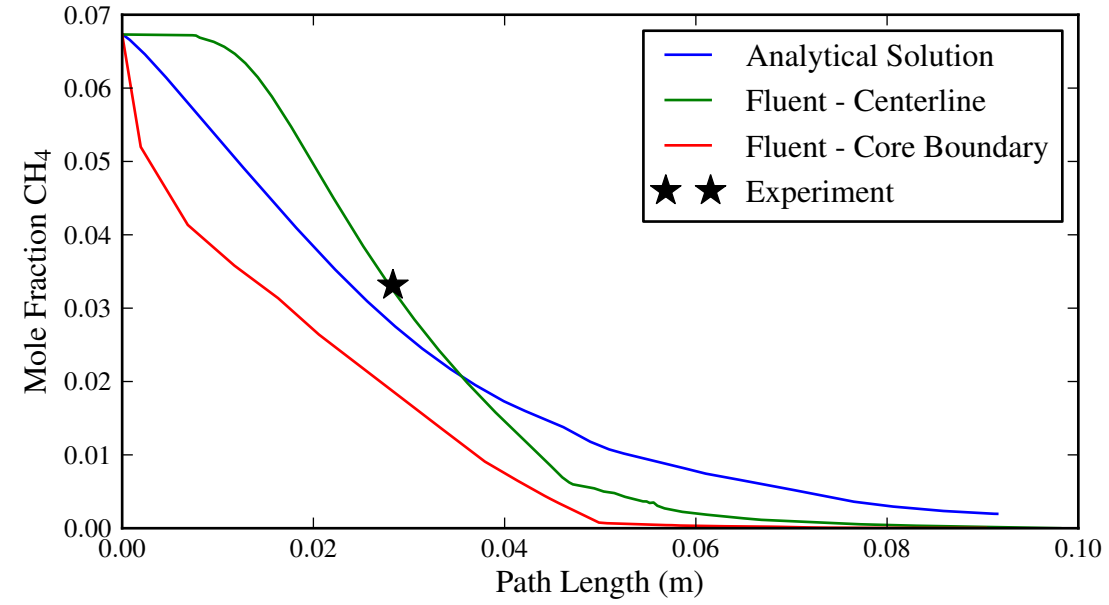

(a) Mole Fraction of CH_4 Comparison

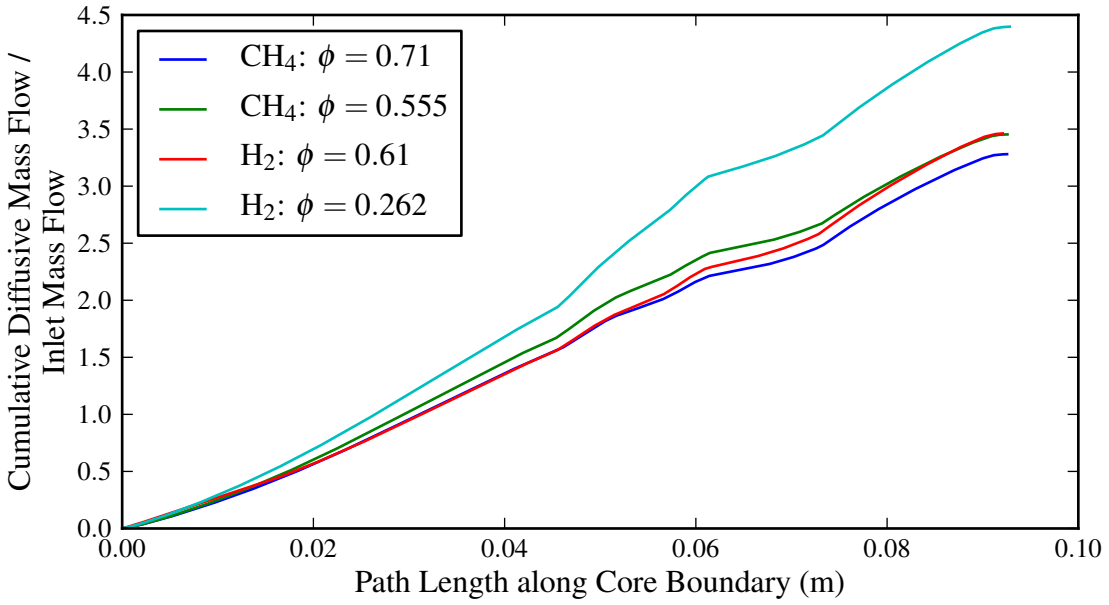

(b) Total Difusive Mass Flow Rate

Figure 5.15: Validating the definition of diffusive mass flow for the two PFR model: (a) compares the mole fraction of CH_4 predicted by the analytical model given by Equation 5.8, the CH_4 reported by CFD on two bounding pathlines for the core region and the experimentally measured value; (b) compares the total diffusive mass flow normalized by the inlet mass flow rate for four equivalence ratios - the nominal stable operating condition and the blowout condition for both methane and hydrogen.

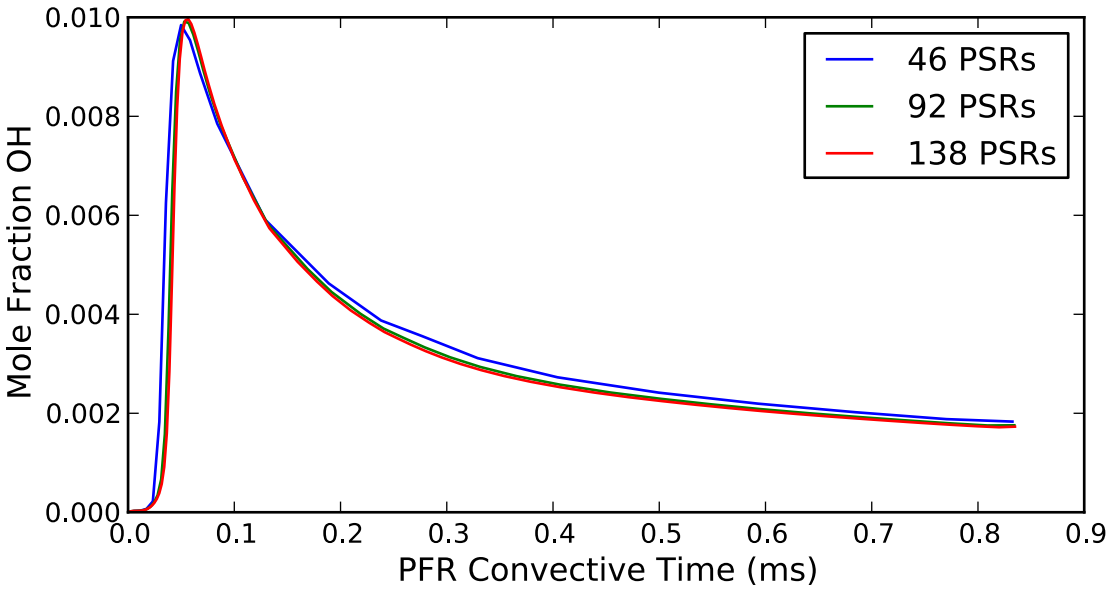

(a) $\phi = 0.61$, Core

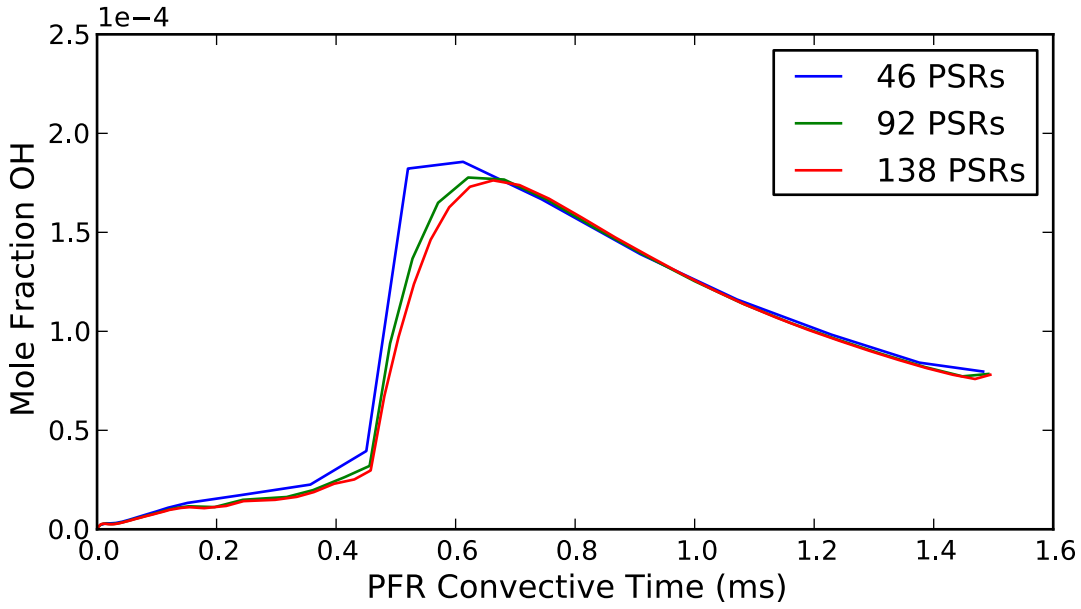

(b) $\phi = 0.23$, Core

Figure 5.16: Hydrogen grid study for the two PFR model, comparing the mole fraction of OH predicted in the core region as a function of convective time in the PFR from the jet inlet to the reactor exhaust at the nominal stable operating condition and blowout for three different grids.

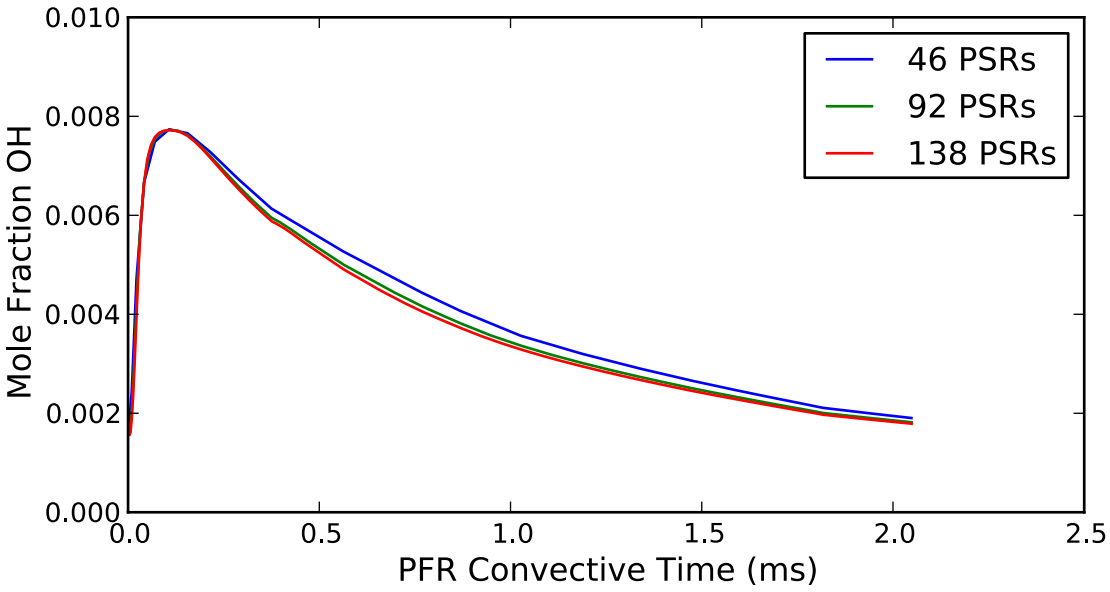

(a) $\phi = 0.61$, Recirculation

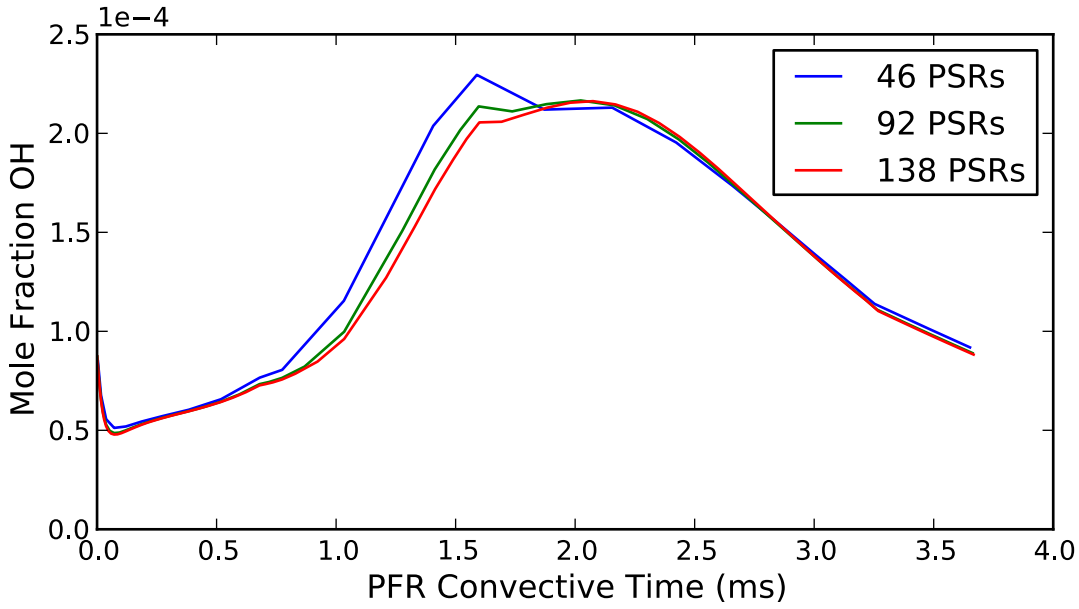

(b) $\phi = 0.23$, Recirculation

Figure 5.17: Hydrogen grid study for the two PFR model, comparing the mole fraction of OH predicted in the recirculation region as a function of convective time in the PFR from near the jet inlet to the point of re-entrainfment at the nominal stable operating condition and blowout for three different grids.

give the same predicted blowout equivalence ratio and temperatures for hydrogen. Figures 5.16 and 5.17 indicate that 42 PSRs is insufficient to resolve the OH peak at blowout, however the 92 PSR and 138 PSR solutions are almost indistinguishable. In order to save on computational time but adequately resolve the development of the radical pool a grid of 92 PSRs is used for the rest of the study.

Figure 5.18 presents the blowout predictions of the two PFR model compared against the experimental results varying the chemical mechanism. Since the single PFR model established that GRI was not the best choice for hydrogen it is not included here. The two mechanisms chosen are Li and UCSD. These two mechanisms produce results in very close agreement. The final blowout temperature matches that found experimentally very well, however the equivalence ratio is underpredicted. Figure 5.19 shows that the two PFR model is stable to a lower equivalence ratio than the single PFR model, however both models predict a similar blowout temperature. Figure 5.20 shows that the two PFR model has a similar stabilization mechanism to the single PFR model. The development of the radical pool prior to re-entrainment in the recirculation region is key. As the equivalence ratio drops, the development of the radical pool moves further around and down the recirculation zone.

Table 5.2: Hydrogen grid study comparing predicted blowout equivalence ratio and temperatures, and time to solution as a function of the number of PSRs used in the two PFR model.

Number of PSRs	ϕ at Blowout	Max Temp at Blowout [K]	Temp at Probe Location [K]	Time to Solution (18 ϕ)
46	0.23	1093	1082	1.3 min
92	0.23	1093	1082	5.6 min
138	0.23	1093	1082	12.6 min

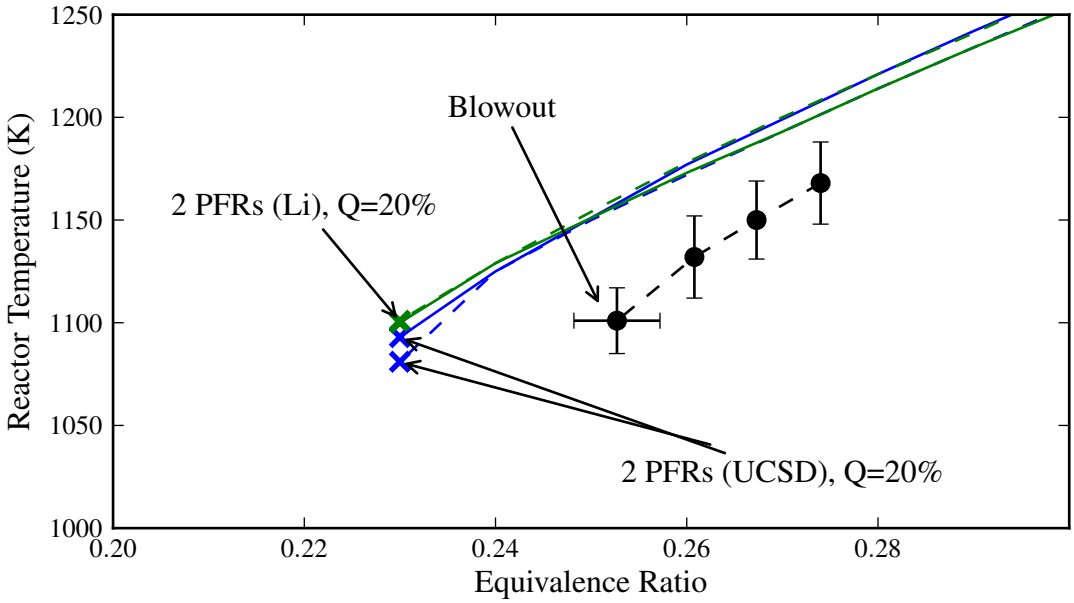

Figure 5.18: Comparison of the two PFR modeling results for hydrogen varying the chemical mechanism. A plot of maximum temperature vs. equivalence ratio is given by the solid lines and the probe location temperature vs. equivalence ratio by the dashed lines. Experimental results are given for comparison.

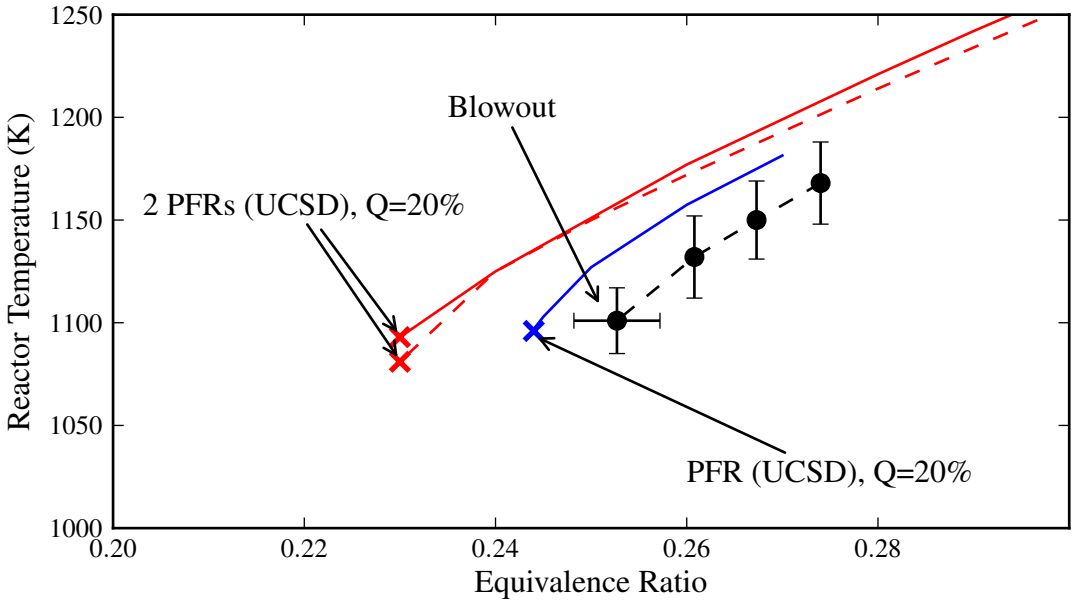

Figure 5.19: Comparison of the single and two PFR modeling results for hydrogen. A plot of maximum temperature vs. equivalence ratio is given by the solid lines and the probe location temperature vs. equivalence ratio by the dashed lines. Experimental results are given for comparison.

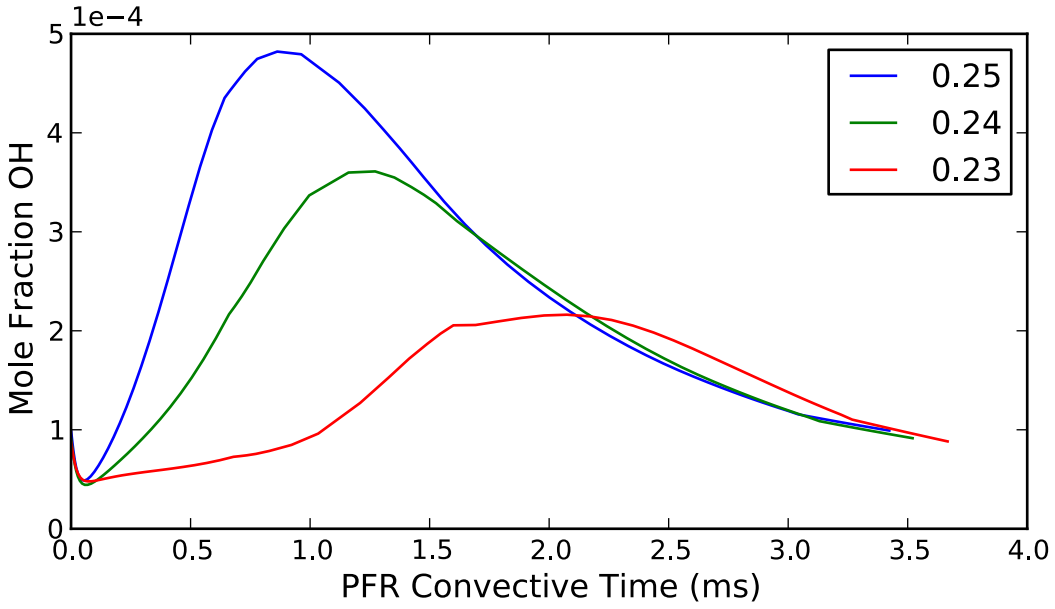

Figure 5.20: Mole Fraction of OH radical, plotted for the recirculation PFR from the point of entrainment near the jet as a function of time along the PFR for hydrogen combustion. Results are given from three different equivalence ratios as blowout is approached.

Contour plots of the mole fractions of hydrogen and OH as well as temperature are given in Figures 5.21, 5.22, and 5.23 respectively. With the contour plots we can make a more direct comparison with the CFD results, for example by comparing Figures 4.9 and 5.22. We do not expect the peaks to be the same since the two PFR model is showing spatially averaged values where-as the CFD shows local quantities, however the general position of the OH peaks for both equivalence ratios shown are similar. In addition, the plot of H_2 in the two PFR model reinforces the CFD plot of H_2 destruction, illustrating the delay and spreading of chemistry as blowout is approached.

5.2.3 Modeling Results: Methane

We begin the study of the two PFR model with pure methane as the fuel with grid size comparison to ensure that a different fuel does not require a different grid resolution. Figures 5.24 and 5.25 compare the development of OH in the core and recirculation regions respectively as a function of convective residence time in each PFR. As for hydrogen, three grid sizes are compared and the development of OH is presented for both the stable operating condition (1800 K) and blowout as predicted by the two PFR model. Finally Table 5.3 shows the predicted blowout equivalence ratio, maximum temperature in the recirculation PFR, the temperature at the approximate location of the probe, and the total computation time for each grid. Although fewer equivalence ratios are tested in a parameter study to determine blowout for methane, the computational times are more than 60 times that needed for hydrogen. This is due to the increase in the number of species needed to describe methane combustion. And as with hydrogen the plots of OH show little difference between these two grids, yet 138 PSRs requires twice the computation time as 92. Therefore, 92 PSRs is the chosen grid for methane as well and will be used for the H_2/CH_4 blends discussed in the following section.

Figure 5.26 presents the blowout predictions of the two PFR model compared

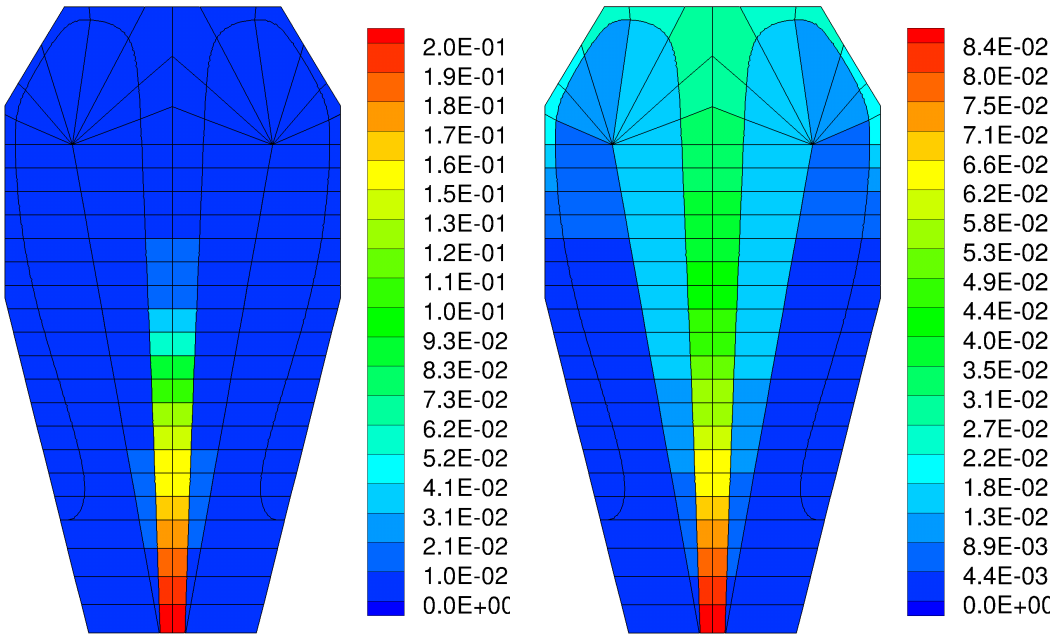

(a) $\phi = 0.61$ (b) $\phi = 0.23$

Figure 5.21: Contour plots of hydrogen mole fraction for the two PFR model with hydrogen as the fuel and UCSD as the mechanism. Results are given for two different equivalence ratios (a) the nominal stable operating condition and (b) blowout as predicted by the two PFR model.

Table 5.3: Methane grid study comparing predicted blowout equivalence ratio and temperatures, and time to solution as a function of the number of PSRs used in the two PFR model.

Number of PSRs	ϕ at Blowout	Max Temp at Blowout [K]	Temp at Probe Location [K]	Time to Solution (10 ϕ)
46	0.51	1474	1382	1.2 hrs
92	0.51	1475	1389	6.3 hrs
138	0.51	1475	1395	23.6 hrs

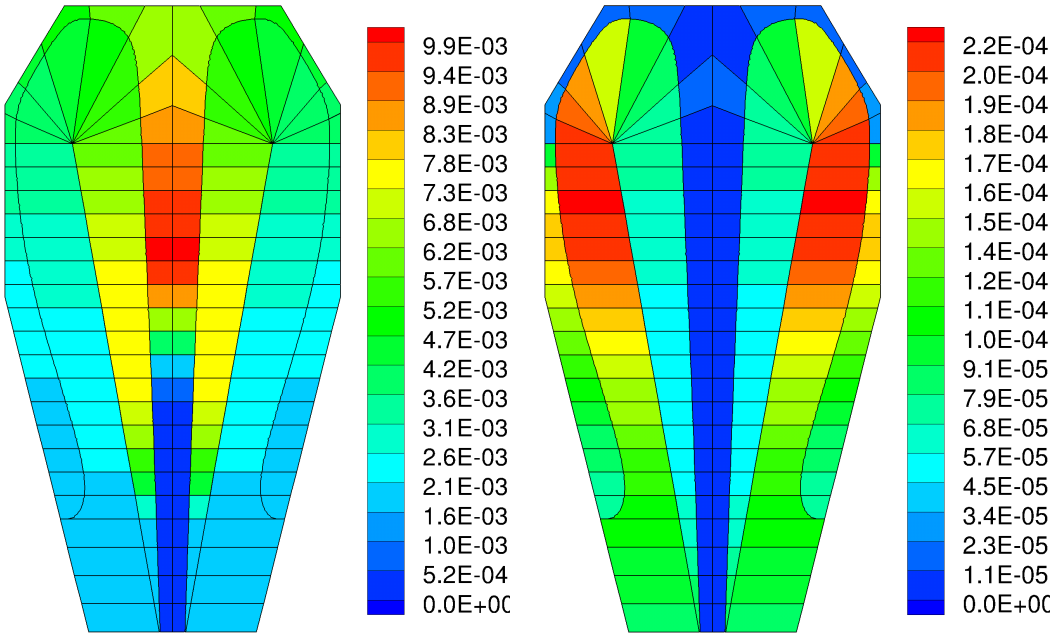

(a) $\phi = 0.61$ (b) $\phi = 0.23$

Figure 5.22: Contour plots of OH mole fraction for the two PFR model with hydrogen as the fuel and UCSD as the mechanism. Results are given for two different equivalence ratios (a) the nominal stable operating condition and (b) blowout as predicted by the two PFR model.

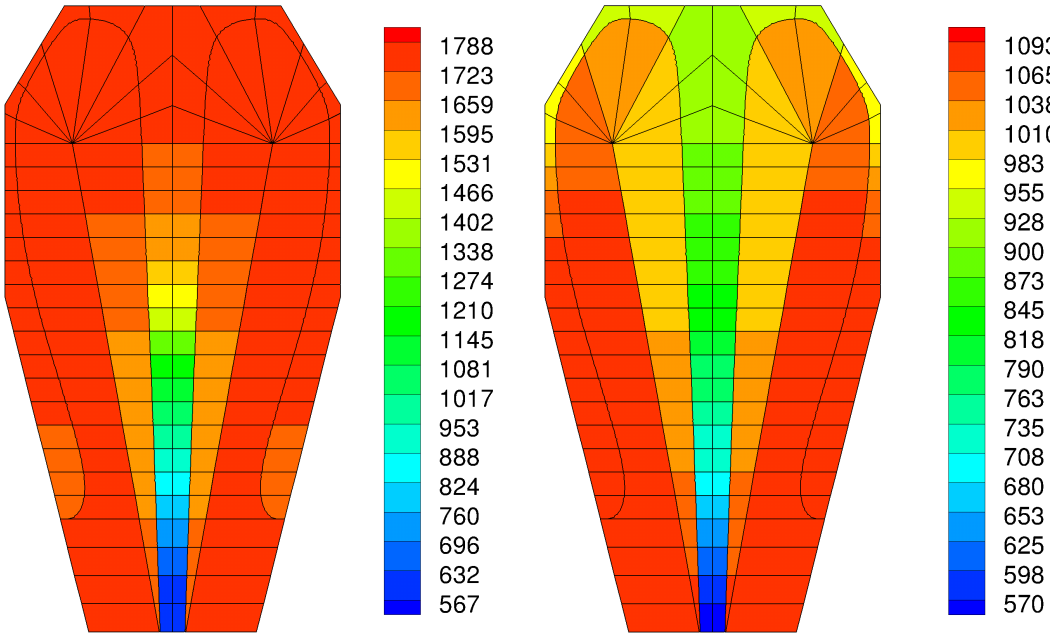

(a) $\phi = 0.61$ (b) $\phi = 0.23$

Figure 5.23: Contour plots of temperature in kelvin for the two PFR model with hydrogen as the fuel and UCSD as the mechanism. Results are given for two different equivalence ratios (a) the nominal stable operating condition and (b) blowout as predicted by the two PFR model.

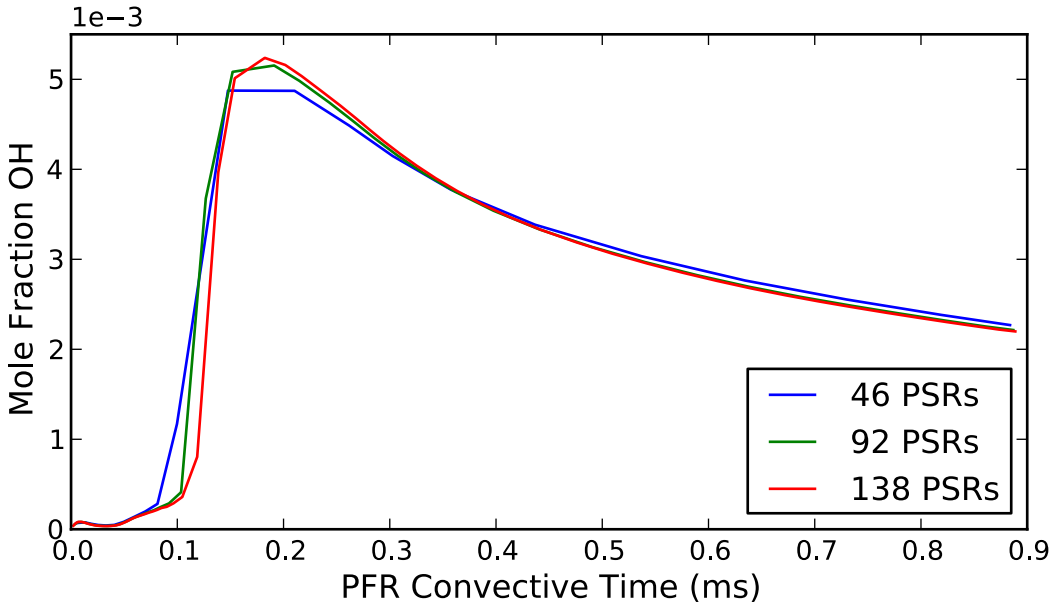

(a) $\phi = 0.71$, Core

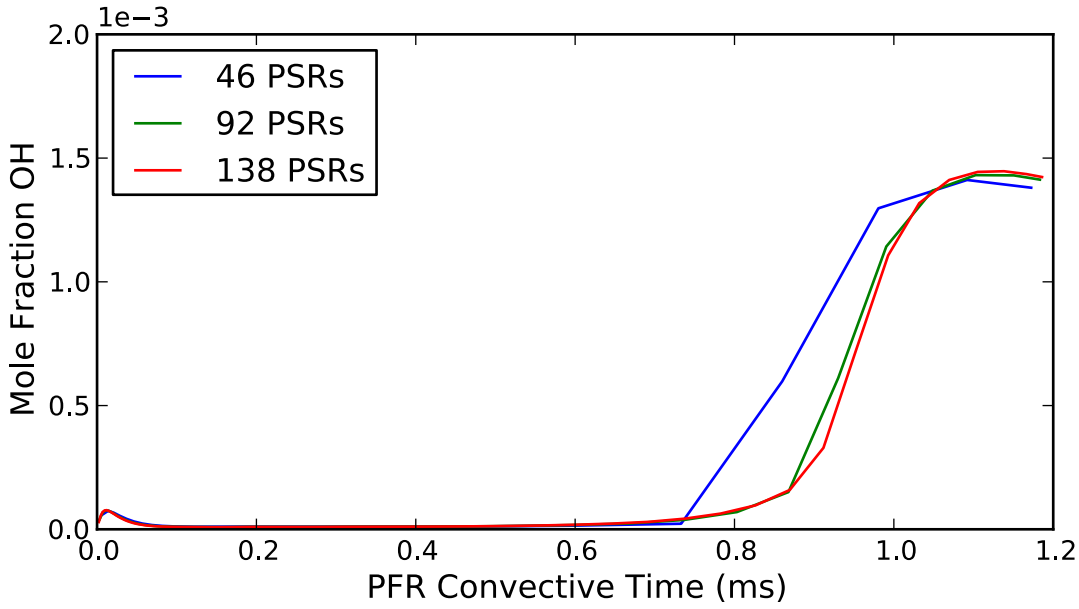

(b) $\phi = 0.51$, Core

Figure 5.24: Methane grid study for two PFR model, comparing the mole fraction of OH predicted in the core region as a function of convective time in the PFR from the jet inlet to the reactor exhaust at the nominal stable operating condition and blowout for three different grids.

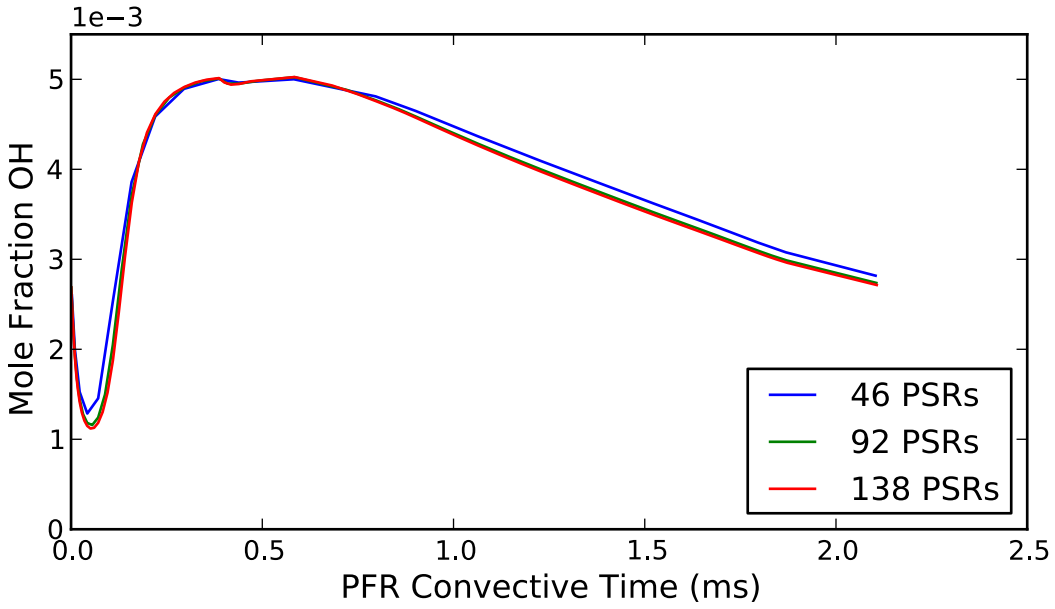

(a) $\phi = 0.71$, Recirculation

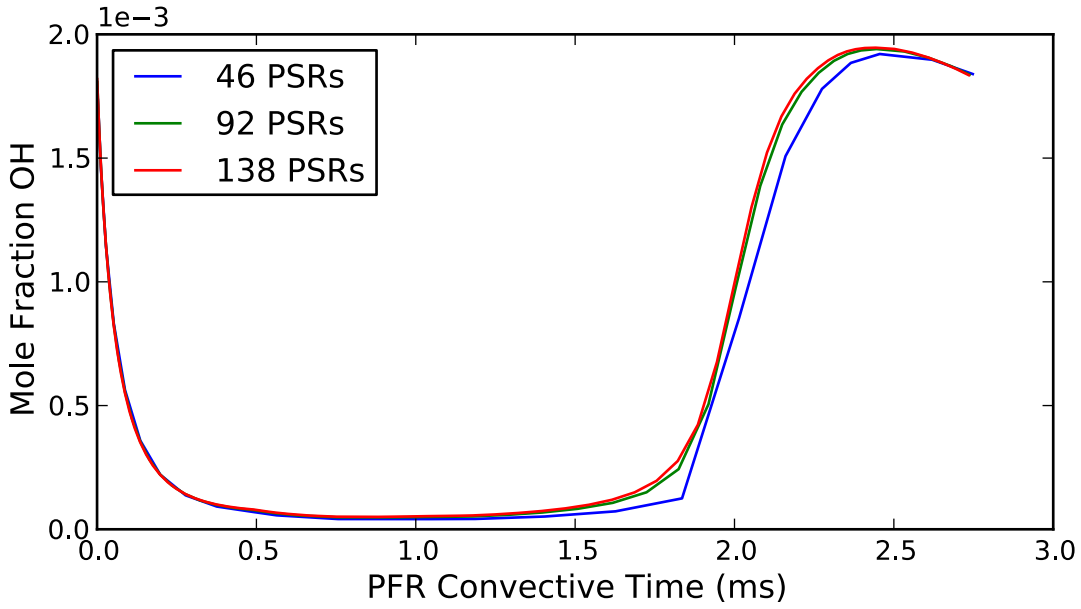

(b) $\phi = 0.51$, Recirculation

Figure 5.25: Methane grid study for the two PFR model, comparing the mole fraction of OH predicted in the recirculation region as a function of convective time in the PFR from near the jet inlet to the point of re-entrainment at the nominal stable operating condition and blowout for three different grids.

against the experimental results varying the chemical mechanism. Since the single PFR model established that the skeletal GRI mechanism closely follows full GRI-3.0, only the skeletal GRI mechanism is tested here against UCSD. As with the single PFR model, the skeletal GRI mechanism stabilizes to lower equivalence ratios than UCSD. This is again more likely due to the shorter ignition delay times predicted by GRI over UCSD for the same inlet equivalence ratio. With the UCSD mechanism the two PFR model predicts a maximum temperature in the recirculation PFR that matches the experimentally measured temperature at blowout well, although the average temperature near the probe location is 100 K less than the measured temperature. The equivalence ratio at blowout is predicted to be slightly lower than that measured experimentally.

Figure 5.27 presents the blowout predictions of the two PFR model against the single PFR model, both with the UCSD mechansim. It is clear from the figure that the two PFR model shows significantly better agreement with experimentally measured data approaching blowout and the blowout condition itself than the single PFR model.

Although the temperature vs. equivalence ratio predictions of the two models are very different, Figure 5.28(a) shows that the two models share a similar trend for OH as blowout is approached. The peak OH decreases in quantity and moves further around and down the recirculation zone. The peaking tendencies are different however with the two PFR model showing a much more distinct OH peak right at the end of the PFR before re-entrainment for all three equivalence ratios approaching blowout. Comparing the CO in Figures 5.28(b) and 5.9(b) for the two CRN models shows differing trends. The single PFR model reveals the peak CO decreasing in the reactor as blowout is approached while the two PFR model shows the peak CO increasing in the recirculation zone. Both are consistent with the CFD results however. The single PFR shows an average for the entire reactor, in which the peak CO concentration does decrease as we approach blowout. The two PFR model shows decreasing CO in the recirculation zone but increasing CO in the core region (see Figure). This is

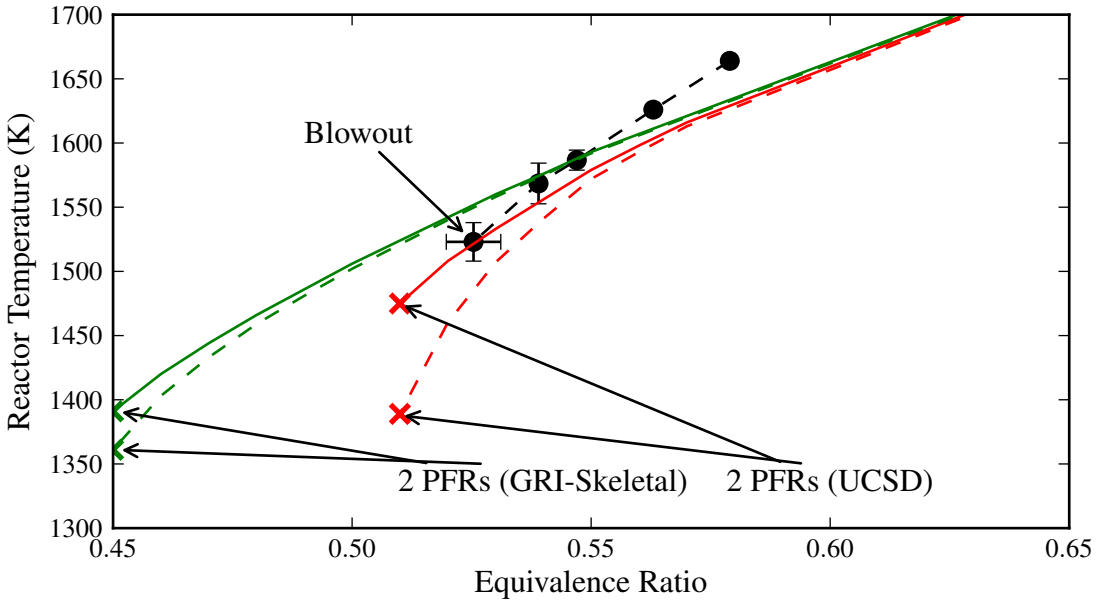

Figure 5.26: Comparison of the two PFR modeling results for methane varying the chemical mechanism. A plot of maximum temperature vs. equivalence ratio is given by the solid lines and the probe location temperature vs. equivalence ratio by the dashed lines. Experimental results are given for comparison.

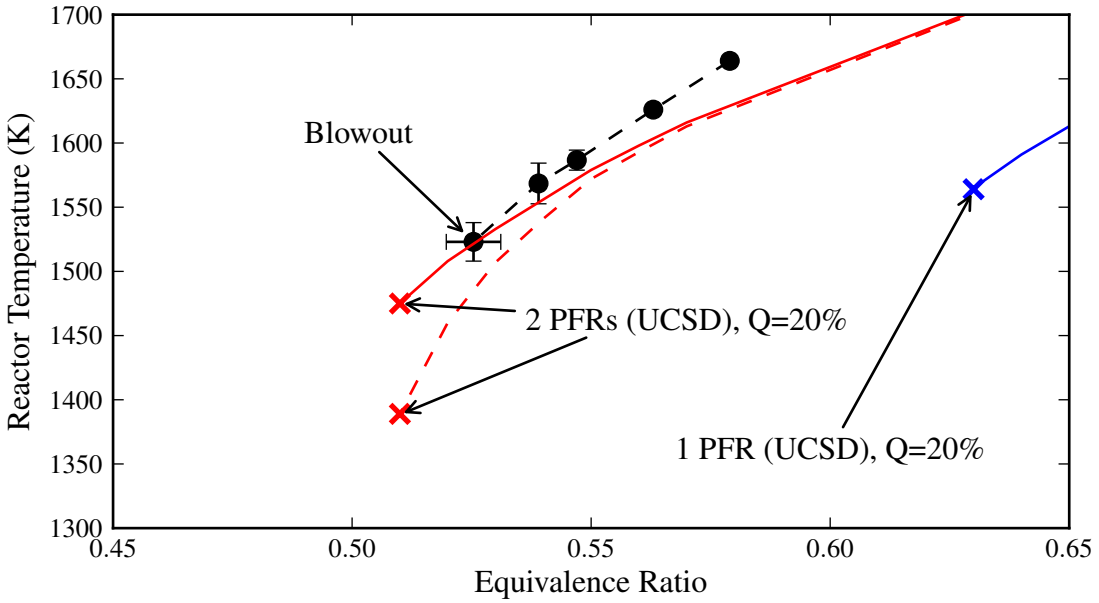

Figure 5.27: Comparison of the single and two PFR modeling results for methane. A plot of maximum temperature vs. equivalence ratio is given by the solid lines and the probe location temperature vs. equivalence ratio by the dashed lines. Experimental results are given for comparison.

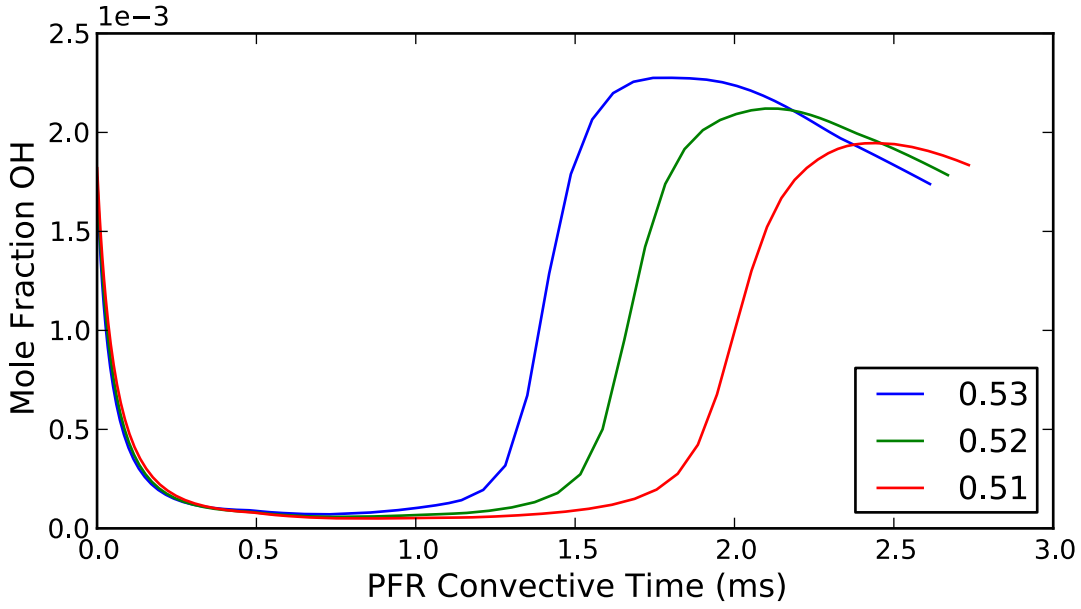

(a) OH

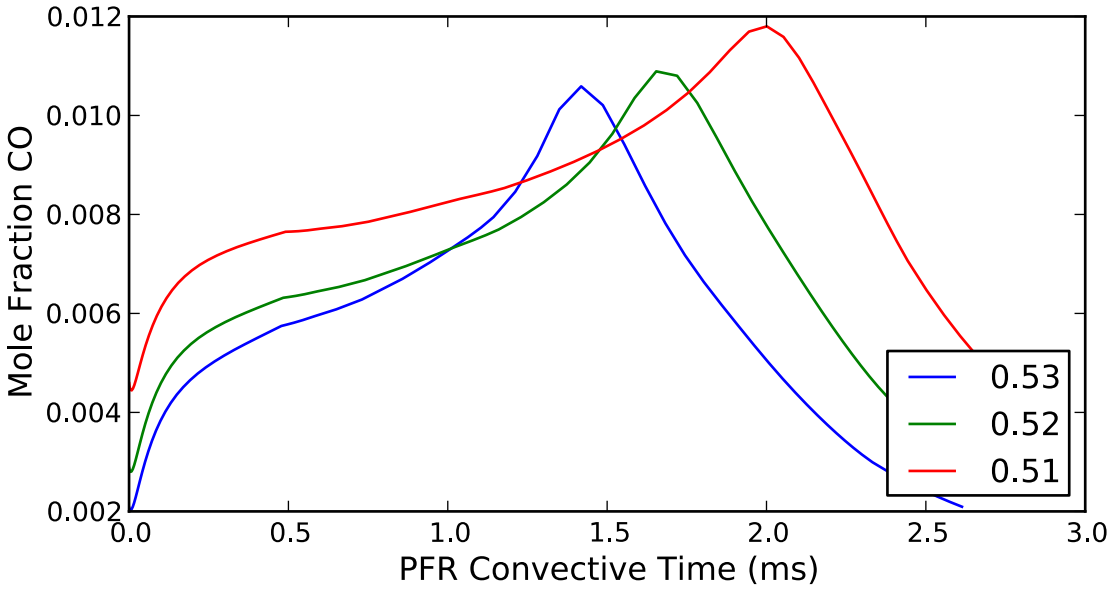

(b) CO

Figure 5.28: Mole Fraction of (a) OH radical and (b) CO, plotted for the recirculation PFR from the point of entrainment near the jet as a function of time along the PFR for methane combustion. Results are given from three different equivalence ratios as blowout is approached.

consistent with the spatial behavior of CO in the CFD.

The behavior of the OH radical in both the single and two PFR models indicate a similar global stabilization mechanism - that the development of the radical pool prior to re-entrainment in the recirculation zone is key. However, because the two PFR model better represents the experimental data both as blowout is approached and the blowout condition itself, another process is at work. We hypothesize that the transport of the radicals and CO through turbulent diffusion in the two PFR model plays a large role in the stabilization of methane combustion.

Contour plots of the mole fractions of methane, CO, and OH, as well as temperature are given in Figures 5.29, 5.30, 5.31. 5.32. With the contour plots for the two PFR model we see similar trends as with the CFD model approaching blowout.

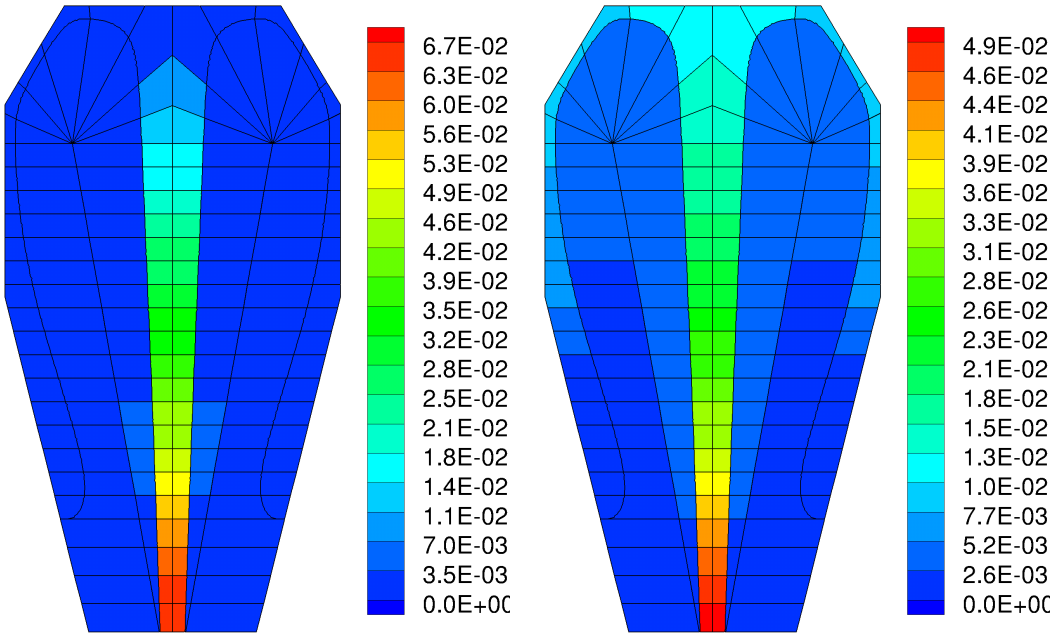

(a) $\phi = 0.71$ (b) $\phi = 0.51$

Figure 5.29: Contour plots of CH_4 mole fraction for the two PFR model with methane as the fuel and UCSD as the mechanism. Results are given for two different equivalence ratios (a) the nominal stable operating condition and (b) blowout as predicted by the two PFR model.

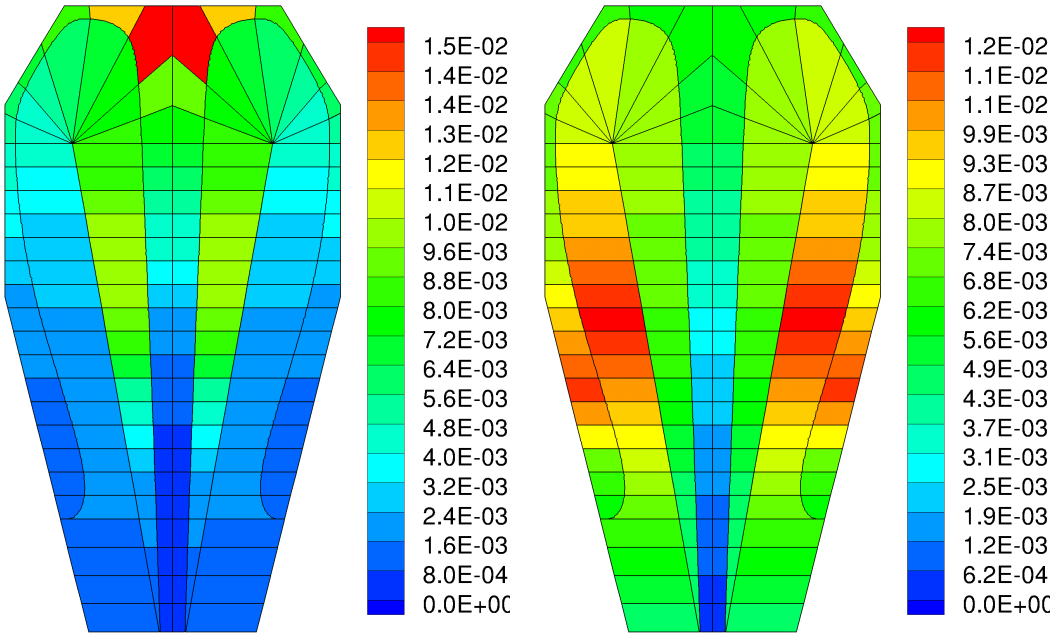

(a) $\phi = 0.71$ (b) $\phi = 0.51$

Figure 5.30: Contour plots of CO mole fraction for the two PFR model with methane as the fuel and UCSD as the mechanism. Results are given for two different equivalence ratios (a) the nominal stable operating condition and (b) blowout as predicted by the two PFR model.

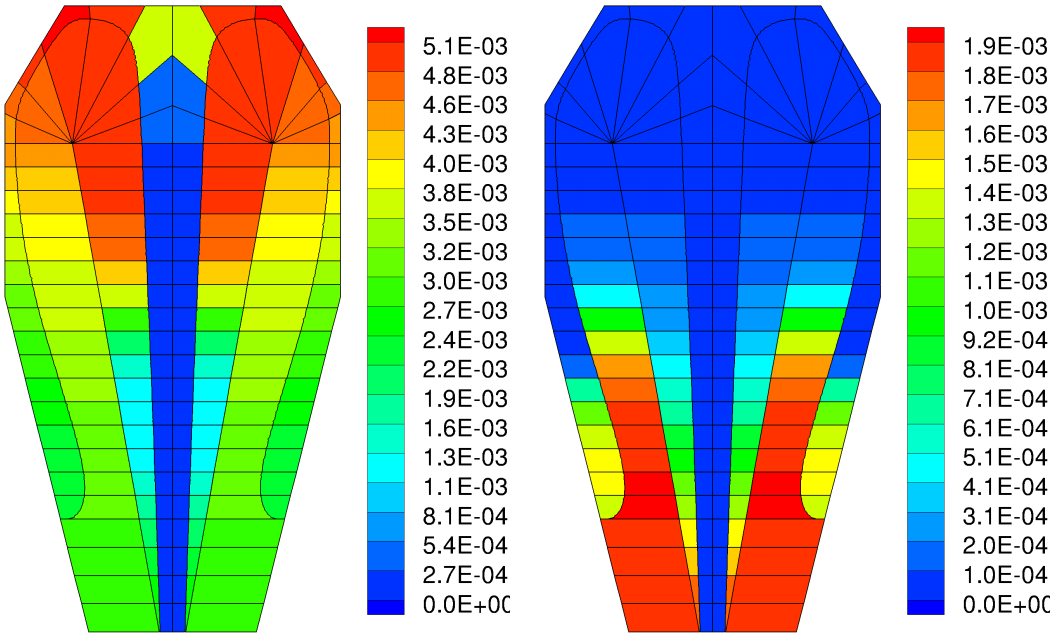

(a) $\phi = 0.71$ (b) $\phi = 0.51$

Figure 5.31: Contour plots of OH mole fraction for the two PFR model with methane as the fuel and UCSD as the mechanism. Results are given for two different equivalence ratios (a) the nominal stable operating condition and (b) blowout as predicted by the two PFR model.

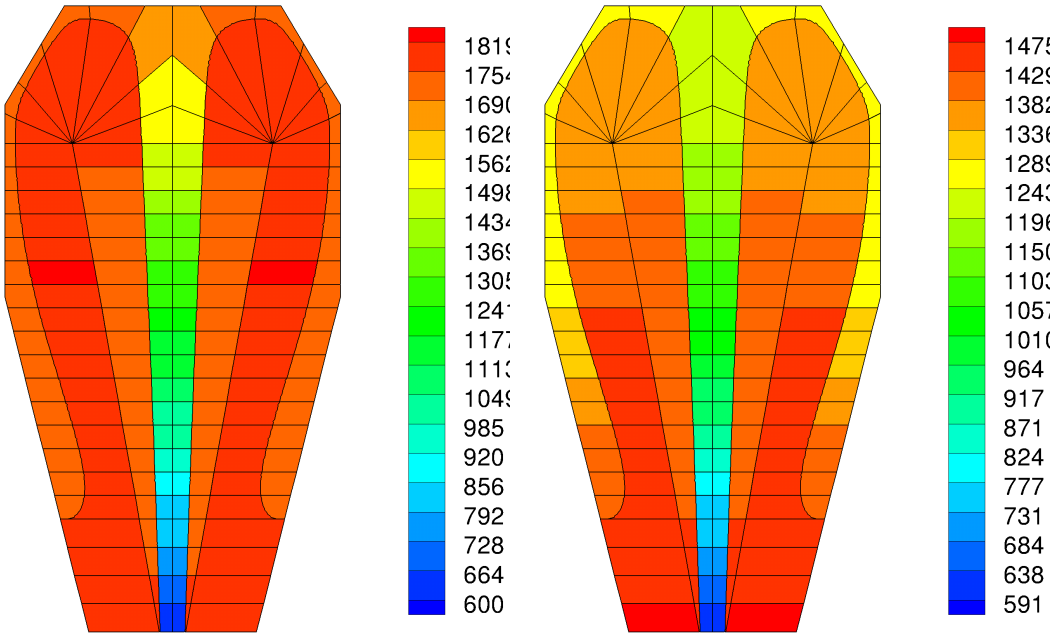

(a) $\phi = 0.71$ (b) $\phi = 0.51$

Figure 5.32: Contour plots of temperature in kelvin for the two PFR model with methane as the fuel and UCSD as the mechanism. Results are given for two different equivalence ratios (a) the nominal stable operating condition and (b) blowout as predicted by the two PFR model.

Methane destruction remains relatively constant and the pool of both CO and OH is pushed further around the recirculation zone. Note that both the contour plots and Figure 5.28 show a distinct peak in OH and CO near the exit of the recirculation PFR (after which re-entrainment occurs). This is in contrast to the very broad peak of OH seen in Figure 5.22 for the two PFR model as blowout is approached for hydrogen.

5.2.4 H_2/CH_4 Blends

Finally, we apply the two PFR model with the UCSD mechanism to the full range of H_2/CH_4 blends tested. Plots of the two PFR model predictions of blowout equivalence ratio and temperature, given as both the maximum temperature in the recirculation PFR and the temperature at the approximate probe location, are shown in Figure 5.33 against the experimental data and the results from the single PFR model. The maximum temperature follows the measured temperatures well across the range of blends, although it consistently underpredicts the measured temperatures by about 50 K. The average temperature at the approximate probe location follows the maximum temperature from pure hydrogen through about 50% hydrogen in the fuel and then begins to diverge. This is when the CO chemistry begins to take over, delaying the heat release in the reactor.

5.3 Conclusions from the CRN Modeling

Overall the single PFR model predicts the temperature at blowout most accurately, however the two PFR model matches the blowout equivalence ratio most closely for the full range of methane hydrogen blends. The behavior of hydrogen as it approaches blowout is affected very little by the inclusion of turbulent diffusive transport in the two PFR model. Both the single and two PFR models follow the JSR data taken for hydrogen as blowout is approached and reasonably capture the blowout condition. For methane however, the inclusion of turbulent diffusive transport is key to following the JSR data as blowout is approached and providing reasonable agreement with the

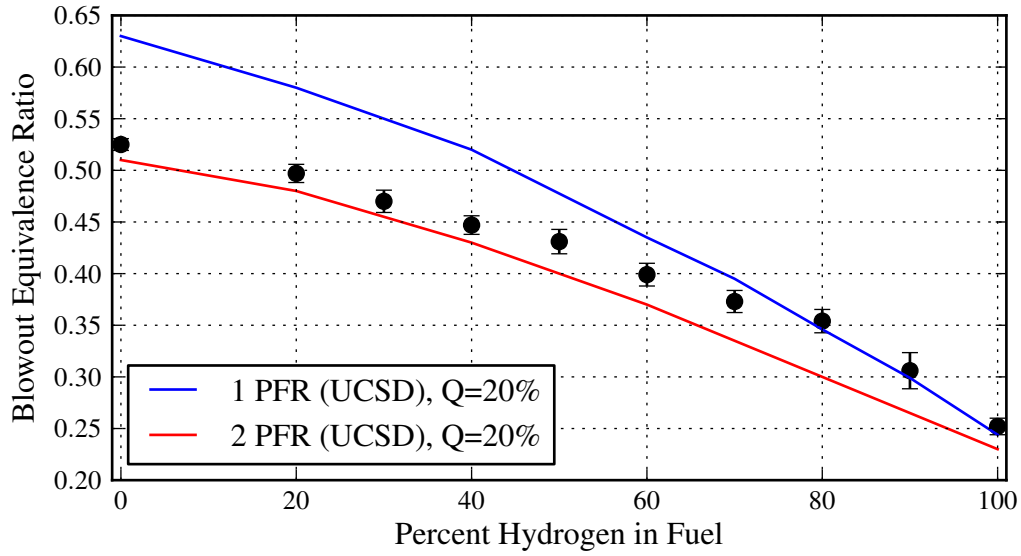

(a) Equivalence Ratio

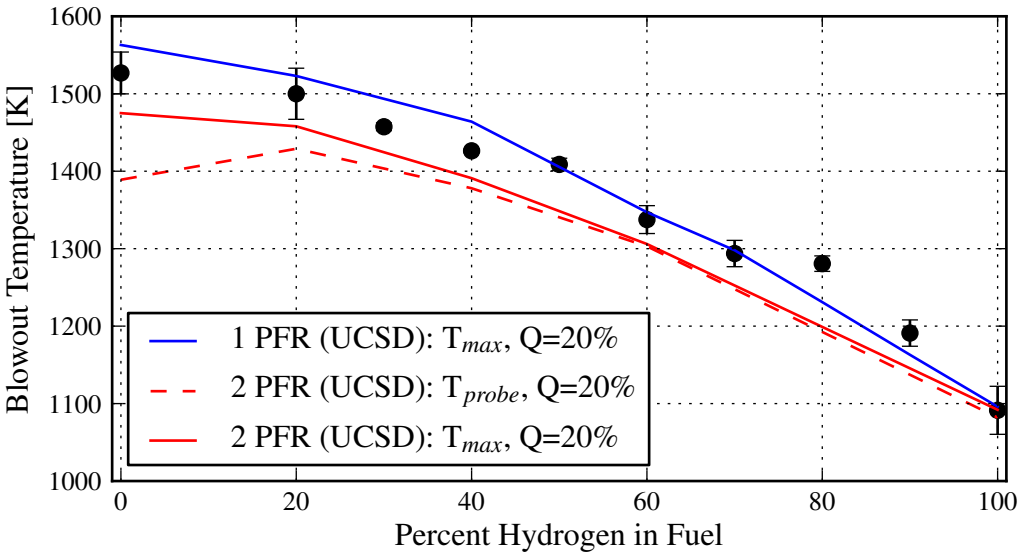

(b) Temperature

Figure 5.33: Two PFR model predictions of blowout compared against experimentally determined blowout (a) temperature and (b) equivalence ratio for CH_4 mixed with increasing amounts of H_2. The predictions of the single PFR model are also provided for reference.

measured blowout condition.

Regardless of the chemical mechanism applied, or whether we consider transport by convection only as in the single PFR model, or transport by both convection and diffusion as in the two PFR model, the story regarding the onset of blowout remains the same and is consistent with that given by CFD as well: the key to the stable operation of the reactor is the ignition event in the recirculation zone, resulting in the development of the radical pool. For pure hydrogen combustion, as the fuel flow rate is reduced and the reactor moves towards blowout the destruction of the fuel slows and spreads, and the development of the radical pool moves further around the recirculation zone. The radical pool must develop (i.e. ignition must occur) before re-entrainment or the reactor will extinguish. For methane, we similarly see the destruction of methane spread, and the net production of CO, and subsequently the net production of OH move further around the recirculation zone until the re-entrainment of radicals can no longer sustain the combustion. For methane however, transport of the CO and radicals through turbulent diffusion appears to be a controlling process in this ignition event. This is most likely due to the fact that the breakdown of hydrogen directly produces an H radical that feeds the chain propagating reaction, however the breakdown of methane has no such direct feedback. It is only in the destruction of methane intermediates that the H radical needed to feed the chain propagating reaction is produced.

Chapter 6
SUMMARY AND CONCLUSIONS

The work presented here examines lean premixed flame stability for multi-component fuel mixtures to support fuel flexibility for industrial combustors. A single Jet Stirred Reactor (JSR), a generic recirculation stabilized combustor, along with gaseous fuels of hydrogen, methane, and hydrogen/methane blends are studied. Experimental data on blowout are collected and a series of models are used to understand the mechanism of extinction in this recirculation-stabilized flame environment. By studying this more generic combustor, the aim is to develop generalizable results and methodologies for understanding and predicting lean blowout of multicomponent fuels.

6.1 Experiments

Experimental data approaching blowout are taken for fuels of pure hydrogen, pure methane, and hydrogen/methane blends in 10% by volume increments. The data relate experimental equivalence ratios to temperatures for each fuel approaching blowout and reveal the final blowout condition for each fuel. These blowout data are obtained by holding the air flow rate constant and decreasing the fuel flow rate until the flame is extinguished. Doing so holds the flow field and turbulence parameters approximately constant as blowout is approached. The reactor is stabilized to lower equivalence ratios and temperatures as the percentage of hydrogen in the fuel increases.

In analyzing the experimental data, it is determined that the JSR experiences blowout at a nearly constant chemical time. This observation can be used as a predictive tool for blowout in the JSR. Using a single Perfectly Stirred Reactor with 20% heat loss and this constant chemical time we can predict the blowout equivalence ratio

across the full range of methane/hydrogen blends very well. This PSR model under-predicts the blowout temperature. A Plug Flow Reactor with the remaining reactor volume is therefore added in series with the PSR. The predicted temperature from the PFR provides much better agreement with that measured experimentally. While this model is predictive it does not give detailed insight on the controlling processes in the JSR as blowout is approached.

Finally, audio recordings are made for fuel blends of 70% hydrogen and greater near blowout and time-localized acoustic events are identified both audibly and through the numerical technique of cross-correlation. The mean time between acoustic events is determined to be between 35 and 50 ms and does not change as the percentage of hydrogen in the fuel is increased. It is suggested that these events are due to extinction/reignition events in the reactor as the combustion process weakens. Future work is needed however to determine the controlling physical processes.

6.2 CFD Modeling

In order to gain insight on the mechanism controlling blowout, two dimensional, axisymmetric computational fluid dynamic (CFD) simulations are carried out for the lean premixed combustion of both hydrogen and methane as the fuel. To develop a CFD model to describe methane combustion a mechanism of reduced size is needed. A 22 species skeletal mechanism derived from GRI-3.0 describing methane combustion is developed using the Directed Relation Graph (DRG) method. In addition the extended method of DRG-aided sensitivity analysis (DRGASA) is used to extend the skeletal mechanism to include reduced NOx chemistry.

In constructing the CFD model, Eddy Dissipation Concept (EDC) is chosen as the model for describing turbulence-chemistry interaction. This model does a reasonable job of predicting the blowout equivalence ratio and temperature for both hydrogen and methane. The model is identified as having limitations in the low Damkohler number regime, for example situations of slow chemistry (CO oxidation) or fast mix-

ing (the jet region of of the JSR). It is also identified as overpredicting reaction rates in the boundary layer. Two limiting modifications of EDC are explored as a result: (1) reaction rates are artificially eliminated in the boundary layer, and (2) the reactive volume of each cell is increased to its limit in the EDC model. Artificially eliminating reactions in the boundary layer has little effect on the prediction of blowout equivalence ratio or temperature for hydrogen combustion. While methane appears to be more sensitive to this modification it still has only a small effect on the prediction of the blowout condition. Eliminating reactions in the boundary layer results in stable combustion at a lower equivalence ratio as for both hydrogen and methane, however the predicted blowout temperature for methane drops by almost 70 K. This is most likely due to the reduced reacting volume, resulting in less CO oxidation and therefore less heat release. Taking the entire model to the EDC limit alters the predicted blowout equivalence ratio significantly for hydrogen, although the predicted blowout temperature is mostly unchanged.

Contour plots from the CFD modeling illustrate the evolution of the flow-field, temperature profiles, and flame structure within the JSR as blowout is approached for both fuels. All reveal the non-homogeneity of the reactor as blowout is approached. For hydrogen, the destruction of the fuel encompasses more of the physical volume of the reactor and the radical pool decreases in quantity and is convected further around the recirculation zone. For methane, the destruction of the fuel spreads but not as significantly as for hydrogen. This is because methane has a key intermediate chain propagating reaction involving CO. Volume is required for the oxidation of CO and the chain branching production of the radical pool. As with hydrogen, both of these events move further around the recirculation zone. Analysis of the models from the perspective of a combusting fluid particle traveling through the jet, into the recirculation zone, and then entraining back into the jet suggests that the blowout condition is dependent on the development of the radical pool. The flame remains stable as long as the radical pool develops significantly enough to achieve ignition

before the hypothetical combusting fluid particle is re-entrained. If it fails to ignite before being re-entrained, the combustion in the entire reactor is extinguished.

6.3 CRN Modeling

Two Chemical Reactor Network (CRN) models are developed using the flow field and reaction fields from the detailed CFD models, in an attempt to captures the bulk of the physical processes responsible for flame stability. The single Plug Flow Reactor (PFR) model follows the concept of the hypothetical combusting fluid particle and assumes that only convective transport is responsible for stability. The recirculation is set at 75% and a nominal heat loss of 20% of the energy input is applied uniformly along the boundary. This model matches hydrogen blowout well, reproducing the ignition event and the development of the pool of radicals before re-entrainment. While the single PFR model with the UCSD chemical mechanism does predict the blowout temperature across the full range of methane/hydrogen fuel blends it fails to adequately predict the blowout equivalence ratio for fuels with high methane concentrations.

A two PFR model is subsequently developed in which the core jet region (of constant mass flow) exchanges mass with the recirculation region through diffusive transport. Entrainment of flow by jet action is confined entirely to the recirculation region, represented by the exhaust of the recirculation PFR being convectively re-entrained at its entrance. The turbulent diffusive transport is defined by a turbulent diffusion coefficient taken from the CFD models along the boundary of the core jet region. A length scale appropriate to the CRN is used, which gives an equivalent diffusive velocity. Equal and opposite mass flows are then assigned between the core and recirculation regions. Heat loss is applied along the boundary of the reactor. This is a more realistic spatial treatment of heat loss than in the single PFR model. A grid of 92 PSRs is determined to be a grid independent solution for the range of H_2/CH_4 fuel blends investigated here. The two PFR model performs about as well in

predicting blowout for hydrogen in the JSR and shows significant improvement over the single PFR model in both following the experimental data approaching blowout and predicting the blowout condition for methane. In fact the two PFR model shows good agreement with both equivalence ratio and temperature at blowout across the full range of H_2/CH_4 blends.

Regardless of the chemical mechanism applied, or whether we consider transport by convection only as in the single PFR model, or transport by both convection and diffusion as in the two PFR model, the story regarding the onset of blowout remains the same and is consistent with that given by CFD as well: the key to the stable operation of the reactor is the ignition event in the recirculation zone, resulting in the development of the radical pool. For pure hydrogen combustion as the fuel flow rate is reduced and the reactor moves towards blowout the destruction of the fuel slows and spreads, and the development of the radical pool moves further around the recirculation zone. The radical pool must develop (i.e. ignition must occur) before re-entrainment or the reactor will extinguish. For methane we similarly see the destruction of methane spread, and the net production of CO, and subsequently the net production of OH move further around the recirculation zone until the re-entrainment of radicals can no longer sustain the combustion. For methane, transport of the CO and radicals through turbulent diffusion appears to be a controlling process in this ignition event. The ignition event for hydrogen, on the other hand, is affected very little by the inclusion of diffusive transport of the radicals. This is most likely due to the fact that the breakdown of hydrogen directly produces an H radical that feeds the chain propagating reaction, however the direct breakdown of methane has no such feedback. It is only in the destruction of methane intermediates that the H radical needed to feed the chain propagating reaction is produced.

BIBLIOGRAPHY

[1] J. P. Longwell and M. A. Weiss, "High Temperature Reaction Rates in Hydrocarbon Combustion," *Industrial Engineering and Chemistry*, vol. 47, no. 8, pp. 1634–1643, 1955.

[2] M. A. Weiss, R. J. Lang, and J. P. Longwell, "Combustion Rates in Spherical Reactors: Effects of Inlet Temperature and Fuel Type," *Industrial and Engineering Chemistry*, vol. 50, no. 2, pp. 257–264, 1958.

[3] K. B. Fackler, *A Study of Pollutant Formation from the Lean Premixed Combustion of Gaseous Fuel Alternatives to Natural Gas*. PhD thesis, University of Washington, 2011.

[4] R. B. Barat, "Jet-Stirred Combustor Behavior Near Blowout: Observations and Implications," *Combustion Science and Technology*, vol. 84, no. 1-6, pp. 187–197, 1992.

[5] S. Nair and T. Lieuwen, "Acoustic Detection of Blowout in Premixed Flames," *Journal of Propulsion And Power*, vol. 21, pp. 32–39, January-February 2005.

[6] T. M. Muruganandam and J. M. Seitzman, "Characterization of Extinction Events Near Blowout in Swirl-Dump Combustors," in *41st AIAA/ASME/SAE/ASEE Joint Propulsion Conference and Exhibit*, no. AIAA 2005-4331, July 2005.

[7] I. Glassman and R. A. Yetter, *Combustion*. Academic Press, fourth ed., 2008.

[8] J. P. Longwell, E. E. Frost, and M. A. Weiss, "Flame Stability in Bluff Body Recirculation Zones," *Industrial and Engineering Chemistry*, vol. 45, no. 8, pp. 1629–1633, 1953.

[9] G. E. Broman and E. E. Zukoski, "Experimental Investigation of Flame Stabilization in a Deflected Jet," *Proceddings of the Combustion Institute*, vol. 8, no. 1, pp. 944–956, 1961.

[10] E. E. Zukoski and F. E. Marble, *Combustion Research and Reviews*, p. 167. London, Butterworths Scientific Publication, 1955. North Atlantic Treaty Organization.

[11] S. Yamaguchi, N. Ohiqa, and T. Hasegawa, "Structure and Blow-off Mechanism of Rod-Stabilized Premixed Flame," *Combustion and Flame*, vol. 62, pp. 31–41, 1985.

[12] S. J. Shanbhogue, S. Hussain, and T. Lieuwen, "Lean Blowoff of Bluff Body Stabilized Flames: Scaling and Dynamics," *Progress in Energy and Combustion Science*, vol. 35, pp. 98–120, 2009.

[13] S. Hoffman, P. Habisreuther, and B. Lenze, "Development and Assesment of Correlations for Predicting Stability Limits of Swirling Flames," *Chemical Engineering and Processing*, vol. 33, pp. 393–400, 1994.

[14] Q. Zhang, D. R. Noble, A. Meyers, K. Xu, and T. Lieuwen, "Characterization of Fuel Composition Effects in $H_2/CO/CH_4$ Mixtures Upon Lean Blowout," in *Proceedings of ASME/IGTI Turbo Expo 2005*, no. GT2005-68907, 2005.

[15] Q. Zhang, *Lean Blowoff Characteristics of Swirling $H_2/CO/CH_4$ Flames*. PhD thesis, Georgia Institute of Technology, 2008.

[16] D. R. Noble, Q. Zhang, A. Shareef, J. Tootle, A. Meyers, and T. Lieuwen, "Syngas Mixture Composition Effects Upon Flashback and Blowout," in *Proceedings of the ASME Turbo Expo 2006*, no. GT2006-90470.

[17] A. Akbari, *Combustion behavior associated with alternative fuels in lean premixed, high-swirl stabilized distributed reactions*. PhD thesis, University of California, Irvine, 2013.

[18] S. L. Bragg, "Application of Reaction Rate Theory to Combustion Chamber Analysis," *Aeronautical Research Council Pub. ARC 16170*, pp. 1629–1633, 1953.

[19] G. J. Sturgess, "Combustor LBO Design Model Evaluation: Final Report," Tech. Rep. FR-23400, Pratt & Whitney, May 1995.

[20] S. R. Turns, *An Introduction to Combustion*. McGraw Hill, 2000.

[21] J. Swithenbank, I. Poll, M. Vincent, and D. Wright, "Combustion Design Fundamentals," *Symposium (International) on Combustion*, vol. 14, no. 1, pp. 627 – 638, 1973.

[22] L. A. Vulis, *Thermal Regimes of Combustion*. McGraw-Hill Book Company, Inc, 1961.

[23] G. Sturgess and D. Shouse, "A Hybrid Model for Calculating Lean Blowouts in Practical Combustors," *AIAA Paper No. 96-3125*, 1996.

[24] Reaction Design, San Diego, *Chemkin-MFC 4.5*, 2010.

[25] J. Nenniger, A. Kridiotis, J. Chomiak, J. Longwell, and A. Sarofim, "Characterization of a Toroidal Well Stirred Reactor," *Symposium (International) on Combustion*, vol. 20, no. 1, pp. 473–479, 1985.

[26] P. Strakey, T. Sidwell, and J. Ontko, "Investigation of the Effects of Hydrogen Addition on Lean Extinction in a Swirl Stabilized Combustor," *Proceedings of the Combustion Institute*, vol. 31, no. 2, pp. 3173 – 3180, 2007.

[27] J. P. Longwell and E. Bar-Ziv, "Modeling of Inhomogeneities in the Toroidal Jet-Stirred Reactor," *Combustion and Flame*, vol. 78, no. 1, pp. 99 – 119, 1989.

[28] J. E. Broadwell and A. E. Lutz, "A Turbulent Jet Chemical Reaction Model: NO_x Production in Jet Flames," *Combustion and Flame*, vol. 114, no. 3-4, pp. 319 – 335, 1998.

[29] I. V. Novosselov, P. C. Malte, S. Yuan, R. Srinivasan, and J. C. Y. Lee, "Chemical Reactor Network Application to Emissions Prediction for Industrial DLE Gas Turbine," in *ASME Turbo Expo 2006: Power for Land, Sea and Air*, no. GT2006-90282, 2006.

[30] R. F. D. Monaghan, R. Tahir, A. Cuoci, G. Bourque, M. Furi, R. L. Gordon, T. Faravelli, A. Frassoldati, , and H. J. Curran, "Detailed Multi-dimensional Study of Pollutant Formation in a Methane Diffusion Flame," *Energy Fuels*, vol. 26, pp. 1598–1611, 2012.

[31] C. A. B. Jr and R. B. Barat, "Simulation of a Toroidal Jet-Stirred Combustor using a Partially Stirred Reactor Model with Detailed Kinetic Mechanisms," *Combustion and Flame*, vol. 135, no. 3, pp. 249 – 259, 2003.

[32] J. Li, Z. Zhao, A. Kazakov, M. Chaos, F. L. Dryer, and J. James J. Scire, "A Comprehensive Mechanism for CO, CH_2O, CH_3OH," *International Journal of Chemical Kinetics*, vol. 39, pp. 109–136, 2007.

[33] G. P. Smith, D. M. Golden, M. Frenklach, N. W. Moriarty, B. Eiteneer, M. Goldenberg, C. T. Bowman, R. K. Hanson, S. Song, W. C. G. Jr., V. V. Lissianski, and Z. Qin, "GRI-Mech 3.0." http://www.me.berkeley.edu/gri-mech/.

[34] M. Petrova and F. A. Williams, "A Small Detailed Chemical-Kinetic Mechanism for Hydrocarbon Combustion," *Combustion and Flame*, vol. 144, pp. 526–544, 2006.

[35] H. Wang, X. You, A. V. Joshi, S. G. Davis, A. Laskin, F. Egolfopoulos, and C. K. Law, "USC Mech Version II: High Temperature Combustion Reaction Model of H2/CO/C1-C4 Compounds," May 2007.

[36] M. Frenklach, H. Wang, and M. J. Rabinowitz, "Optimization and Analysis of Large Chemical Kinetic Mechanisms Using The Solution Mapping Method - Combustion of Methane," *Progress in Energy and Combustion Science*, vol. 18, pp. 47–73, 1992.

[37] "Chemical-Kinetic Mechanisms for Combustion Applications." San Diego Mechanism web page, Mechanical and Aerospace Engineering (Combustion Research), University of California at San Diego. http://combustion.ucsd.edu.

[38] Z. Qin, V. V. Lissianski, H. Yang, W. C. Gardiner, and S. G. Davis, "Combustion Chemistry of Propane: A Case Study of Detailed Reaction Mechanism Optimization," *Proceedings of the Combustion Institute*, vol. 28, pp. 1663–1669, 2000.

[39] S. G. Davis, A. V. Joshi, H. Wang, and F. Egolfopoulos, "An Optimized Kinetic Model of H_2/CO Combustion," *Proceedings of the Combustion Institute*, vol. 30, pp. 1283–1292, 2005.

[40] H. Wang and M. Frenklach, "A Detailed Kinetic Study of Aromatics Formation in Laminar Premixed Acetylene and Ethylene Flames," *Combustion and Flame*, vol. 110, pp. 173–221, 1997.

[41] S. G. Davis, C. K. Law, and H. Wang, "Propene Pyrolysis and Oxidation Kinetics in a Flow Reactor and Laminar Flames," *Combustion and Flame*, vol. 119, pp. 375–399, 1999.

[42] A. Laskin, H. Wang, and C. K. Law, "Detailed Kinetic Modeling of 1, 3-Butadiene Oxidation at High Temperatures," *International Journal of Chemical Kinetics*, vol. 32, no. 10, pp. 589–614, 2000.

[43] J. Li, Z. Zhao, A. Kazakov, and F. L. Dryer, "An Updated Comprehensive Kinetic Model of Hydrogen Combustion," *International Journal of Chemical Kinetics*, vol. 36, no. 10, pp. 566–575, 2004.

[44] Y. Kochar, T. Lieuwen, and J. Seitzman, "Laminar Flame Speeds of C1-C3 Alkanes at Elevated Pressure and Temperature with Dilution," *6th US National Combustion Meeting*, no. 21H3, 2009.

[45] J. M. Bergthorson and P. E. Dimotakis, "Premixed laminar C1-C2 stagnation flames: Experiments and Simulations with Detailed Thermochemistry Models," *Proceedings of the Combustion Institute*, vol. 31, pp. 1139–1147, 2007.

[46] M. O. Conaire, H. J. Curran, J. M. Simmie, W. J. Pitz, and C. K. Westbrook, "A Comprehensive Modeling Study of Hydrogen Oxidation," *International Journal of Chemical Kinetics*, vol. 36, no. 11, pp. 603–622, 2004.

[47] T. Weydahl, M. Poyyapakkam, M. Seljeskog, and N. E. L. Haugen, "Assesment of Existing H_2/O_2 Chemical Reaction Mechanisms at Reheat Gas Turbine Conditions," *International Journal of Hydrogen Energy*, vol. 36, pp. 12025–12034, 2011.

[48] A. S. Tomlin, T. Turanyi, and M. J. Pilling, *Comprehensive Chemical Kinetics: Low-Temperature Combustion and Autoignition*, vol. 35, ch. 4: Mathematical Tools for the Construction, Investigation and Reduction of Combustion Mechanisms. Elsevier Science, 1997.

[49] H. Wang and M. Frenklach, "Detailed Reduction of Reaction Mechanisms for Flame Modeling," *Combustion and Flame*, vol. 87, pp. 365–370, 1991.

[50] D. Nicol, *A Chemical Kinetic and Numerical Study of NOx and Pollutant Formation in Low-Emission Combustion.* PhD thesis, University of Washington, 1995.

[51] C. K. Law, C. J. Sung, H. Wang, and T. F. Lu, "Development of Comprehensive Detailed and Reduced Reaction Mechanisms for Combustion Modeling," *AIAA Journal*, vol. 41, no. 9, pp. 1629–1646, 2003.

[52] T. F. Lu and C. K. Law, "A Directed Relation Graph Method for Mechanism Reduction," *Proceedings of the Combustion Institute*, vol. 30, pp. 1333–1341, 2005.

[53] G. Paczko, P. M. Lefdal, and N. Peters, "Reduced Reaction Schemes for Methane, Methanol, and Propane Flames," *Twenty-first Symposium (International) on Combustion/The Combustion Institute*, pp. 739–748, 1986.

[54] N. Peters and F. A. Williams, "The Asymptotic Structure of Methane-Air Flames," *Combustion and Flame*, vol. 68, pp. 185–207, 1987.

[55] A. N. Yannacopoulos, A. S. Tomlin, J. Brindley, J. H. Merkin, and M. Pilling, "Error Propagation in Approximations to Reaction-Diffusion-Advection Equations," *Physics Letters A*, vol. 223, pp. 82–90, 1996.

[56] T. Lu and C. K. Law, "A Criterion Based on Computational Singular Perturbation for the Identification of Quasi Steady State Species: A Reduced Mechanism for Methane Oxidation with NO Chemistry," *Combustion and Flame*, vol. 154, pp. 761–774, 2008.

[57] U. Maas and S. B. Pope, "Simplifying Chemical Kinetics: Intrinsic Low-Dimensional Manifolds in Composition Space," *Combustion and Flame*, vol. 88, pp. 239–264, 1992.

[58] O. Gicquel, N. Darabiha, and D. Thevenin, "Laminar Premixed Hydrogen/Air Counterflow Flame Simulations using Flame Prolongation of ILDM with Differential Diffusion," *Proceedings of the Combustion Institute*, vol. 28, pp. 1901–1908, 2000.

[59] J. A. V. Oijen and L. D. Goey, "Modeling of Premixed Laminar Flames using Flamelet-Generated Manifolds," *Combustion Science and Technology*, vol. 161, pp. 113–137, 2000.

[60] A. Belcadi, M. Assou, E. Affad, and E. Chatri, "Construction of a Reduced Mechanism for Modelling Premixed Combustion of Methane-Air," *Combustion Theory and Modelling*, vol. 11, no. 4, pp. 603–613, 2007.

[61] C. J. Sung, C. K. Law, and J. Y. Shen, "Augmented Reduced Mechanism for NO Emission in Methane Oxidation," *Combustion and Flame*, vol. 125, pp. 906–919, 2001.

[62] R. B. Edelman and O. F. Fortune, "A Quasi-Global Chemical Kinetic Model for the Finite Rate Combustion of Hydrocarbon Fuels with Application to Turbulent Burning and Mixing in Hypersonic Engines and Nozzles," *AIAA Paper*, no. 86, 1969.

[63] P. Gokulakrishnan, S. Kwon, A. Hamer, M. Klassen, and R. Roby, "Reduced Kinetic Mechanism for Reactive Flow Simulation of Syngas/Methane Combustion at Gas Turbine Conditions," in *Proceedings of the ASME Turbo Expo*, (Barcelona, Spain), pp. 513–521, 2006.

[64] D. J. Hautman, F. L. Dryer, K. P. Schug, and I. Glassman, "A Multiple-Step Overall Kinetic Mechanism for the Oxidation of Hydrocarbons," *Combustion Science and Technology*, vol. 25, pp. 219–235, 1981.

[65] J. Duterque, R. Borghi, and H. Tichtinsky, "Study of Quasi-Global Schemes for Hydrocarbon Combustion," *Combustion Science and Technology*, vol. 26, pp. 1–15, 1981.

[66] W. P. Jones and R. P. Lindstedt, "Global Reaction Schemes for Hydrocarbon Combustion," *Combustion and Flame*, vol. 73, pp. 233–249, 1988.

[67] D. G., P. C. Malte, A. J. Hamer, R. J. Roby, and R. C. Steele, "Development of a Five-Step Global Methane Oxidation-NO Formation Mechanism for Lean-Premixed Gas Turbine Combustion," *Journal of Engineering for Gas Turbines and Power*, vol. 121, no. 2, pp. 272–280, 1999.

[68] I. V. Novosselov and P. C. Malte, "Development and Application of an Eight-Step Global Mechanism for CFD and CRN Simulations of Lean-Premixed Combustors," *Journal of Engineering for Gas Turbines and Power*, p. 021502, 2008.

[69] B. Jiang, D. Ingram, D. Causon, and R. Saunders, "A global simulation method for obtaining reduced reaction mechanisms for use in reactive blast wave flows," *Shock Waves*, vol. 5, pp. 81–88, 1995.

[70] M. Molnar and C. J. Marek, "Reduced Equations for Calculating the Combustion Rates of Jet-A and Methane Fuel," Tech. Rep. TM-212702, NASA, 2003.

[71] M. Lamnaouer, R. C. Ryder, A. Brankovic, and E. L. Petersen, "Reduced Combustion Time Model for Methane Gas in Gas Turbine Flow Fields," *Journal of Natural Gas Chemistry*, vol. 18, pp. 145–155, 2009.

[72] J. F. Griffiths, "Reduced Kinetic Models and Their Application to Practical Combustion Systems," *Progress in Energy Combustion Science*, vol. 21, pp. 25–107, 1995.

[73] T. Lu and C. K. Law, "Toward Accommodating Realistic Fuel Chemistry in Large-Scale Computations," *Progress in Energy and Combustion Science*, vol. 35, pp. 192–215, 2009.

[74] T. Lu and C. K. Law, "On the Applicability of Directed Relation Graphs to the Reduction of Reaction Mechanisms," *Combustion and Flame*, vol. 146, pp. 472–483, 2006.

[75] T. F. Lu and C. K. Law, "Systematic Approach To Obtain Analytic Solutions of Quasi Steady State Species in Reduced Mechanisms," *Journal of Physical Chemistry*, vol. 110, pp. 13202–13208, 2006.

[76] W. Stein *et al.*, *Sage Mathematics Software (Version 4.5)*. The Sage Development Team, 2010. `http://www.sagemath.org`.

[77] X. L. Zheng, T. F. Lu, and C. K. Law, "Experimental Counterflow Ignition Temperatures and Reaction Mechanisms of 1,3-Butadiene," *Proceedings of the Combustion Institute*, vol. 31, no. 1, pp. 367–375, 2007.

[78] "Skeletal Mechanism for the Reactive Flow Simulation of Methane Combustion." University of Washington, Mechanical Engineering, Laboratory for Energy and Environmental Combustion. http://faculty.washington.edu/malte/pubs/reports/SkeletalMethane.inp.

[79] J. C. Kramlich and P. C. Malte, "Modeling and Measurement of Sample Probe Effects on Pollutant Gases Drawn from Flame Zones," *Combustion Science and Technology*, vol. 18, no. 3-4, pp. 91–104, 1978.

[80] J. C. Y. Lee, *Reduction of NO_x Emission for Lean Prevaporized-Premixed Combustors*. PhD thesis, University of Washington, 2000.

[81] R. B. Dean and W. J. Dixon, "Simplified Statistics for Small Number of Observations," *Analytical Chemistry*, vol. 23, no. 4, pp. 636–638, 1951.

[82] A. H. Lefebvre and D. R. Ballal, *Gas Turbine Combustion: Alternative Fuels and Emissions*. Taylor & Francis Group, 3rd ed., 2010.

[83] L. Rayleigh, *The Theory of Sound*, vol. Vol. 2. New York: Dover, 1945.

[84] S. Ducruix, T. Schuller, D. Durox, and S. Candel, "Combustion Dynamics and Instabilities: Elementary Coupling and Driving Mechanisms," *Journal of Propulsion and Power*, vol. 19, no. 5, pp. 722–734, 2003.

[85] ANSYS, Inc., *ANSYS Fluent, Academic Research, Release 13.0*, 2010.

[86] J. Nanduri, D. R. Parsons, S. L. Yilmaz, I. B. Celik, and P. A. Strakey, "Assessment of RANS-Based Turbulent Combustion Models for Prediction of Emissions from Lean Premixed Combustion of Methane," *Combustion Science and Technology*, vol. 182, no. 7, pp. 794–821, 2010.

[87] K. B. Fackler, M. F. Karalus, I. V. Novosselov, J. C. Kramlich, and P. C. Malte, "Experimental and Numerical Study of NO_x Formation From the Lean Premixed Combustion of CH_4 Mixed with CO_2 and N_2," *Journal of Engineering for Gas Turbines and Power*, vol. 133, 2011.

[88] B. F. Magnussen, "On the Structure of Turbulence and a Generalized Eddy Dissipation Concept for Chemical Reaction in Turbulent Flow," in *19th American Institute of Aeronatuics and Astronautics Aerospace Science Meeting*, Jan 12-15, 1981. St. Louis Missouri.

[89] B. F. Magnussen, "Modeling NO_x and Soot Formation by the Eddy Dissipation Concept," in *International Flame Research Foundation, First Topic Oriented Technical Meeting*, Oct 17-19, 1989. Amsterdam, The Netherlands.

[90] I. R. Gran and B. F. Magnussen, "A Numerical Study of a Bluff-Body Stabilized Diffusion Flame. Part 2. Influence of Combustion Modeling and Finite Rate Chemistry," *Combustion Science and Technology*, vol. 119, pp. 191–217, 1996.

[91] I. S. Ertesvag and B. Magnussen, "The Eddy Dissipation Turbulence Energy Cascade Model," *Combustion Science and Technology*, vol. 159, pp. 213–235, 2000.

[92] B. F. Magnussen, "The Eddy Dissipation Concept a Bridge between Science and Technology," in *ECCOSMAS Thematic Conference on Computational Combustion*, June 21-24, 2005. Lisbon, Portugal.

[93] L. Kjaldman, A. Brink, and M. Hupa, "Micro Mixing Time in the Eddy Dissipation Concept," *Combustion Science and Technology*, vol. 154, pp. 207–227, 2000.

[94] N. Peters, *Turbulent Combustion*. Cambridge University Press, 2000.

[95] C. K. Law, *Combustion Physics*. Cambridge University Press, 2006.

[96] M. M. Holton, "Autoignition delay time measurements for natural gas fuel components and their mixtures," Master's thesis, University of Maryland, College Park, 2008.

[97] J. C. Y. Lee, *Reduction of NOx Emission for Lean Prevaporized-Premixed Combustors*. PhD thesis, University of Washington, 2000.

[98] W. H. McAdams, *Heat Transmission*. New York, NY: McGraw-Hill, Inc, 3rd ed., 1954.

[99] V. S. Arpaci, *Conduction Heat Transfer*. Addison-Wesley Publshing Company, 1966.

[100] Incropera, DeWitt, Berman, and Lavine, *Introduction to Heat Transfer*. John Wiley & Sons, fifth ed., 2007.

Appendix A

PARAMETER SPACE FOR SKELETAL MECHANISM DEVELOPMENT

Table A.1: Parameter space for generation of PSR database on methane oxidation. Residence times given in ms, Pressure in atm and Temperature in (K). Blowout residence times greater than the maximum residence time considered (3ms) precluded the inclusion of a PSR under those conditions.

ϕ		0.4		0.5		0.6		0.7		0.8		0.9		1.0	
P	T_{in}	τ_{blow}	τ_{max}	τ_{blow}	τ_{max}	τ_{blow}	τ_{max}	τ_{blow}	τ_{max}	τ_{blow}	τ_{max}	τ_{blow}	τ_{max}	τ_{blow}	τ_{max}
1	300	-	-	1.668	3.000	0.393	3.000	0.179	3.000	0.113	3.000	0.087	3.000	0.079	3.000
1	500	-	-	0.728	3.000	0.237	3.000	0.125	3.000	0.085	3.000	0.068	3.000	0.063	3.000
5	500	1.958	3.000	0.370	3.000	0.152	3.000	0.089	3.000	0.064	3.000	0.054	3.000	0.050	3.000
10	600	5.925	3.000	0.626	3.000	0.124	3.000	0.049	3.000	0.028	3.000	0.021	3.000	0.020	3.000
15	700	2.296	3.000	0.359	3.000	0.080	3.000	0.031	3.000	0.018	3.000	0.013	3.000	0.012	3.000
20	750	0.886	3.000	0.173	3.000	0.047	3.000	0.020	3.000	0.011	3.000	0.009	3.000	0.008	3.000
25	800	0.553	3.000	0.121	3.000	0.036	3.000	0.016	3.000	0.009	3.000	0.007	3.000	0.007	3.000
30	840	0.347	3.000	0.084	3.000	0.027	3.000	0.012	3.000	0.007	3.000	0.006	3.000	0.005	3.000

Appendix B

THERMOCOUPLE HEAT TRANSFER CORRECTION, JSR THERMAL RESPONSE, AND REACTOR HEAT LOSS

B.1 Thermocouple Heat Transfer Correction

An R-type thermocouple (TC) has been used for all temperature measurements in this work, but as noted by Lee [97] the measured TC temperature is less than the actual gas temperature due to the effects of heat transfer. Since the experimental setup in this work closely follows that of Fackler, the assumptions detailed by Fackler [3] are also assumed here. We neglect catalytic effects because of the ceramic coating on the thermocouple bead as well as conduction along the thermocouple wire because of its small diameter. As a result conservation of energy applied at the surface of the thermocouple bead reduces simply to Equation B.1.

$$Q_{convection} = Q_{radiation} \tag{B.1}$$

B.1.1 Convection

The convective term in Equation B.1 is given by Equation B.2 where:

- A is the surface area of the TC bead, which is approximated as a sphere with a 1 mm diameter.
- h is the convective heat transfer coefficient
- T_{gas} is the actual gas temperature

- T is the measured TC temperature

$$Q_{convection} = A * h * (T_{gas} - T) \tag{B.2}$$

The convective heat transfer coefficient, h is given by Equation B.3, where:

- Nu_D is the Nusselt number for flow around a sphere
- k is the thermal conductivity of air at the combustion temperature T_{gas}
- D is the diameter of the diameter of the TC bead (1 mm)

$$h = Nu_D * k/D \tag{B.3}$$

The Nusselt number correlation is given by Equation B.4 for flow around a sphere at Reynolds numbers between 17 and 70,000 [98], where:

- V is the bulk flow velocity around the thermocouple taken from CFD simulations. It is 30 m/s at the nominal temperature measurement location.
- D is the diameter of the TC ($1.0e-3$ m)
- ν is the viscosity of the air at the combustion gas temperature, T_{gas}

$$Nu_D = 0.37 * \left(\frac{V * D}{nu}\right) * *0.6 \tag{B.4}$$

B.1.2 Radiation

The TC bead is assumed to be a small object in a large cavity at constant temperature, thus the radiation exchange between the two is given by Equation B.5, where

- σ is the Stefan-Boltzman constant ($5.67E-8$ W/m^2-K^4)

- ϵ is the emissivity of the TC tip, measured by Steele [80] to be 0.258.
- T_{wall} is the temperature of the JSR wall.

$$Q_{radiation} = \sigma \varepsilon A(T^4 - T_{wall}^4). \tag{B.5}$$

We must now determine T_{wall}. As noted in by Fackler [3], the average wall temperature predicted by the 3D CFD model can be as much as 150 K greater than that predicted by the 2D model at the nominal operating condition. He also showed the average wall temperature predicted by the 3D simulation to agree well with measurements taken with an optical pyrometer at the nominal operating condition. Because we lacked the ability to collect these measurements near blowout and we did not run 3D CFD near blowout, we must rely on the 2D CFD simulations for T_{wall}. We note that at the nominal operating condition the maximum wall temperature value in the 2D simulation is approximately equal to the average value in the 3D, therefore this is taken as the T_{wall} for the radiation calculations.

For completeness, Figure B.1 shows the effect of T_{wall} on the corrected gas temperature at blowout for both hydrogen and methane. The wall temperature range is taken from the 2D CFD simulations at blowout with reactions in the boundary layer: the minimum being the area weighted average of the reactor walls and the maximum being the maximum on the reactor walls. The resulting correction ranges from 21 to 34 K for hydrogen and 43 to 65 K for methane.

B.2 JSR Thermal Response

To determine the thermal time response of the ceramic reactor we consider a classic 1-D time unsteady conduction problem (see Arpaci [99] for more details). Let's take a plate of thickness L, insulated at $x = 0$ and at an initial temperature T_o, and then apply a new temperature T_∞ at $x = L$ and $t = 0$. If we let $\theta = T - T_\infty$, and $\alpha =$

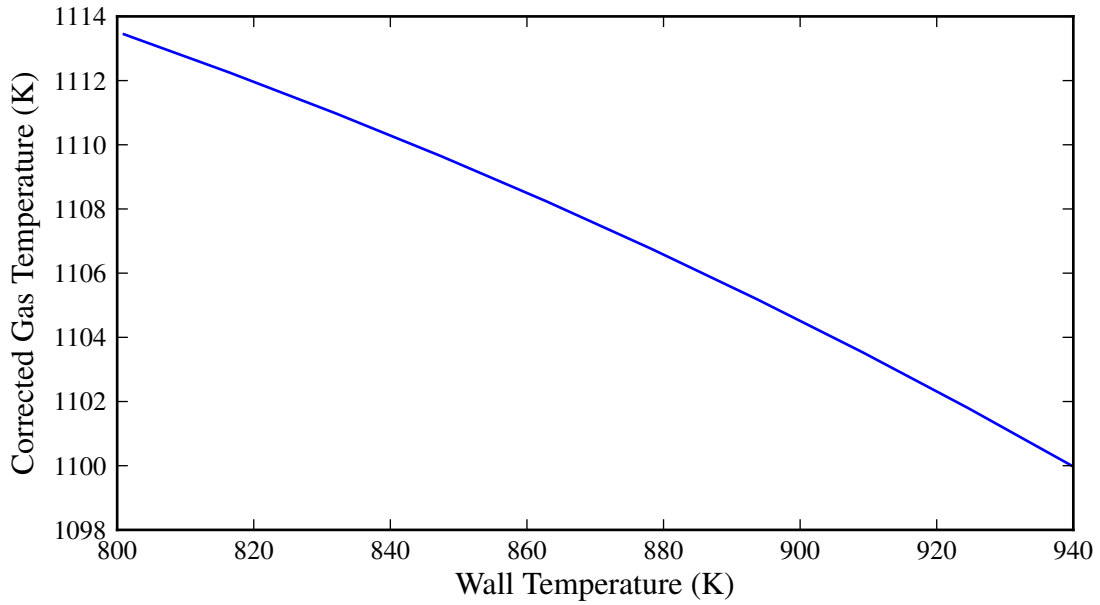

(a) Hydrogen

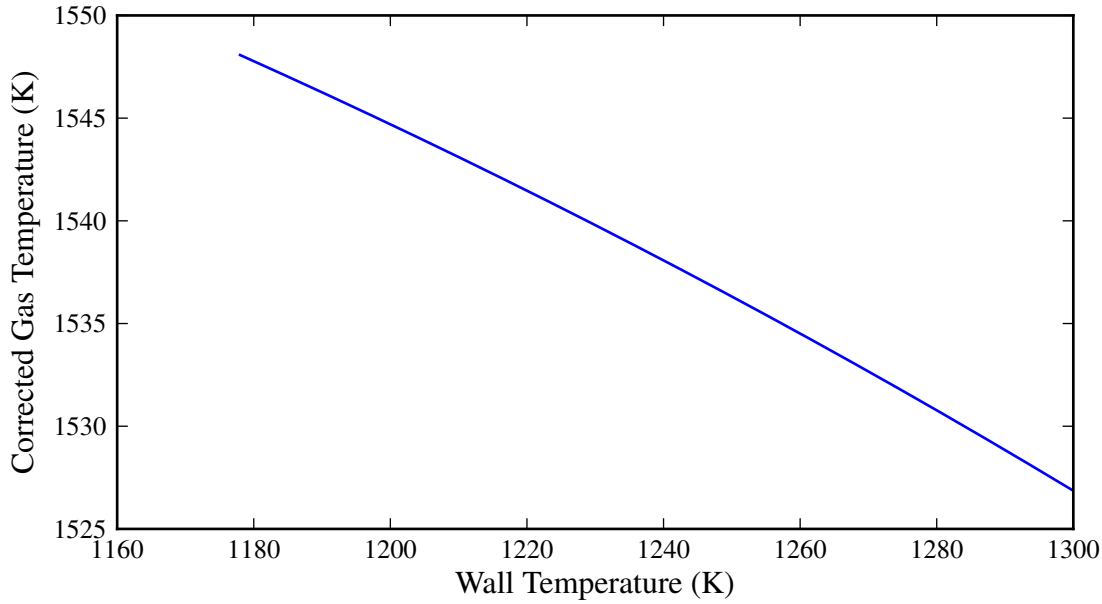

(b) Methane

Figure B.1: Corrected gas temperature at blowout as a function of wall temperature. The measured blowout temperatures for hydrogen and methane are 1082 and 1482 K respectively.

Table B.1: Material properties of the reactor ceramic.

Specific Heat (C_p)	880 J/kg-K
Density (ρ)	2710 kg/m^3
Thermal Conductivity @750K	3.04 W/m-K

thermal diffusivity, then the governing equation and boundary conditions are given as

$$\frac{\partial\theta}{\partial t} = \alpha\frac{\partial^2\theta}{\partial x^2}, \qquad \theta(x,0) = \theta_o = T_o - T_\infty$$
$$\frac{\partial\theta(0,t)}{\partial x} = 0, \quad \theta(L,t) = 0. \tag{B.6}$$

Solution by separation of variables leads to the following

$$\theta(x,t) = \sum_{n=0}^{\infty} a_n e^{-\alpha\lambda_n^2 t} cos\lambda_n x \tag{B.7}$$

where

$$\lambda_n L = (2n+1)\pi/2, \quad n = 0, 1, 2, 3....$$

We see that we have exponential decay of temperature in time. We can therefore rewrite this as $e^{-t/\tau}$ where τ is the exponential time constant. The leading order exponential time constant is equal to

$$\tau_o = \frac{4L^2}{\alpha\pi^2}. \tag{B.8}$$

Properties of the ceramic (94% Alumina) are given in Table B.1. The density and thermal conductivity are taken from the GREENCAST -94 PLUS product data sheet. GREENCAST did not provide a specific heat so it was taken from a product data sheet from another manufacturer of Alumina, Accuratas.

The nominal thickness of the ceramic is taken to be 4.5 cm. This gives a leading order exponential time constant of 10 minutes.

B.3 Reactor Heat Loss

Previous analysis of the JSR at the nominal operating condition of 1800 K showed the heat loss to be about 20% of the reactor loading based on the lower heating value of the fuel for both pure methane and pure hydrogen. This agreed well with a simple one-dimensional heat transfer model and what was predicted by the conjugate heat transfer model in the CFD [3].

For blowout in this study we attempt to quantify the heat loss for both methane and hydrogen by all three methods: (1) an overall energy balance (2) a simple one dimensional heat transfer model and (3) CFD.

For the first method, the measured concentrations of O_2, CO, and CO_2 and the (unadjusted) inlet and sampling location temperatures are used. It was determined that the heat loss is about 23% for hydrogen and 17% for methane based on a reactor loading using the higher heating value of the fuel. When the temperatures were adjusted for heat transfer effects the heat loss was determined to be 20% for hydrogen and 12% for methane. This heat loss calculation is very sensitive to the outlet temperature. The value of the outlet temperature however is very sensitive to the wall temperature which is a best guess from CFD (see section above on Thermocouple Heat Transfer Correction).

This overall energy balance does not include unburned fuel in the exhaust which is thought to be substantial. Hydrogen concentration was measured at the nominal sampling location, however the actual amount is thought to be substantially more due to oxidation in the probe. Unburned methane can only be determined from CFD. Including unburned fuel in the calculation causes a further decrease in the percentage of heat loss based on reactor loading. (Using unburned fuel values from CFD at blowout hydrogen heat loss would drop to 16% and methane to 10%).

A simple one-dimensional heat transfer calculation can also be performed near blowout. The calculation follows the same methodology as Fackler [3]. The thermal

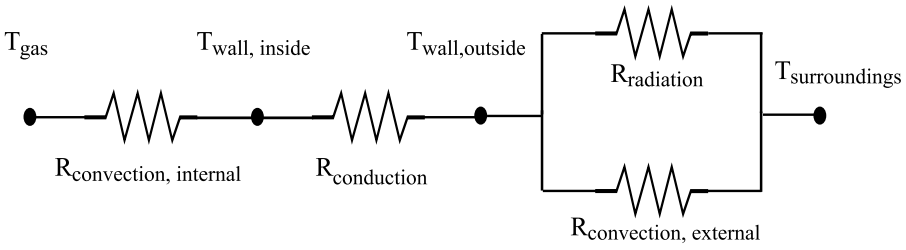

Figure B.2: One dimensional thermal circuit for JSR at blowout.

circuit used in the calculation is shown in Figure B.2. Heat is transferred to the inside wall of the reactor by convection only. The radiation from CO_2 and H_2O is very small due to the small beam length and is therefore neglected in this calculation. The heat convected to the wall is then transferred through the ceramic by conduction. Radiative and convective losses through the exhaust ports are considered negligible due to the small area. Heat is then transferred to the ambient environment by both convection and radiation.

Fackler's [3] measured ambient temperature is used in this calculation. The conductivity of the ceramic is taken to be 2.3 W/m-K. The convective heat transfer coefficient is estimated to be 140 W/m^2-K for Hydrogen and 150 W/m^2-K for methane at blowout using a correlation from Incropera [100] for an impinging round jet. A natural convection heat transfer coefficient for the outside of the reactor is estimated to be 12 W/m$^2 - K$. Finally the ceramic is assumed to have an emissivity of 0.9. The analysis is based on the idea that the reactor volume can be approximated by two concentric spheres whose inner and outer radii result in surface areas equal to the inner and outer heat transfer areas of the JSR. It is estimated from the simple one-dimensional heat transfer calculation that for hydrogen the total heat transfer is 184 W (16% heat loss), and for methane 316 W (17% heat loss). Also, as Fackler found at 1800 K, all modes of heat transfer accounted for in this analysis are of equal importance.

Finally, CFD can be used as well in an attempt to determine the heat loss at blowout. CFD consistently shows 18% heat loss based on a reactor loading using the higher heating value for both hydrogen and methane at blowout.

As a result of this analysis a nominal heat loss is chosen to be 20% of the reactor loading based on the higher heating value of the fuel and varied to as low as 12% when performing the sensitivity analysis on the CRN.

Appendix C

FLUENT USER DEFINED FUNCTION

This is an example of the UDF used to eliminate reaction rates in the boundary layer when using the EDC model. A separate 'source' was needed for each species in the mechanism. The following is for O_2 in hydrogen combustion.

```
#include "udf.h"

/*******************************************************
SET REACTION RATE IN BOUNDARLY LAYER TO ZERO
*******************************************************/

real Re_y(cell_t c, Thread *t)
{ return C_R(c,t)*sqrt(C_K(c,t))*C_WALL_DIST(c,t)/C_MU_L(c,t); }


DEFINE_SOURCE(o2_source,cell,thread,dS,eqn)
{
  real source = 0;            /* Initialize the source term */
  real reactrate, mdot, tau;  /* Variables for calculating reaction rate */
  real time_step;             /* Time_step for calc-tau-edc */
  real c1, c2, cfl_fac;       /* Constants for EDC model */

  int i = 0;                /* Index of species equation */
```

```
  /* Hard Code Model Constants */
  c1      = 2.1377;
  c2      = 0.40825;
  cfl_fac = 0.1;

  if (Re_y(cell,thread) <= (real)200.)
    {
      /* In the boundary layer, calculate the EDC reaction rate */
      tau       = calc_tau_edc(cell, thread, time_step, c2, cfl_fac);
      mdot      = calc_mdot_edc(cell, thread, c1, tau);
      reactrate = mdot*(C_YI_EDC(cell,thread,i)-C_YI(cell,thread,i));
      /*units kg_i/m3-s */

      /* Disable EDC in the boundary layer by setting a source */
      /* term with the opposite effect. */

      source    = -reactrate;
    }
  else
    {
      /* Leave the EDC model alone everywhere else in the domain. */
      source = 0;
    }

  /* C_UDSI(cell,thread,i)=source; */
  return source;
}
```

Appendix D

EXPERIMENTAL RAW DATA

Table D.1: Measured methane profile obtained with the GC under nominal operating conditions (1800K). Total air flow rate is 0.00113 kg/s with an inlet equivalence ratio of 0.71.

Distance from Centerline (mm)	Measured Methane (dry ppm)
0	35400
1	29600
2	3095
3	35

Table D.2: Measured hydrogen (dry ppm) at the nominal sampling location, approaching blowout.

Equivalence Ratio	Measured H_2 (dry ppm)	Uncorrected Temperature [C]	Corrected [K]
0.273	908	856	1147
0.267	1447	840	1129
0.260	2896	820	1107
0.254	6287	796	1080

Table D.3: Raw experimental data for blowout of H_2/CH_4 blends at constant air mass flow rate of 0.001084 kg/s. T_R is the uncorrected temperature measured at the nominal sampling location at blowout; T_C is the corrected temperature at the nominal sampling location; T_P is the measured temperature in the Premixer, just before entering the nozzle; ϕ Input is calculated from the measured fuel and air flow rates; ϕ Exhaust is calculated from the measured gas concentrations at the nominal sampling location; Loading is based on the higher heating value of the fuel; τ is the average residence time in the reactor.

H_2 %	Date	M_{H_2} [kg/s]	M_{CH_4} [kg/s]	T_R [C]	T_C [K]	T_P [C]	ϕ Input	ϕ Exhaust	ϕ Increment	Loading [kW]	τ [ms]
100	10/8/12	8.0898E-06	0	819	1106	279.1	0.2543	0.2682	0.0062	1.1471	4.2159
100	2/10/12	8.0898E-06	0	796	1080	280.3	0.2543	0.2439	0.0062	1.1471	4.3070
100	7/15/11	8.0898E-06	0	805	1090	277.2	0.2543	0.2514	0.0064	1.1471	4.2614
100	9/20/12	7.8936E-06	0	802	1087	277.9	0.2481	0.2510	0.0062	1.1193	4.2915
90	7/28/11	6.73274E-06	5.97683E-06	889	1182	283.3	0.3060	0.2870	0.0175	1.287	4.266
90	8/4/11	6.73274E-06	5.97683E-06	899	1193	282.6	0.3060	0.2930	0.0175	1.287	4.2305
90	10/8/12	6.73274E-06	5.97683E-06	902	1197	283.6	0.3060	0.3051	0.0175	1.287	4.2204
80	10/10/12	5.60059E-06	1.11549E-05	974	1277	289.3	0.3537	0.3387	0.0113	1.414	3.953
80	10/10/12	5.60059E-06	1.11549E-05	982	1287	289.5	0.3537	0.3404	0.0113	1.414	3.9289
80	10/10/12	5.60059E-06	1.11549E-05	976	1280	289	0.3537	0.3524	0.0113	1.414	3.9472
70	10/29/12	4.37027E-06	1.49175E-05	995	1299	292.2	0.3730	0.3760	0.0107	1.448	3.868
70	10/29/12	4.37027E-06	1.49175E-05	983	1284	291.9	0.3730	0.3707	0.0107	1.448	3.9041
70	10/29/12	4.37027E-06	1.49175E-05	996	1300	292	0.3730	0.3746	0.0107	1.448	3.8653
60	10/11/12	3.51085E-06	1.85307E-05	1047	1390	294.7	0.4048	0.4070	0.0110	1.527	3.700
60	10/11/12	3.51085E-06	1.85307E-05	1055	1367	294.6	0.4048	0.4105	0.0110	1.527	3.6784
60	10/15/12	3.42238E-06	1.80133E-05	1019	1323	294	0.3938	0.3896	0.0110	1.486	3.7810

Table D.3: (continued)

H_2 %	Date	M_{H_2} [kg/s]	M_{CH_4} [kg/s]	T_R [C]	T_C [K]	T_P [C]	ϕ Input	ϕ Exhaust	ϕ Increment	Loading [kW]	τ [ms]
60	11/5/12	3.51085E-06	1.85307E-05	1044	1354	295.3	0.4048	0.4051	0.0110	1.527	3.7082
60	11/5/12	3.42238E-06	1.80133E-05	1012	1315	294.5	0.3938	0.3883	0.0110	1.486	3.8009
60	11/5/12	3.42238E-06	1.80133E-05	1009	1311	294.1	0.3938	0.3885	0.0110	1.486	3.8096
50	10/15/12	2.72183E-06	2.17312E-05	1093	1409	297.9	0.4306	0.4341	0.0118	1.593	3.562
50	10/15/12	2.72183E-06	2.17312E-05	1090	1405	297.6	0.4306	0.4306	0.0118	1.593	3.5691
50	10/15/12	2.72183E-06	2.17312E-05	1096	1413	298	0.4306	0.4343	0.0118	1.593	3.5539
40	10/18/12	2.03402E-06	2.43E-05	1111	1427	300	0.4471	0.4470	0.0099	1.6351	3.5030
40	10/18/12	2.03402E-06	2.43E-05	1110	1425	300	0.4471	0.4461	0.0099	1.6351	3.5055
40	10/18/12	2.03402E-06	2.43E-05	1112	1428	300.2	0.4471	0.4469	0.0099	1.6351	3.5005
30	10/25/12	1.44265E-06	2.69E-05	1139	1456	301.1	0.4698	0.4661	0.0108	1.6966	3.4215
30	10/25/12	1.44265E-06	2.69E-05	1142	1460	301.2	0.4698	0.4680	0.0108	1.6966	3.4145
30	10/25/12	1.44265E-06	2.69E-05	1138	1455	300.8	0.4698	0.4656	0.0108	1.6966	3.4239
20	10/22/12	9.43539E-07	2.99E-05	1192	1518	302.8	0.5026	0.5053	0.0088	1.7961	3.2853
20	10/22/12	9.1052E-07	2.89E-05	1167	1486	302.7	0.4938	0.4896	0.0088	1.7330	3.3436
20	10/22/12	9.1052E-07	2.89E-05	1176	1498	303.5	0.4938	0.4985	0.0088	1.7645	3.3234
0	9/24/12	0	3.29E-05	1198	1513	304.3	0.5234	0.5248	0.0080	1.8270	3.2572
0	9/24/12	0	3.34E-05	1219	1540	305	0.5314	0.5395	0.0080	1.8550	3.2100
0	9/24/12	0	3.29E-05	1203	1519	305.1	0.5234	0.5216	0.0080	1.8273	3.2465
0	10/8/12	0	3.29E-05	1216	1536	306.6	0.5234	0.5326	0.0080	1.8273	3.2189

Appendix E

CRN HEAT LOSS STUDY

E.1 Single PFR Model

We performed a sensitivity study in which the heat loss is varied based on the analysis completed in Appendix B. Figure E.1 shows how the results form the single PFR model change for hydrogen when the heat loss is varied from 20% to 15% and Figure E.2 shows how the results from the single PFR model for methane change when the heat loss is varied from 20% to 15% and then to 12% using the UCSD mechanism. The blowout temperature remains constant while the model is stabilized to lower equivalence ratios. Reducing the heat loss in the single PFR model provides worse agreement for hydrogen while for methane a reduction in heat loss to 12% allows the model to follow the data towards blowout much more closely, predicting a blowout equivalence ratio within 2% and a temperature within 25 K. Based on the analysis in Appendix B a heat loss of 20% for hydrogen and 12% for methane are not be consistent with one another.

As shown in Figure E.3, the single PFR model predicts blowout temperature well regardless of the amount of heat loss assumed. The percentage of heat loss only affects the prediction of blowout equivalence ratio. Assuming a 15% heat loss rate brings much better agreement for pure methane and high methane blends. The predicted blowout equivalence ratios for pure methane and pure hydrogen matches experimental values within 7.5% (from 18%), and 10% (from 4%) respectively.

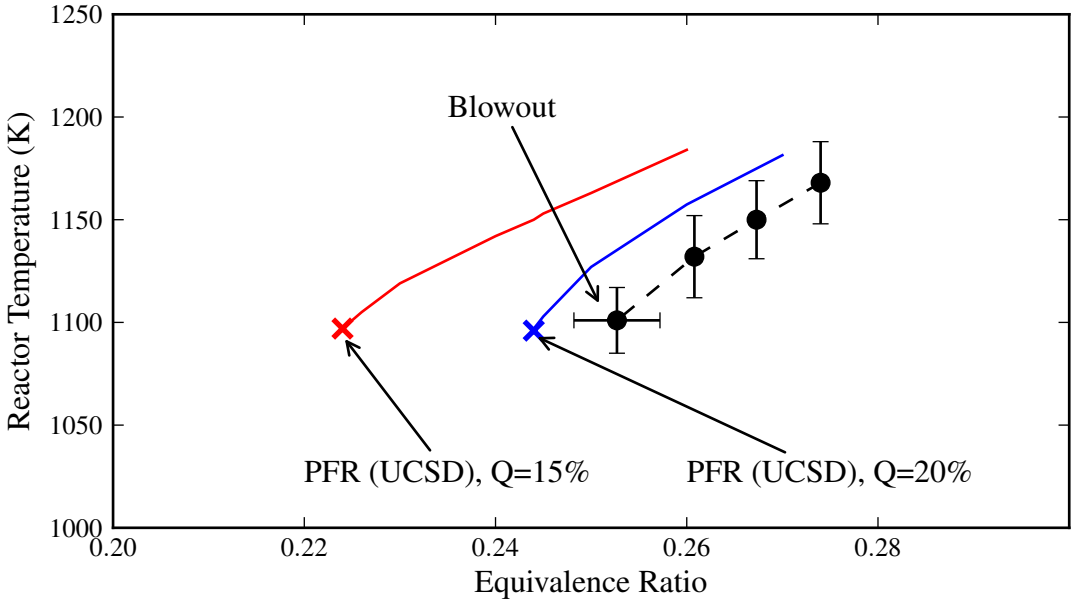

Figure E.1: Effect of varying heat loss on the single PFR model for hydrogen.

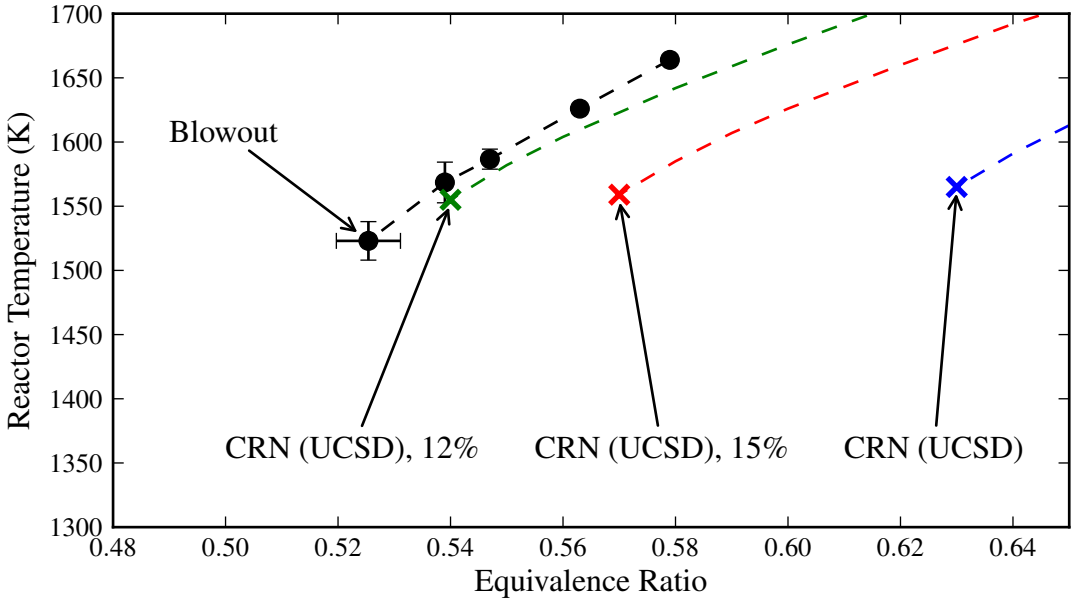

Figure E.2: Effect of varying heat loss on the single PFR model for methane.

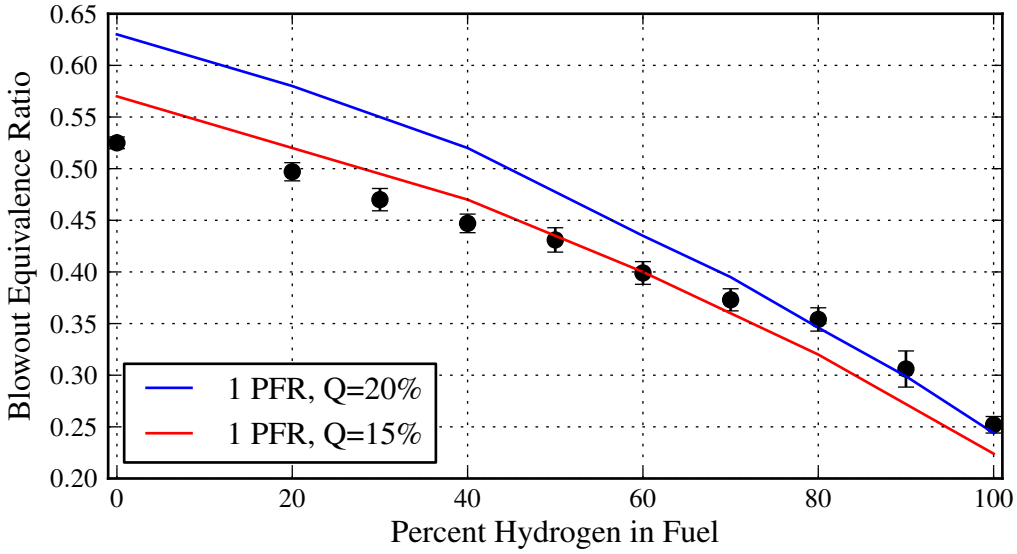

(a) Equivalence Ratio

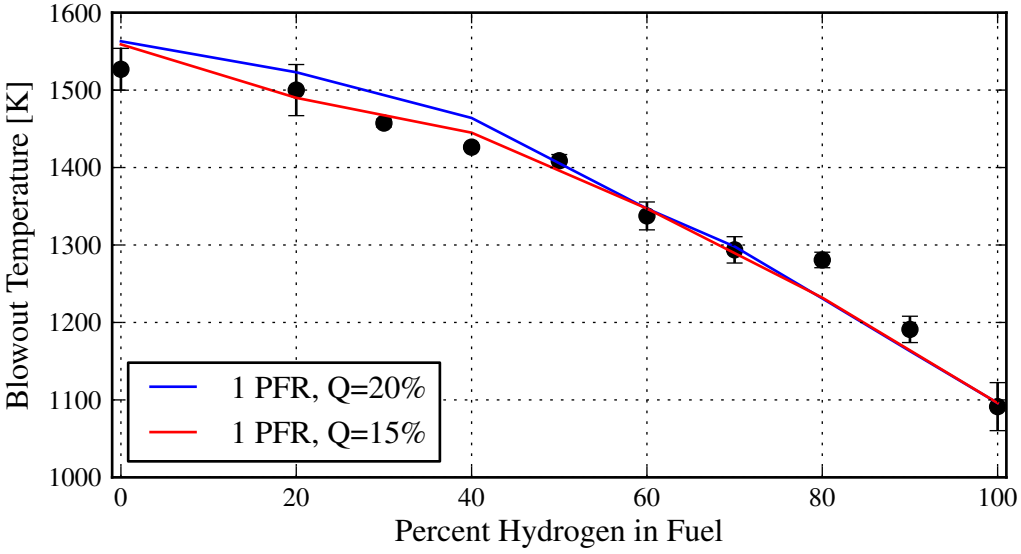

(b) Temperature

Figure E.3: Single PFR model predictions of blowout compared against experimentally determined blowout (a) temperature and (b) equivalence ratio for CH_4 mixed with increasing amounts of H_2.

E.2 Two PFR Model

A similar sensitivity analysis on heat loss is performed for the two PFR model. Figure E.4 shows the behavior of hydrogen with 15% and 20% heat loss. Reducing the heat loss does not improve the agreement between the two PFR model and the experimental data.

Figure E.5 shows the results of methane with 15% and 20% heat loss in the two PFR model.

We can compare the single and two PFR models through Figures E.2 and E.5. If we consider the maximum temperature in the recirculation PFR, the two PFR model matches the measured blowout temperature more closely than the single PFR model. With the single PFR model 15% heat loss allows the model to most closely follow

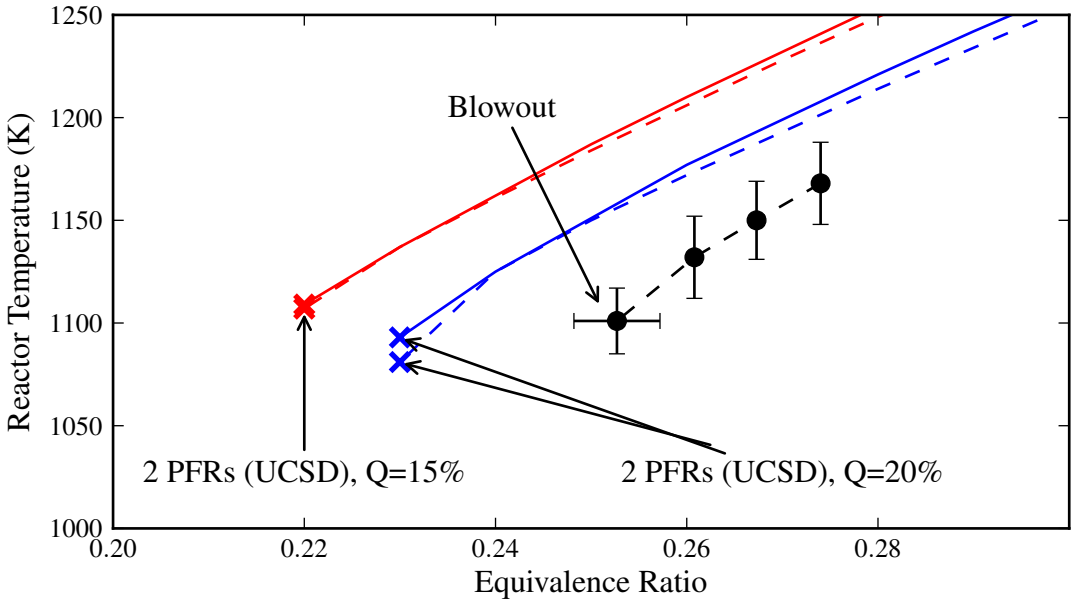

Figure E.4: Comparison of the two PFR modeling results for hydrogen varying the amount of heat loss. A plot of maximum temperature vs. equivalence ratio is given by the solid lines and the probe location temperature vs. equivalence ratio by the dashed lines. Experimental results are given for comparison.

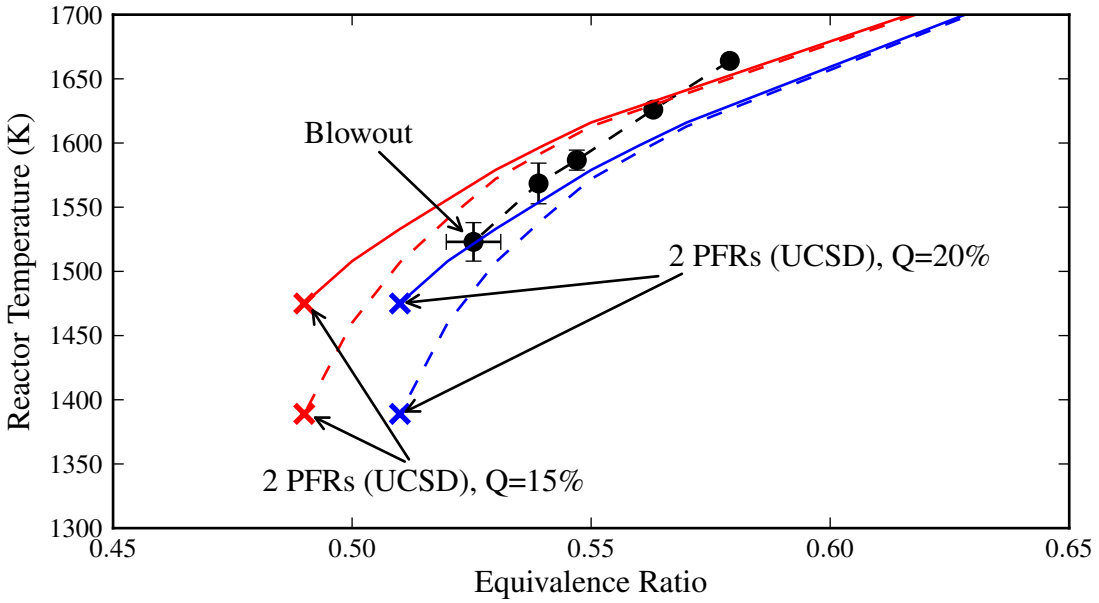

Figure E.5: Comparison of the two PFR modeling results for methane varyingthe amount of heat loss. A plot of maximum temperature vs. equivalence ratio is given by the solid lines and the probe location temperature vs. equivalence ratio by the dashed lines. Experimental results are given for comparison.

the measured temperature vs. equivalence ratio, while with the two PFR model 20% heat loss brings the model in line with the experimental measurements.

Figure E.6 shows the effect of heat loss on the two PFR model in predicting blowout behavior for the full range of fuel blends. The percentage of heat loss only affects the prediction of the blowout equivalence ratio, and a heat loss rate of 20% provides the best agreement across the full range of fuel blends. As with the single PFR model, the predicted temperature at blowout is not much affected by varying the heat loss. The small deviations are most likely due to the step size of 0.01 in equivalence ratio used in determining blowout.

Varying the heat loss for the two CRN models has little effect on the predicted blowout temperature, but does change the predicted blowout equivalence ratio regardless of the fuel.

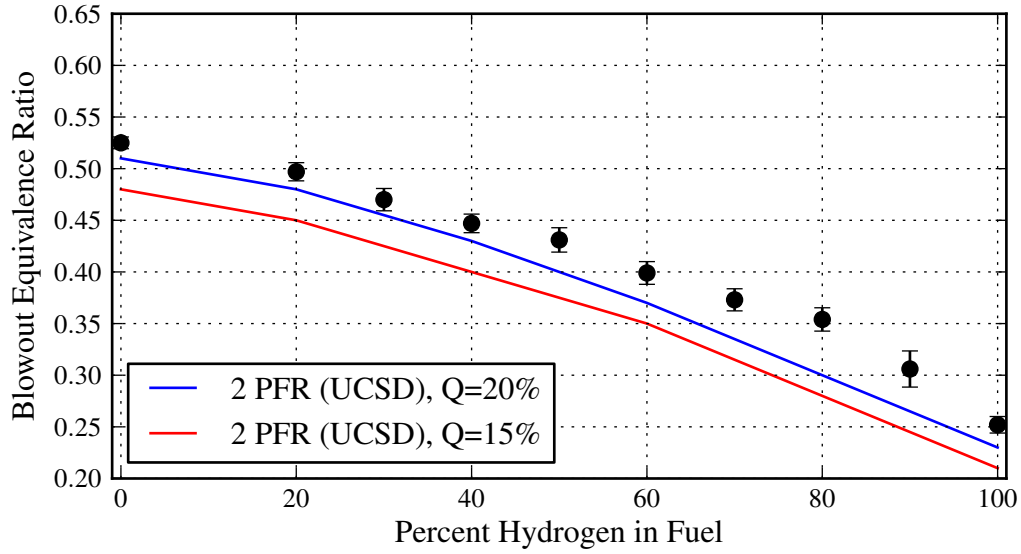

(a) Equivalence Ratio

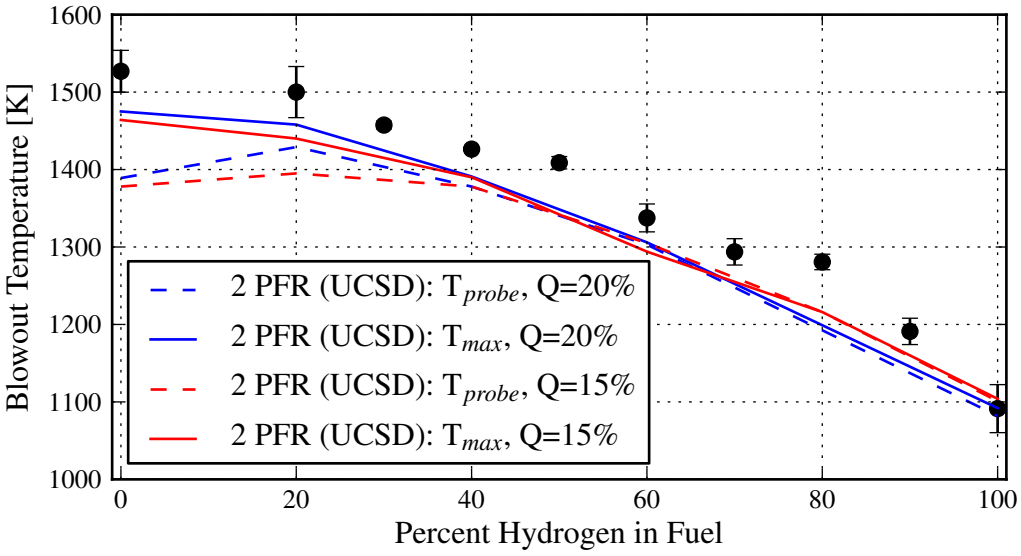

(b) Temperature

Figure E.6: Two PFR model predictions of blowout compared against experimentally determined blowout (a) temperature and (b) equivalence ratio for CH_4 mixed with increasing amounts of H_2.

Appendix F

ANALYSIS OF ACOUSTIC EVENTS

One possible explanation of the acoustic events near blowout for hydrogen combustion involves ignition of the fuel/air mixture by a hot surface. Unburned fuel and air may reach a hot surface, such as the stagnation point at the top of the reactor. This mixture ignites and a flame propagates across the reactor, producing the 'popping' sound. To explore this possibility we use Law's criterion for ignition at a hot surface to compare the time to ignition for hydrogen and methane (since we do not experience the acoustic events with methane blowout) [95]. The ignition criterion is essentially a relationship between the heat transfer from the wall to the combustible mixture and the energy generated by reactions. Before ignition is acheivable there is always heat transfer from the hot wall to the cold gas, and at the first instant of ignitability heat transfer ceases. There is now so much heat generation in the reacting mixture that it does not need to receive heat from the wall any longer in order to sustain the reaction. This is referred to as the 'adiabaticity' criterion for ignition.

The development of the criterion relies on the following assumptions:

- Isobaric process.
- Constant c_p.
- Environment is sufficiently cold such that reaction is frozen in the time of interest
- Extent of reactant consumption is small in effecting ignition
- Reaction is initiated only in a thin layer next to the hot surface

- In the reaction zone (i.e. inner solution) characteristic times of transient processes are much longer than those of diffusion and reaction.

- Single step chemistry.

We can therefore neglect the conservation of species equation and solve only the conservation of energy equation with an asymptotic method. The details of this can be found in [95] beginning on page 319. The solution of the 'inner expansion' of the energy equation (i.e. the reaction zone) reveals:

$$\Delta = \frac{2\epsilon Da_C e^{-\tilde{T}_a/\tilde{T}_s}}{\beta^2} \geq 1 \tag{F.1}$$

where β is a characteristic heat loss rate to the cold ambience from the reaction zone, and ϵ is the small parameter for the perturbation solution given by $\epsilon = \tilde{T}_s^2/\tilde{T}_a$. The variable $\tilde{T}_s^2$ is the temperature at the surface and $\tilde{T}_a^2$ is the activation energy, with both stoichiometrically scaled. To explain the nomenclature further, let's take a one step reaction:

$$\nu'_F F + \nu'_O O \longrightarrow \nu''_P P \tag{F.2}$$

where the subscripts F, O, and P refer to the fuel, oxidizer, and products respectively. The amount of heat released per unit mass of fuel consumed is given by

$$q_c = \frac{\sum_{k=1}^{N} h_k^o W_K(\nu''_K - \nu'_K)}{W_F(\nu''_F - \nu'_F)}. \tag{F.3}$$

The stoichiometric mass ratio of the ith species to the fuel is given by

$$\sigma_i = \frac{W_i(\nu''_i - \nu'_i)}{W_F(\nu''_F - \nu'_F)} \tag{F.4}$$

where W is the molecular weigth. The stoichiometric scalings are then expressed as

$$\widetilde{h^s} = \frac{h^s}{Y_{F,B}q_c}, \qquad \widetilde{T} = \frac{c_p T}{Y_{F,B}q_c}, \qquad \widetilde{Y_F} = \frac{Y_F}{Y_{F,B}}, \qquad \widetilde{Y_O} = \frac{Y_O}{\sigma_O Y_{F,B}} \tag{F.5}$$

where h^s is the enthalpy of formation, Y refers to species mass fraction, the subscript B refers to the free stream, and c_p is the specific heat. Finally, the last definition needed is that for Da_C.

$$Da_C = \frac{l_o^2 B_C}{\lambda / c_p} \tag{F.6}$$

where t is the time to ignition, ρ is the density of the mixture, l_o is a characteristic length scale, and B_C is given by

$$B_C = B \left(\frac{\nu_F' W_F}{Y_{F,B}} \right) \left[\frac{\sigma_O (p\bar{W})/(R^o W_O)}{(q_c/c_P)} \right]^{\nu_O'} \left[\frac{p\bar{W}/(R^o W_F)}{(q_c/c_P)} \right]^{\nu_F'} (Y_{F,B} q_c / c_P)^{\alpha} \tag{F.7}$$

where p is the pressure and R^o is the gas constant. For the ignition of an unconfined mixture by a flat plate the heat transfer is given by the outer solution of the energy equation such that $\beta = (\tilde{T}_s - \tilde{T}_\infty)/\sqrt{\pi \tilde{t}}$. The variable $\tilde{t}$ is a nondimensional time expressed as

$$\tilde{t} = \frac{\lambda / c_p \rho}{l_o^2} t \tag{F.8}$$

where λ is the thermal conductivity.

The final relationship for the time to ignition is given by

$$t = \frac{\rho \tilde{T}_a (\tilde{T}_s - \tilde{T}_\infty)^2 e^{\tilde{T}_a / \tilde{T}_s}}{2\pi \tilde{T}_s^2 B_C Y_{O,B}^{0.5}}. \tag{F.9}$$

Using a single step global reaction for hydrogen taken from [11] as Equation F.10 and a single step global reaction for methane taken from [20] as Equation F.11, a plot of time to ignition for the measured blowout equivalence ratio for each fuel vs. surface temperature normalized to the experimentally measured blowout temperature for each fuel is given in Figure F.1. The average and maximum surface temperatures are taken from CFD near the blowout condition.

$$k_{H2} = 1.8 \times 10^{13} \exp(-17614/T) [\mathrm{H_2}] [\mathrm{O_2}]^{0.5} \tag{F.10}$$

$$k_{CH4} = 1.3 \times 10^{8} \exp(-24358/T) [\mathrm{CH_4}]^{-0.3} [\mathrm{O_2}]^{1.3} \tag{F.11}$$

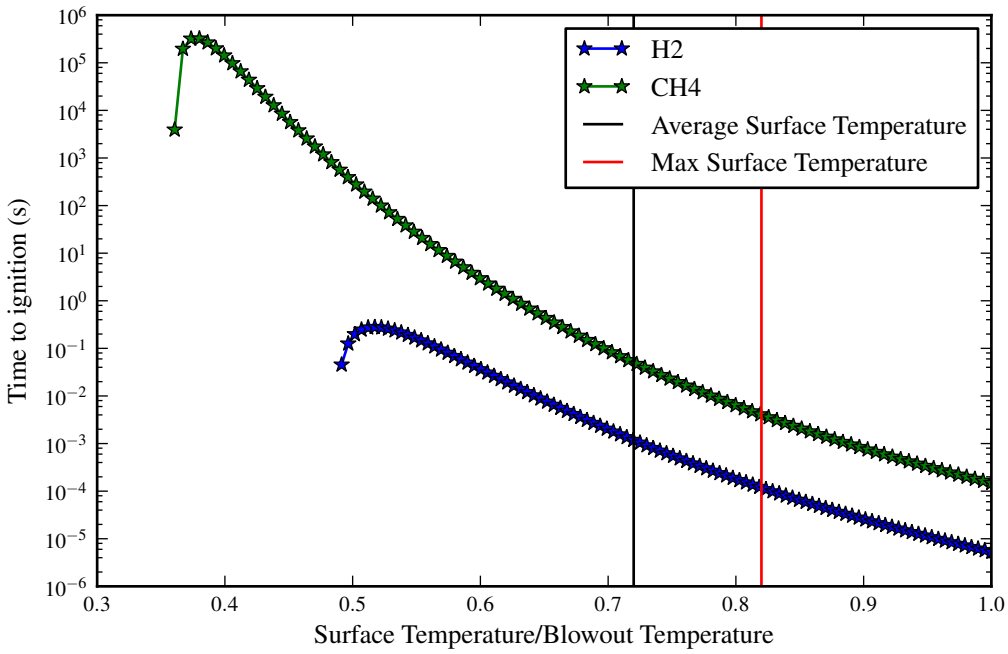

Figure F.1: Comparing time to ignition for hydrogen and methane under blowout conditions.

Figure F.1 illustrates the discrepancy in ignition times for H_2 and CH_4. At the maximum surface temperature the time to ignition for H_2 is about 0.1 ms whereas the time to ignition for CH_4 is almost 4ms. For comparison, the acoustic events near blowout for H_2 occur every 50 ms on average.